Finite Element Modelling of the Small Punch Test for Structure Critical Design

By

Victoria Brown

A thesis submitted for the doctor of Philosophy

The University of Sheffield

Department of Materials Science and Engineering

November 2020

Abstract

The development of nuclear fusion reactors presents complex challenges in materials design and development. To ensure that structure critical materials can withstand the conditions within the pressure vessel extensive testing must be carried out. This will include, in part, the testing of specially irradiated specimens. The intensity of the irradiation means that only a small volume of material will be produced and available for testing. Necessitating the development of small scale mechanical testing. One such test method is small punch testing. For small punch testing to be considered a viable testing technique for structure critical design a reliable correlation between small scale and bulk scale must be made.

In this thesis the creation of a small punch test finite element model was presented. The model, created in Abaqus 2017, was used as a basis for the optimisation of Johnson-Cook materials and damage model parameters of P91 and Eurofer97 steels at room temperature. An effective method for the optimisation of the Johnson-Cook materials model parameters was developed. This method utilised the scripting capabilities of Abaqus in conjunction with the SciPy optimise module within Python to perform inverse analysis via the Nelder-Mead algorithm. The results were successfully validated by use of the Considére Criterion, demonstrating that they were conservative with a confidence of 95%. The early stages of a method for the optimisation of the Johnson-Cook damage model parameters were presented, with the effects of the friction between sample and punch head was also highlighted.

The force-deflection curve analysis methodologies provided in the code of best practice and ASTM standard were also analysed. Examination of the proof stress and UTS estimation methods provided in the code of best practice methods displayed an overestimation when calculating values from steel tests at room temperature.

Overall, the basis for the development of a novel method for the calculation of Johnson-Cook materials and damage behaviour from a small punch test was presented. Through effective validation this, and further work has the potential to be applied in the design and quality assurance of structural materials for future fusion reactors.

Acknowledgements

I would express my gratitude for my supervisors, Brad Wynne and Amy Gandy for their support and patience throughout this project. I would also like to thank Mark, and the other members of the Small punch test team at CCFE for their technical advice over the last 4 years.

To all of my family and friends, I want to say how appreciative I am of the encouragement through the most difficult parts of this process.

And finally, I would like to thank Ed. Without your constant support and kindness, none of this would have been possible. Thank you.

This work has been carried out within the framework of the EUROfusion Consortium and has received funding from the Euratom research and training programme 2014-2018 and 2019-2020 under grant agreement No 633053. The views and opinions expressed herein do not necessarily reflect those of the European Commission. This work has also been supported by the RCUK [grant number EP/T012250/1] and the UK Government Department for Business, Energy and Industrial Strategy (BEIS).

"She was also, by the standards of other people, lost. She would not see it like that. She knew where she was, it was just that everywhere else didn't."
— Terry Pratchett, Equal Rites

"But then science is nothing but a series of questions that lead to more questions, which is just as well, or it wouldn't be much of a career path, would it?"
– Terry Pratchett & Stephen Baxter*,* Long Earth

Contents

Table of Figures

Nomenclature

Tensile tests

σ – Stress (MPa)

$\sigma_{engineering}$ – Engineering stress (MPa)

σ_{true} – True stress (MPa)

F – Applied force (N)

A_0 – Initial specimen cross section (mm^2)

A – Instantaneous specimen cross section (mm^2)

ε – Strain

$\varepsilon_{engineering}$ – Engineering strain

ε_{true} – True strain

L – Original gauge length (mm)

ΔL – Change in gauge length (mm)

Compression tests

h – Instantaneous specimen height (mm)

h_0 – Initial specimen height (mm)

Three-point bend tests

C – Distance between two lower supports (mm)

L – Support span (mm)

r – Radius of plunger (mm)

d – Depth of beam (mm)

b – Width of beam (mm)

D – Deflection at centre of beam (mm)

m – slope of tangent to loading portion of load deflection curve (N/mm)

Vickers Hardness test

HV – Vickers hardness (kgf/mm^2)

A – contact area (mm^2)

α – face angle of the indenter (136.0˚)

d_V – mean Vickers indentation diagonal length (mm)

Charpy impact test

A – Impact energy (J)

M – Mass of hammer (kg)

g – Gravitational potential energy (9.81 m/s^2)

ΔH – The difference between initial and final height of the hammer (mm)

Small ring test

$\dot{\Delta}$ – creep deformation rate

η and β – conversion factors that vary with specimen dimensions

a and b – major and minor axis dimensions of an elliptical specimen

b_0 – specimen depth

d – specimen thickness

P – load

Two bar test

L_0 – gauge length

k – length of loading pin supporting end

D_i – diameter of loading pins

b – bar width

d – specimen thickness

$\dot{\Delta}_{ss}^{c}$ – creep deformation rate

β – conversion factor dependant on specimen dimensions

$\dot{\varepsilon}^{c}$ – Equivalent uniaxial minimum creep rate

Small Punch test

D – Sample Diameter (mm)

h – Sample Thickness (mm)

r – Punch Radius (mm)

D_r – Receiving die diameter (mm)

L – Chamfer Length (mm)

F – Punch force (N or kN)

v – Punch displacement (mm)

u – Sample deflection (mm)

F_M – Maximum punch force reached (N or kN)

v_M – Punch displacement at F_m (mm)

u_M – Sample deflection at F_m (mm)

F_F – Punch force at sample failure (N or kN)

v_F – Punch displacement at F_f (mm)

u_F – Sample deflection at F_f (mm)

F_A – Punch force at the elastic-plastic transition (N or kN)

v_A – Punch displacement at F_a (mm)

u_A – Sample deflection at F_a (mm)

F_B – Force at a deflection of 0.5mm

E_{Pl} – Plastic energy required to deform sample to F_M

E_{el} – Elastic energy required to deform sample to F_M

E_{Tot} – Total energy required to deform sample to F_M

$\sigma_{0.2}$ – Yield or proof stress estimation (MPa)

$\beta_{\sigma 0.2}$ – Geometric correlation coefficient proof stress estimations

UTS – Ultimate tensile strength (MPa)

β_{UTS} – Geometric correlation coefficient for ultimate tensile strength estimations

u_i – displacement at the onset of plastic instability (mm)

F_i – force at the u_i (N or kN)

Small Punch Creep Test

σ – equivalent uniaxial creep stress

k_{SP} – ductility related coefficient

Ψ_{EFS} – the force to stress ratio

u_{min} – the deflection at the point in which the deflection rate reaches a minimum

$\dot{\varepsilon}_{min}$ – minimum strain rate

Ductile to brittle transition temperature using the small punch test

T_{SP} – Small punch ductile to brittle transition temperature

T_{CVN} – Charpy ductile to brittle transition temperature

α – Correlation factor usually ≈ 0.4

Finite element modelling

U^h – Displacement approximation

n_d – Number of nodes forming the element

d_i – The displacement of the ith node

N_i – The shape function

u_i - Displacement in the x direction

v_i - Displacement in the y direction

w_i - Displacement in the z direction

Simplex Algorithm

n – Number of variables

y_i – Function

P_i – Point along the function y_i

P_j – Point along the function y_i

y_h – Maximum possible value of y_i

y_l – Minimum possible value of y_i

$\bar{P}$ – A centroid point between y_h and y_l where $i \neq h$

P_h – highest value of P

α – The reflection coefficient (always positive)

γ – The expansion coefficient

β – The contraction coefficient

1. Introduction

A key element in making nuclear fusion power plants a reality, and thus putting electricity generated from fusion power on to the grid, is the development and validation of new materials capable of withstanding the ultra-extreme conditions found within the reactor vacuum vessel. Temperatures up to 100 million degrees Celsius, heavy neutron loading, and significant fatigue cycles are all factors that must be considered [1]. As such, the material property requirements include high resistance to irradiation damage, excellent creep resistance, and good high-temperature strength, which by itself is a significant demand for material development [2]. However, because of end-of-life requirements necessitating that no material can be significantly radioactive 100 years after removal from the reactor, the number of elements that are suitable is limited making material development a grand challenge [3], [4]. Moreover, there is currently no experimental facility capable of producing the conditions of the fusion reactor vessel on a large enough scale to produce enough exposed material to undertake standard property assessment, particularly the high flux density of high energy neutrons [5]. Thus, the use of full-scale methods available to accurately assess the material's potential performance in-service are currently not viable and this has led to a significant investment in research into the use of small-scale testing techniques, e.g., miniaturised tensile testing. Of these methods, small punch testing has shown great promise at indirectly obtaining macroscale properties such as ultimate tensile strength through empirical correlation. In this thesis, finite element modelling combined with inverse analysis is explored as a potential method for gaining more confidence in the correlation between small punch data and macro-scale properties. This is undertaken with the ultimate aim of generating enough confidence in small punch testing that the data it produces is sufficiently robust to be used in design calculations.

1.1 Why nuclear fusion?

Since the industrial revolution of the 18th-century carbon emissions into the atmosphere have steadily increased, leading to an overall rise in global temperatures [6]–[9]. Global warming has been the subject of many recent headlines because of possible contributions to extremes in weather experienced across the world [9]. Increased global temperatures and extreme weather have highlighted the need to find new, carbon free means of producing electricity. A move away from fossil fuels is vital if the temperature rise capped is to be at 1.5˚C [10]. One promising route is nuclear power. Nuclear fission has been employed in many countries over the last few decades, but it has proven to be problematic. Several serious accidents, military connections, and the production of waste that will be hazardous for at least one million years has led to a largely negative public opinion [11]–[13].

Nuclear fusion, however, has yet to be implemented on the commercial level and is still in the early stages of development, but it promises clean energy without the negative public perception that nuclear fission has [1], [14].

1.2 Nuclear fusion and fission

The mass of an atomic nucleus is less than its constituent parts because a proportion of the nucleon mass is converted to energy that binds the nucleus together, known as the binding energy. Binding energy is governed by the mass-energy relationship described by Einstein's Equation, $E=mc^2$ [15]. Each element has a distinct binding energy per nucleon. The greater the binding energy per nucleon, the more stable the nucleus, as illustrated in Figure 1.1, which shows Fe^{56} to have the highest binding energy, making it the most stable nucleon. Much heavier nucleons than those around Fe^{56} are therefore less stable suggesting that if they split they would become more stable. This is known as nuclear fission. On the other hand, lighter nucleons have less binding energy per nucleon associated with them so the driving force is for them to fuse, become heavier, and therefore become more stable. This is known as nuclear fusion. With the increase in stability comes a decrease in overall energy, meaning a large amount is released in the form of kinetic energy for both the fission and fusion reactions [16], [17].

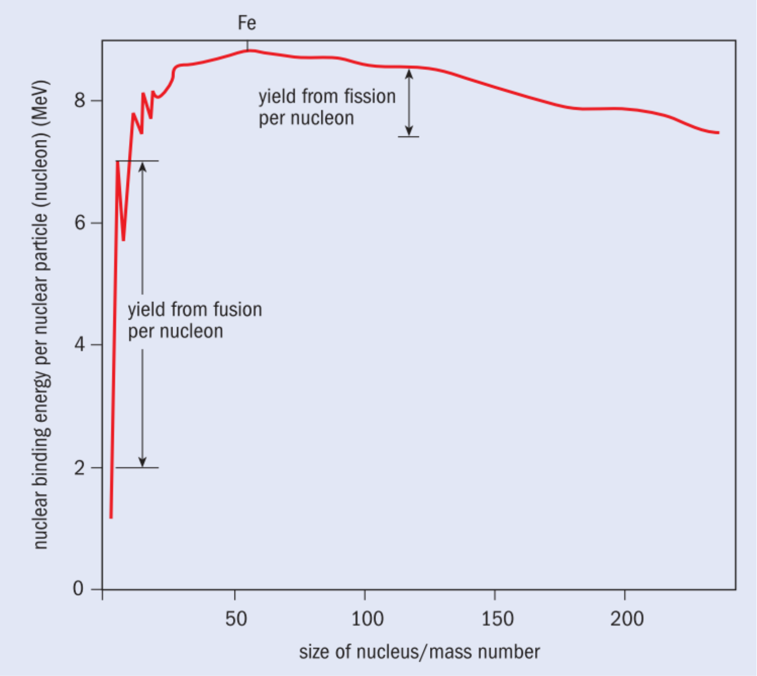

Figure 1.1: Diagram of the binding energy per nucleon for known nuclides. Important/notable isotopes have been highlighted [17].

For both fission and fusion some fundamental forces must be taken into consideration, namely the Coulomb repulsive force and the strong nuclear force.

The Coulomb repulsion is the electromagnetic force that acts between particles of the same charge. Operating over a range of length scales, its effect is proportional with the inverse square of the separation distance, i.e., the repulsive force is very high at close separation distances. This prevents such particles from coming into contact. In atomic nuclei the Coulomb repulsion is counteracted by the attractive strong nuclear force.

The strong nuclear force is over 100 times stronger than the electromagnetic force [18]–[20]. It has an effective distance of 1fm (10^{-15}mm), and therefore only affects objects within and approaching the nucleus of an atom [21]. Thus, two positively charged protons can exist in close proximity to one another at a particular equilibrium distance, as illustrated graphically (Figure 1.2), where the Coulomb repulsion balances out the strong nuclear force.

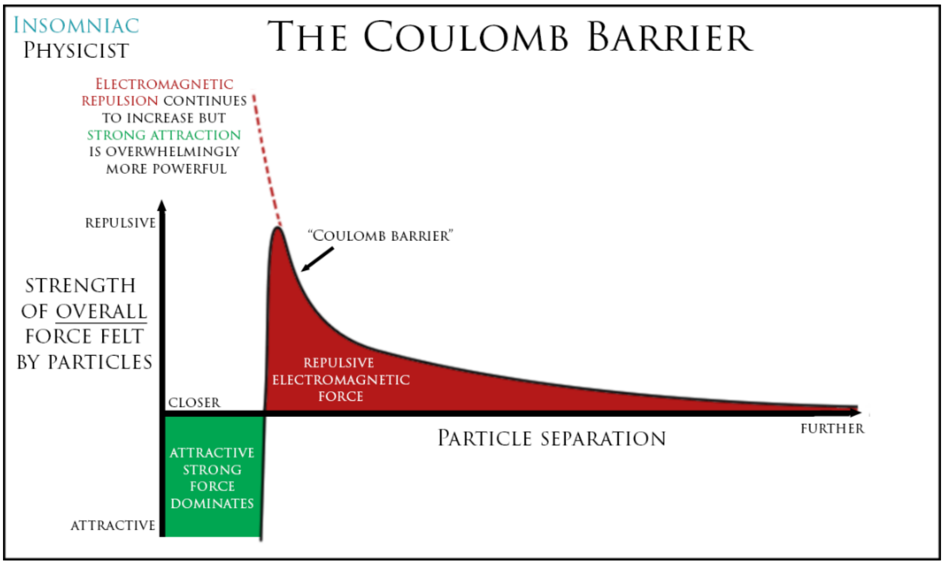

Figure 1.2: A graph displaying the force experienced by two protons coming into close proximity with each other. The Coulomb barrier can be seen in red, and the strong force energy well in green Image from: "Layman's Astronomy 1.02: Stars, Waves and nuclear fusion" [22].

Some heavier isotopes, such as Pb^{205} and U^{235}, have nuclei with radii that are near the limit of the effective strong nuclear force distance, meaning Coulomb repulsion is the dominant force [23], [24], which in turn means the energy barrier for fission, is relatively low. The classic example is U^{235} where the fission reaction is triggered by absorption of a slow moving thermal neutron to form U^{236}, which quickly decays to two lighter elements and neutrons, leading to a small mass loss that is converted into energy that heats steam to drive a turbine to generate electricity [25].

Much like fission, the nuclear fusion reaction is energetically driven. The strong nuclear force has a large effect over small nuclei (everything lighter than iron), thus fusing two light isotopes together will produce a product that is substantially more stable along with high energy by-products [21].

One reaction in particular is favoured by engineers for its energy production potential due, in part, to its high cross section. It consists of two hydrogen isotopes; Deuterium ($^{2}_{1}H$) and Tritium ($^{3}_{1}H$). Deuterium contains an extra neutron giving it an atomic mass of 2.014, whereas tritium has two extra neutrons giving it an atomic mass of 3.016 [26]. Fusing deuterium and tritium produces the largest amount of energy compared to other hydrogen-based reactions making it ideal for power generation applications. High energy neutrons (14.1 MeV) and helium nuclei (at 5.5 MeV) are produced. This reaction, often described as the D-T reaction, can be seen in Equation 1.1 [17].

$$^{2}_{1}H + ^{3}_{1}H \rightarrow ^{4}_{2}He + ^{1}_{0}n \ (+17.6MeV)$$

Equation 1.1

Achieving the conditions required for fusion is challenging. Either pressures equal to those at the centre of the sun, or temperatures upward of 150 million degrees Celsius are needed [27]. To initiate fusion on the scales needed for energy production on Earth, reaching high temperatures is the only realistic option. This is achieved by producing a plasma. A plasma is an ionised gas and is the only state in which nuclear fusion can be sustained [28]. The ionisation separates nuclei from their accompanying electrons. In this state the free nuclei have sufficient energy to overcome the electrostatic repulsion and fuse [17]. To maintain continuous fusion reactions temperatures of 100-200 million degrees Celsius are required [1].

Maintaining and controlling a fusion plasma presents some interesting engineering challenges. The plasma vaporises anything that it comes into contact with, meaning that it must be controlled by means other than physical containment. Two methods are usually implemented, either inertial or magnetic confinement. Magnetic confinement is favoured in Europe and Japan. It utilises strong electromagnets which surround a toroidal pressure vessel (Figure 1.3). When active, the magnets trap the plasma along the field lines, thus containing it without the need for material contact. This style of reactor has been named Tokamak. Two such reactors are located at Culham Centre for Fusion Energy (CCFE) in Oxfordshire, UK. CCFE is part of a group of research organisations in Europe known as Eurofusion [29].

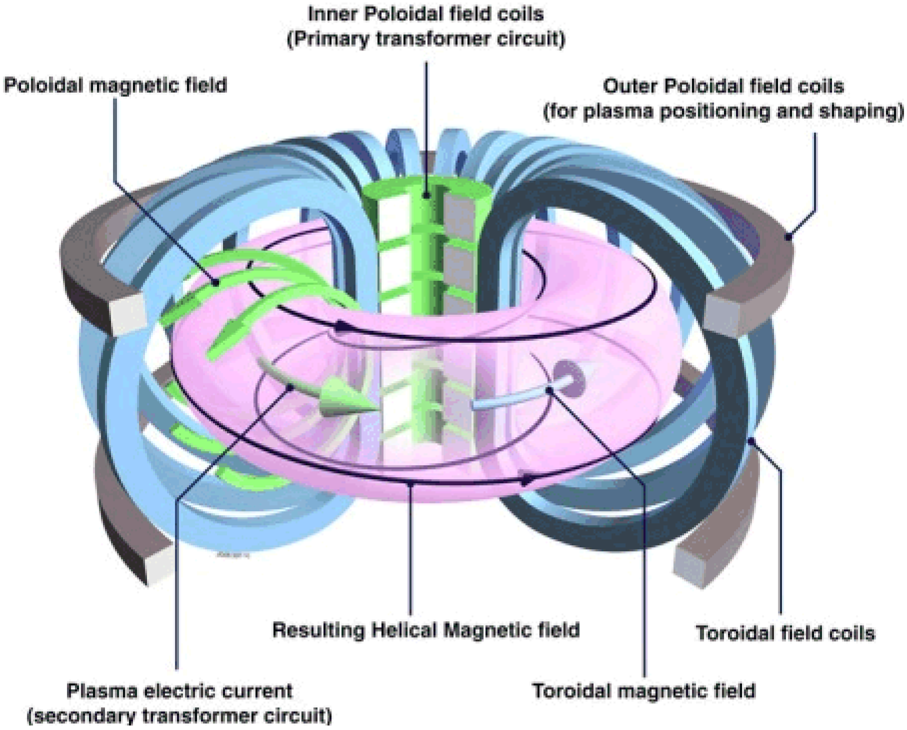

Figure 1.3: A diagram of the TOKAMAK type reactor with key features labelled [30]

The Joint European Torus (JET), currently the world's largest magnetic fusion reactor, is managed by CCFE and used by scientists globally. The JET facility is seen as the basis for the next stage in Fusion power generation, ITER.

ITER is currently under construction and with first plasma planned for December 2025 will be the largest Tokamak reactor experiment ever. The aim of the ITER project is to test several aspects of the plant for their commercial viability with the eventual goal of reaching a return of energy (Q) of 10, i.e., the energy produced from the fusion reaction will be ten times that which is put in to start and maintain it. If successful, ITER will lead onto the next phase of the commercialisation of fusion power. This new project will be called DEMO and will essentially be a trial run for all future fusion power plants (Figure 1.4).

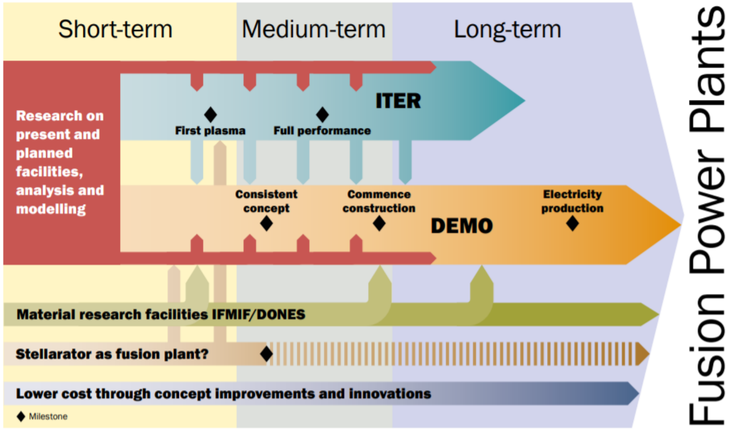

Figure 1.4: An overview of the roadmap to power generation by nuclear fusion. Diagram from " European Research Roadmap to the Realisation of Fusion Energy" [31].

While fusion energy has the potential to produce vast amounts of clean electricity, it also presents significant engineering challenges that must be overcome. The plasma facing components in particular experience conditions that require special consideration.

A major source of material damage and property degradation is caused by high energy neutron radiation. The neutrons emitted from the D-T fusion reaction have a distinct neutron spectrum and is noticeably different to that of a fission reaction (Figure 1.5).

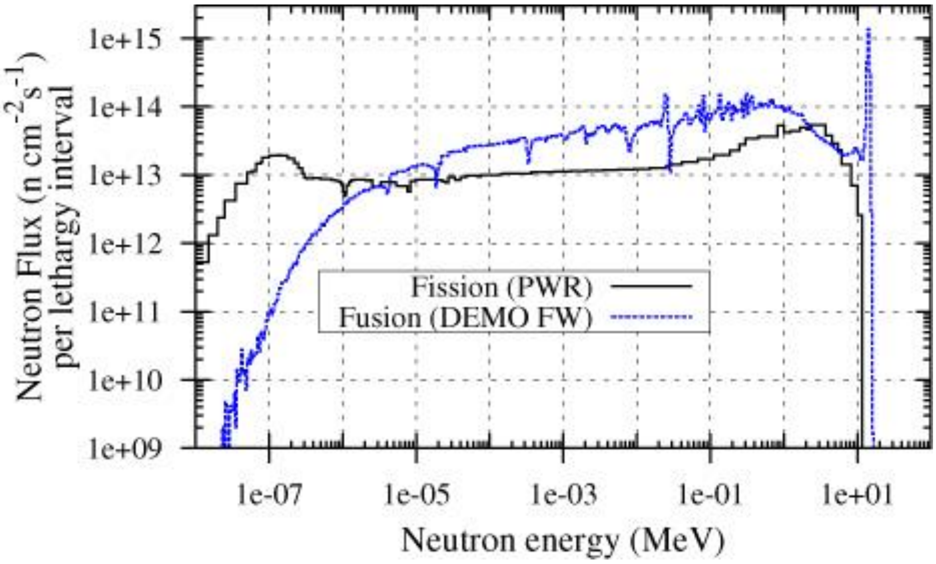

Figure 1.5: A graph showing the neutron spectrum of neutrons produced by fission and fusion reactions. Note the large peak at 14MeV for the fusion reactions [32]

It can be seen from Figure 1.5 that there is a large spike in the predicted neutron flux at the 14MeV point in the fusion reaction for DEMO. This is in sharp contrast to the neutron spectrum from fission which has a maximum energy of around 5MeV with its flux peak much lower than that. This makes it difficult to predict the potential levels of damage induced by fusion reactions from fission data and experience.

The extremely high energy neutrons illustrated in Figure 1.5 above present the biggest challenge as they carry a huge potential for damage. When a high energy neutron enters a lattice it is likely to interact with the atoms within it. If a particle interacts directly, i.e., collides with an atom in the lattice it may knock it off its lattice position and impart a proportion of energy to it. This atom may then go on to knock further atoms off their place, in a phenomenon known as a displacement cascade, leading to the formation of interstitial-vacancy pairs. This can cause several larger defects to form in the lattice, which have the potential to coalesce and form stacking fault tetrahedra, dislocations, and voids [33], [34].

The combined effects of being exposed to radiation also produces macroscale changes to materials. These can include, embrittlement, swelling, and transmutation, leading to mechanical and geometric changes [5], [32], [33], [35]–[37].

Radiation embrittlement is one of the primary concerns for materials within nuclear reactors and can occur via various possible mechanisms [38]. The predominant mechanism is initiated by a direct change to the lattice. Displaced atoms cause vacancy interstitial pairs leading to point defects. These grow and coalesce to form dislocations loops and voids [38].

The extreme temperatures within the reactor can cause high rates of diffusion. The diffusion can cause elements that were in solid solution to migrate and segregate into the areas of high damage, thus forming zones that are enriched or depleted of certain alloying elements. The enriched zones may then go on to precipitate particles that can stop dislocation movement and therefore increase strength and concurrently make the material brittle [38]. Generally speaking, any mechanism that disrupts the movement of dislocations will produce a hardening effect.

Void swelling is caused by the formation of voids within the irradiated materials. These voids can agglomerate and form pores, leading to a geometrical change on the macro scale. The process in which such voids and pores form is not clear, but it is thought to be a combination of implantation of hydrogen and helium, along with the formation of vacancies as described above [36], [39], [40]. Void swelling can lead to distortion and macro-scale geometrical changes, thus presenting significant complications in design and operation [40].

Irradiation by neutron bombardment has a significant effect on the creep properties of a material [35]. Creep is defined as time dependant plastic deformation at elevated temperatures under a fixed stress [35], [41], [42]. Governed by diffusion and grain boundary movement, creep is highly sensitive to temperature and lattice changes. Through the disruption of dislocation movement, phenomenon like embrittlement and void swelling will fundamentally change creep behaviour. In some cases the embrittlement and voids slow creep, only to increase it after a certain displacements per atom (dpa) threshold [35], [43], [44].

It should be noted that the damage effects are concentrated at the surface of plasma facing components. As can be seen in Figure 1.6 the damage effects appear to drop off rapidly away from the surface [32].

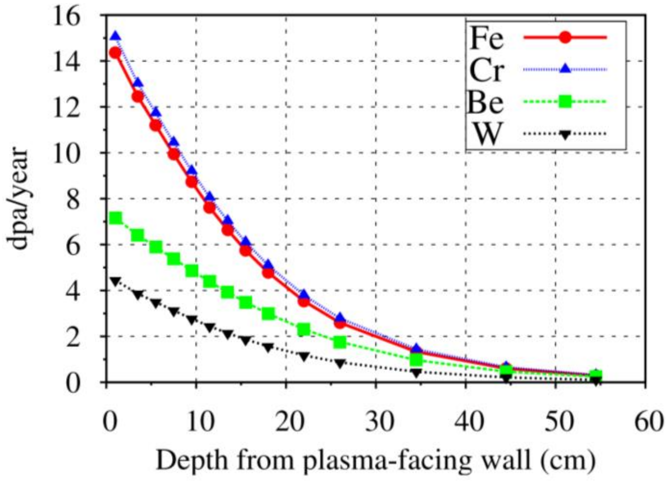

Figure 1.6: A graph showing the change in rate of damage for materials within the fusion reactor [32]

While the general consequences of radiation damage on materials are widely recognised, little is known about the effect that 14MeV fusion neutrons will have. Especially at the fluxes expected in a fusion reactor (10^{15} n $cm^{-2}s^{-1}$), which are expected to produce damage in the range of 20 displacements per atom, dpa, in the first wall [5], [32], [45]. Any new materials and components must be tested appropriately. However, there are currently no facilities or reactors that produce 14MeV neutrons at a sufficient flux for testing. To overcome this a specialised facility is to be built, dubbed the International Fusion Materials Irradiation Facility, or IFMIF [46].

IFMIF is a project jointly run by Japan and the EU. The facility will make use of two accelerators in parallel which will be capable of producing a suitable flux of 14MeV neutrons. While producing the required amount of damage will be possible, it will only be able to produce it in a volume of 0.5L (Figure 1.7). This becomes an issue when it comes to mechanical testing. Full scale tests require large amounts of material, which simply will not be available. Subsequently new methods of testing a material's mechanical properties are needed [46], [47].

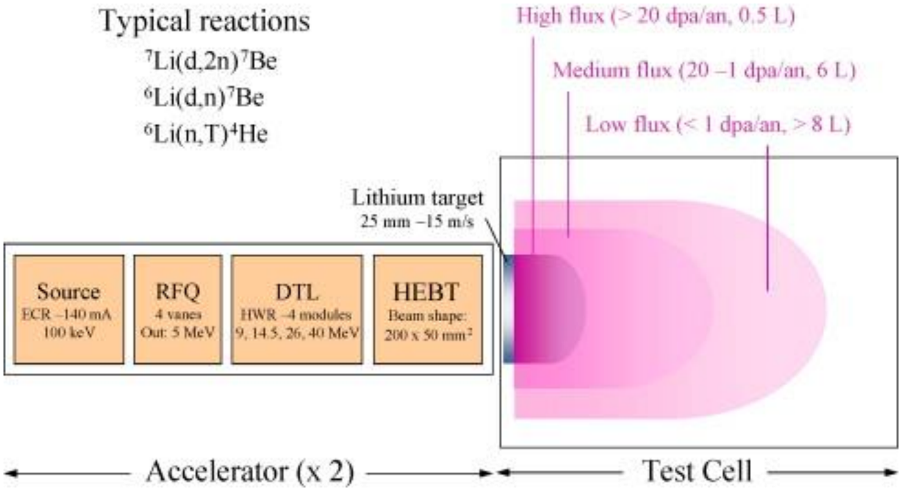

Figure 1.7: A diagram of the IFMIF facility accelerator with important features labelled [46]

Transmutation leads to difficulties at the end of reactor service life. Some elements have high absorption cross sections for the high energy neutrons produced in fusion. Absorption of these can lead to activation of these elements leading them to decay and transmute. This can produce hydrogen, helium, and other elements. The hydrogen, and helium within the lattice can cause further embrittlement [37]. Some of the activated elements can also remain radioactive for thousands of years, thus making dismantling and recycling a problem. The effects of this can be seen in the current decommissioning of fission reactors. They will require special facilities to store radioactive components for up to 10^6 years [11]. To avoid this problem, the fusion community has agreed to eliminate any alloying element that can become radioactive long term. Ultimately any component in the reactor must be recyclable 100 years after decommissioning [48]–[50]. To get around this problem, the fusion community has agreed to eliminate any element that can become radioactive long term. The materials developed with this concept are known as low or reduced activation materials. They follow a simple rule: any material exposed to radiation within a fusion reactor must be able to be recycled in around one hundred years of being removed from the reactor [4], [48]–[52].

Along with the difficulties outlined above, the influence of material transmutation must be taken into account. Transmutation occurs when a neutron is 'captured' by an elemental atom, the atom then becomes unstable and can generally emit a helium atom or a single proton. This process has two effects. The first being a build-up of gas within the material which can have serious effects like swelling and embrittlement. The second being the change of the elemental atoms themselves. Once an atom has emitted a He or H it will no longer be the same element. This process can in turn produce unstable/radioactive atoms, which will continue to emit radiation over time. In some cases, this can be for many thousands of years [37].

While reduced activation materials, will reduce the need for long term nuclear waste disposal, they present their own unique set of challenges. To be considered low activation an element's activity must fall below the safe handling limit within a hundred years (Figure 1.8). While elements like iron and chromium fall into this bracket, there are some that clearly do not, namely molybdenum. Some of these can sometimes be part of standard alloys used in structural applications today, thus making said alloys not appropriate for fusion reactors. Using this information, a new set of materials has been developed. One alloy in particular, Eurofer97, a 9Cr structural steel designed to replace CR-1Mo steels has become the current standard that other alloys are assessed against [50].

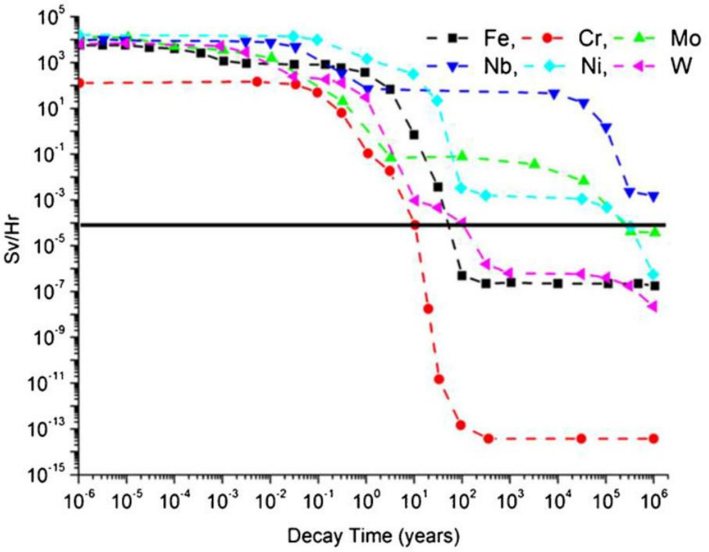

Figure 1.8: A graph showing the change in activity over time for various common alloying elements. The black line shows ITER administrative limit for hands on maintenance [52], [53]

As with existing materials, any new alloy developed must go through the same rigorous testing to ensure that it is safe for use in a fusion reactor. Along with the irradiation testing from IFMIF, standardised testing will also be required. However, as with all new materials there are relatively small volumes available for testing in the first place, thus reducing the amount of material needed for a test would allow for more tests to be carried out on the same volume of material.

A possible answer to such material availability issues is small scale testing. While simple in concept, small-scale testing comes with its own difficulties. To explain this, it is pertinent to first define small-scale testing.

1.3 Small scale mechanical testing

The term small scale mechanical testing covers a range of tests from simple tensile tests to the more complicated small punch tests. Test sample size can range in size from millimetres to as small as a few nanometres across. This section will focus on tests which require samples on the millimetre length scale [54].

This group of testing techniques is particularly useful for nuclear applications. Firstly, as explained above, there may be a limited amount of material available for testing; and secondly an irradiated sample will pose a radiation risk, thus reducing the overall volume of material used in a test will be beneficial in reducing any potential exposure to operators [54].

Some of these small scale tests are miniaturised replicas of those performed at the bulk scale. Such tests include tensile, bend, and Charpy (Figure 1.9). Other tests are performed exclusively on the small-scale, these include microhardness, and small punch testing [54].

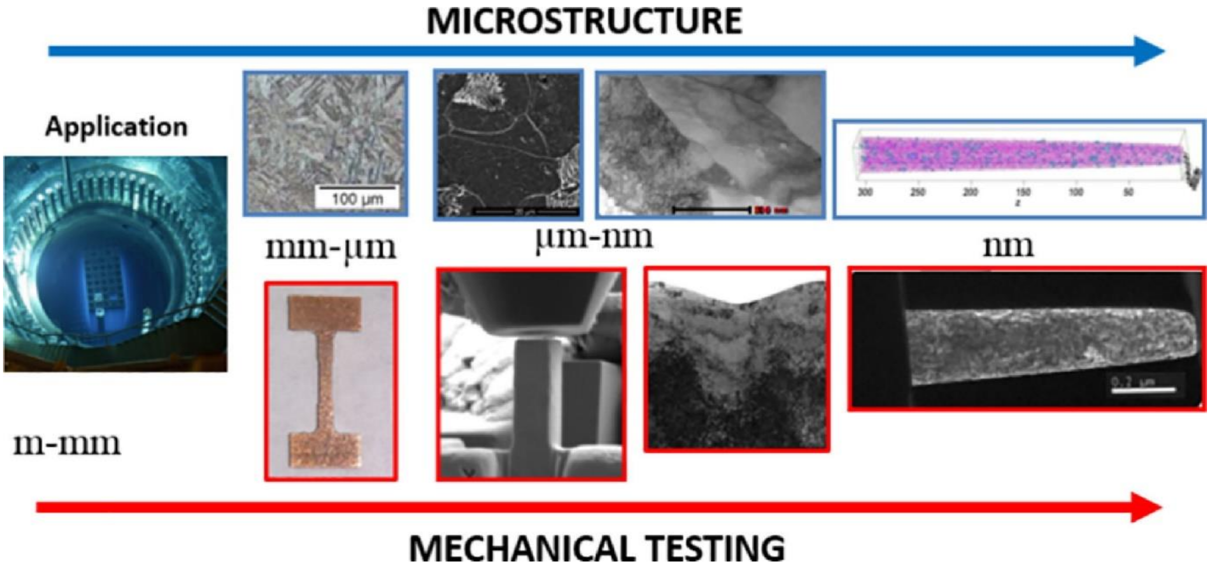

Figure 1.9: A diagram displaying the length scales that small scale testing cover, compared with the length scale of materials in service [54].

A common problem seen across all small-scale testing techniques is the apparent change in material behaviour with decreasing size. In most cases, materials appear to have superior properties when tested at the smaller scale [55], [56]. The changes observed, however, do not show a systematic difference to their bulk scale counterparts making the implementation of small-scale testing much more complex. This is thought to be due to several factors, which will be discussed further on.

Small scale testing methods have been employed for plant life monitoring and extension. However, due to indirect measuring they are still unsuitable for alloy and reactor design work [56].

1.4 Thesis Aims and Objectives

The aims of this thesis are:

1. To develop a robust and consistent methodology for extracting bulk mechanical material property data from the data acquired from the small punch test.
2. To develop criteria that establish the level of confidence in the quality of the bulk mechanical material property data using the method developed.
3. Give recommendations on the worthiness of small punch testing for further research investment on the roadmap for qualification of fusion related materials.

These will be achieved through the following objectives:

a) Fully understanding the best practise guide for small punch testing and its role in ensuring consistency and reliability.

b) Using the code of best practice and ASTM standard as a basis, create a finite element model of the small punch test using the Abaqus 2017 software package.

c) Utilise robust material behaviour models included in the software, namely the Johnson-Cook plastic and damage models.

d) Complete sensitivity testing and validation of the model to ensure the best possible outcome.

e) Provide a model that is a simple engineering solution that produces results that could be considered a suitable basis for further development.

f) Adapt the model for an investigation into the use of inverse analysis for the prediction of the Johnson-Cook model parameters.

g) A Python script will be created that will use the simplex method to find optimal values for each of the Johnson-Cook model parameters.

h) The results from the optimisation will be assessed empirically to ensure accuracy and validity.

To communicate how this was achieved, the thesis is split into the following Chapters:

Chapter 2 – Literature review: This Chapter will provide an in-depth look at the background behind small scale testing and small punch testing. It will also include an overview of finite element simulation and inverse analysis with respect to the small punch test.

Chapter 3 – Methodologies: Chapter 3 describes the general methodologies used in the succeeding Chapters.

Chapter 4 – Small Punch test data analysis: Looking at the estimation methods provided in the code of best practice, ASTM standard, and round robin will prove useful for furthering understanding of the small punch test before starting the simulation portion of the project.

Chapter 5 – Model building and validation: Chapter 5 will offer an in depth look at the construction of the small punch test finite element model including the validation of several key variables.

Chapter 6 – Optimisation of the Johnson-Cook Plasticity constants: This Chapter focuses on the inverse analysis of the Johnson-Cook plasticity values. Operating off the work started in Chapter 5, this section builds on it through the use of scripting software to automate the analysis and produce a workable method for future unknown alloys.

Chapter 7 – Optimisation of the Johnson-Cook Damage constants: This Chapter builds the basis for the optimisation of the Johnson-Cook damage constants. This will be a development from the work completed in Chapter 6.

2. Literature Review

2.1 Introduction

To begin this study an overall understanding of the subject area needs to be attained. To do this, an overview of mechanical and small-scale testing will be needed to provide context for small punch testing. An understanding of sample irradiation and its limitations will also be desirable. Finally, a review of relevant small punch testing research will be conducted. This literature review will follow the following outline:

- Overview of mechanical testing
- Overview of small-scale testing
- Working with irradiated samples
- Overview of the small punch test
- History of small punch testing
- The current standard
- Any current/relevant research
- Simulation and inverse analysis work to date
- Takeaways from the literature search
- Gaps in knowledge and where this research will sit

2.2 The complexities of small scale testing

One of the main drivers for this project was to find a means of counteracting the problems induced by a decrease in specimen length scale. In simple terms, a significant decrease in sample size can lead to the apparent increase in measured properties [54], [57].

This is attributed to two main causes, firstly the extrinsic factor of sample size, and crystal structure; and secondly, an intrinsic effect produced by microstructure [57]. It is believed that the intrinsic factor has the biggest effect on the change in properties with length scale [54], [57].

On the bulk scale, there are several microstructural features that govern how a specimen will behave. Namely, grain boundaries, and dislocations. As the length-scale of a specimen decreases, relative size of these features increase, thus increasing the effect they have on the material. A material containing small grains or a high dislocation density is particularly susceptible to this. If the specimen size is decreased further, the likelihood of it including a large number of defects decreases, thus increasing the apparent properties more so. This has been illustrated by Hosemann in Figure 2.1 [54].

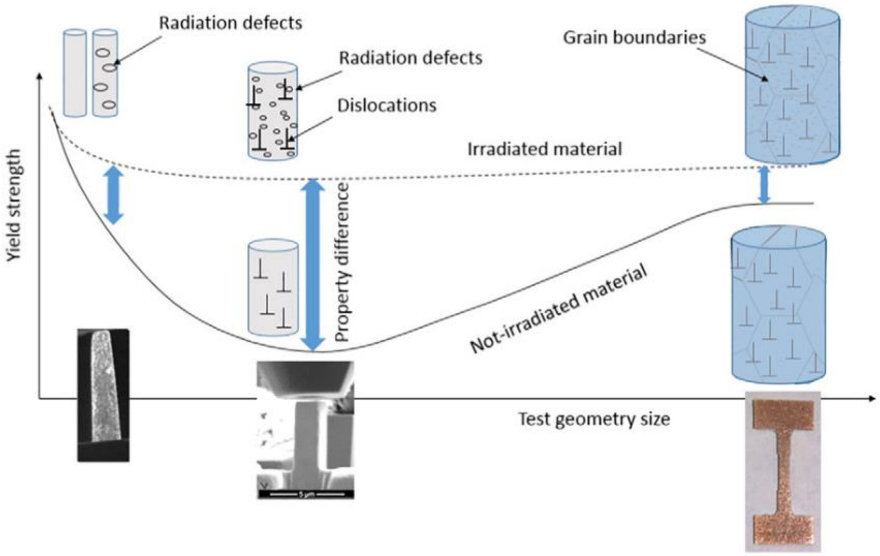

Figure 2.1: A diagram illustrating the effect that a change in length scale has on the recorded properties of a material. Note how a large decrease in scale causes a large increase in yield strength. Figure by Hosemann [54].

It is also prudent to note that while there will be an overall increase in measured properties, there will be some specimens that do contain a high number of defects and so will exhibit properties far lower than those shown in the bulk.

Non-conservative results, and the possibility for a wide spread in the data, make any prediction of properties exceedingly complex. These factors highlight the need for the development of a reliable way of obtaining viable results from small scale tests.

2.3 Overview of mechanical testing

Mechanical testing is an overarching term that is used to describe a group of tests designed to measure certain properties like yield strength and ultimate tensile strength. These can range from the simple tensile test to more complex torsion tests. Some typical testing methods, their uses and standard procedures will be outlined below.

2.3.1 Uniaxial Tensile testing

Tensile testing is a well-established method that places a length of material under uniaxial tension and applies force until the material breaks (Figure 2.2). The most common output from a tensile test is a stress-strain graph. Both the stress and the strain can be easily calculated from the starting geometry of the test piece, the applied force, and the test piece deformation [58].

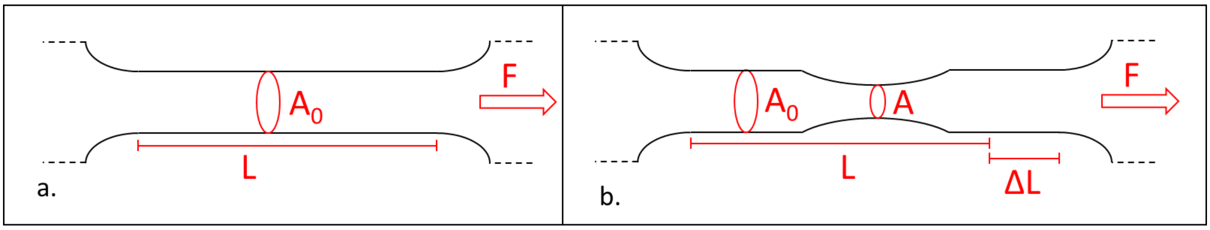

Figure 2.2: a) An undeformed tensile sample with relevant features labelled: L = gauge length; A_0 = Initial cross sectional area; F = applied force. b) A deformed tensile sample with the change in geometry labelled: A = cross sectional area at thinnest point ΔL = change in gauge length. Diagram of the tensile test piece adapted from "Tensile testing, 2nd edition" [59]

Stress is defined as the relationship between the force applied to an object and its cross sectional area and is measured in Pascals, Pa. Engineering stress is the simplest to calculate and uses the cross sectional area measured prior to deformation [60].

For engineering stress,

$$\sigma = \frac{F}{A_0}$$

Equation 2.1

Where:

- σ = stress
- F = applied force
- A_0 = original cross sectional area of the test piece

In a uniaxial tensile test, strain is defined as a unitless value which describes the change in gauge length while the test piece is subject to applied stress [60].

For engineering strain,

$$\varepsilon_{engineering} = \frac{\Delta L}{L}$$

Equation 2.2

Where:

- $\varepsilon_{engineering}$ = strain
- ΔL = change in gauge length
- L = original gauge length

A more accurate measure of stress is true stress. This takes into account the change in cross sectional area over the deformation and thus uses an instantaneous cross sectional area [60]:

$$\sigma = \frac{F}{A}$$

Equation 2.3

Where:

- σ = stress
- F = applied force
- A = instantaneous cross sectional area of the test piece

This can be difficult to measure so a conversion between the engineering and true stress has been devised [60].

For true stress

$$\sigma_{true} = \sigma_{engineering}\left(1 + \varepsilon_{engineering}\right)$$

Equation 2.4

To match this, true strain can also be calculated using the engineering values:

$$\varepsilon_{true} = ln\left(1 + \varepsilon_{engineering}\right)$$

Equation 2.5

Engineering stress and engineering strain can be plotted against each other to form a stress-strain graph (Figure 2.3)

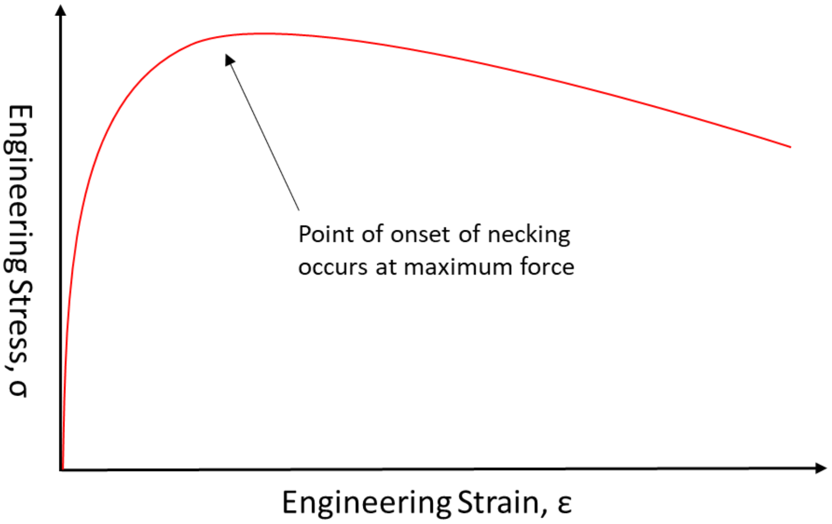

Figure 2.3: Diagram of an engineering stress-strain curve adapted from "Tensile testing, 2nd edition" [59]

This graph can be used to obtain the Young's modulus, yield strength, ultimate tensile strength, strain to failure, and Poisson's ratio of a material. Such data can also be used to form a correlation which defines the point of onset of plastic instability. This is known as the Considére criterion [61]–[64]. It uses the relationship between stress, force and cross sectional area to form a differential which will precisely predict the onset of plastic instability, otherwise known as the ultimate tensile strength, UTS.

In a standard tensile test:

$$\sigma = F/A$$

$$F = \sigma A$$

At maximum force, $dF = 0$

$$dF = d(\sigma A) = 0$$

Differentiation by parts

$$d(\sigma A) = \sigma dA + A d\sigma = 0$$

therefore, true deformation $d\varepsilon = \frac{dl}{l}$

therefore

$$\frac{d\sigma}{\sigma} = -\frac{dA}{A}$$

volume is constant in plastic deformation ($V = constant$)

$$d(LA) = 0$$

differentiation by parts

$$LdA + AdL = 0$$

therefore

$$\frac{dL}{L} = -\frac{dA}{A} = d\varepsilon$$

therefore

$$\frac{d\sigma}{\sigma} = d\varepsilon$$

so, at the point of necking:

$$\frac{d\sigma}{d\varepsilon} = \sigma$$

Equation 2.6

this can be plotted as Figure 2.4.

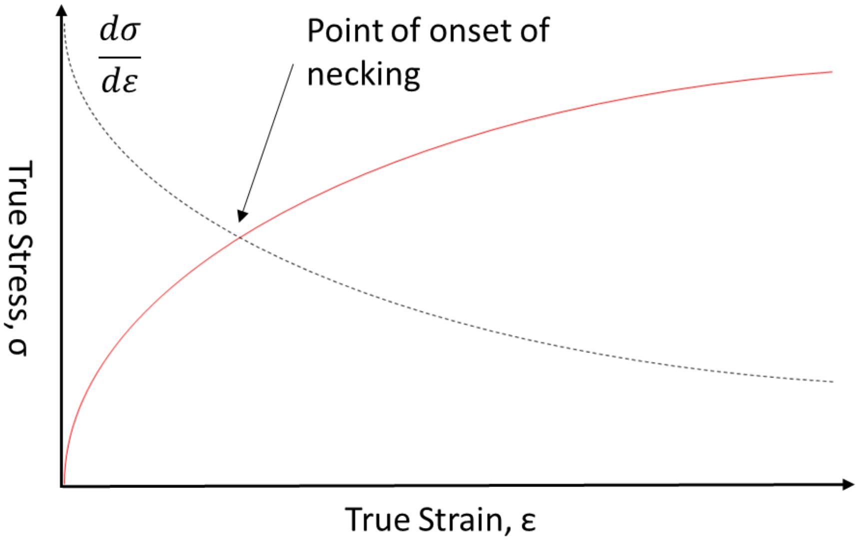

Figure 2.4: Diagram of the Considére criterion for plastic instability. The true stress strain curve has been plotted against its derivative. The point in which they cross denote the point at which plastic instability starts. This can be taken as the ultimate tensile strength. [62]

The tensile test can also provide information about fracture behaviour and whether a material is predominately brittle or ductile. This can be determined from the aforementioned stress-strain graph, but the test piece itself can also provide some insight into this. As seen in Figure 2.5, the morphology of the broken test pieces is indicative of a materials ductility.

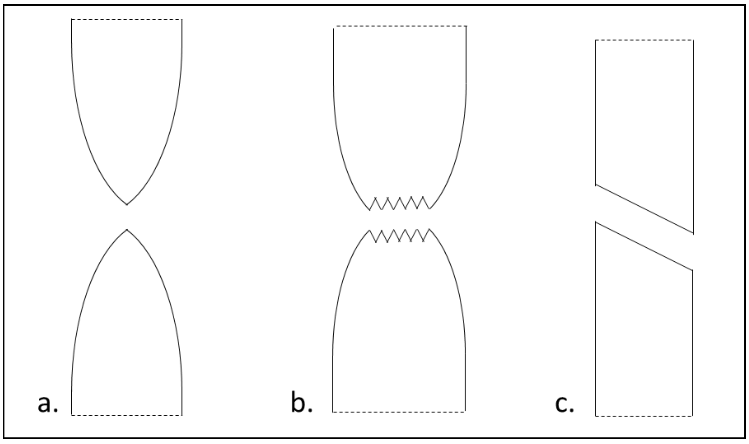

Figure 2.5: Diagram of the different fracture morphologies in the tensile test a) completely ductile, b) mixed brittle and ductile behaviour c) completely brittle. Adapted from " Tensile testing, 2nd edition" [59]

Simplicity and the array of useful information that can be obtained has made tensile testing the primary method for quality control across many metal manufacture industries, making it the bench mark in mechanical testing [65]. Tensile testing has standards available from the American Society for Testing and Materials (ASTM), and the British Standards Institution (BSI) [66], [67].

In reality, engineering components will experience stresses other than plane stress. Leading to the development of many different mechanical tests. These aid in the understanding of more complex material behaviour.

A note on surface grains

It is at this point that the importance of representative samples is outlined. For a mechanical test to be considered polycrystalline, and therefore a good representation of a bulk material it must fulfil particular criteria. One example outlined by Kocks [68], states that for a sample to be representative of bulk behaviour it must have on average 100 grains in the cross section. Therefore, if a wire sample were to be 3mm in diameter, the grains would have to be, on average, less than 0.1mm across.

Ensuring this would mean that the influence from surface grains would be kept to a small percentage. The grains on the surface of a sample are not constrained in the same manner as internal grains and therefore behave differently [68]. Consequently, if the percentage of grains at the surface was too high then the overall behaviour of the material will change. This can become a serious problem when assessing annealed metals or small samples.

An example of the effect of diameter reduction can be seen in Figure 2.6. Here, two diameters have been selected from the same piece of material. Diameter b is half the size of diameter a. Diameter a has 40 grains, and of those 40, 18 are surface grains. Diameter b has a total of 12 grains, with 10 being at the surface, meaning that the total percentage of surface grains has jumped from 45% to 83%. Thus the behaviour of these two samples would be markedly different.

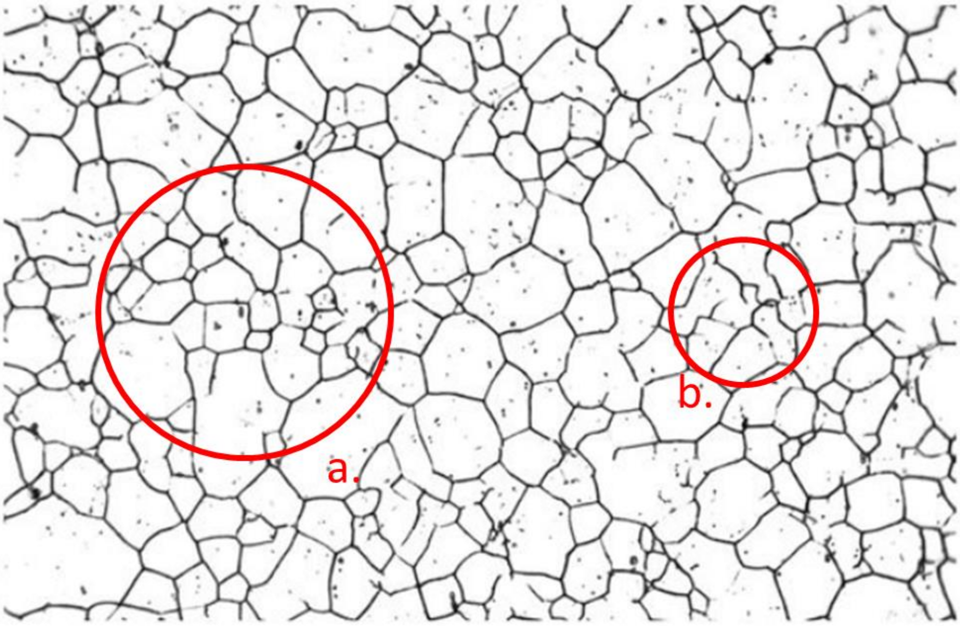

Figure 2.6: Diagram showing two potential samples from a piece of steel. Original micrograph from Leica Microsystems [69].

2.3.2 Uniaxial Compression Testing

The compression test is similar in many ways to the tensile test, but compresses the specimen instead of placing it under tension (Figure 2.7). Values such as the young's modulus, and yield strength can be extracted from compression test results. These are calculated in the same manner as the tensile test using Equations 2.1-2.5. However, the compression test cannot provide UTS values due to the lack of necking. This test also measures the compressive strength which provides valuable information on how a material behaves under compressive loads in fabrication conditions such as forging and rolling [70].

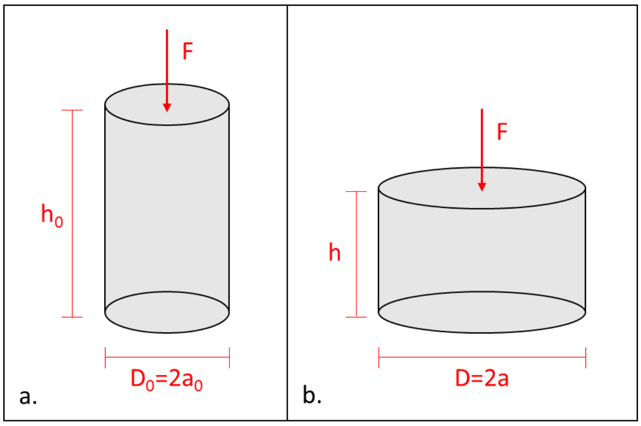

Figure 2.7: Diagram of a compression test piece, a) prior to and b) after testing, adapted from "Applied Metal Forming: Including FEM Analysis" [71]

For Homogeneous compression (Figure 2.7), the effective strain, ε is [71]:

$$\varepsilon = ln\frac{h_0}{h}$$

Equation 2.7

Where:

- h_0 = the initial sample height
- h = the instantaneous sample height

To calculate the flow stress, the true contact area, A, between the specimen and die needs to be defined. This is [71]:

$$A = A_0\frac{h_0}{h}$$

Equation 2.8

Where:

- A_0 = the initial contact area

Therefore, the flow stress, σ, is [71]:

$$\sigma = \frac{F}{A}$$

Equation 2.9

where:

- F = applied force

Compression tests have the added factor of friction between the specimen and die platen. This friction has been shown to have a marked effect on results produced [72]–[75]. A phenomenon known as barrelling can be observed. This is where the friction seen between the end surfaces of a sample and the compression system leads to the ends being constrained thus producing a barrel shaped specimen (Figure 2.8).

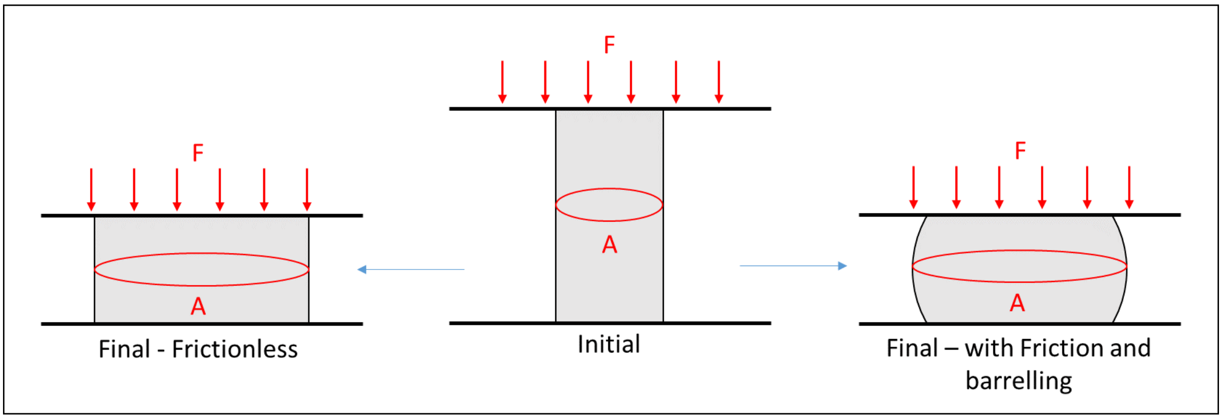

Figure 2.8: Diagram showing the effect of contact friction on the morphology of the deformed compression test piece [70], [71]

The formation of the barrel shaped specimen by friction is driven by the formation of dead zones at the interface between specimen and loading dies [71], [76]. This effect is illustrated in Figure 2.9 with the areas highlighted in red and orange being the stagnant or dead zones and the green being an area of concentrated shear strain and reduced sliding. Such a non-uniform strain profile gives rise to most of the deformation occurring along the outer edges of the specimen, thus producing the barrel shape [71], [76].

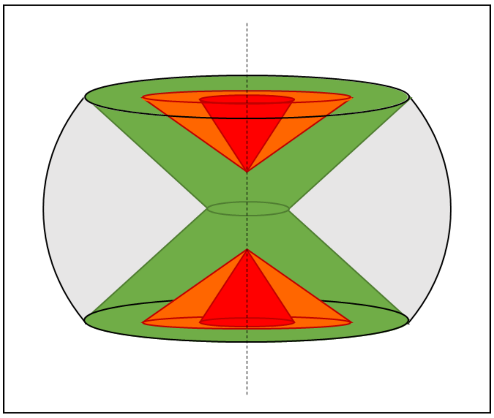

Figure 2.9: Diagram illustraitng the effect that contact friction can have on the internal strains of a compression test piece. Orange and red zones are stagnant and dead zones, and green indicates areas of large amounts of shear strain [71], [76]

The geometric change also leads to deviation from uniform, uniaxial stresses to non-uniform triaxial states, thus moving any results away from pure plane stress and strain [72]. For the compression test to be completely comparable with the tensile test, all friction must be eliminated. This is not possible. To counteract this, several papers have produced long and complex mathematical derivations that can convert triaxial stresses to the desired uniaxial, which will not be discussed here [72], [75].

While the compression test can provide valuable information about compressive behaviour, the complex calculations needed to counteract the friction effects makes this technique less universally viable than the tensile test.

2.3.3 Three-point Bend testing

Bend testing, and specifically the three-point guided test is used to determine a material's reaction to bending. This is achieved by supporting a length of material at both ends and applying a load to the centre. The ASTM standard dictates specific apparatus geometries for each type of bend test, an example can be seen in Figure 2.10. Such control allows for consistent calculation of the flexural stress, stain, and modulus.

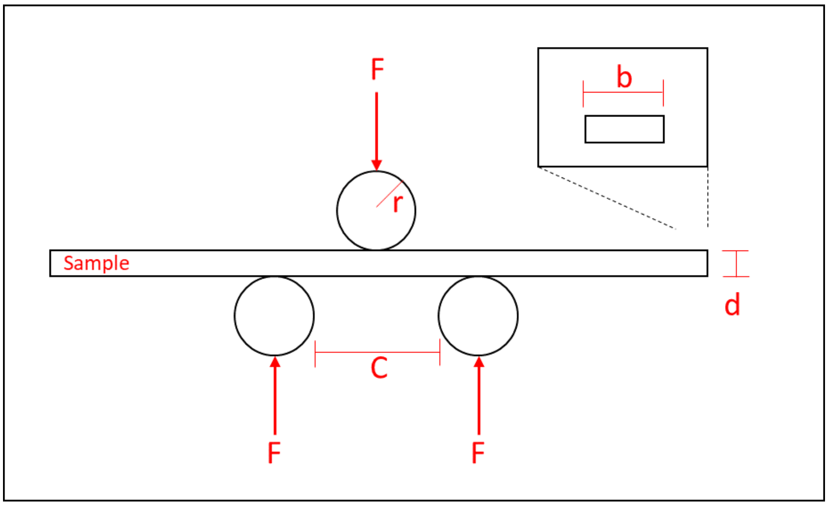

Figure 2.10: Diagram displaying the three point bend test. Adapted from, " ASTM E290 - 14: Standard Test Methods for Bend Testing of Material for Ductility" [77]

Where:

- F = applied load, N
- C = the distance between the two lower supports, mm
- L = support span, mm
- r = the radius of the plunger, mm
- d = the depth of the beam/sheet, mm
- b = beam/sheet sample width, mm

This produces a deformation, from which the shear, deflection, moment, and load can be recorded. Both the recorded moment and the load-deflection data can be used to determine the flexural modulus, or the resistance to bending [77].

The flexural stress, σ_f (MPa), can be calculated using [77], [78]:

$$\sigma_f = \frac{3PL}{2bd^2}$$

Equation 2.10

The flexural strain, ε_f, can be calculated using [77], [78]:

$$\varepsilon_f = \frac{6Dd}{L^2}$$

Equation 2.11

Where:

- D = deflection at centre of the beam, mm

The flexural modulus or elastic modulus in bending , E_B, can be calculated using the following [77], [78]:

$$E_B = \frac{L^3 m}{4bd^3}$$

Equation 2.12

Where:

- m = the slope of the tangent to the initial straight line portion of the load-deflection curve, N/mm

Another common use for the bend test is the analysis of the behaviour of a metal sheet under cyclic deformation [79]. This is achieved by plotting the force displacement graphs (Figure 2.11). For polycrystalline metals, these graphs can also display a phenomenon known as the Bauschinger effect [79], [80]. The Bauschinger effect is defined as the decrease in yield stress with a change in strain direction, or in this case, loading and unloading of the specimens. Such graphs can also be used to identify hardening behaviour.

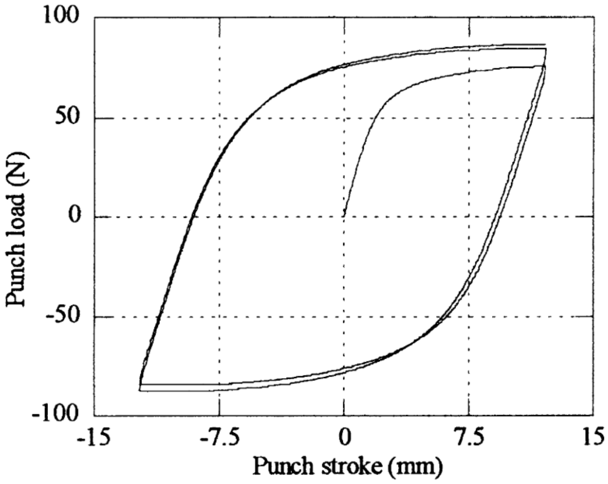

Figure 2.11: A measured load-stroke curve for a mild steel sheet of a 1.2mm thickness. The graphs display both the Bauschinger effect and hardening. Diagram from "Finite element analysis of the three-point bending of sheet metals" [79].

Aside from the numerical results obtained from bend tests, they can also be used as a visual indicator for crack formation under bending and tension. The analysis of sample surface, angle of bends, and cracks is important in the measure of the ductility.

Much like the uniaxial tensile test, the bend test can provide a range of information about a material. However, because of the shear forces applied, the results are not as widely applicable as that of the tensile test.

2.3.4 Vickers hardness testing

There are several types of hardness test available, but the most commonly used is the Vickers Hardness test. The Vickers hardness test uses a pyramidal diamond tipped indenter to indent the material with a set amount of force (Figure 2.12 a). Vickers hardness relies on a highly accurate pyramidal indenter to provide consistent results. This indenter is ideally highly polished with face angles of 136.0˚ as outlined in the ASTM standard E92 (Figure 2.12 b) [81].

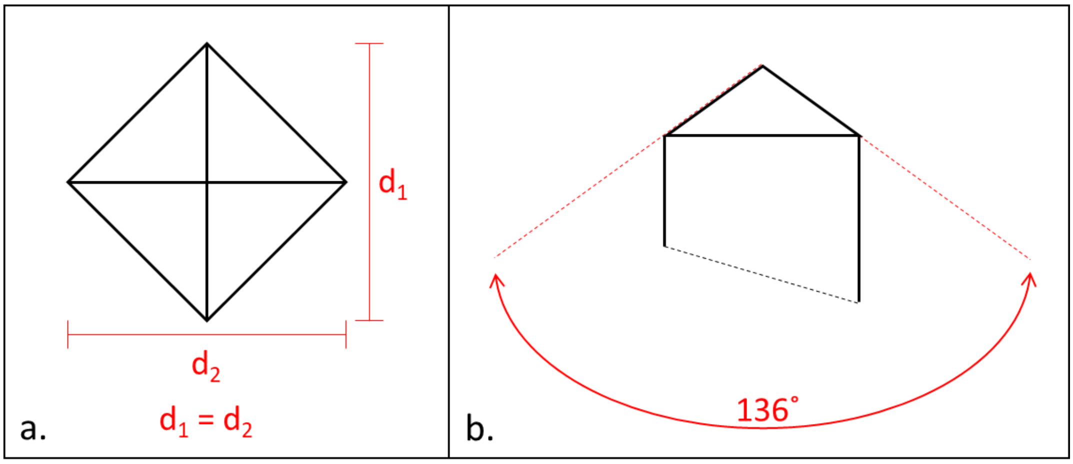

Figure 2.12: Diagram of a Vickers indenter. a) displaying the required dimensions and b) the required angle of 136 ˚ for the tip [81].

Because the standard dictates the geometry of the punch head, the contact area, A, of the test can be readily calculated [81]:

$$A = \frac{d_V^2}{2sin\frac{\alpha}{2}} = \frac{d_V^2}{1.8544}$$

Equation 2.13

Where:

- α = face angle of the indenter (136.0˚)
- d_V = mean Vickers indentation diagonal length (mm)

The hardness value can then be determined [81]:

$$HV = \frac{F}{A}\ [kgf/mm^2]$$

Equation 2.14

It is generally accepted that the relationship between Vickers hardness and tensile strength is such that is can be used reliably [82]. This relationship is as follows, if hardness is recorded in MPa, then in general:

$$\sigma_{UTS} = \frac{HV}{3}$$

Equation 2.15

The ductility and hardening behaviour of the specimen play a large role in the hardness test and thus the above relationship should be taken as more of an estimation rather than a direct correlation [82]. While the hardness test can provide some information about the tensile properties of a material, it cannot be used as reliably as a tensile test

2.3.5 Charpy impact test

The Charpy impact test is a high strain rate analysis method most commonly used to determine the relative toughness of a material. This is achieved by measuring the energy needed to fracture a notched specimen [83], [84]. The fracture energy is measured by releasing a striker from a set height, point A in Figure 2.13, swings through to impact the specimen at B, and reaches its final height at C. The difference in striker height between A and C can then be converted into impact energy (Equation 2.16).

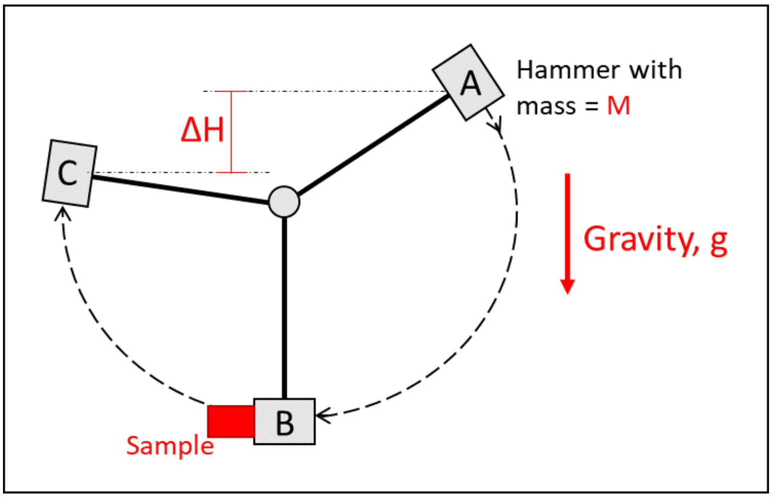

Figure 2.13: Diagram of the Charpy test. The striker starts at initial position, A, swings through to impact B, and reaches its final height at C. Adapted from "ASTM E23 – 18 Standard Test Methods for Notched Bar Impact Testing of Metallic Materials" [83], [84].

The impact energy, A (Joules), can be calculated using the following [84]:

$$A = Mg\Delta H$$

Equation 2.16

Where:

- M = mass of hammer
- g = gravitational constant
- ΔH = the difference between initial and final height of the hammer

The standard test uses a specimen with either a v-shaped or a u-shaped notch (Figure 2.14).

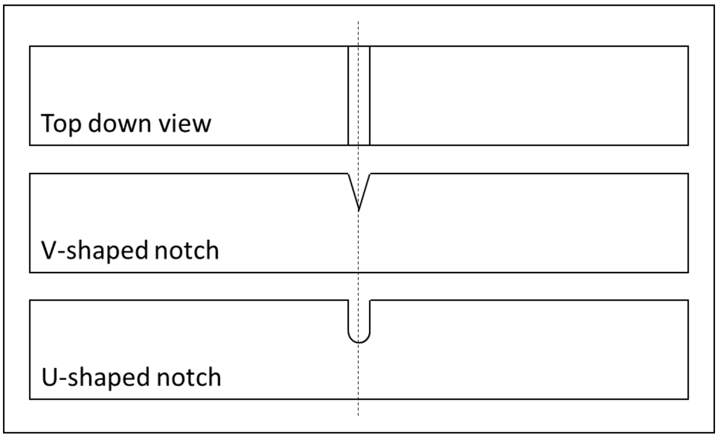

Figure 2.14: Diagram showing the notch types on a Charpy test [83]

The Charpy impact test can also be used to determine the Ductile to Brittle Transition Temperature, DBTT, of a material. A series of tests can be completed over a range of temperatures. At some point some materials will display a drastic change in the energy needed to fracture the sample, this is the DBTT.

The Charpy impact test differs from the others discussed here due to the high strain rates involved. This makes using the Charpy impact test for determining tensile properties unworkable.

2.3.6 Creep and stress rupture testing

Structural materials that experience high temperature conditions may be susceptible to creep or rupture. Creep is defined as deformation over time at a constant load, the effects of which can be exacerbated by high temperatures. For metals creep is typically activated at 35% of the melting temperature [85]. If the material fails under creep conditions, then it has ruptured [86].

A creep test can define the load bearing capability of a material for a limited deformation; while a rupture test measures the ultimate load carrying ability of a material as a function of time [87]. Both tests work in conjunction with another as the rupture test will give information on the point at which a material will fail, the creep test will describe the behaviour over a finite deformation. For both tests a sample is held under a constant load, or constant stress at a specified temperature until it either reaches a predetermined level of deformation or it ruptures [87].

Results are usually visualised in a creep strain - time graph (Figure 2.15). Such a graph provides a way of identifying the stages of creep displayed by a specimen.

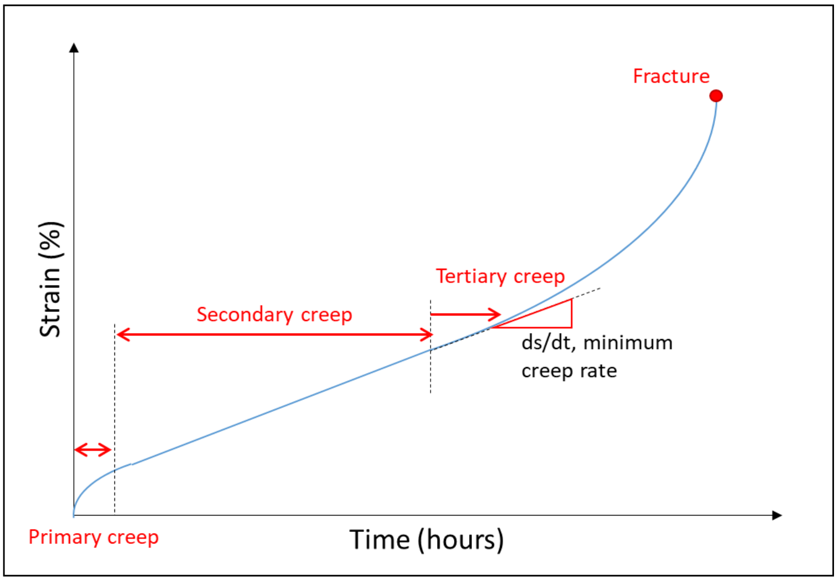

Figure 2.15: Diagram of a strain-time graph outlining the different stages of creep. Adapted from ASTM E139 - 11: Standard Test Method for Conducting Creep, Creep-Rupture, and Stress-Rupture Tests of Metallic Materials [87]

As this test operates with uniaxial forces, it is possible to calculate the stress and strain at any desired point [87].

Stress, σ, can be calculated using:

$$\sigma = \frac{F}{A_0}$$

Equation 2.17

Where:

- F = applied force
- A_0 = minimum cross sectional area of the specimen prior to the test

Strain, ε, can be found by:

$$\varepsilon = \frac{\Delta L}{L_0}$$

Equation 2.18

Where:

- ΔL = change in gauge length
- L_0 = gauge length prior to the test

Two other important metrics needed when analysing creep behaviour are the elongation and reduction in cross sectional area.

The elongation is defined as the change in gauge length over the span of the test, and is expressed as a percentage [87]. It is calculated thusly:

$$\%Elongation = \left[\frac{L_f - L_0}{L_0}\right] * 100$$

Equation 2.19

Where:

- L_f = final gauge length
- L_0 = initial gauge length

The reduction of area is only relevant if the sample has a circular cross section. It is defined as the change in minimum cross section over the length of the test expressed as a percentage [87]. It can be calculated as:

$$\%Area\ reduction = \left[\frac{A_f - A_0}{A_0}\right] * 100$$

Equation 2.20

Where:

- A_0 = initial cross sectional area of gauge
- A_f = final cross sectional area of gauge

As creep behaviour is temperature dependant it can be useful to plot the final results from each of the above values at different temperatures. Although this requires a large body of tests over a range of temperatures, such information can be very useful when considering high temperature engineering applications [87].

Creep and stress rupture tests are notably sensitive to testing conditions, meaning that reproducing results can be especially challenging. It is advised that results produced from such tests should be evaluated with this in mind, and multiple tests should be used where possible [87].

2.3.7 Fatigue Testing

Some components experience cyclic loading throughout their operational lifetimes. This can produce material fatigue, which is characterised as the reduction of strength and failure under cyclic loading. To determine how many cycles a material or component can withstand the fatigue test can be performed [88].

The fatigue test applies cyclic loads to either a specimen, component, or structure. The test is carried out for a set number of cycles or until the specimen fails. The change in stress response is recorded along with cycles to failure [88].

Loading is usually predominantly elastic, and can be applied using a variety of waveforms depending on that experienced by the component in operation (Figure 2.16). These generally consist of triangular loading, block loading or sinusoidal loading.

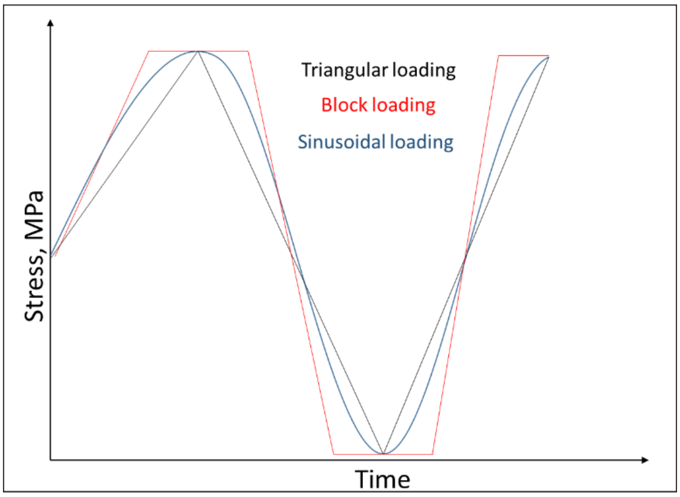

Figure 2.16: A diagram displaying the three different loading methods used in fatigue testing: triagnular (black line), block (red line), and sinusoidal (Blue line). Adapted from "5 - Mechanical and durability testing of aerospace materials" [89].

The ASTM standard E466-15 recommends the use of both unnotched and notched specimens for axial loading. The geometry of which must ensure that failure occurs in the desired location and the effect of specimen gripping is minimised [88]. The general geometry of unnotched specimens can be seen in Figure 2.17.

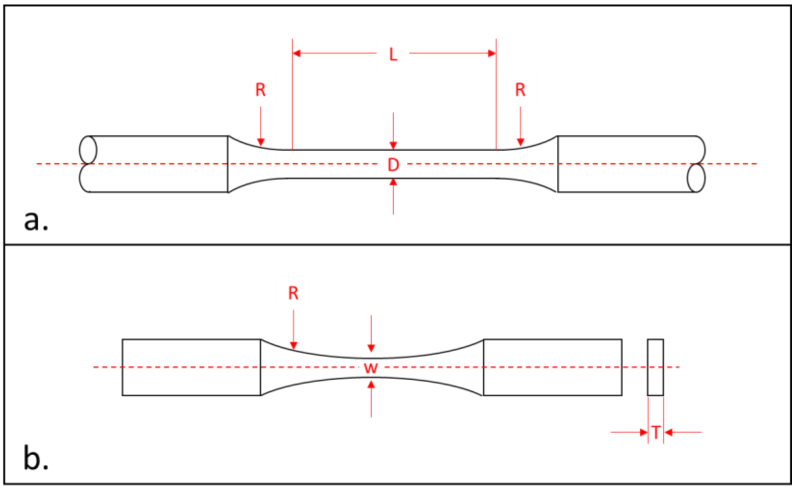

Figure 2.17: Diagrams displaying the two unnotched specimen shapes recommended by ASTM E466-15: a. Specimens with circular cross section and tangentially bending fillets; b. Specimens with rectangular cross sections and a continuous radius gauge [88].

The results of fatigue testing can be plotted in a stress-life (S-N) diagram [90]. Maximum stress is plotted against fatigue life in cycles (N) which is on a logarithmic scale and multiple tests are displayed in one diagram. This allows for a comparison of a range applied stresses for a particular material. As seen in Figure 2.18, the S-N diagram has two distinct sections; constant amplitude and staircase. Constant amplitude tests are self-explanatory where the same load is applied over the duration of the test. The staircase method displays the mean fatigue strength at 7 million cycles so applied load may vary over the course of testing. The fatigue limit is also highlighted in this diagram as where the maximum stress measured no longer decreases with increasing number of cycles [88], [90].

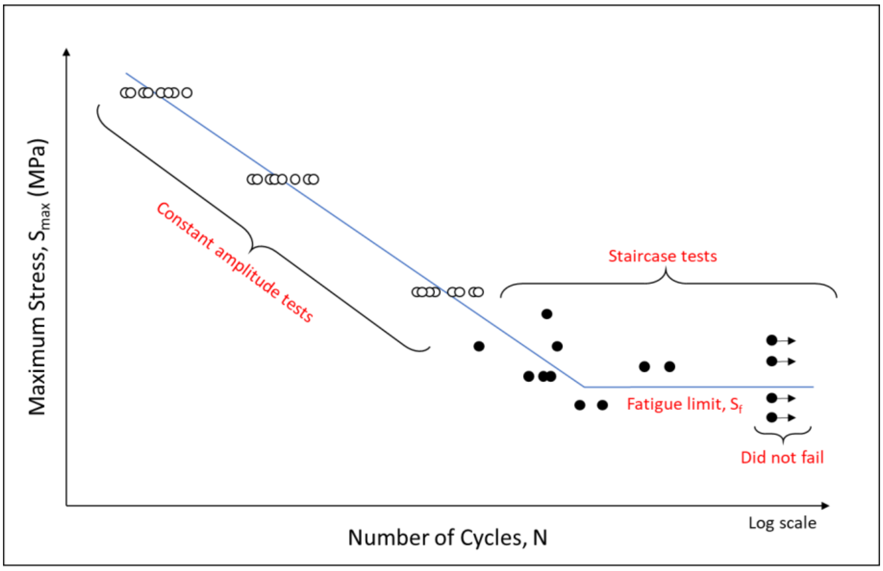

Figure 2.18: A diagram showing a typical stress-life diagram. Note the two types of tests employed, constant amplitude and staircase. [90]

If a specimen is tested to failure, then the rate of crack formation and growth can also be measured.

One important factor to note in fatigue testing is the large effect that the processing history of the material has on the results. So it is recommended that the processing history of the material along with sample preparation methods are included in the S-N diagrams. This will ensure that the results can be interpreted correctly [88], [90].

The results produced by the fatigue test aid in the process of material selection for service under cyclic loading conditions.

2.4 Irradiated samples and the hot cell environment

2.4.1 Plant life extension

The extension of the service lifetime of the current nuclear fleet is common place. Plant life extension, PLEX, is driven by increasing electricity demand and lack of new build [91]. The relatively low running cost of nuclear power also incentivises PLEX. However, the conditions within a reactor mean that material deterioration over its lifetime is a serious concern [92].

To extend the operational life of a reactor, a rigorous testing of structure-critical components must be carried out. Testing provides the assurance that a reactor is safe to run for its extended lifetime [92].

Much of this stems from the technical justification of service life, or service life prediction. The initial prediction is usually conservative, thus making the argument for lifetime extension reasonable.

As the components of a reactor have to be tested in situ, a lot of emphasis is placed on non-destructive evaluation, NDE. Along with being non-destructive, any testing must be reliable in order to obtain the extension of the operating licences. It is good to note that small-scale testing has been used here as a semi non-destructive method, as test pieces can be taken from an in service component by a scoop cutter sampling method (Figure 2.19) [93], [94].

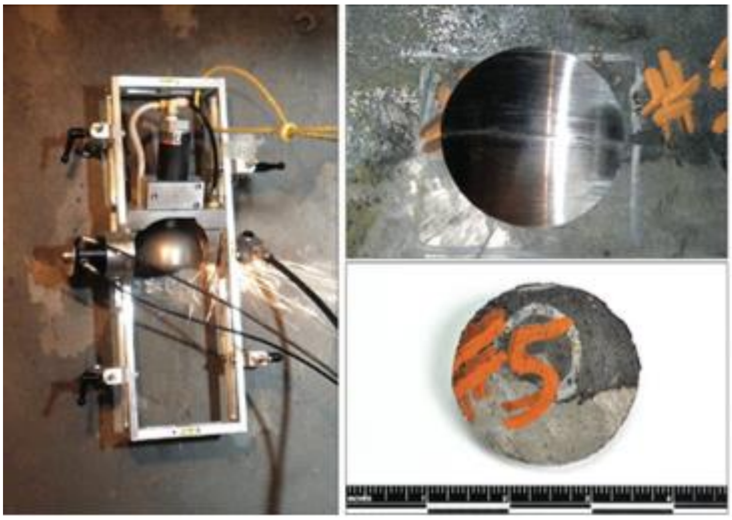

Figure 2.19: Scoop cutter sampling apparatus, indent left behind, and removed sample. Image from "The Use of Miniature Test Specimens in Fitness-for-Service Evaluation" [95].

2.4.2 Plant design

Design is an integral part of engineering and can be considered to be the creative process in finding a solution to a problem. For example, when designing a power plant many design features will be put in place to combat any future problem that arises, thus creating a system that runs safely and efficiently over a number of decades [96], [97].

A large portion of plant design is the prediction of its full lifetime. This is exceedingly complex, relying on large investments and work hours. Rigorous pre-build testing is required to ensure that each piece will exceed the desired plant lifetime. But when done correctly it is able to forecast the time dependant reliability of each component [98].

After the design and build of a plant, routine testing will be required over the operational lifetime [98].

2.4.3 Sample irradiation

All of the previously discussed mechanical testing techniques work well within the field of general materials engineering. However, testing materials in the nuclear industry involves another layer of complexity. To provide assurance that a material will function properly within a nuclear reactor, a full understanding of how it will behave after being exposed to radiation is required. As described in Chapter 1, radiation can fundamentally change a material's microstructure which then has the potential to severely affect its performance. This problem is particularly important in the design of the first generation of commercial fusion reactors. Due to the high flux of extremely energetic neutrons experienced in the core of a fusion reactor, a specialised facility is required to replicate this. This facility, known as the International Fusion Materials Irradiation Facility or IFMIF, will fulfil this requirement. However even with such a facility, only a volume of 0.5L could be irradiated to the highest levels of neutron flux of about 10^{18} n/m^2 s with a broad peak near 14MeV leading to a damage of 20 dpa/fpy [99], [100].

2.4.4 Irradiated sample handling

Handling irradiated specimens is potentially hazardous. While the overall risk to an operator is relatively low, it is imperative that it is kept this way by putting in safeguards and procedures in place. A large part of this is the reduction of any potential exposure. This can be achieved by either shielding a user from direct contact with any irradiated samples or by reducing the overall volume of material being handled [101].

However, in the case of highly irradiated materials shielding is the only option, and one of the safest ways to handle irradiated materials is in a hot cell facility. Current hot cell facilities for spent fission fuel are capable of withstanding up to 10^5 Sieverts a year [102], [103]. Such cells would be more than capable to facilitate the handling of irradiated samples.

What is a hot cell?

A hot cell is a remote handling facility designed specifically for handling highly radioactive objects. They consist of a large shielded container with a window in one or two sides to allow operators to see in. These windows are typically made of a lead glass tank filled with zinc bromide (Figure 2.20).

The primary way of handling items within the cells is with master-slave manipulators [102], [104]. Master slave manipulators are a set of hydraulic arms that extend through the wall of the cell. Operated by a skilled technician, the arms are capable of performing intricate work, such as metallographic prep and microscopy. To ensure that work in the cells can be done as easily as possible a lot of process have been streamlined [103], [105]. This philosophy can be applied to small-scale testing.

Figure 2.20: Photograph of the hot cell facility in Argonne National Laboratory [106]

2.4.5 Requirements for a viable testing technique

Taking the limitations of working with the master-slave manipulators into account, several requirements for an applicable small-scale test technique can be formed [105], [107], [108]:

- The test must be resource efficient

- Can produce consistently reliable results
- Data processing should be simple enough to be applied readily
- Large volume of tests needed, so quick and simple is ideal
- Ideally existing methods and infrastructure would be utilised

Applying these requirements to a selection of small-scale tests allows for the most promising methods to be selected.

2.5 Overview of small-scale mechanical testing

Small scale mechanical testing of irradiated materials has been in development since the 1960s and is still very much an active area of research [54], [109]. Generally, the term small scale refers to samples ranging from nm to mm in length. Such a wide-ranging length scale gives scope for a large number of testing techniques and also a large number of challenges to overcome. To appreciate these problems, a basic understanding of these testing techniques must be attained.

2.5.1 The problem of size

To be able to confidently predict material behaviour under irradiation, large, reliable datasets are required. This means that any small-scale testing technique must be both cost effective and simple to analyse. Figure 2.21 plots a range of testing methods against their cost effectiveness and ease of analysis [54]. It is immediately evident none of the discussed techniques yet fit into the easy/cost effective portion, thus highlighting the need for further development in the small scale testing field.

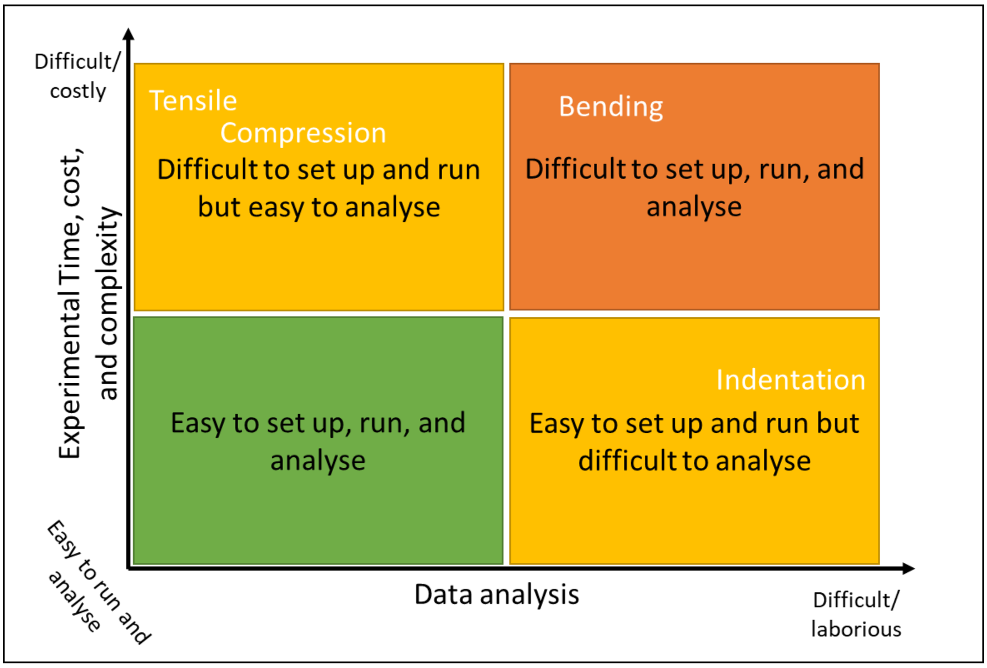

Figure 2.21: Diagram displaying the challenges involved in small-scale testing. Adapted from " Small-scale mechanical testing on nuclear materials: bridging the experimental length-scale gap" [54]

2.5.2 Tensile testing

Tensile testing was one of the first techniques to be miniaturised. This was done relatively easily by using thin foils and wires in place of the standard sized samples (Figure 2.22). However, these tests proved variable so a more complex and reliable approach was developed [54], [110], [111].

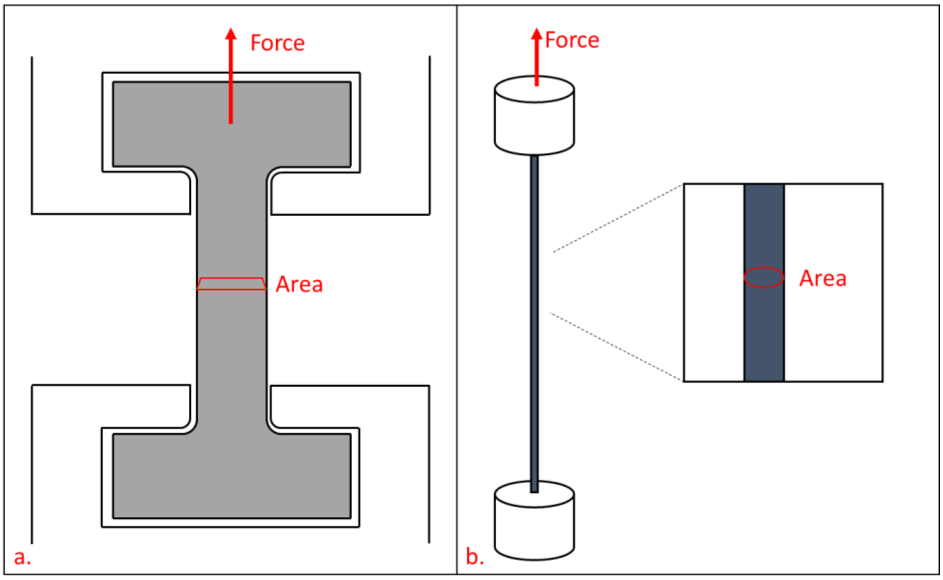

Figure 2.22: a) Diagram showing the miniaturised tensile test. b) Diargram showing the miniaturised wire tensile test. Adapted from " Small-scale mechanical testing on nuclear materials: bridging the experimental length-scale gap" [54]

Today, the miniaturised tensile test is applied as a pseudo non-destructive technique as specimens can be obtained by taking scoops out of in service components without effecting their structural integrity [94]. With the development of this technique came bodies of work displaying the potential for small-scale tensile testing to be equivalent to its full sized counterpart [94]. However, in 2017 an ASTM regulated study proved that this was not the case [112]. The study found that the UTS, proof stress, and elongation to failure values did not match certified ones. It is observed that the work hardened areas produced in the machining of the samples formed a large proportion of the final specimens. This is thought to have led to highly variable UTS and proof stress values.

This study also works well in highlighting a fundamental issue present in small-scale testing. That is that when sample sizes are reduced, features like crystallographic and surface defects, and work hardening volumes form a large portion of a specimen and so can have a great effect on any results produced (see section 2.2). Such effects mean that the relationship between full sized and small-scale test results is a complex one, thus making any numerical association between the two difficult. This can be applied to any miniaturised testing method.

When small-scale tensile testing is studied in terms of its applicability for engineering (visualised in Figure 2.18), it can be seen that while the results are easily analysed, specialist equipment is required and thus is expensive to run. This is not including the facilities needed for handling irradiated samples [54].

2.5.3 Microcompression

Microcompression, is a uniaxial test that is currently used in a range of irradiation tests at multiple length scales (Figure 2.23) [113]. However, because the sample size is, on average, smaller than a single grain, microcompression must be considered a single crystal test technique [54], [57], [114]. Microcompression has several limitations. Slipping of interfaces during the test, and problems with sample alignment and compliance are widespread [54], [115]. Such problems make testing unreliable, making extended hot cell runs inadvisable.

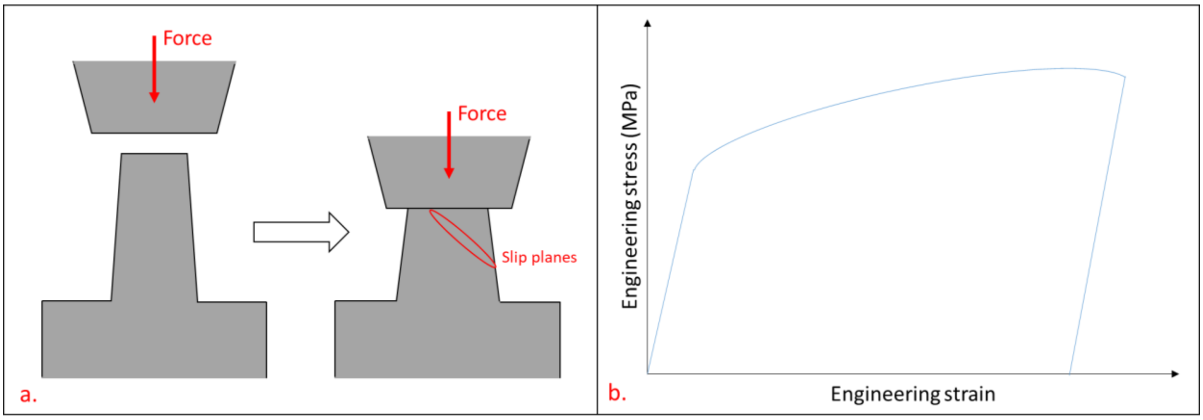

Figure 2.23: a) Diagram showing the microcompression test piece highlighting the slip planes present afte compression. b) Diagram displaying the stress/strain curve of the microcompression test. Both adapted from "Small-scale mechanical testing on nuclear materials: bridging the experimental length-scale gap" [54]

The length scales that microcompression tests operate under (µm to nm) mean that very specialised methods are required for sample preparation, testing and analysis, thus making the technique costly and impractical for producing large bodies of data [54].

Much like the small-scale tensile test, microcompression is simple to analyse but length scale (sub grain) makes direct comparison with bulk values impossible.

2.5.4 Bend testing

Both cantilever and three point bend tests can be miniaturised [116]. In-situ (cantilevers cut into the bulk) and ex-situ (sample extracted from the bulk) tests are possible, and can be used to obtain yield, and elastic properties (Figure 2.24). However, any post yield behaviour needs to be validated with finite element analysis [117]. The main issue with this method is the specimen size. In general, they are around the size of a TEM sample making preparation complicated and requiring specialised equipment [54].

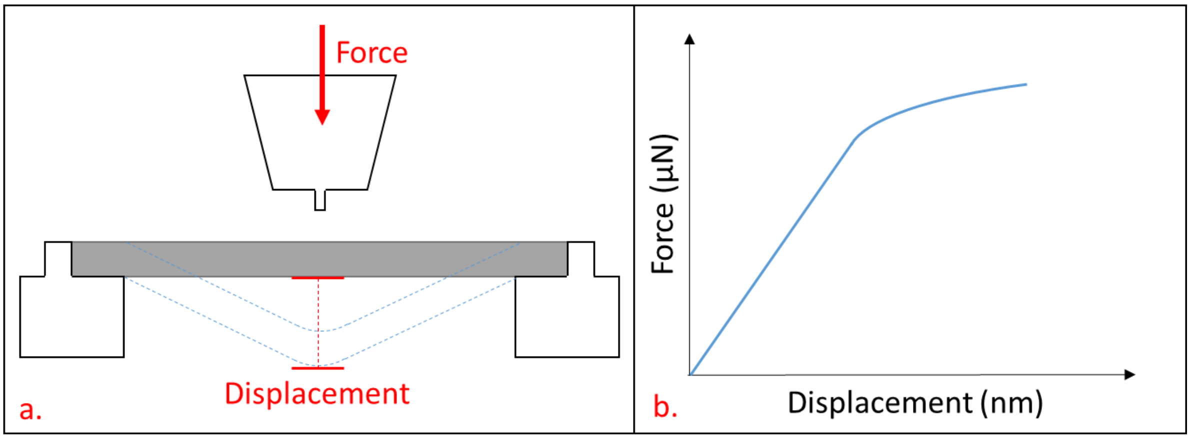

Figure 2.24: a) Diagram showing the miniaturised bend test. b) and the force-displacement curve produced by the test. Both adapted from "Small-scale mechanical testing on nuclear materials: bridging the experimental length-scale gap" [54]

2.5.5 Nanoindentation

Because of its simplicity, nanoindentation is one of the most established examples of small-scale testing. It involves pressing either a pyramidal or spherical headed indenter into a material at a set force. The indenter is then removed, the size and depth of the mark left behind is measured. Relating the indent geometry to the force applied with the indentation allows for the successful estimation of certain mechanical properties (Figure 2.25). The properties that can be estimated are Young's modulus, hardness, and strain rate sensitivity [54], [118], [119].

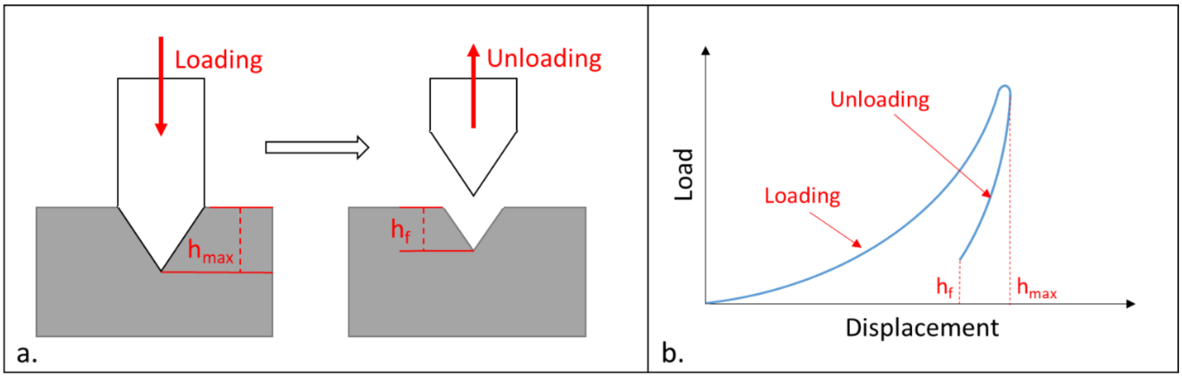

Figure 2.25: a) Diagram showing the nanoindentation test, and b) the load displacement graph from it. Where: h_{max} *= maximum displacement,* h_f *= final depth of indentation. Both adapted from "Nanoindentation Techniques"* [119]

Nanoindentation played a critical role in establishing the understanding of the relationship between decreasing sample size and increasing materials properties [54], [118].

Nanoindentation is relatively simple to set up and is material efficient, only requiring a small volume of material to provide a large number of tests. However due to the test size, forming a correlation between results and bulk materials values is problematic, requiring complex simulation and mathematical models [54], [118]. This level of analysis is labour intensive and time consuming. It should also be noted that the problems present in classic hardness testing are also present here [82]. Such indentation tests do not produce any necking data so it is impossible to gain a full picture of material behaviour with indentation alone [120].

2.5.6 Small Ring Tensile testing

The small ring tensile test is a relatively new technique developed as a high sensitivity small scale test with an aim of determining tensile properties. It holds specific advantages, such as; ease of test setup with the use of pins; self-aligning specimens; and a relatively large gauge length. Much like other small scale tests in this section, it was also designed as a pseudo non-destructive test, as specimens could be crafted out of small scoops taken from components in operation [121], [122].

The small ring tensile test consists of a small ring shaped specimen that has been machined down to a specific geometry (Figure 2.26) [121], [122].

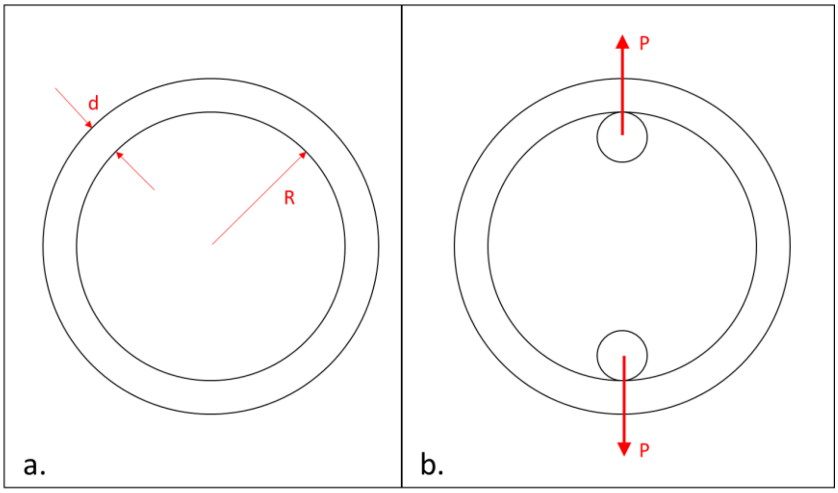

Figure 2.26: Diagrams displaying the basic geometry of a small ring test: a. the specimen thickness, d, is highlighted along with radius, R; b. once loaded into the apparatus, force, P, is applied with two pins. The circular geometry of the specimen allows for it to self align as load is applied [121], [122].

A tensile load is then applied to the specimen via two pins until the specimen fractures. Using the applied force and change in specimen geometry, equivalent stress and creep strain rate can be calculated (Figure 2.27, and Equations 2.21 and 2.22)

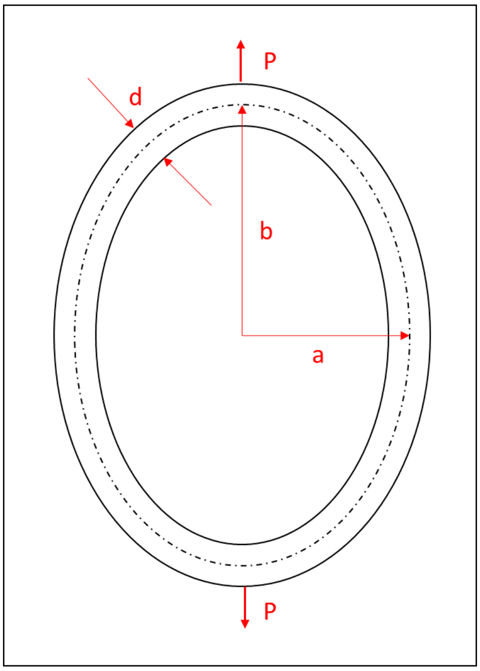

Figure 2.27: adapted from "The development of a novel technique for small ring specimen tensile testing" [121]

Equivalent uniaxial reference stress, σ_{ref}:

$$\sigma_{ref} = \eta \frac{Pa}{b_0 d^2}$$

Equation 2.21

Equivalent uniaxial creep strain rate, $\dot{\varepsilon}^c$:

$$\dot{\varepsilon}^c(\sigma_{ref}) = \frac{d}{4ab\beta}\dot{\Delta}_v$$

Equation 2.22

where:

- $\dot{\Delta}$ = creep deformation rate
- η and β = conversion factors that vary with specimen dimensions
- a and b = major and minor axis dimensions of an elliptical specimen
- b_0 = specimen depth
- d = specimen thickness
- P = load

2.5.7 Two Bar testing

As a development from the small ring tensile test, the two bar test was established. Used mainly for the testing of creep and creep rupture behaviour, the two bar test also utilised specimen creation via machining and loading using pins (Figure 2.28) [123]. The two bar test also can be used as a pseudo non-destructive test.

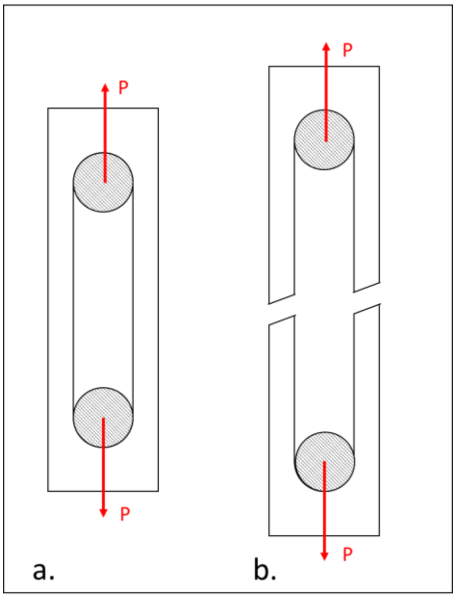

Figure 2.28: A diagram of the two bar test showing the placements of the pins applying a load, P with a. showing before deformation and b. showing after deformation and failure.

The specimen geometry (Figure 2.29) allows for the creation of full creep strain v time graphs. The two bar test presents an improvement on the small ring test by eliminating any bending effects present around the pin supports.

By optimising the geometry of the specimen (Figure 2.29), it is possible to measure fully tensile behaviour. In particular, creep strain rate can be calculated using Equation 2.23 [123].

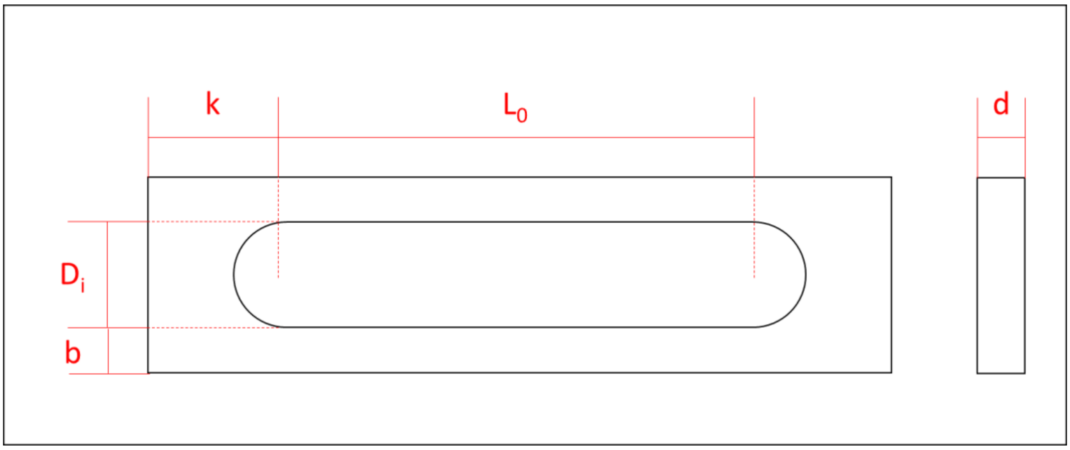

Figure 2.29: adapted from Analysis and design of a small two bar creep test specimen [123]

Where:

- L_0 = gauge length
- k = length of loading pin supporting end
- D_i = diameter of loading pins
- b = bar width
- d = specimen thickness

Equivalent uniaxial minimum creep rate, $\dot{\varepsilon}^c$:

$$\dot{\varepsilon}^c = \frac{\dot{\Delta}^c_{ss}}{\beta L_0}$$

Equation 2.23

Where:

- $\dot{\Delta}^c_{ss}$ = creep deformation rate
- β = conversion factor dependant on specimen dimensions

When used in conjunction with finite element modelling, the two bar test can be useful in aiding the prediction or remaining operational life

2.5.8 Small Punch testing

Small punch testing consists of a small disk-shaped specimen clamped in between two dies which is then deformed in a biaxial manner by a punch to failure (Figure 2.30) [124]. The test is controlled by either punch force, or displacement rate [125], [126]. The punch force and punch displacement are recorded along with sample deflection, which can then be plotted as a force-displacement or force-deflection graph [125], [126]. This graph can then be used to obtain information about the material being tested. Much like the small-scale tensile test, the small punch test can also be considered pseudo non-destructive [94]. This is due to the scooping method employed to obtain the testing material [94], [127].

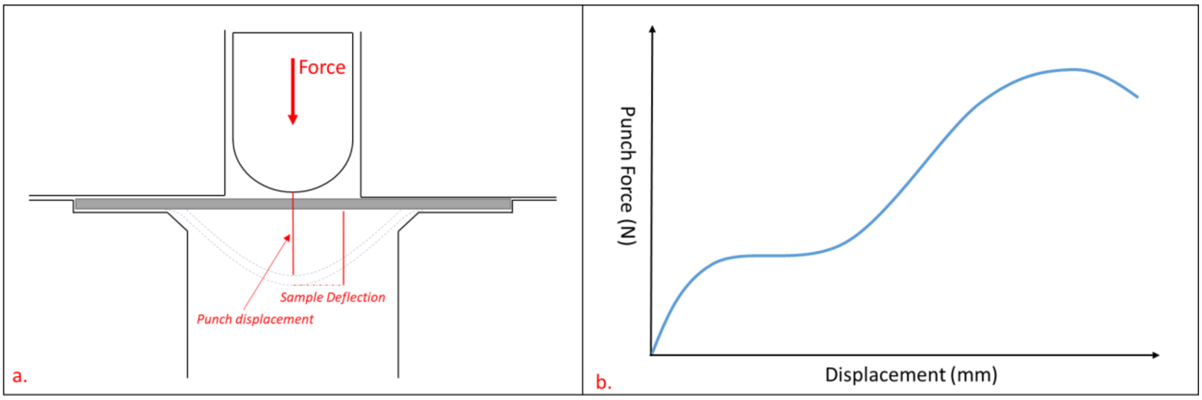

Figure 2.30: a) Diagram showing the small punch test. b) and the force-displacement graph from it. Adapted from "European standard on small punch testing of metallic materials" [128]

Much like other small-scale tensile techniques, small punch test results are affected by specimen size. In general, testing on such a small length scale (8mm x 0.5mm) means that certain factors what are seemingly insignificant on the bulk scale become increasingly important. Noticeably any effects caused microstructural features or defects become magnified significantly. For a smaller specimen, the relative size of said feature/defect grows, thus increasing its influence on the material behaviour as a whole [54], [129].

The small punch test can be used to produce estimates for yield stress, tensile strength, DBTT, and even the reconstruction of a full stress strain curve [128], [130], [131]. These factors show that small punch is a technique deserving of further research to help develop the method for use in structure critical design.

Small punch testing is already used in the analysis of irradiated samples for PLEX schemes [128], [132], [133]. PLEX in an ongoing monitoring scheme that focuses on the change in a materials performance over time [91], [92]. Whereas plant/structure design involves the accurate prediction of properties to ensure that an initial lifetime value is met [134]. Ideally these predictions will be conservative i.e. they will be an underestimation of a materials capability. This should ensure that a plant can run safely (from a materials perspective) for its lifetime [135].

One of the foremost issues with small punch testing is that the established analysis techniques do not always produce conservative results [128], [133]. Further research and understanding is needed to ensure this. This can be achieved, in part, with finite element analysis [136]–[138]. Much like nanoindentation this means that the analysis step will be more complex but with the right research small punch testing has potential to be a useful technique for structure critical design.

Small punch testing is the focus of this thesis and will be further explained in this review.

2.6 A brief history of small punch testing

For nuclear plant life extension or next generation plant design, reliable and repeatable test data is paramount. Over the lifetime of a power plant, the volume of test material needed can become particularly large, making the development of a dependable non-/semi- destructive test method beneficial [139]. Developed in the 1980s, the small punch test was initially designed for testing post irradiation behaviour of materials for nuclear applications [124], [125]. Transmission electron microscopy sized samples (disks 3mm in diameter) were initially used but since then the test has evolved into using larger disks (8mm in diameter) [125], [140], [141].

Interest in the small punch test has grown significantly in the last 50 years, with a sharp increase after 2000 (Figure 2.31). This is due to, in part, the potential application in the fission and fusion industries.

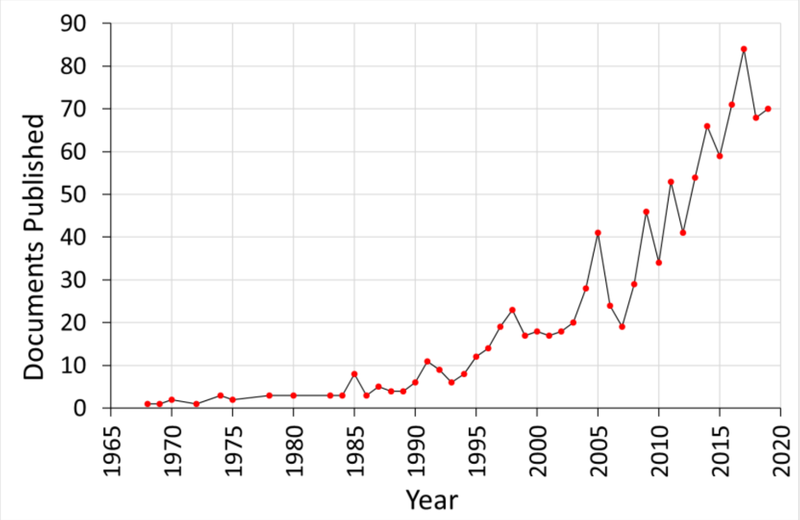

Figure 2.31: Scopus review on all documents published on small punch testing [142].

Manahan et al. [140] explain that the need for small scale testing for neutron irradiated samples is partly cost based. Small scale tests are also advantageous when testing irradiated samples because, of "*space limitations in irradiation experiments*". They were some of the first to propose small punch testing as a potential method for mechanical testing of irradiated materials. It is summarised that small punch testing of TEM sized samples has the potential of producing data on biaxial stress/strain, biaxial ductility, stress relaxation and biaxial creep. The initial tests show good reproducibility [140]. Misawa et al. [143] presented a method of the small punch test to measure fracture toughness. The small punch test produced Ductile to Brittle Transition Temperature, DBTT, results that matched well with v-notched Charpy tests. Thus concluding that SP tests show good potential for testing DBTT.

Following on from Misawa et al., Kameda and Buck [144] also noted the potential of SP tests to evaluate the DBTT of a given metal. The effect of intergranular impurities on the DBTT change on irradiated samples was tested. A correlation between DBTT and impurity concentration was found. This relationship agrees with results found in Charpy v-notch tests, making small punch a good low volume alternative for traditional DBTT tests. This was also confirmed by others over the next few years and decades [145]–[147]. Another paper that used test based on a 3mm diameter TEM sample was that by Mao and Takahashi. They also used the fracture behaviour of a small punch test to successfully form a relationship with fracture toughness. They were also amongst the first to mention that the force-displacement curve of a small punch test could be related to yield stress and UTS [146].

By the early 2000's, the focus of small punch research had moved from analysing DBTT to looking at the analysis of tensile properties [126], [148]. Campitelli et al. [148] utilised a finite element model to calculate the force deflection curve from a small punch test. In particular, they confirmed that a change in strain hardening can be measured. Displaying the potential using SP as a method for measuring the change in strain hardening with irradiation. However due to the complex deformation involved in small punch, direct comparisons between bulk and small scale cannot be made. For example, Kumar et al. explain that unlike a tensile test, the point of maximum force in a SP test does not equate to the true UTS. This is because the maximum force in a small punch does not directly correlate to the onset of necking. In small punch tests it is thought that the onset of necking is prior to maximum punch force. Through the use of finite element modelling and tests on a CrMoV ferritic steel, Kumar et al. found that a punch displacement of 0.48mm correlated with a change in minimum specimen thickness, indicating the initiation of necking at room temperature. This, therefore gave a reasonable point to provide a good estimation of UTS [149].

Over the last decade some complementary techniques have been developed that use the small punch test as their basis, namely the hydraulic bulge test and the small punch fatigue test [150]–[152].

The hydraulic bulge test has been recently adapted into a small scale test with specimens 10mm in diameter and 0.5mm thick. High pressure hydraulic oil is used to deform the specimen in place of a punch. This allows for a larger area of deformation but increases the effect of clamp and die geometry. When used in conjunction with the small punch test, the hydraulic bulge test can aid in providing a broader picture of material deformation behaviour [152].

Small punch fatigue was developed as a way to improve the efficiency of fatigue testing for industries such as aerospace and nuclear. As well as using less material than its full scale counterpart, small punch fatigue also allows for the testing of very specific areas, such as the heat affected zone in welds. The experimental setup consists of two punches, one above and one below the specimen. Force is then applied to each punch alternatively, thus creating the cyclic loading required for fatigue testing. This set up allows for general fatigue testing techniques (discussed in section 2.3.7) to be applied to a small punch sample [150], [151].

2.7 Guidance on small punch test

The cumulation of the research completed since the 1980s has led to the production of a guidance of best practice for the small punch testing of metallic materials [128]. The guide was initially drafted in 2007 and has since been brought up to date [153]. The most recent update published regarding the status of the European Standard on small punch testing was at the SSTT conference in 2018 [128]. It describes the current status of the updated guidance with regard to changes made to the 2007 CWA 15672 [128], [133]. At time of writing, the European standard, "*BS EN 10371. Metallic materials. Small punch test method*", is still in draft form awaiting public comment [154]. Such a standard can assist in the production of increased consistency of results between labs.

As of July 2020 an ASTM standard has been published, entitled: "*ASTM E3205 – 20, Standard Test Method for Small Punch Testing of Metallic Materials"* [155].

An overview of the current guidance will now be discussed.

2.7.1 Apparatus Geometry

The updated guidance includes two different sample sizes; standard, and miniature. The smaller, miniature test is still in the early stages of development, and so is not included in this research. The key dimensions of which can be found in Table 2.1.

Table 2.1: The geometries for the standard and miniature small punch tests, as outlined in the code of best practice [93], [128], [155]

	Standard	**Miniature**
Sample diameter, D [mm]	8	3
Sample thickness, h [mm]	0.5	0.25
Punch radius, r [mm]	1.25	0.5
Receiving die diameter, D_r [mm]	4	1.75
Chamfer length, L [mm]	0.2 x 45°	0.2 x 45°

Both tests consist of the same basic setup as seen in Figure 2.32. The sample is clamped between two dies, with the receiving (lower) die having a set diameter and chamfer dimension.

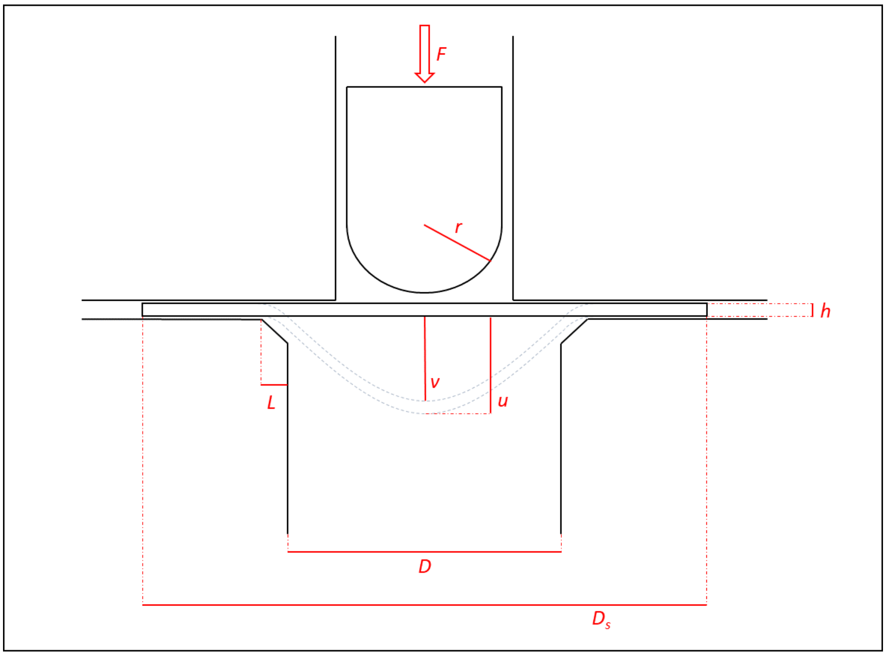

Figure 2.32: Diagram of the small punch test, displaying the important geometric features, the values of which can be found in table 2.1. [93], [128]

The dies holding the specimen in place generally are not required to clamp it with any load. This is known as clamping without load. If a clamping load were to be applied it may have an effect on the stress response of the specimen and should therefore be noted in the rest report [93].

This setup is typically placed within a temperature and atmosphere-controlled vessel, with thermocouples placed throughout the components. This allows for high temperature tests and/or controlled atmosphere tests. One such example being a high temperature test in an argon (or other inert) atmosphere to limit the effect of oxidisation [136], [156].

The punch generally consists of a single hemispherical punch head or a single sphere driven down with a flat headed punch as illustrated in Figure 2.33.

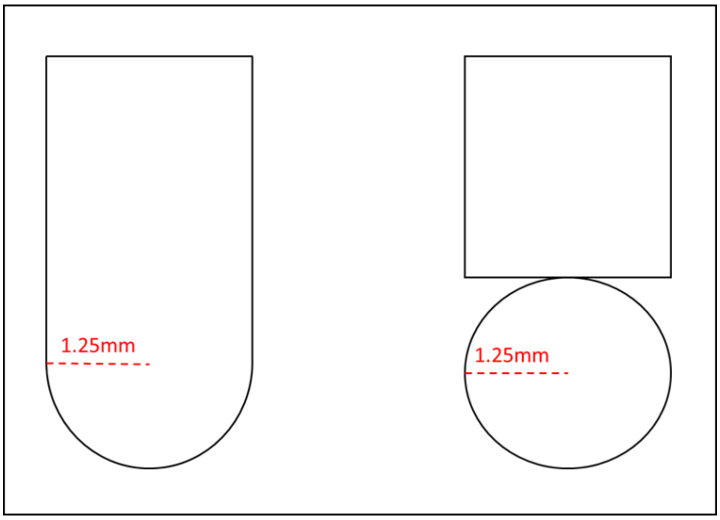

Figure 2.33: Diagram showing the two types of punch heads used in the small punch test [93], [128]

2.7.2 Sample preparation

To achieve the required specimen dimensions (Table 2.1), samples must be prepared accordingly. Firstly, they are machined down to a thickness of 1.1 times the desired height, h. Then, to reduce the effect of work hardening, they are ground down to the desired thickness. Firstly, with a course grit paper of P320, followed by a fine grit paper of P1200 to achieve a sample height of h±1%.

This preparation is in accordance with CWA 15627 and has not been altered in subsequent editions [93], [128].

2.7.3 Data analysis

For a small punch test, three key values are recorded; punch force, F; punch displacement, v; and sample deflection, u. This can be plotted as either a punch force- punch displacement or punch force-sample deflection graph, a diagram of which can be seen in Figure 2.34. A set of arbitrary points can be taken along this curve to allow for ease of comparison between tests.

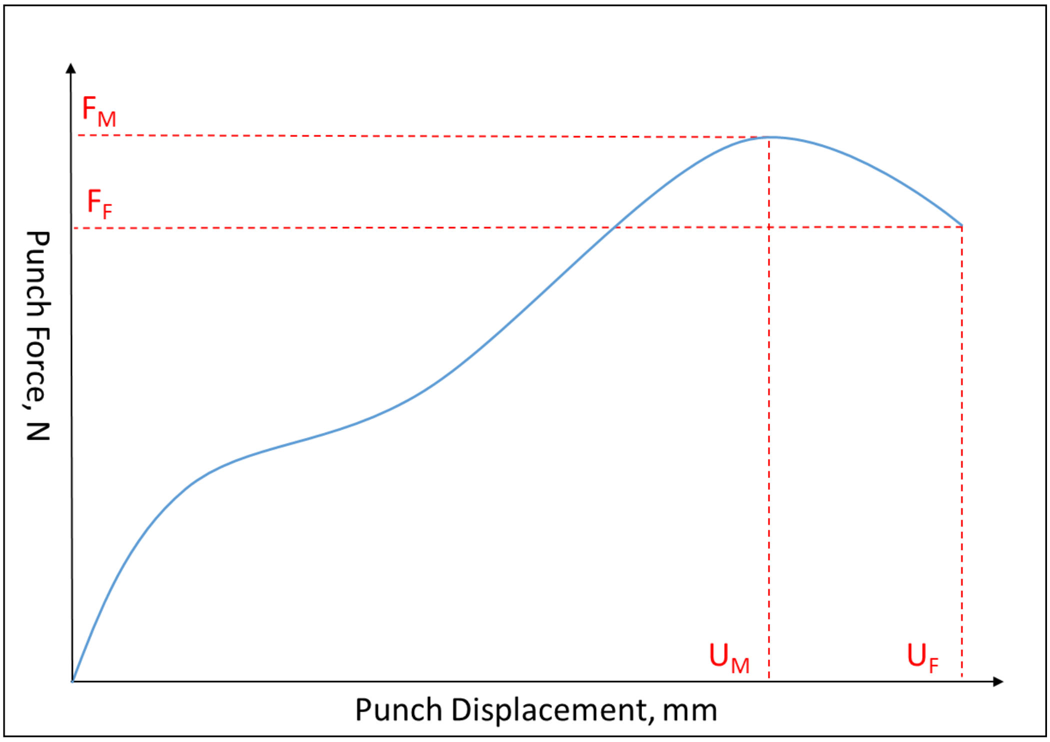

Figure 2.34: Diagram of the force-displacement curve produced by the small punch test, important values have been labelled and are described below [93], [128].

Four points can be given which define the maximum punch force, and the force at failure:

- F_M is maximum force
- U_M is displacement at maximum force
- F_F is force at failure, defined as 0.8*F_M
- U_F is displacement at time of failure

It must also be noted that the area under the curve is often taken as the total energy to deform the sample to the point of failure.

A portion of the curve from 0-0.5mm displacement/deflection encompasses the initial elastic loading and transition to plastic deformation. Plotting this smaller curve allows another set of constants to be defined (Figure 2.35) [128]:

- F_B – arbitrary value of force at 0.5mm of displacement
- U_B – point of 0.5mm displacement
- F_A – the elastic plastic transition force
- U_A – the displacement at point, F_A

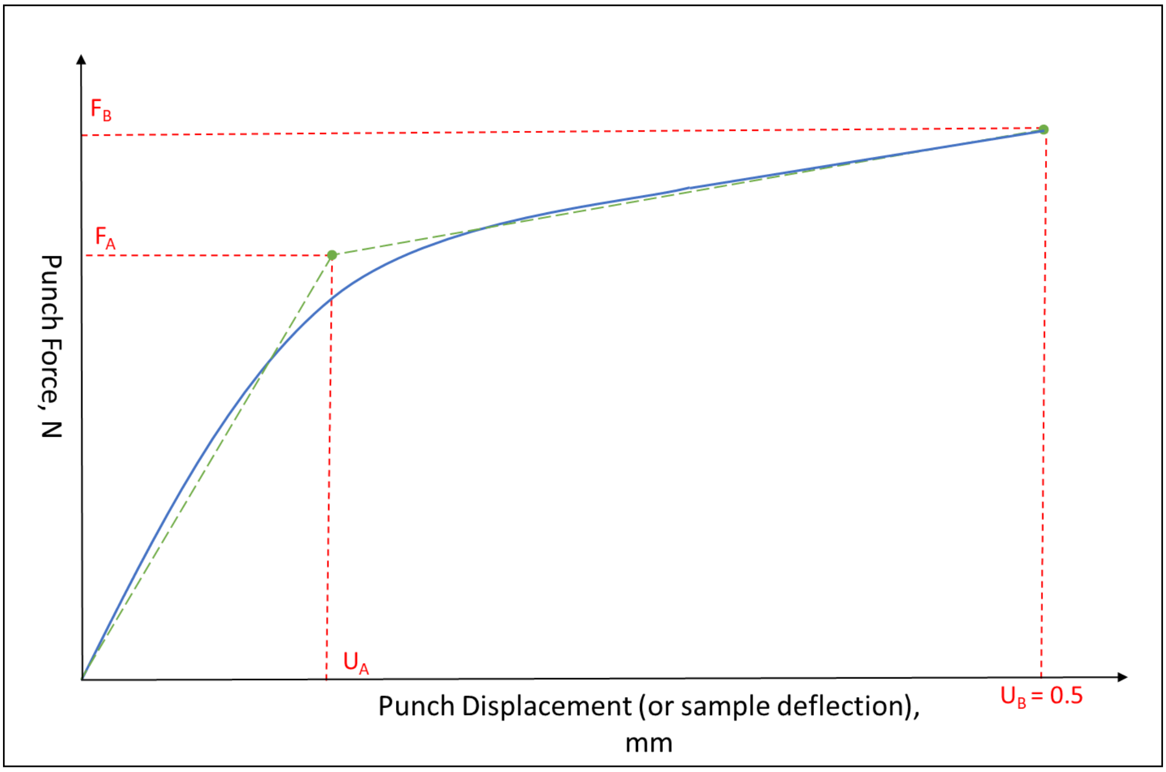

Figure 2.35: Diagram of the force-displacement curve produced by the small punch test up to a displacement of 0.5mm. Some relavent values are also given [93], [128]

To find F_A a bilinear function $f(u)$ from the origin through the points A and B is needed (Equation 2.24) in conjunction with the error minimisation function seen in Equation 2.25 [128]:

$$f(u) = \begin{cases} \frac{f_A}{u_A} \, for \; 0 \leq u < u_A \\ \frac{f_B - f_A}{u_B - u_A}(u - u_A) + f_A \, for \; u_A \leq u \leq u_B \end{cases}$$

Equation 2.24

$$err = \int_0^{u_B} [F(u) - f(u)]^2 du$$

Equation 2.25

Varying F_A in a set area will find the best fit for $f(u)$. This best fit can then be used to calculate U_A and F_A. Taking the gradient from the origin to F_A gives a good approximation of the elastic loading and thus can be used in calculating the total elastic energy of the system. This is achieved by using the spring constant Equation:

$$f = kx$$

Equation 2.26

So in this case:

$$k = {}^{F_A}/_{U_A}$$

Equation 2.27

As the total energy of deformation has been defined as the total area under the curve. It can be assumed that the total energy to achieve the maximum force is the area up to F_M. Then taking the gradient found in the minimisation function and plotting a line down from F_M produces a triangular area (Figure 2.36).

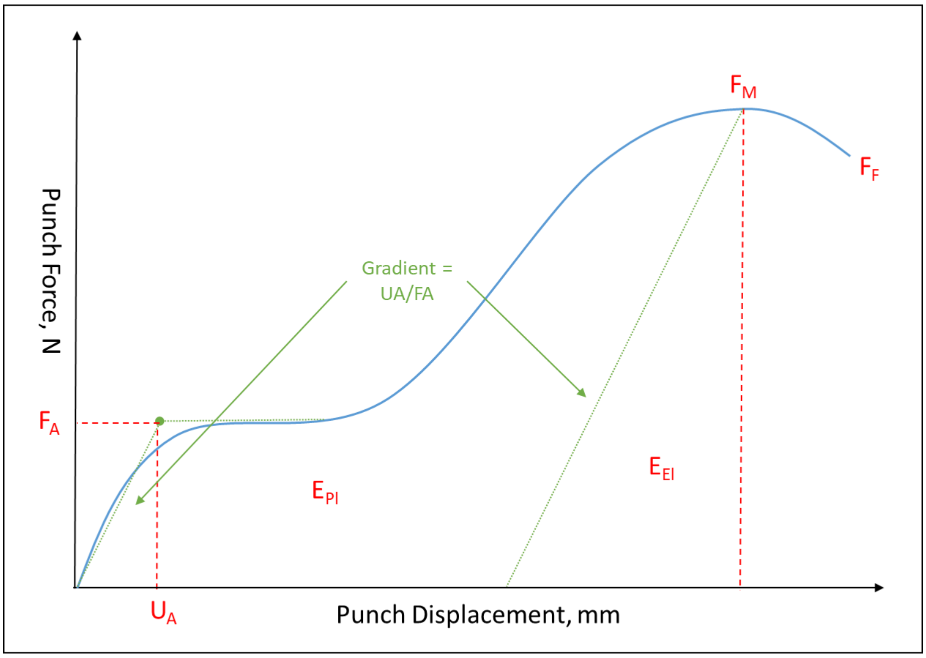

Figure 2.36: Force-deflection graph displaying the composition of the total energy in the system as defined areas under the force-deflection curve.

This area is taken to be the total elastic energy in the system E_{El}:

$$E_{El} = 0.5\frac{(F_M^2 \times U_A)}{F_A}$$

Equation 2.28

From here, plastic energy, E_{Pl}, can also be determined:

$$E_{Pl} = E_{Tot} - E_{El}$$

Equation 2.29

Where, E_{Tot}, is the total area under the curve up to F_M.

From these values, some tensile properties can be estimated. This is done by using the points identified on the curve and extrapolating out values which correlate to the proof stress, $R_{p0.2}$, and ultimate tensile strength, UTS.

Estimation of proof stress

The proof stress or yield stress, $\sigma_{0.2}$, can be estimated using the following Equation [128], [147], [157]:

$$\sigma_{0.2} = \beta_{\sigma_{0.2}} \frac{F_A}{h_0^2}$$

Equation 2.30

Where:

- F_A – the elastic plastic transition force defined earlier
- $\beta_{\sigma 0.2}$ – a geometric correlation coefficient
- h_0 – the sample thickness in mm

$\beta_{Rp0.2}$ is dependent on both the sample geometry and test material. For any steel with a proof stress of between 200 and 1000 MPa using standard sample geometry (D = 8mm), $\beta_{\sigma 0.2}$ can be taken as the values shown in Table 2.2 [128]:

Table 2.2: The values of $\beta_{Rp0.2}$ for sample deflection and punch displacement tests [128].

Curve	**$\beta_{\sigma 0.2}$**
Sample deflection (u)	0.510
Punch displacement (v)	0.479

Estimation of ultimate tensile strength

As with the estimation of proof stress, finding the ultimate tensile strength, UTS, on a small punch curve is a simple process. The update to the standard provides two possible methods for achieving this [128].

The first method, which has previously produced the most reliable results uses the maximum force achieved during the test, F_m [157]. It is also largely similar to the process of estimating $\sigma_{0.2}$ [128], [157].

$$UTS = \beta_{UTS} \frac{F_m}{h_o u_m}$$

Equation 2.31

Where [128], [157]:

- F_m – maximum force recorded during the test
- u_m – the sample deflection at the maximum force
- h_0 – sample thickness
- β_{UTS} – a geometric correlation coefficient

Another method has more recently been introduced which uses a value separate from F_M. This value is denoted u_i and has been numerically determined. As a parameter (one largely independent of tensile properties) u_i is associated with the onset of plastic instability. Like the previous method this one also utilises β_{UTS} a geometric factor.

$$R_m = \beta_{UTS} \frac{F_i}{h_0^2}$$

Equation 2.32

Where [128], [131]:

- F_i – the force at the point of onset of plastic instability, u_i

The values for u_i, and recommended in the standard for the standard test geometry and ferritic-martensitic steels are given in Table 2.3 below [128], [157].

Table 2.3: Values showing the point of onset of plastic instability and ***$\beta_{\sigma UTS}$*** *for sample deflection and punch displacement tests* [128].

Curve	**u_i/v_i (mm)**	**$\beta_{\sigma UTS}$**
Sample deflection (u)	0.552	0.192
Punch displacement (v)	0.645	0.179

Such estimations provide a quick and simple way for assessing small punch curves and the test materials.

Estimation of creep stress

The small punch test can also be used to analyse creep properties. This is achieved by changing from a displacement rate controlled test to force controlled tests. Small punch creep tests take much longer than the standard SP tests, and are usually carried out at elevated temperatures. The output from a small punch creep test consists of a deflection vs time graph as seen in Figure 2.37. Many tests can be added to the one graph thus allowing for a quick evaluation of changes in temperature or applied force [133].

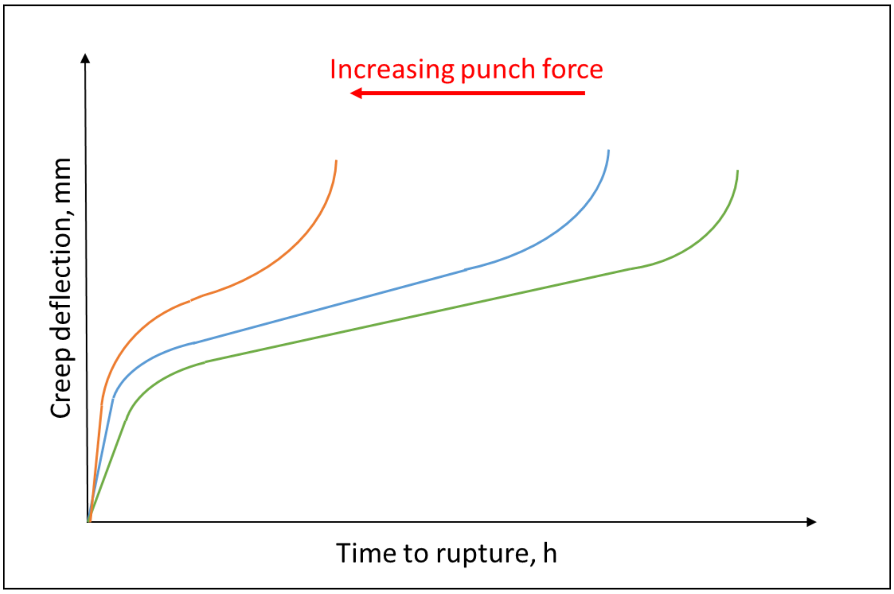

Figure 2.37: Diagram showing the changes in behaviour by increasing the punch force in the small punch creep test. An increase in punch force leads to a reduction in time to rupture [93] .

The most useful value calculated from standard creep test is the creep stress, as explained previously. However, for a small punch creep test, this cannot be measured directly as the relation between punch force and stress is not simple. To solve this, two separate relationships have been devised.

The first was included in the original CWA 15627:

$$\frac{F}{\sigma} = 3.33k_{SP}\frac{r^{1.2}h_0}{(0.5D)^{0.2}}$$

Equation 2.33

Where:

- F = punch force
- σ = creep stress
- r = punch radius
- D = receiving die diameter
- k_{SP} = ductility related coefficient

This correlation had been used for some time but as k_{SP} is material and temperature dependant its viability is limited [128], [133]. Another correlation has been developed which is based on minimum deflection rate:

$$\Psi_{EFS} = \frac{F}{\sigma} = 1.916u_{min}^{0.6579}$$

Equation 2.34

Where:

- Ψ_{EFS} = the force to stress ratio
- u_{min} = the deflection at the point in which the deflection rate reaches a minimum

The minimum deflection rate can also be used to calculate the creep strain:

$$\dot{\varepsilon}_{min} = 0.3922u_{min}^{1.191}$$

Equation 2.35

Ductile to Brittle Transition Temperature

Being able to calculate the ductile to brittle transition temperature, DBTT, was one of the first techniques developed with small punch test data. Through a simple correlation it is possible to convert the small punch DBTT to an estimation of a Charpy test DBTT:

$$T_{SP} = \alpha T_{CVN}$$

Equation 2.36

Where:

- T_{SP} = Small punch DBTT
- T_{CVN} = Charpy DBTT
- α = correlation factor usually ≈ 0.4

To determine the DBTT in a small punch test, the energy of the test is required. As briefly stated above, this can be taken as the integral of the curve up to u_m:

$$E_{SP} = \int_0^{u_m} F(u)du$$

Equation 2.37

Fracture mechanics

While the estimation of DBTT shows that it is possible to analyse the fracture behaviour of a material using small punch; the difference in sample thickness between a standard fracture toughness sample and a SP specimen means that any correlation will be impractically complex [128]. It is advised that any fracture analysis of a small punch test is to be taken as semi-quantitative at most, and should be used instead as a form of vetting technique to reduce the number of tests that need to be completed at full scale [128].

Applicability of correlation Equations

The Equations and methods outlined above have been applied to a range of materials. For example the tensile correlations (proof stress and ultimate tensile strength) have been shown to work for a very wide range of steels [128]. While the creep and DBTT correlations have also been applied to a large range of steels, the main focus has been on structural steels, such as P91, P92 and Eurofer97, along with some stainless steels, i.e., 316L [126], [133], [147].

The behaviour of all three tests types (tensile, creep and DBTT) can be readily found in literature, for P91 in particular [126], [133], [147]. Examples of this behaviour are included in Figures 2.38 – 2.40.

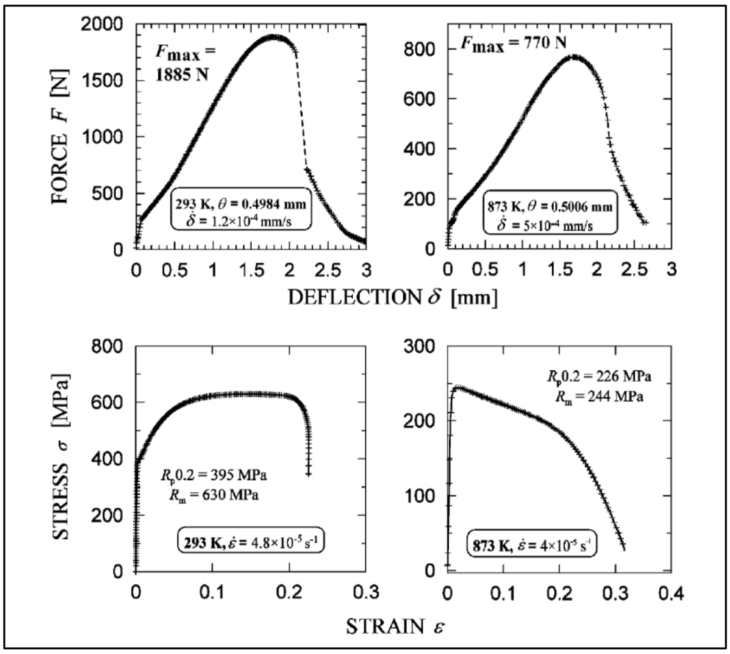

Figure 2.38: The small punch test behaviour of P91 steel compared with standardised tensile behaviour. Two temperatures are included here (293K and 873K). Note the large change in maximum force in the small punch test curve with an increase in temperature, this matches the behaviour seen in the tensile curve [126].

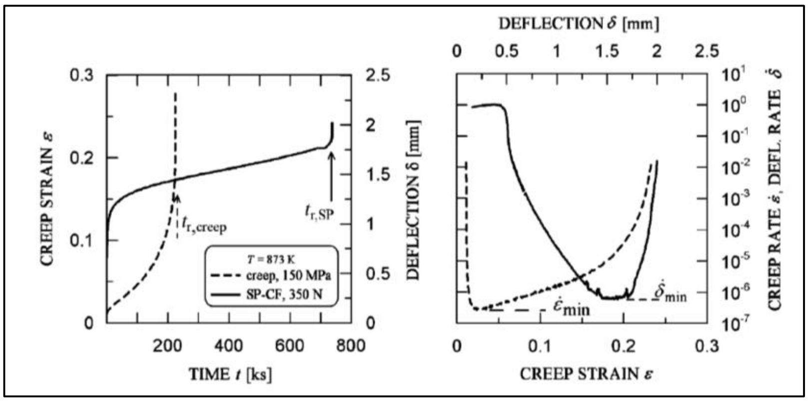

Figure 2.39: The small punch creep test behaviour of P91 steel compared with the standardised creep test curve. Both creep strain and creep rate are shown. Note the large difference in curve shape seen in the creep strain vs time graph. [126]

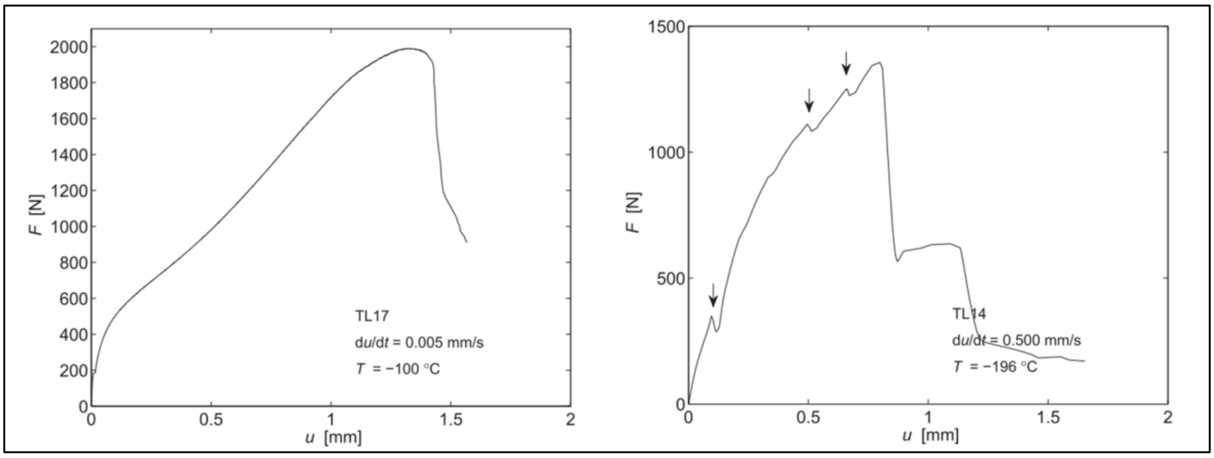

Figure 2.40: Graphs showing the ductile and brittle behaviour for P91 steel in a small punch test. The results from which were used to determine the ductile to brittle transition temperature. Tests were carried out at -100˚C and -196˚C respectively [158].

Like most correlations, the ones described here have their limitations, and in particular the tensile and creep equations are best suited for a range of steels and not much else.

While the tensile behaviour can be applied to a wide range of steels, it breaks down when calculating more brittle materials such as titanium alloys [128], [133]. The creep behaviour equations are even more limited in their applicability, this is due to both material and temperature sensitivity of the K_{SP} constant [128]. It is also noted that it is not appropriate for softer forging steels [128].

The ductile to brittle transition behaviour methods are better suited to a wider range of materials. This is because it looks at a change in behaviour which can be observed in brittle and ductile materials alike [147]

In general, the methods and Equations outlined in this section are applicable for ductile steels. This is probably one of the main limitations of small punch testing at this time. However, with further research along with experimental results used in conjunction with finite element modelling this may be rectified.

2.8 Sources of inconsistent results in small punch testing

Small punch testing is sensitive to many factors, and so can produce inconsistent results. To counter this, the possible factors affecting the results must be considered and understood [136], [156].

Starting with the factor that affects all small scale tests, the reduced sample size. As previously stated a reduction in sample size increases the relative effect of any defects present. Microstructure and surface finish form a large part in this. While heterogeneous microstructure is inherent and cannot be altered, the surface effects can be. This is achieved by grinding both surfaces down to a set finish (P1200 as stated in the code of best practice, ASTM standard and round robin). This ensures that any relatively large surface defects are either ground away or reduced to an acceptable size i.e. they should no longer be a major point of stress concentration and possible source of premature fracture [54].

Testing apparatus also contributes to inconsistencies in results. There are several factors to consider here, distortion during loading, punch alignment and wear, and die geometry.

The small punch test can involve high levels of loading (kN), leading to a distortion of the apparatus itself as it reacts to the load. This is known as compliance and is well documented in small punch testing [132], [137], [148], [159], [160]. To mitigate this, two things can be done. Firstly, a compliance correction factor can be added to the force-displacement data (Figure 2.41). Secondly, using sample deflection data instead of punch displacement can reduce the effect of machinery distortion. This is down to the fact that the sample deflection will be less affected by the apparatus around it, whereas the punch displacement is heavily affected due to it being part of said machinery.

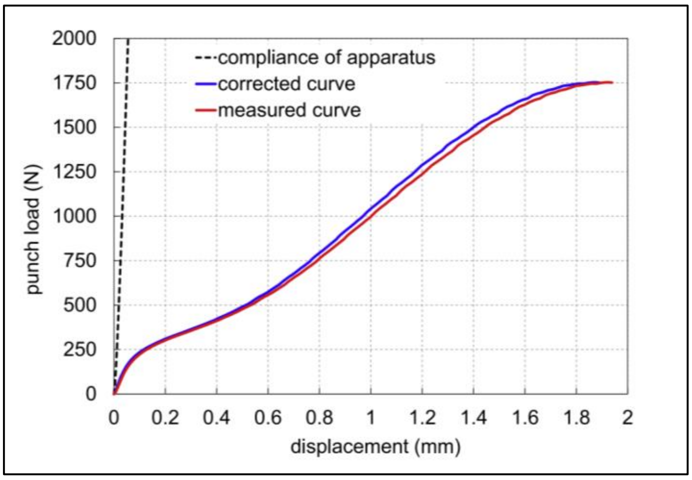

Figure 2.41: Diagram from "European standard on small punch testing of metallic materials" displaying the compliance present in the small punch test apparatus [128]

Due to its small size, a misalignment of the punch by even a couple of mm can have a marked effect on the final results [128]. Any misalignment can cause a change in the deformation shape and unwanted friction with the punch guide.

After some time, the punch will start to wear, causing a change in head shape and surface finish. Both of these factors will play a role in producing inconsistent results over a series of tests. A change in shape may cause the areas of stress concentration to move, thus producing an erroneous time to fracture. And any change in surface finish will have an effect on the friction between punch and sample [147].

Both the upper and lower die play vital roles in the small punch test. The upper die is vital in ensuring that the sample does not move throughout the test. Whereas the lower die does this in conjunction with guiding the shape of the sample as it bends. The chamfer in particular plays a vital role in this, as it guides the deformation and flow of the sample [161]. The standard recommends a chamfer of 0.2mm x 45˚ which can be seen in Figure 2.24 [128]. It is possible that, like the punch, the lower die will start to wear over time. Such a change in the geometry of the chamfer has the potential to affect test results [162].

Atmosphere can have a significant effect on a materials behaviour, particularly at high temperatures. This is due to the potential oxidisation of the sample surface. In this case an oxide layer can affect the friction between the sample and punch. Oxides also tend to be brittle and so could cause small fractures in the surface thus affecting the final results [156]. To get around this, some tests are carried out in an inert atmosphere such as argon. This is particularly helpful when working at high temperatures or with alloys that oxidise quickly in air. However, the presence of an argon atmosphere has shown to have an effect on results even when at RT with an oxidisation resistant alloy. This is thought be due to a change in friction between sample and punch [136], [163]. Any change in test atmosphere must be carefully considered.

2.9 Finite element modelling of small punch testing

2.9.1 What is FEM?

In both science and engineering it is vital that the mechanics behind certain phenomena are understood. This can be achieved by simulations. However, in most cases the things that need simulating involve complex mathematical models, and therefore are extremely computationally expensive to resolve for a whole system. To get around this, a system i.e. a tensile test, can be discretised into small elements to which the mathematical Equations can be applied. With the Equations applied to each element the system as a whole can be solved. Applying this can greatly reduce the computational time, without sacrificing much accuracy [164].

2.9.2 FEM fundamentals

The geometry of the component of a finite element model is the first of the building blocks required for an accurate analysis. Aside from the obvious role of ensuring that the model is geometrically correct, the geometry also plays a role in forming the locations of boundary conditions, meshes, and other any other required constraints [164].

Forming the mesh is achieved by dividing the geometry up into N_e element and N_N nodes and is otherwise known as domain discretisation. Each node is connected to its neighbours to form an element and each of these nodes and elements are given unique numbers. This method of applying the mesh ensures that there is no overlapping of elements, or any gaps between them. Together, the elements form a whole domain i.e. they make up the complete component geometry [164].

For finite element modelling to work, each element/node has to be based on a coordinate system. This system is defined on the local level, for each element, and on the global level, for the component, or domain as a whole.

To define the displacement of an element, the interpolation of the displacement of its nodes must be taken [164]. This is given as:

$$U^h(x, y, z,) = \sum_{i=1}^{n_d} N_i(x, y, z) d_i$$

Equation 2.38

Where:

- U^h = displacement approximation
- n_d = number of nodes forming the element
- d_i = the displacement of the ith node
- N_i = the shape function

For the case where there are 3 degrees of freedom (x, y, and z, directions) d_i can be given in the form:

$$d_i = \begin{Bmatrix} u_i \\ v_i \\ w_i \end{Bmatrix}$$

Equation 2.39

where:

- u_i = displacement in the x direction
- v_i = displacement on the y direction
- w_i = displacement in the z direction

The shape function of an element is the assumed shape that it will take with respect to the nodal coordinates. It has the general form of:

$$N(x, y, z) = [N_1(x, y, z), N_2(x, y, z), \dots\ N_{n_d}(x, y, z)]$$

Equation 2.40

and in the case of Equation 2.41, where there are 3 degrees of freedom, this can be taken as submatrix:

$$N_i = \begin{bmatrix} N_{i1} & 0 & 0 \\ 0 & N_{i2} & 0 \\ 0 & 0 & N_{i3} \end{bmatrix}$$

Equation 2.41

This is also often taken as $N_{i1} = N_{i2} = N_{i3} = N_i$

When this is applied to each element, a displacement field is produced. This method assumes that each node is independent of those around it, thus making the application of boundary conditions simple. If a node is set to be static, then it can simply be removed from the matrix, in Equation 2.41. This method can also be applied to the addition of properties to each element [164], [165].

The addition of properties is achieved by substituting out the displacment at each node with the desired constitutional Equation. The interpolation between each node will give an approximation of the solution of the element. This method is also valid for mass and stiffness [164].

When a force is applied to the domain, it is also descretised and applied to each node separately as vectors. Surface force vectors and body force vectors are combined to form a total force vector, f_e. This can also be decribed in terms of the mass and stiffness matricies [164], [165].

All of these factors come together to produce a finite element model. The formation of a finite element model relies on the creation of shape functions, then apply constitutional Equations to the functions. This will allow for the analysis of the full domain or component [164].

2.9.3 Applications in engineering

Finite element analysis is used across engineering, from structural applications to metal forming and machining [166]–[168]. Meaning that there is a large body of information displaying its validity in the field. A large advantage of finite element analysis is its ability to replicate mechanical tests to a high degree of accuracy. Making the method a leading candidate in aiding the development of new testing techniques.

2.9.4 Small punch testing

Due to the complex nature of the deformation in small punch, and the many sources of inconsistency/uncertainty, it is wise to study the test using FEM. This has already been examined extensively with investigations varying from overall deformation trends to in-depth looks at fracture mechanics [131], [173]. To understand the FEM work done thus far, a summary of some relevant papers can be created.

The deformation profile of a small punch test specimen has many potential sources of uncertainty, so studying the test using finite element modelling (FEM) is prudent. Looking at the literature to date on the topic will give an insight into current simulation methods and will allow for an informed decision on the best route forward.

From a practical standpoint it is wise to understand how the finite element modelling of small punch testing has been carried out in the literature. FEM software and materials models used will provide some necessary information for this project. Several key points were noted:

- The FEM software used
- The method of modelling material plasticity
- The method of modelling material damage/failure
- The friction coefficient used for the sample-punch interaction
- The optimisation algorithm used (where applicable)

By far the most common software package used was Abaqus [130], [131], [136], [161], [169], [170].

The use of plasticity models to describe the sample deformation is largely inconsistent, as there is no one clear method used more than others. Some papers used very simple elastic and yield data [136], [169], others used pre-existing data and models [130], [170], [171], and some appeared to have created their own constitutive models of flow stress [131], [172].

Only three of the papers reviewed included any sort of material damage/failure. Two used the GTN damage model [148], [170], while the final one used the Cockroft–Latham damage criterion [171]. Both models that utilised the GTN damage model did so using Abaqus software, whereas, the third model was completed in DEFORM.

Those that include optimisation/ inverse analysis as part of their remit, mostly use MATLAB in conjunction with Abaqus [169], [170]. Of the optimisation packages available in MATLAB, the golden search algorithm is the most popular. One paper in particular uses an "inverse finite element method" thus making it unclear what exact methodology was used, meaning that reproduction is not possible [130].

The conclusions analysed varied in their confidence of finite element analysis (FEA) as a viable analysis technique. While some stated with confidence that FEA can accurately predict material behaviour [130], [169], [172]. Others were clear in stating that, while the methods show promise, they are still in their infancy and need further development [170], [171]. Of course there are some discrepancies in the dates of said papers, but there was enough of an overlap in opinions that all papers could be considered relevant.

As shown, there is a well-established body of work around the finite element modelling of the small punch test. However, this is not without limitations, and the two main areas that current literature seems to fall short on is; inconsistent specimen, punch, and die geometries; and the lack consideration of friction between the punch and specimen.

In 2007 a publicly available code of best practice guide was created, the CWA 15627 – Small Punch Test Method for Metallic Materials [93]. This outlined the recommended specimen and apparatus geometries (Table 2.1). However, since then a few bodies of research have been published that do not adhere to this guidance [130], [169], [170]. While the methodologies presented show potential, the difference in geometries used in their simulations limit any comparison with work from other institutions. Specifically, the work completed by Li et al. on the construction of a stress strain curve using small punch data and FEM would be of particular interest if applied to the geometries outlined in the guidelines [130]. As it is, the simulations have been completed on specimens with a diameter of 10mm, a thickness of 0.5, with a punch of 2.4mm and receiving die of 5mm. The geometry of the chamfer was also omitted, making reproduction of the research difficult.

The importance of friction in the small punch test is well documented [147]. A number of the papers surveyed here included the value of the friction coefficient for the interaction between punch and sample [130], [169], [170]. Those that did include their friction coefficient values showed a variation between μ=0.2 and μ=0.4 [136], [171], [172].

Simonovski et al. highlight this in their work on the analysis of curved specimens [161]. The variation in friction coefficient significantly changed the morphology of the specimen deformation (Figure 2.42), which in turn altered the location of stress concentration.

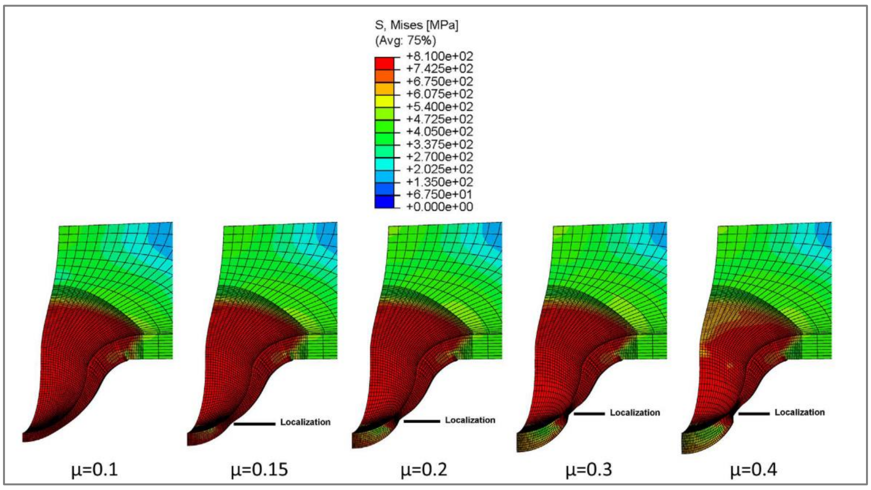

Figure 2.42: A diagram of the small punch simulations by Simonovski et al. showing the stress localisation caused by a change in friction coefficient [161]

The importance of friction in the small punch test means that it must be seen as a fundamental element when creating a simulation. If this were to be omitted, any results would be taken as not representative of experimental small punch test behaviour. So it is recommended that when creating a new simulation, the effect of friction on the system is analysed and an appropriate coefficient selected.

2.10 Inverse analysis

2.10.1 What is inverse analysis?

In its most rudimentary form, inverse analysis is the optimisation of a function through iterating the input variables until a best fit is found. Optimisation usually involves error minimisation through the use of an algorithm [174].

In engineering an inverse problem typically consists of a set of experimental data with unknown governing Equation parameters. With the assistance of simulation, it is possible to use inverse analysis to obtain the values of the governing Equation. Usually the error between simulated and experimental data is calculated and used as a goal function for the inverse process i.e. the algorithm will change variables to reduce this error as much as possible, ideally to zero.

2.10.2 Search algorithms

Any engineering problem with unknown Equation parameters has many possible solutions. One way of solving this is to cover every possible solution until the best is found, known as sequential searching. However, this will be extremely computationally expensive and inefficient. To reduce this a smarter way of finding the optimal solution can be used. By employing an interval searching, the possibilities can be narrowed down to a smaller group. This has the potential to vastly reduce the required calculation time. But as with all time saving measures, there is the possibility of reducing the accuracy of the results. A balance must be struck between computational time and accuracy [175]. Some of these search functions for nonlinear problems are as follows.

Direct search algorithms

The direct search method is a method of optimisation that does not require the derivative of the objective function. Instead all direct search algorithms work on point values of the objective function. The main thing to note with direct search methods, is that they were mainly developed heuristically. Meaning that they lack the full mathematical proofs, and rather rely on experience to prove their validity. Despite this, direct search methods are in general reliable, robust and do not often fail to find a local minimum [176].

Direct search methods are particularly useful in optimising problems where finding derivatives is not feasible, also when there is inherent unpredictable error present in the initial data set (experimental data for instance) [176]. These facts mean that direct search methods can be widely and easily applied.

Two notable direct search algorithms are the simplex (Nelder-Mead) and the golden section [177], [178].

Golden search functions by successively reducing the search area until a minimum is found [178]. Whereas simplex systematically iterates through a series of options gradually minimising each until an optimal result is found [179], [180].

Genetic algorithms

Although not used in this thesis, it is pertinent to briefly touch on genetic algorithms. Genetic algorithms is a method mainly used for the optimisation of functions [181].

Inspired by evolution, genetic algorithms work on the basis of generational changes. Most start with a random set of estimated values, or chromosomes. These are all individually assessed and their results compared. Those that have better matches are selected to reproduce [181]. This reproduction creates a new generation of estimates, which can then undergo the same assessment as the previous generation. An illustration of this can be seen in Figure 2.43 [181].

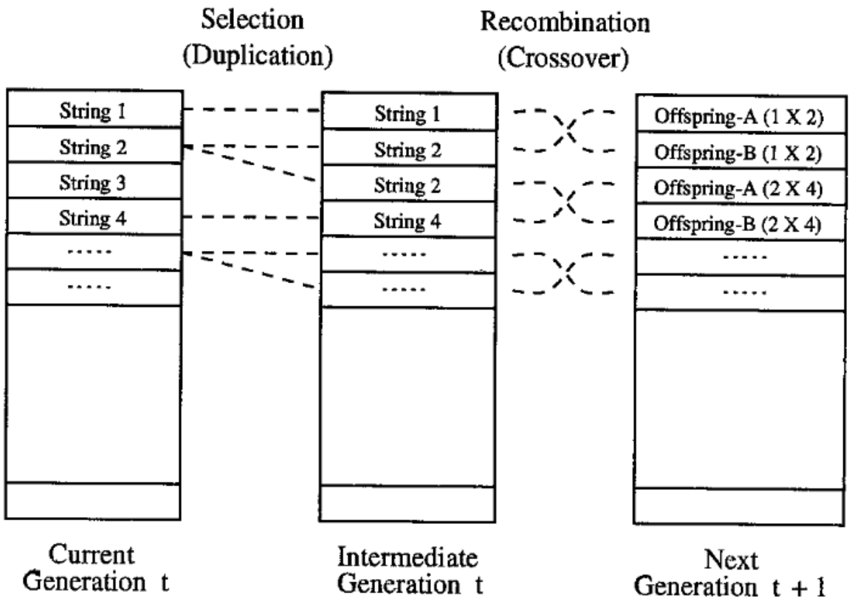

Figure 2.43: Diagram illustrating the different stages of development in a genetic algorithm. From "A genetic algorithm tutorial" [181].

While genetic algorithms are exceedingly effective at finding global optimisations, they are extremely expensive and can take a long time to complete. This is due to the whole population of estimates needing to be regenerated and recalculated with each new generation [181], [182]. It is due to the computational expense required of genetic algorithms that they are not considered further in this thesis.

Simplex search algorithm (Nelder Mead 1965)

As devised by Nelder and Mead in 1965, the simplex algorithm (otherwise known as the Nelder-Mead algorithm) is a direct search method for multidimensional unconstrained optimisation [177], [180].

This method is based on the idea of a simplex (a shape based on triangles and tetrahedrons) to visualise the possible solutions to a function with n variables. This simplex exists as a four-dimensional surface with n+1 vertices. Each vertex being a possible solution. The highest vertex in the system is identified and replaced with a new solution. This is iterated on and leads to the convergence of a minimum and thus an optimised solution.

As stated, the simplex method starts with a function of *n* variables. This function has no constraints and P_0, P_1, … P_n are the n+1 points of the simplex. For a function y_i the point P_i can be defined [177]. High and low values of the function are also defined, such that:

- y_h = maximum possible value of y_i
- y_l = minimum possible value of y_i

A centroid point between these two values is also taken as $\bar{P}$, where i ≠ h, and $[P_iP_j]$ is the distance from P_i to P_j.

For each step in the optimisation, P_h is replaced, using one of three operations. These are, reflection, contraction, and expansion.

The reflection operation, P*, is defined by:

$$P^* = (1+\alpha)\bar{P} - \alpha P_h$$

Equation 2.42

where:

- α = the reflection coefficient (always positive)

If the distance between P* and $\bar{P}$ is equal to the α multiplied by the distance between $\bar{P}$ and P_h. Then, P* can replace P_h, and a new simplex is formed.

If the reflection operation creates a new minimum, then the expansion operation is used:

$$P^{**} = \gamma P^* + (1-\gamma)\bar{P}$$

Equation 2.43

Where:

- γ = the expansion coefficient

The expansion coefficient is always greater than one and is the ratio of the distance between P** to $\bar{P}$ and P* to $\bar{P}$. Where this operation successfully produces a new minimum, then P_h is replaced with P** and a new simplex is created.

Finally, if P* is less than P_h, but is still maximum, then the contraction operation is used:

$$P^{**} = \beta P_h + (1-\beta)\bar{P}$$

Equation 2.44

Where:

- β = the contraction coefficient

The contraction coefficient falls between 0 and 1 and is the ratio of the distance between P** to $\bar{P}$ and P to $\bar{P}$.

If any of these operations fail, then the simplex will be restarted.

To decide on whether the optimisation has finished or not, a comparison of the "standard error" is used:

$$\sqrt{\frac{\sum(y_i - \bar{y})^2}{n}}$$

When this falls below a predetermined value, then the simplex algorithm is deemed finished [177]. A visualisation of this can be seen in Figure 2.44.

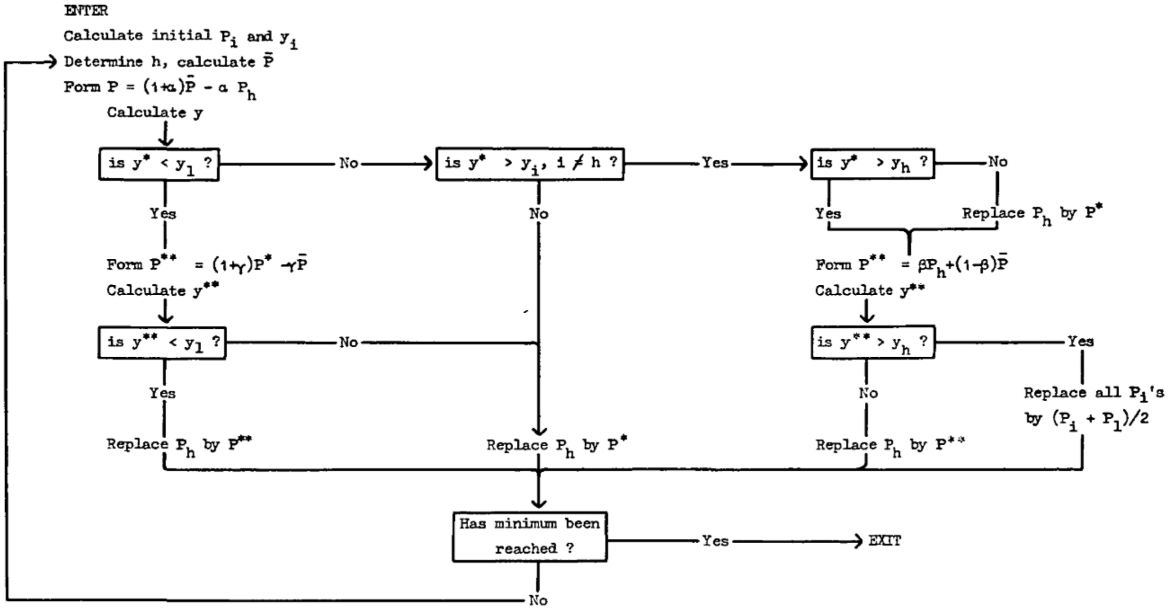

Fig. 1.—Flow diagram

Figure 2.44: Diagram illustrating the different stages in the Nelder-Mead simplex search method. From "A Simplex Method for Function Minimization" [177]

The simplex method has been proven to be robust and computationally compact. However, as with most direct search methods, there is a possibility of the algorithm finding a false minimum. Such methods must rely on good starting estimates [177]. The simplex method has been used numerous times in the fields of science and engineering and has thus proved itself a valuable tool for simulation and function optimisation. This method will be used in this thesis.

2.11 Inverse analysis and small punch

Small size and complex deformation means that material properties cannot be directly calculated/recorded. To solve this, inverse analysis can be employed. Much like the examples used above, the inverse analysis of small punch testing requires simulated and experimental data. Several papers have been published on this topic and will be summarised.

Of the papers analysed the majority used Abaqus and Matlab. The inverse analysis was applied with these pieces of software in different ways [138], [169], [170].

The golden section algorithm was used by S. Yang et al. [169], [170]. It was noted that the golden section method produced on average 2.55% error. But when compared to neural networks and enumeration it is much quicker and more efficient. Neural networks in particular are noted as requiring large amounts of computational time and space. For the purposes of engineering applications golden search would be preferable. As it is more efficient and can effectively and conservatively predict materials tensile parameters from small punch curves.

Only one paper applied the Simplex method to small punch inverse analysis [183]. The focus of the paper was the assessment of non-active nuclear reactor materials. An emphasis on simplicity of application led to the decision to use the Simplex optimisation method. The Simplex method does not require gradient estimation and so is computationally efficient. One of the main conclusions drawn was that due to the nature of the simplex method, there exists the possibility of producing non-unique results. This was especially prevalent when the coefficients in a constitutive model are correlated. It was also noted that while these results may not be "absurd" they still do not properly represent the material behaviours and thus have inherent errors.

Two papers utilised neural networks and genetic algorithms [130], [138]. Both of these papers utilised Abaqus. Peñuelas et al. [138] utilised an evolutionary genetic algorithm. It was found that this process could produce materials parameters with high accuracy, but has to be rerun for every change in sample geometry, test temperature and material. This is true of every inverse analysis process, but as other papers have stated running a genetic algorithm is computationally expensive [169], [170]. Thus rendering this method inefficient.

Li et al. [130] utilised a neural network for the prediction of the Holloman model from the small punch curve. The results from this were then used in conjunction with linear fitting and interpolation techniques to construct a full stress strain curve. This was achieved by selecting a set of parameters and using them in various combinations to complete 360 individual simulations. The results of these simulations were then fed into the neural network and used to train it. This produced results that appeared to be in good agreement with experimental values. However, much like the previous paper, this method is computationally expensive and so not suitable for engineering applications requiring large volumes of results efficiently.

One final paper, takes a different direction than the others. Egan et al. [172] use the inverse analysis method to optimise the deformed sample geometry. A combination of curve fitting, direct search, and genetic algorithms were used to achieve this. It is concluded that the plastic properties were predicted without any "accurate preknowledge". However, how this was exactly achieved was not clearly stated, making any recreation of this method difficult. The overall concept of this method is interesting.

2.12 Inverse analysis and Johnson-cook

When analysing the current research completed on the inverse analysis of the Johnson-Cook models it became clear that there was a certain amount of vagueness surrounding the exact methods used. Most of the papers revolve around machining, subsequently not all methods used will be relevant for small punch applications. However, providing an overview of the inverse analysis of Johnson-Cook parameters will provide a helpful insight into current approaches.

All of the studies utilised goal functions, which were mainly based on the error between the experimental and simulated values. However, there is a general lack of specifics on the optimisation of these functions. Methods varied from "trial and error" to systematically testing all possibilities between sets of boundaries [184]–[188]. While useful for proof of concept studies, such methods are expensive and inefficient, thus not suitable for the production of many results.

As stated previously, these studies provided a good proof of concept in which several important conclusions were drawn.

The first being the importance of initial input values for inverse analysis. A change in starting values can have a significant effect on the final optimised results, and so should be studied and understood fully for each new material.

Secondly, is the production of non-unique results, i.e. the possibility of incorrect solutions producing similar graphical results to the correct solutions. In extreme cases these incorrect results may be far from physically possible and could be considered “absurd” [185]. This is related in part to the previous statement as a particular starting value may lead to such results.

Even with these challenges, all of the studies are positive about the application of inverse analysis to accurately determine the values of the Johnson-Cook parameters.

2.13 An Introduction to Eurofer97 and P91

At this point it seems sensible to introduce the two steels that will be the focus of this project, Eurofer97 and P91. It can be seen thus far that both steels have been commonly used throughout the development of small punch testing.

Known as a Reduced Activation Ferritic-Martensitic (RAFM) steel, Eurofer97 is essentially the reduced activation analogue of P91 [189]. P91 steel is a well-established structural steel but cannot be used in parts of fusion reactors that experience high levels of radiation. This is due to the presence of certain alloying elements that transmute into active elements when exposed to high levels of neutron bombardment [37], [189]. As stated in section 1.2 any material used in a fusion reactor must fall under the safe handling limit 100 years after being removed from the reactor [50]. Many of the alloying elements in P91 do not meet this criteria (Illustrated in Figure 1.8), so the development of a new alloy, Eurofer97, was necessary [189]. The composition of both alloys is provided in Table 2.4, where the change from a typical steel alloy to reduced activation is evident.

Table 2.4: Compositions of Eurofer97 and P91 steels in weight percent

Chemical element	**Eurofer97 (wt%)** [190]	**P91 (mean wt %)** [191]
Al	<0.01	0.006
As	*	0.005
B	<0.002 (ALAP)	0.0009
C	0.09-0.12 (target 0.11)	0.12
Co	<0.01 (ALAP)	-
Cr	8.50-9.50 (target 9.00)	8.32
Cu	<0.01	0.05
Mn	0.20-0.60 (target 0.4)	0.41
Mo	<0.005	1.02
N	0.015-0.045 (target 0.030)	0.041
Nb	<0.005	0.084
Ni	<0.01	0.1
O	0.01	0.0015
P	<0.005	0.0091
S	<0.005	0.001
Sb	*	0.001
Si	-	0.24
Sn	*	0.005
Ta	0.10-0.14 (target 0.120	-
Ti	<0.02	0.002
V	0.15-0.25	0.235
W	1.0-1.2 (target 1.1)	0.001
Zr	*	0.001

(ALAP: As low as possible, *: As + Sn + Sb + Zr = 0.05)

Both alloys exhibit comparable tensile properties, whereas P91 has superior creep resistance. This is due to the size and location of carbides present in both alloys [189].

P91 in its as tempered state generally produces grain sizes ranging from 14-50 µm with a ferrite-martensite dual phase microstructure. Such a large range is due to the many possible heat treatments that can be applied. With each one completed to create a specific microstructure for a required application [192], [193]. An example of this grain size can be seen in Figure 2.45 which shows an EBSD scan of an as tempered P91 steel for use in small punch testing. The EBSD scan also helps to display the texture of the alloy.

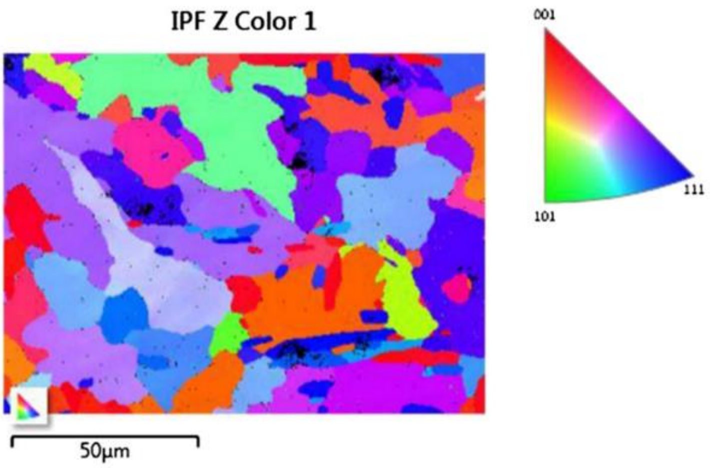

Figure 2.45: EBSD of as tempered P91 steel used for small punch tests by Al-Abedy et al. [193]

Much like P91, Eurofer97 has a large range of potential grain sizes, 10-55μm, which are directly affected by heat treatments. Again this allows for the microstructure to be altered to fit certain applications, such as altering carbide size to aid in creep resistance [194], [195]. An example of the microstructure and texture as shown in optical, SEM, and EBSD can be seen in Figure 2.46.

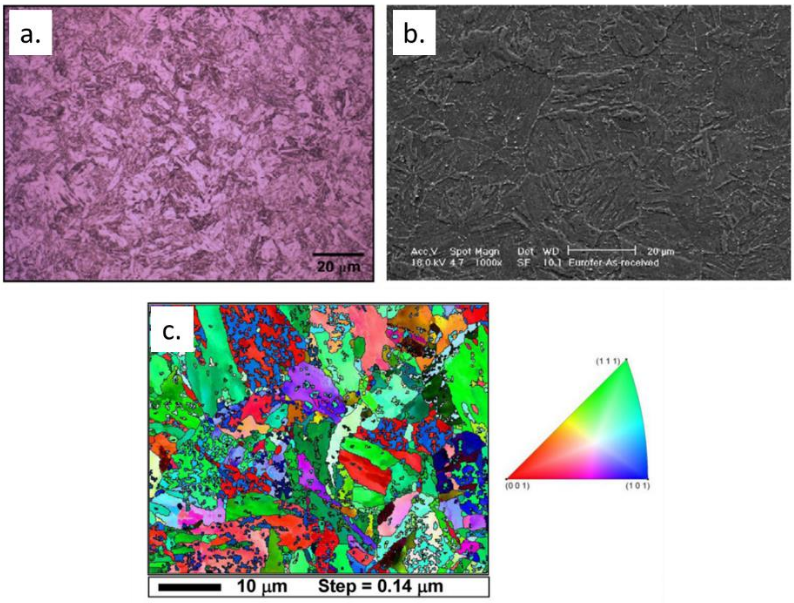

Figure 2.46: An example of Eurofer 97 in an as tempered condition. The dual phase can be seen in optical (a.) and SEM (b.) with martensite laths, carbides, and prior-austenite grains. The texture can be seen in c. with an EBSD scan [194]

2.14 Gaps in knowledge and where this research will sit

Looking at the current research landscape surrounding the simulation of small punch testing, it has become clear that there are some areas that need further development. This is particularly clear in the area of forming some sort of engineering solution. Meaning that all of the knowledge gained to date can be applied to a system of work that will combine small punch experimental data with a finite element model to aid in the design of the next generation of fusion reactors. In particular, there is a need for 3D models as they have the potential to be used to assess inhomogeneities and geometrical changes in detail.

2.15 Conclusions

In this literature review details of small punch testing were given. This was done in the context of small scale testing and finite element analysis for nuclear applications. From here several conclusions can be made:

1. For further application in nuclear fusion it will be imperative that tests continue to be hot cell compatible ready for when irradiated samples become available from IFMIF.
2. The application of FEM and inverse analysis will be vital in ensuring that small punch will be capable of producing good estimates for bulk scale material properties.
3. Finally, both of the above conclusions will be useless unless the importance of finding an engineering solution is considered. Proof of concept work has been completed and now the next step will be to look toward applying the knowledge to material design and fusion engineering.

It is clear that the success of small punch testing is reliant on the application of finite element analysis. They will work in combination to build a complete picture of the small punch test.

3. Methodology

3.1 Introduction

This study focused around the use of data analysis and finite element simulation rather than physical experiments, and was split into four main phases: small punch curve analysis; model building and validation; inverse analysis of the Johnson-Cook plasticity model; and inverse analysis of the Johnson-Cook damage model. Each of these sections were broken down into smaller steps.

1. Small punch curve analysis:
    a. Obtain small punch test experimental data for P91 steel and Eurofer97 steel.
    b. Determine the procedures needed for identifying the key points in both deflection and displacement curves, such as elastic-plastic transition, as outlined in the code of best practice, ASTM standard and round robin.
    c. Create a Python 3 script that analyses force-deflection data from small punch tests with respect to the methods outlined in the code of best practice, ASTM standard and round robin.
    d. Use aforementioned Python script to identify points of interest on the curve such as the elastic-plastic transition force.
    e. Utilise the results produced from the script to estimate the UTS and proof stress for each small punch curve.
2. Model building and validation:
    a. Identify the essential components (and their geometries) of the small punch apparatus that must be included in the simulation.
    b. Use a combination of literature sources to identify the elastic properties of the material chosen for the test specimen.
    c. Obtain tensile and small punch data for a relevant alloy, i.e., P91.
    d. Use experimental tensile data sourced from MatDB to calculate an appropriate estimation of the Johnson-Cook plasticity and damage models.
    e. Create the necessary components in the finite element software, and assemble them.
    f. Perform sensitivity tests to refine and improve the model, in areas such as mesh size and sample-punch contact friction behaviour.
3. Inverse analysis of the Johnson-Cook material model
    a. Utilise the scripting feature within Abaqus to create a Python script that can interface with and control the simulation.
    b. Create an optimisation routine within the script that will complete an inverse analysis on the Johnson-Cook material model.
    c. Using the estimated Johnson-Cook values from section 2, complete the optimisation on all P91 and Eurofer97 small punch curves.
    d. Using an empirical correlation determine the validity of the optimised Johnson-Cook constants in comparison to full scale tensile data.
4. Inverse analysis of the Johnson-Cook failure model
    a. Adapt the Python script created in the previous section to optimise the Johnson-Cook damage model.
    b. Using this script perform an analysis on the effect of sample-punch contact friction in the necking and failure portion of the small punch test.
    c. Determine the appropriate method for applying friction, either a static value, a varied value, or a value to be optimised along with the Johnson-Cook constants.

3.2 Experimental data

Material data was obtained from two main sources. Firstly, small punch test data of Eurofer97 was provided by Culham Centre for Fusion Energy (CCFE). As Eurofer97 is a relatively new alloy, P91 steel, which is a similar but well-established alloy was also selected for analysis. Tensile test, and small punch test data for P91 was obtained from the Online Data Information Network for Energy (ODIN) provided by the European Commission Joint Research Centre [191].

Data received from CCFE was in the form of text files that included: punch load, punch displacement, sample deflection, time elapsed, and temperature. All tests were completed using the code of best practice and ASTM standard guidelines for a room temperature test.

The data received from ODIN was in the form of excel files that included comprehensive information about the test including: machine operators, date created, test conditions, sample dimensions, material source, test temperature, punch force, and sample deflection.

All test samples from both CCFE and ODIN were in accordance with the code of best practice, i.e., having dimensions 8mm diameter and a thickness of 0.5mm, and having both faces ground to a p1200 grit finish. All tests were carried out at room temperature in air. Punch force-sample deflection curve were extracted from each test, while punch force-punch displacement curves were extracted from the Eurofer97 datasets only. This allowed for punch force-sample deflection curves from both sources to be compared with the additional punch force-punch displacement data from CCFE acting as a contrast.

After all of the data was collected and formatted, the following sets of usable data were prepared (Tables 3.1 and 3.2). Simplified identification names were assigned to each sample:

Table 3.1: Eurofer97 – Sample names for the Eurofer97 small punch data provided by CCFE, along with their simplified identification numbers

Full Sample Identification	Simplified identification
001_Eu97p1200B_SC_RT	Sample 001
002_Eu97p1200C_SC_RT	Sample 002
003_Eu97p1200E_SC_RT	Sample 003
004_Eu97p1200A_SC_RT	Sample 004
005_Eu97p1200B_SC_RT	Sample 005
006_Eu97p1200C_SC_RT	Sample 006
007_Eu97p1200D_SC_RT	Sample 007
008_Eu97p1200E_SC_RT	Sample 008
009_Eu97p1200F_SC_RT	Sample 009
010_Eu97p1200G_SC_RT	Sample 010
011_Eu97p1200H_SC_RT	Sample 011

Table 3.2: P91 – Sample names for the P91 small punch data provided by the European Commission, along with their simplified identification numbers

Full Sample Identification	Simplified Identification
MATDB_2500060_190312	Sample 60
MATDB_2500062_190312	Sample 62
MATDB_2500063_190312	Sample 63
MATDB_2500064_190312	Sample 64
MATDB_2500065_190312	Sample 65
MATDB_2500067_190312	Sample 67
MATDB_2500068_190312	Sample 68

From this data, force-displacement graphs were plotted for each test, examples of which can be seen in Figure 3.1.

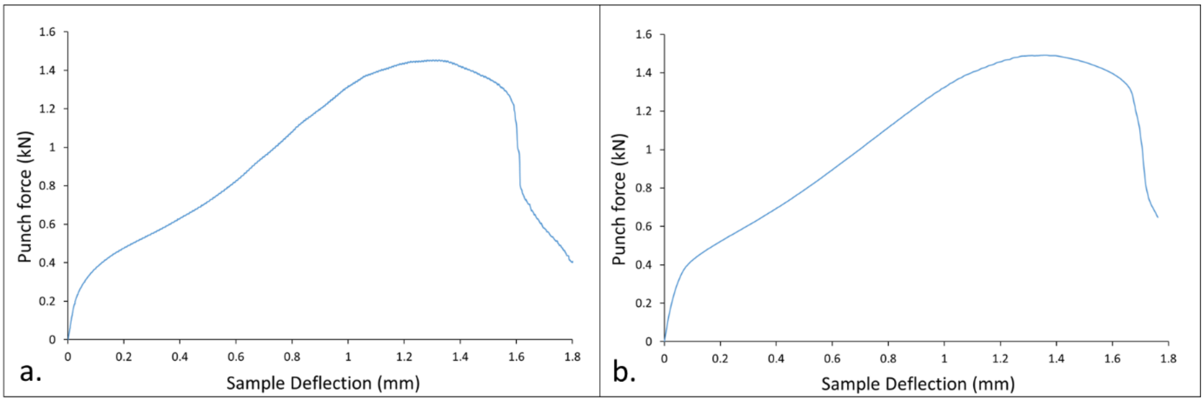

Figure 3.1: Punch force – sample deflection graphs for a) Eurofer97, and b) P91

3.3 Small Punch Test curve analysis –proof stress and UTS

All of the test data received was analysed using methods outlined in the code of best practice, ASTM standard and round robin [128], [133], [155]. The results from which were used to evaluate the data and provide validation to the methods provided within the guide.

3.3.1 Python script

Python 3 was used to construct a script that would identify important values outlined in the code of best practice, ASTM standard and round robin, a summary of which can be found in Table 3.3 [93], [128], [133], [155]. A full explanation of how these values are found was provided in Literature Review section 2.7.3.

Table 3.3: A summary of the significant values that can be extracted from small punch force-deflection data.

Point of interest	Definition
F_M	Maximum punch force
U_M	displacement at maximum force
F_F	Force at failure defined as $0.8*F_M$
U_F	displacement at point of failure
F_B	force at U_B
U_B	displacement of 0.5mm
F_A	elastic to plastic transition force
U_A	displacement at F_A
E_{Tot}	total energy to failure
E_{El}	elastic energy to failure
E_{Pl}	plastic energy to failure

A user interface was created allowing a user to import a text file in the form of either force-deflection or force-displacement data. For the Eurofer97 data it would then allow for a user to visually identify the beginning and end of the test (the P91 data provided had already been trimmed appropriately so this step was not required). The script then systematically went through the data and identified values for each of the points of interest given in Table 3.4. The results of which were saved as text files and displayed visually as graphs (Figure 3.2).

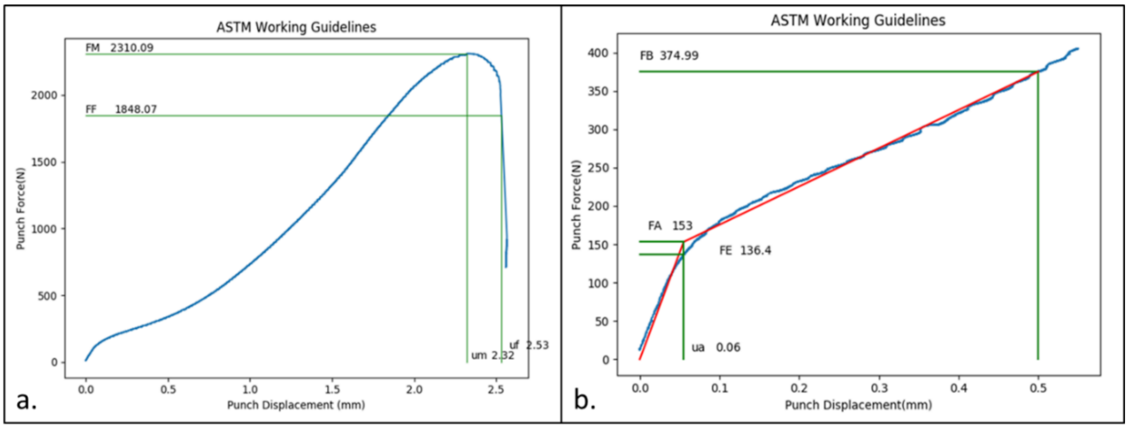

Figure 3.2: An example of the initial graphs produced by the ASTM Working Guidelines script. a) the full force-displacement curve showing maximum force and force at failure, b) the first portion of the force-displacement curve showing the elastic plastic transition force.

The results of the python script analysis were then collated and used to calculate estimates for the proof stress and ultimate tensile strength (UTS) for each individual test.

3.3.2 Proof stress estimation

As stated in the literature review, the proof stress or yield stress, can be estimated using the following Equation [93], [128], [133]:

$$\sigma_{0.2} = \beta_{\sigma_{0.2}} \frac{F_A}{h_0^2}$$

Equation 3.1

Where:

- F_A – the elastic plastic transition force defined earlier
- $\beta_{\sigma 0.2}$ – a geometric correlation coefficient
- h_0 – the sample thickness in mm

With a specimen diameter of 8mm, $\beta_{\sigma 0.2}$ can be taken as constants shown in Table 3.5.

Table 3.4: The values of $\beta_{\sigma 0.2}$ for sample deflection and punch displacement tests [128]

Curve	**$\beta_{\sigma 0.2}$**
Sample deflection (u)	0.510
Punch displacement (v)	0.479

3.3.3 Ultimate tensile strength estimation

As discussed in the literature review, the estimation of ultimate tensile, σ_{UTS}, strength can be achieved by using one of two Equations:

$$\sigma_{UTS} = \beta_{\sigma UTS} \frac{F_m}{h_0 u_m}$$

Equation 3.2

$$\sigma_{UTS} = \beta_{\sigma UTS} \frac{F_i}{h_0^2}$$

Equation 3.3

Where:

- F_m – maximum force reached during tests
- u_m – displacement at Fm
- R_m – Ultimate tensile strength estimate
- F_i – Punch force at a predetermined deflection, u_i
- h_0 – Sample thickness in mm
- $\beta_{\sigma_{UTS}}$ – geometric correlation factor

All experiments were carried out using the standard geometry outlined previously so, $\beta_{\sigma_{UTS}}$ = 0.278 for Equation 3.2, and $\beta_{\sigma_{UTS}}$ = 0.192 for Equation 3.3

3.4 Model building

The finite element model was made using Abaqus 2017. A full explanation of this process along with validation and sensitivity tests can be found in Chapter 5.

3.4.1 Geometry

The starting point for building the small punch model is identifying the parts necessary to simulate the test, as seen in Figure 2.25. Once this setup had been agreed work could commence on the formation of the model itself. This started by creating each component as individual parts. These parts were built to the geometric specifications outlined in the code of best practice, ASTM standard and round robin (Table 3.5).

Table 3.5: All dimensions required to create a small punch test simulation in line with the code of best practice , ASTM standard and round robin

Feature	**Dimension**
Sample diameter, D_s [mm]	8.00
Sample thickness, h [mm]	0.50
Punch radius, r [mm]	1.25
Upper Die diameter [mm]	3.00
Receiving die diameter, D [mm]	4.00
Chamfer length, L [mm]	0.20 x 45°

To enable the model to run on a single PC the computational cost was kept as low as possible. To achieve this, the punch and dies were set as analytical rigid shells (Figure 3.3). Thus, the need to apply a mesh and material properties is negated. The sample however, was generated as a revolved deformable solid. This allowed the part to have a material and mesh applied.

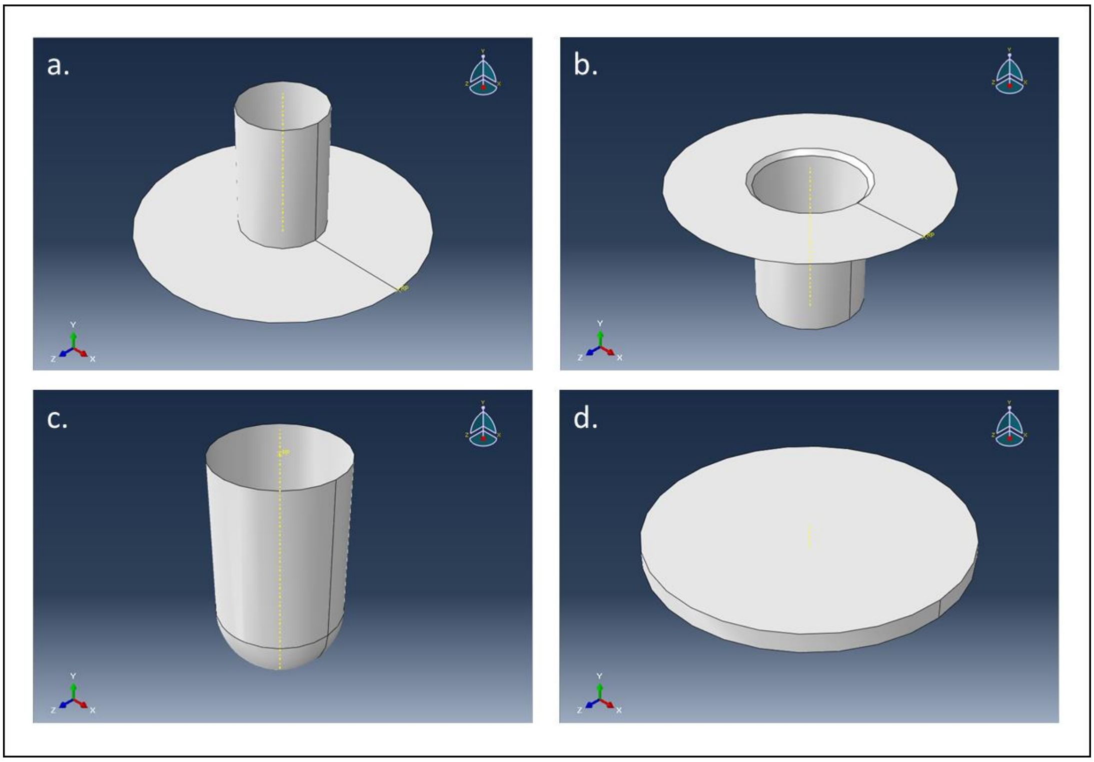

Figure 3.3: Screenshots of the small punch test components, a) the upper die as an analytical rigid shell, b) the lower die as an analytical rigid shell, c) the punch as an analytical rigid shell, d) the sample as a deformable solid

3.4.2 Selection of material properties

It is important at this point to note that Abaqus works as a unitless system, thus allowing the user to define any units used. However, it is common practice to use SI(mm) outlined in Table 3.6. For the sake of clarity, and consistency with other possible users, it was decided that the model would keep with these units.

Table 3.6: An overview of the units used throughout the simulation

Quantity	**Unit**
Length	mm
Force	N
Mass	Tonne (10^3 kg)
Time	s
Stress	MPa (N/mm^3)
Energy	mJ (10^{-3} J)
Density	Tonne/mm^3

There was a lack of Johnson-Cook properties in the literature for any relevant 9Cr steel. Subsequently, tensile data was sourced to facilitate the calculation of estimates for the Johnson-Cook material model (Equation 3.4). The details of which can be found in Chapter 5 (Section 5.5). The final estimates have been provided in Table 3.7. These were assigned to the sample.

Johnson-Cook material model

The Johnson-Cook material model takes the form of:

$$\sigma = \left[A + B\varepsilon_p^n\right][1 + Cln\dot{\varepsilon}^*][1 - T_H^m]$$

Equation 3.4

Where:

- σ – flow stress
- ε_p – equivalent plastic strain
- $\dot{\varepsilon}^*$ - dimensionless plastic strain rate
- T_H – homologous temperature
- A – Yield stress or $R_{0.2}$ at room temperature
- B – modulus of strain hardening
- C – strain rate sensitivity
- n – exponent of strain hardening
- m – exponent of thermal weakening

However, due to the low deformation rates involved in small punch testing, it was possible to negate the second bracket, $[1 + Cln\dot{\varepsilon}^*]$ (explained fully in Chapter 5, Section 5.5). Thus making the initial estimation process much simpler.

Johnson-Cook failure model

The Johnson-Cook failure model takes the form of:

$$\varepsilon^f = [D_1 + D_2 expD_3\sigma^*][1 + D_4 ln\dot{\varepsilon}^*][1 + D_5T_H]$$

Equation 3.5

Where:

- ε^f – equivalent strain to fracture
- σ^* - dimensionless pressure-stress ratio
- $\dot{\varepsilon}^*$ - dimensionless strain rate
- T_H - homologous temperature

Due to the specialist nature of calculating values for this model, it was not possible to produce specific estimates. A series of simulations were completed using literature sourced values. The best match was then chosen to be the starting estimate for both P91 and Eurofer97 tests.

Starting values for the small punch simulation of P91 and Eurofer97

The complete set of material property values have been collated in Table 3.7.

Table 3.7: An overview of the starting properties attributed to the sample. These were designed to reflect the behaviour of P91 steel

Property	**Value**
Mass density (Eurofer97)	7.76E-9 (Tonne/mm^3) [173]
Young's Modulus	210000 (MPa) [173]
Poisson's Ratio	0.3 [173]
Johnson-Cook (plastic)	A = 510 (MPa) B = 666 (MPa) n = 0.459 m = 1.615 T_m = 1420 (˚C) T_T = 25 (˚C)
Johnson-Cook (damage) Sourced from [196] – selection criteria explained in Chapter 5	D1 = 0.05 D2 = 0.8 D3 = - 0.44 D4 = - 0.046 D5 = 0 T_m = 1420 (˚C) T_T = 25 (˚C) $\dot{\varepsilon}_{ref}$ = 1

3.4.3 Mesh

Plastic

A C3D8R mesh was applied to the sample. Element size was set as 0.1, as it was taken as an appropriate balance between computational cost and precision (Figure 3.4). An explanation of this can be found in section 5.3.4. To aid in the automation of data collection and visual analysis, a partition was created down the centre of the sample.

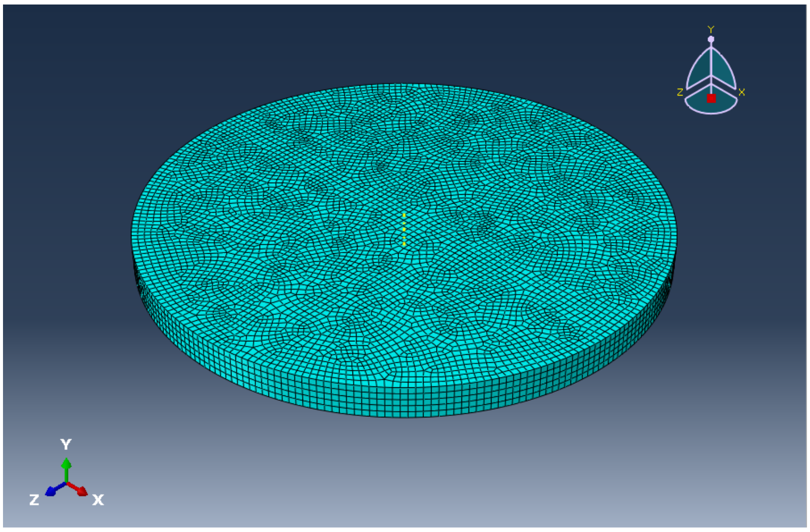

Figure 3.4: A screenshot of the meshed sample. A mesh size of 0.1 was used here. Note the regular mesh down the centre to allow for consistent analysis of results

Damage

A C3D8R mesh and element deletion was applied to the sample. Sensitivity analysis proved that, for the damage tests, a finer mesh at the centre of the sample was beneficial in producing more realistic necking and failure behaviours. An element size of 0.1 was selected for the outer portion with 0.05 as the inner disk (Figure 3.5). While this did increase the computational time required, the increase in accuracy was sufficient.

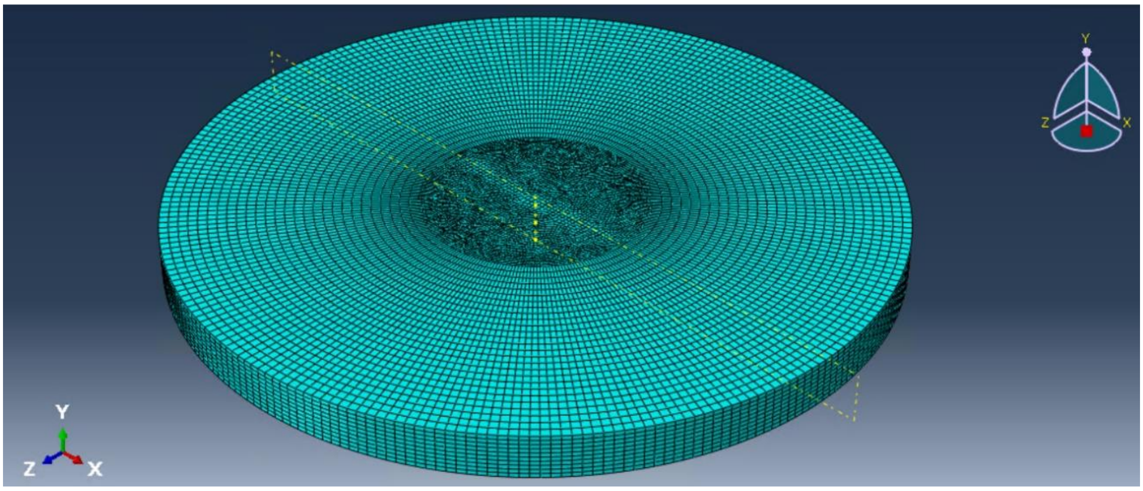

Figure 3.5: A screenshot of the refined mesh. This was specifically used for analysing the damage. The outer portion has a mesh size of 0.1 with the centre at a mesh size of 0.05

3.4.4 Assembly

Once all of the parts had been created, they can be assembled as seen in Figure 3.6.

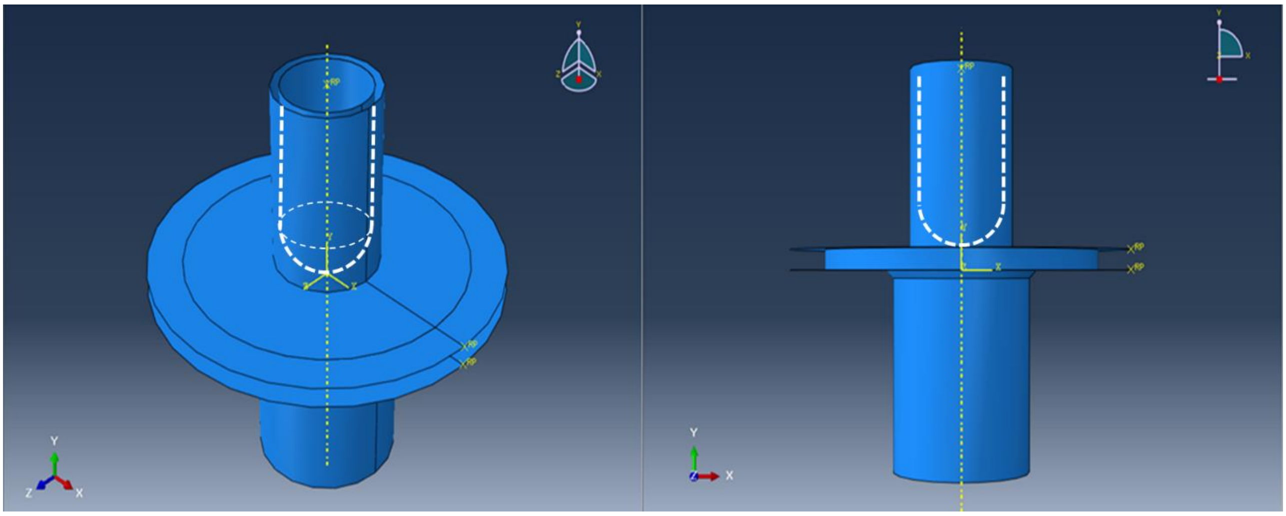

Figure 3.6: Screenshots of the assembled small punch test from two different angles. The punch can be seen outlined in white.

3.4.5 Interactions

From the assembly the interactions between the parts were defined. This included the friction coefficients. The friction coefficient between all components was taken to be the general metallic interaction of μ = 0.3. A full explanation of this can be found in section 5.6.

3.4.6 Step

The step was then created, defined as dynamic, explicit, and was given the attributes summarised in Table 3.8:

Table 3.8: An overview of the attributes given to step 1 of the simulation

Name	**Value**
Basic	
Time period	*
Nlgeom	On
Incrementation	
Type	Automatic
Stable increment estimator	Global
Max time increment	Unlimited
Time scaling factor	1
Mass Scaling	
Region	Whole Model
Type	Target Time Inc.
Frequency/Interval	*
Factor	None
Target Time Increment	0.01
Other	
Linear bulk viscosity parameter	0.06
Quadratic bulk viscosity parameter	1.2

* varies with total punch displacement

The step time period and frequency of mass scaling vary with the punch displacement. On average a full 2.5mm punch displacement takes around 350 seconds so any displacement smaller than this will mean that the step time is reduced accordingly to achieve the desired displacement rate.

3.4.7 Field output requests

The main field output requests required here were:

- Reaction force, RT
- Displacement, UT
- Von Mises stress, MISES
- Plastic equivalent strain, PEEQ
- Element status, STATUS

3.4.8 Boundary conditions

The boundary conditions are also applied at this point, holding the die in place, i.e., encastre. A movement condition along the y-axis was added to the punch. It will move at a constant displacement rate over the step to a user defined total displacement.

3.4.9 Creating a Job

The job could now be created. Parallelisation and precision were specified at this point. All four of the computer's cores would be utilised, and double precision was necessary for the explicit solver.

The job was then submitted.

3.4.10 Results

Once the simulation was complete, the results could be found in the '.odb' file. From here, text files of selected punch force, displacement, and sample deflection data were produced, which was particularly useful for obtaining force-displacement/deflection data. The deformed sample could also be viewed here, allowing for visual analysis as well as identification of areas of high stress and strain concentration.

Along with xy data, results could be analysed visually, as seen in Figure 3.7. This could show stress or strain concentrations and can act as a quick validation method i.e. making sure that the sample is deforming somewhat correctly.

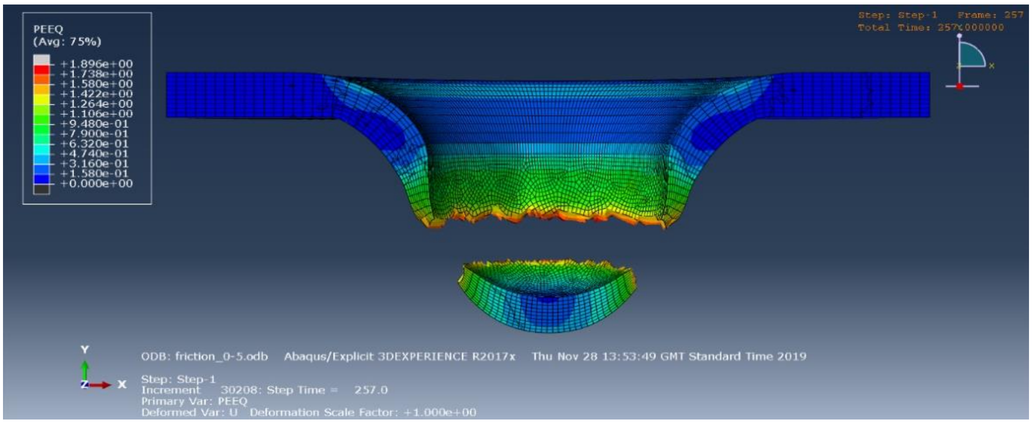

Figure 3.7: A screenshot of a deformed, failed small punch sample. Such screenshots allowed for visual analysis of the effects of things like friction and mesh size.

It is at this point that the xy data could be used to perform sensitivity tests. This was done to fine tune the single-run test before beginning the multi-run inverse analysis. Details will be included in Chapter 5.

3.5 Inverse analysis – Optimisation of the Johnson-Cook materials models

The optimisation of the Johnson-Cook models was split into two distinct sections. The first considered Johnson-Cook materials model, and the second focused on Johnson-Cook failure model with the potential for also including friction coefficient.

To optimise the constants within the material section of Abaqus, a script was required. To start with a simplified flow chart of the optimisation was created (Figure 3.8).

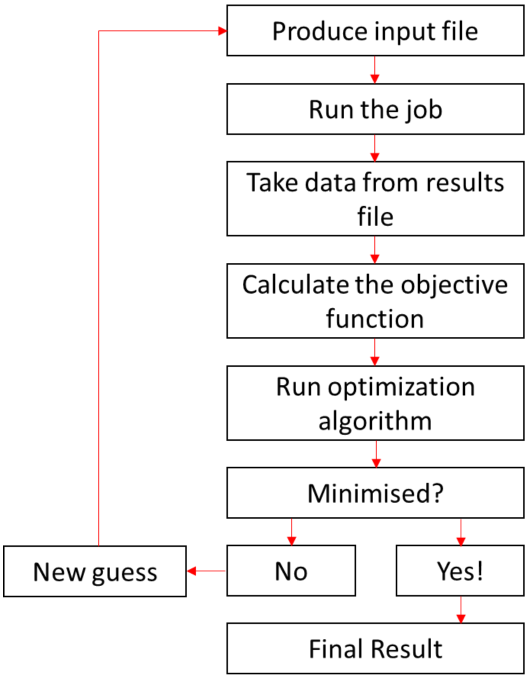

Figure 3.8: A flow diagram depicting the workings of the optimisation script used for the inverse analysis of the Johnson-Cook parameters

3.5.1 Input file

Creating the input file made use of the scripting functionality within Abaqus, which permitted the compete building, running and analysis of a simulation to be extracted in macro form. From here, this was changed into a script with Python 2. Thus, allowing for the addition of a loop which ran the simulation iteratively, alternating the JC values with each one. Controlling the iteration of said values was the SciPy module specifically the optimize-minimize function. This module, combined with an error function allowed for the optimisation of the Johnson-Cook models (Equations 3.4 & 3.5).

The estimated values were then given as the initial inputs for the optimisation routine.

3.5.2 Job

The subsequent section of the code established the rest of the model, submitted the job, and waited for completion.

3.5.3 Extract data

After the simulation has completed punch force, punch displacement, and sample deflection were extracted from the '.odb' file and saved to a text file.

3.5.4 Objective function

The punch force and sample deflection were collected and formatted for use in the objective function. In this case the objective function is an absolute value of the error between experimental and simulated results.

$$r = \sum (simulated\ curve - experimental\ curve)^2$$

Equation 3.6

3.5.5 Optimisation algorithm

The r value produced by the error function was then input into the minimisation function, which employed the Nelder-Mead algorithm. As explained in Literature Review section 2.10.2, the Nelder-Mead (or Simplex) algorithm is a commonly used direct search method that does not require derivatives or boundaries. This means that it is not computationally expensive and so should be able to provide adequate results in a short amount of time.

The only caveat being that, as with all direct search methods, the Nelder-Mead algorithm is designed to find local minima, so good starting estimates are essential.

If the r value was not deemed optimal, a new set of estimated values were produced, fed back into the script and it was resubmitted. The new estimates were printed to a text document along with r. This is iterated on until the optimisation function found a minimum.

To ensure that the best outcome was achieved a series of tests were devised as a range of displacements, and friction coefficients. These were then compared to find the optimal combination of displacement and friction coefficient.

4. Small punch curve analysis

The small punch test has the capability of providing key mechanical property information about structural alloys. In recent years a code of best practice and an ASTM standard have been developed which outlines a standard testing procedure and a series of data analysis methods, including conversion to equivalent macroscopic properties. For this study, some small punch test data was obtained and analysed using the methods outlined in the code of best practice and ASTM Standard, the results of which are included in this Chapter. A discussion of the validity of the calculations provided, particularly for macroscopic properties, is also included.

4.1 Small punch test data

Two similar alloys were selected. The first alloy, Eurofer97, was provided by CCFE; and the second, P91, was sourced from the European Commission Joint Research Centre's Online Data Information Network for Energy, ODIN. Details such as composition were covered in the methodology.

4.1.1 Conditions of each experiment

Each set of test data was provided with information about testing conditions. These were collated into tables to give an overall picture of the tests available. The conditions for the P91 tests can be found in Table 4.1, and the conditions for the Eurofer97 tests can be found in Table 4.2.

Table 4.1: Test conditions for the P91 small punch test restults received from the ODIN database

Test ID	**Simplified ID**	**Temperature (˚C)**	**Atmosphere**	**Test control**	**Displacement Rate (mm/s)**	**Data available**
2500060	60	22	air	displacement	0.05	Deflection only
2500061	61	22	air	displacement	0.5	Deflection only
2500062	62	22	air	displacement	0.005	Deflection only
2500063	63	22	air	displacement	0.05	Deflection only
2500064	64	22	air	displacement	0.5	Deflection only
2500065	65	22	air	displacement	0.005	Deflection only
2500066	66	22	air	displacement	0.0005	Deflection only
2500067	67	22	air	displacement	0.005	Deflection only
2500068	68	22	air	displacement	0.005	Deflection only
2500069	69	22	air	displacement	0.0005	Deflection only

Table 4.2: The test conditions for the Eurofer97 small punch test results received from CCFE

Test ID	**Simplified ID**	**Temperature**	**Atmosphere**	**Test control**	**Displacement rate (mm/s)**	**Data available**
001_Eu97p1200B_SC_RT	001	RT	Air	Displacement	0.003	Displacement and deflection
002_Eu97p1200C_SC_RT	002	RT	Air	Displacement	0.003	Displacement and deflection
003_Eu97p1200E_SC_RT	003	RT	Air	Displacement	0.003	Displacement and deflection
004_Eu97p1200A_SC_RT	004	RT	Air	Displacement	0.003	Displacement and deflection
005_Eu97p1200B_SC_RT	005	RT	Air	Displacement	0.003	Displacement and deflection
006_Eu97p1200C_SC_RT	006	RT	Air	Displacement	0.003	Displacement and deflection
007_Eu97p1200D_SC_RT	007	RT	Air	Displacement	0.003	Displacement and deflection
008_Eu97p1200E_SC_RT	008	RT	Air	Displacement	0.003	Displacement and deflection
009_Eu97p1200F_SC_RT	009	RT	Air	Displacement	0.003	Displacement and deflection
010_Eu97p1200G_SC_RT	010	RT	Air	Displacement	0.003	Displacement and deflection
011_Eu97p1200H_SC_RT	011	RT	Air	Displacement	0.003	Displacement and deflection

4.1.2 The experimental data

The test data was provided in two different formats. The Eurofer97 data in the form of text files that included test time, punch displacement, sample deflection, punch load, and temperature readings from three different thermocouples. All further information was provided in the file name including sample identification, sample preparation, and test temperature. The P91 data came in the form of excel files. Along with punch force and sample deflection data, these files provided information such as the lab which carried out the test, the material used (including composition and processing), test conditions, punch force, and sample deflection.

P91

The data provided for P91 allowed for the production of force-deflections curves, which can be seen in Figure 4.1.

The force-deflection data produced curves of two distinct shapes over the set of data. The first curve shape (sample 60 in Figure 4.1) displayed a smooth transition between elastic loading, through plastic deformation to necking and failure. The second curve shape (sample 67 in Figure 4.1) did not display a distinct transition between elastic loading and plastic deformation, and the failure appeared to be abrupt with no real necking region. Of the 10 curves, 4 curves generally matched the first shape, and 3 generally matched the second shape. The remaining 3 curves (Samples 61, 66, and 69 in Figure 4.1) are discussed below.

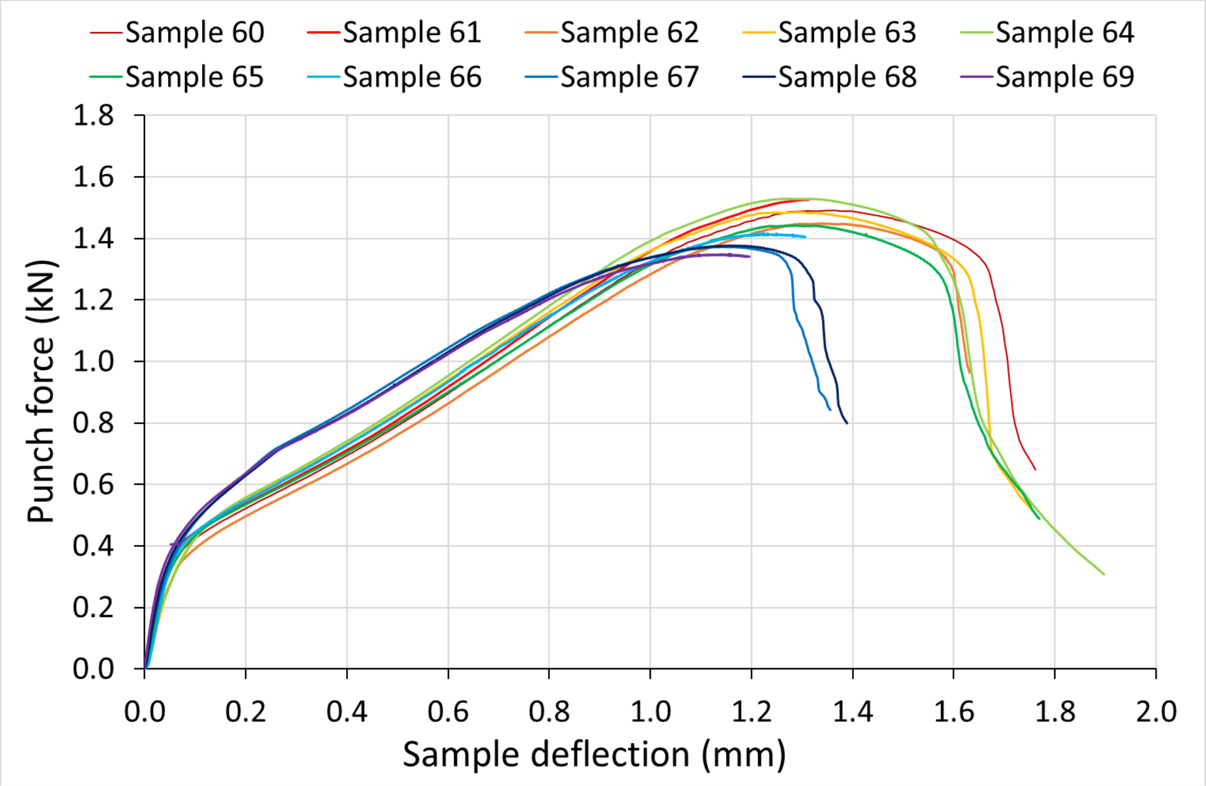

Figure 4.1: Graph displaying the force deflection curves for P91 steel

Samples 61, 66, and 69 did not contain complete curves (Figure 4.2). The information provided with the experimental data did not show anything abnormal with those tests in particular, and the curves did not indicate premature failure. In the interest of displaying the variation in small punch testing, these tests will be included where possible, i.e., in the analysis of elastic-plastic transition forces.

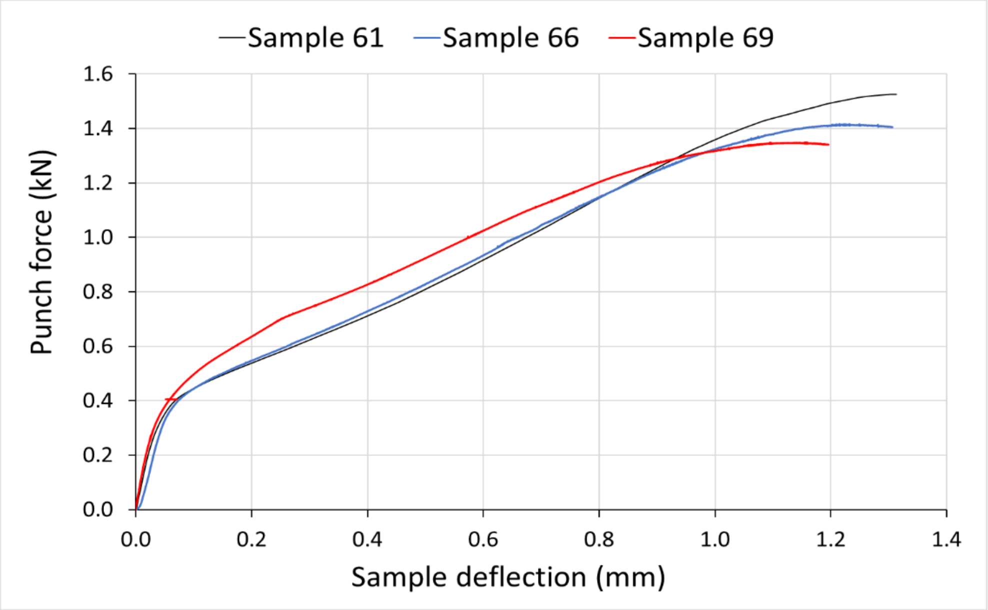

Figure 4.2: The P91 small punch curves received from the ODIN database that were incomplete

This variation is indicative of small punch testing as the small length scale increases the possibility for large variations in data for the same material under the same conditions.

Eurofer97

The Eurofer97 data gave both force-displacement and force-deflection curves, as seen in Figures 4.3 and 4.4. As with the P91 data, there are two distinct curve shapes present within the data. The first curve shape (sample 001 in Figure 4.3) displayed a smooth transition between elastic loading, through plastic deformation to necking and failure. The second curve shape (sample 005 in Figure 4.3) also followed the smooth transition up until the point of necking where there appeared to be a more abrupt failure with little to no real necking.

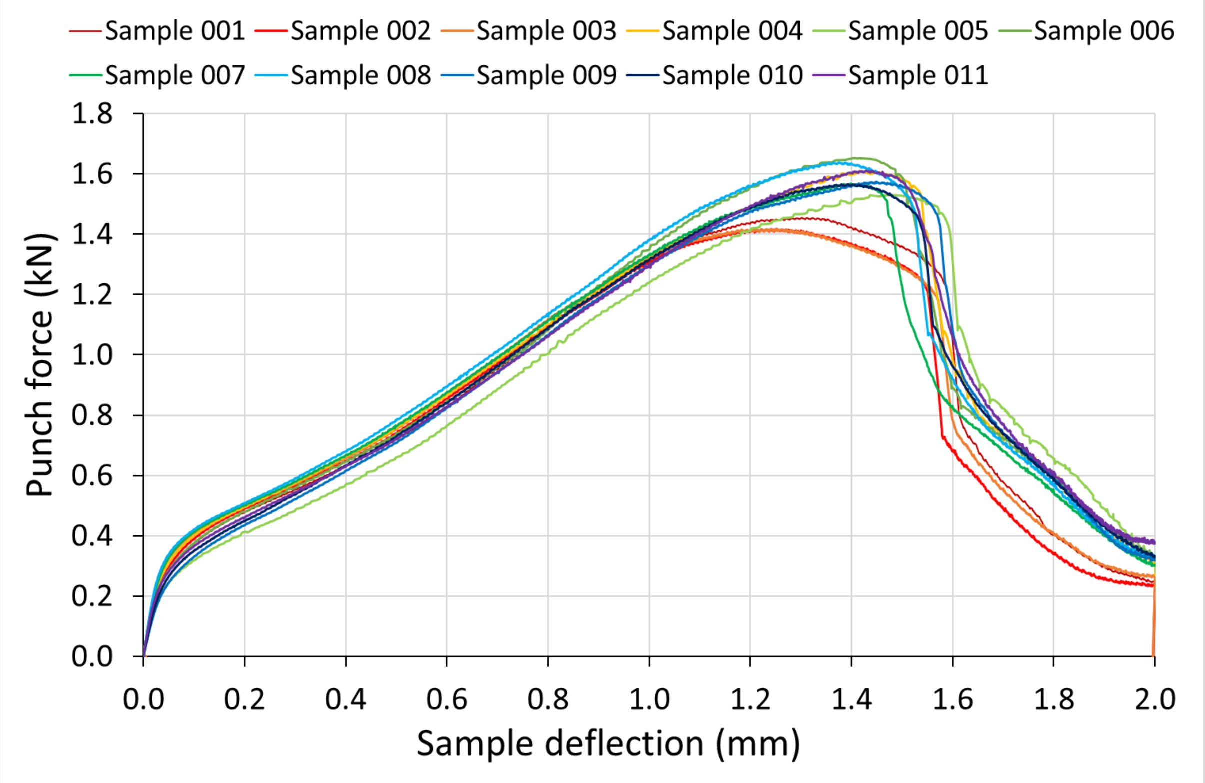

Figure 4.3: Graph displaying the force deflection curve for Eurofer97 steel

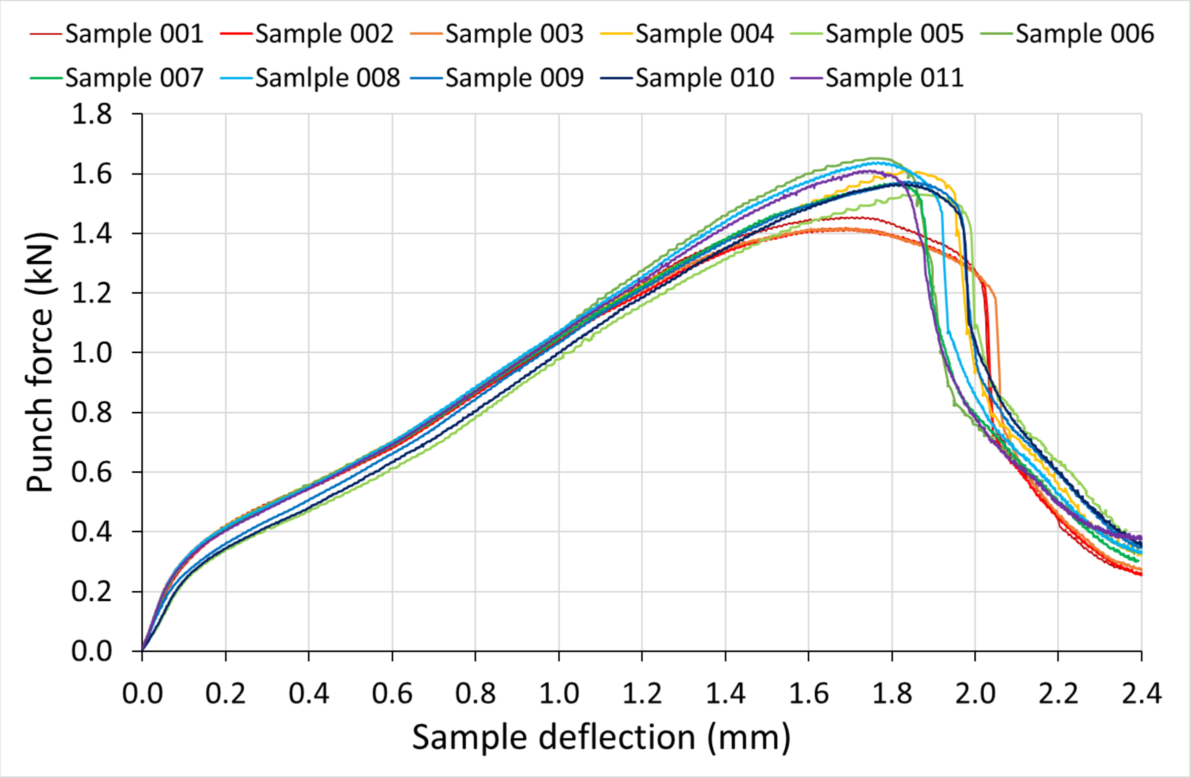

Figure 4.4: Graph displaying the force displacment curve for Eurofer97 steel

A comparison between punch displacement and sample deflection recording methods is included in Figure 4.5.

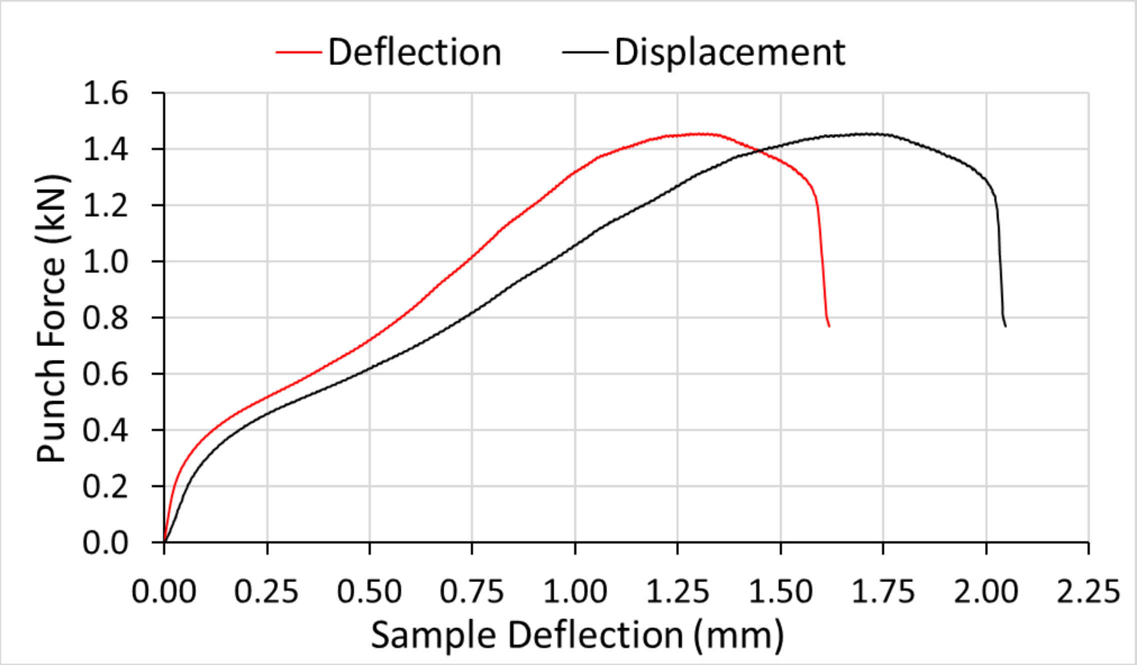

Figure 4.5: Graph showing the typical difference in punch displacment and sample deflection for the same test.

Comparison of both alloys

A comparison of P91 and Eurofer97 has been included in Figures 4.6 and 4.7. As can be seen the first curve shapes for both materials display very similar force-deflection curves. Whereas the second graph shape shows a greater variation between the two alloys.

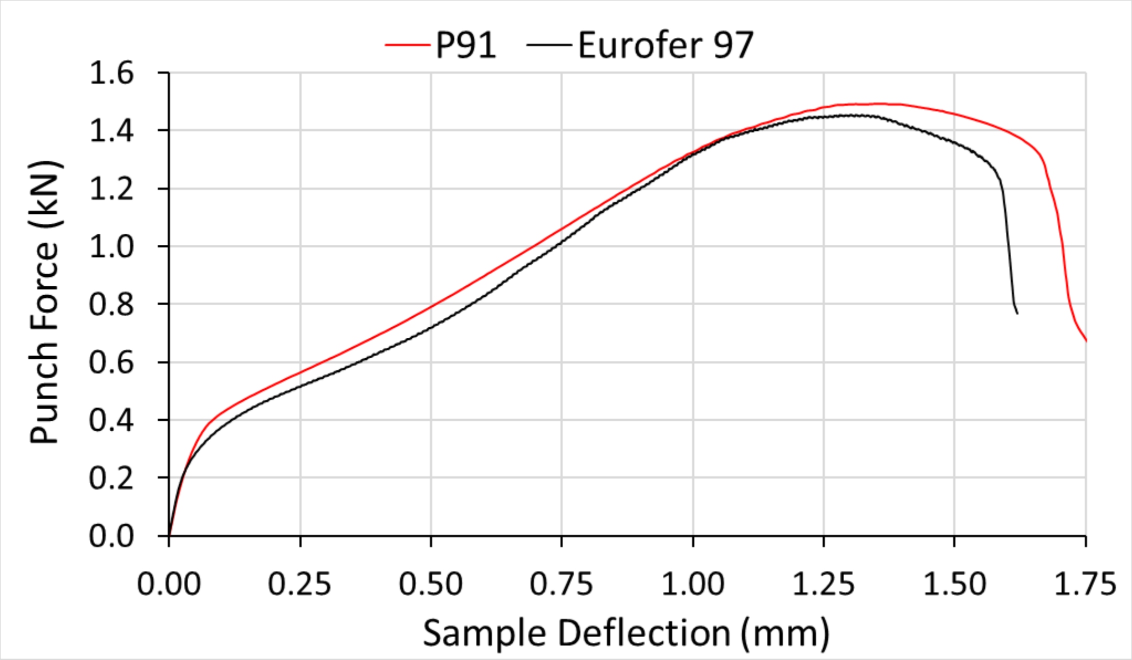

Figure 4.6: Graph displaying a comparison of the force deflection for both Eurofer97 and P91 steels displaying a simular curve shape.

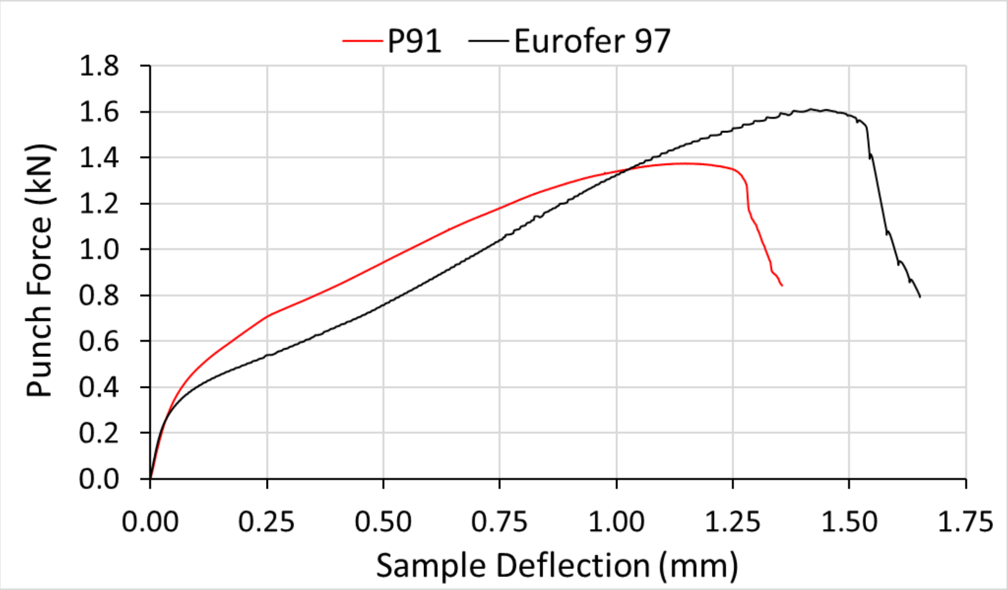

Figure 4.7: Graph displaying a comparison of the punch force – sample deflection for both Eurofer97 and P91 steels displaying a simular curve shape.

4.2 Overview of the code of best practice calculations

Following on from above, forming the best possible understanding of the small punch test is imperative in ensuring its validity in materials development.

Creating a consistent method that can be applied across all tests provides the best possible chance for comparison across labs. Such methods have already been developed with the aid of a CEN workshop, and round robin which lead to the production of a code of best practice and an ASTM standard [128], [133], [155].

Following the guide ensures the consistency of all calculations performed and that all results produced can be considered comparable with those from other institutions. It is imperative that all work surrounding it is completed to the highest possible accuracy and consistency. This includes data analysis.

4.2.1 Points of interest

The guide highlights certain points along the force-displacement curves which are required for calculations [128]. These values are:

- F_a - The point of the elastic plastic transition.
- u_a (v_a) - The sample deflection (punch displacement) at F_a
- F_m – The maximum punch force reached
- u_m (v_m) – The sample deflection (punch displacement) at F_m
- F_F – The force at which the sample fails, nominally $0.8F_m$
- u_f (v_f) - The sample deflection (punch displacement) at F_f

A full explanation of these values including relevant diagrams, was included in the literature review.

4.3 Development of Python 3 script

It was decided that the best way to provide assured consistency in analysing the experimental curves was to automate it. This would require the production of a script.

4.3.1 Objectives of the script

This script would have several objectives:

1. To allow the user to input a text file through a graphical user interface, GUI
2. Allow the user to select the start and end of the test
3. Use the inputs and automatically run through the calculations outlined above
4. Produce a text file with all of the results of the calculations and produce graphs highlighting these points on the curve itself

In order to complete these aims a scripting language was first selected.

4.3.2 Why python?

After an initial search two languages were shortlisted; MATLAB and Python. Both of which could provide the scientific packages needed for the analysis of the data. After further discussion with the supervisory team at CCFE, Python was settled on as the language of choice. This was mainly due to the fact that Python is open source which would fit with the open access ethos at CCFE.

4.3.3 Python version and modules used

For this work Python 3 was selected. As was the nature of Python, the base code had limited functionality, with the possibility of expanding with added modules. For scientific applications, the recommended module is SciPy, and specifically the package NumPy [197], [198]. Additional modules that facilitate the GUI and graphing capabilities are; matplotlib, TkInter, and pandas [199]–[201].

Released in 2008, Python 3 was introduced as an evolution to Python 2. As such it provided fixes for a number of bugs, thus forcing backwards incompatibility.

4.3.4 Breakdown of actual script

The script started with the generation of a graphical user interface, GUI (Figure 4.8). A browse button was added which facilitated the selection of a text file from the computer. From there the script proceeded to open the file and read the data. The second section of the script permitted the user to define the beginning and end of the test from a series of curves (Figures 4.9 a-f). It was decided that this portion should not be optimised, as the Eurofer97 data in particular was in its raw form i.e. the force and displacement data before and after the test was recorded. Because of this, there were some inconsistencies within the data sets and having a human element in this section was deemed necessary.

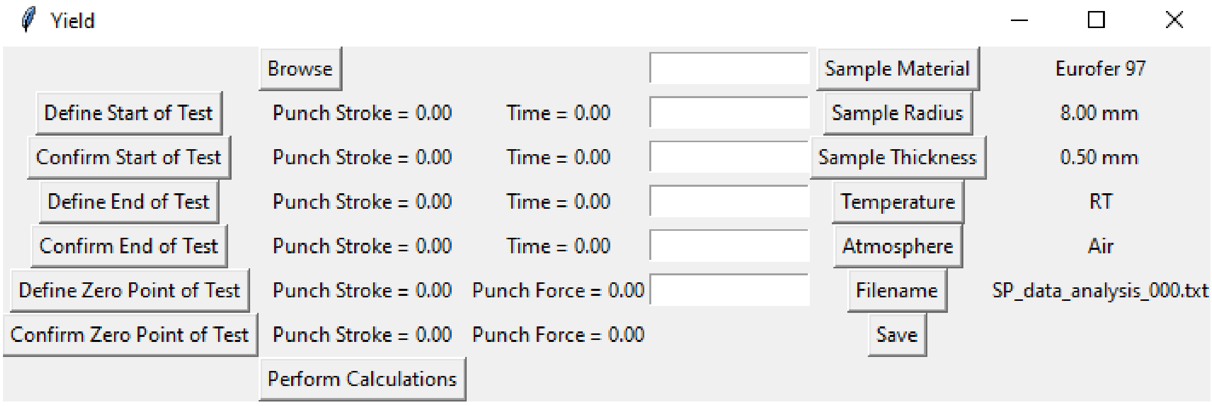

Define Start of Test: Punch Stroke = 0.00 Time = 0.00
Confirm Start of Test: Punch Stroke = 0.00 Time = 0.00
Define End of Test: Punch Stroke = 0.00 Time = 0.00
Confirm End of Test: Punch Stroke = 0.00 Time = 0.00
Define Zero Point of Test: Punch Stroke = 0.00 Punch Force = 0.00
Confirm Zero Point of Test: Punch Stroke = 0.00 Punch Force = 0.00

Sample Material: Eurofer 97
Sample Radius: 8.00 mm
Sample Thickness: 0.50 mm
Temperature: RT
Atmosphere: Air
Filename: SP_data_analysis_000.txt

Figure 4.8: The graphical user interface created by the python script.

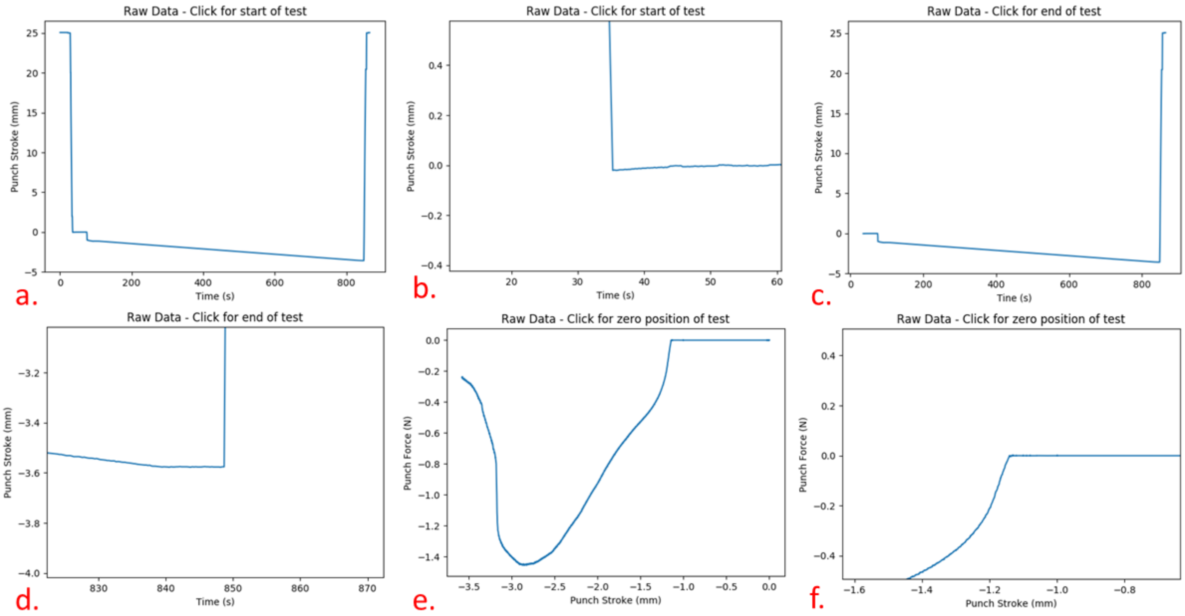

Figure 4.9 (a-f): Images of the user data selection screens. The script allowed a user to click on each of the graphs in turn to define the beginning and end of a test

The next step was to prompt the script to complete the calculations as outlined in the literature review (Section 2.7.3).

At the time of writing the script (2016), the bilinear method for finding f_A was recommended for both displacement and deflection curves. Therefore, both forms of data were analysed using this method.

The bilinear function $f(u)$ was used in conjunction with the error minimisation function (Equations 4.1 and 4.2 respectively) to identify the elastic plastic transition force, F_A [128].

$$f(u) = \begin{cases} \dfrac{f_A}{u_A} \; for \; 0 \le u < u_A \\ \dfrac{f_B - f_A}{u_B - u_A}(u - u_A) + f_A \; for \; u_A \le u \le u_B \end{cases}$$

Equation 4.1

$$err = \int_0^{u_B} [F(u) - f(u)]^2 du$$

Equation 4.2

Along with determining the value of F_A, the script also identified the maximum punch force, F_M, punch force at failure, F_F, and their respective displacement values. An estimation of the energy of the system was also recorded as elastic energy component, E_{El}, plastic energy component, E_{Pl}, and total energy, E_{TO}. Again, further details are available in the literature review.

4.3.5 Results format

To complete the aims outlined above the results produced from this script would be given in two formats. Firstly, the values calculated in each test would be saved in a text file, along with the force-displacement/ deflection curve data.

The second portion of the results would provide a visualisation of said values in relation to the force-displacement/ deflection curve. This was best displayed in graphical form using 3 different graphs. The three separate graphs would help provide clarity as the majority of the values are clustered over the first 0.5mm of movement. Examples of these graphs can be seen in Figures 4.9, 4.10, and 4.11.

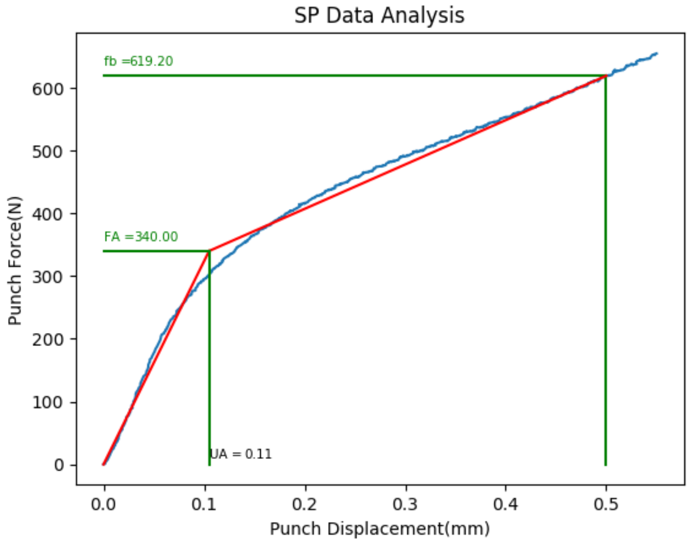

Figure 4.10: An example of the first graph produced with the Python 3 script highlighting any important values

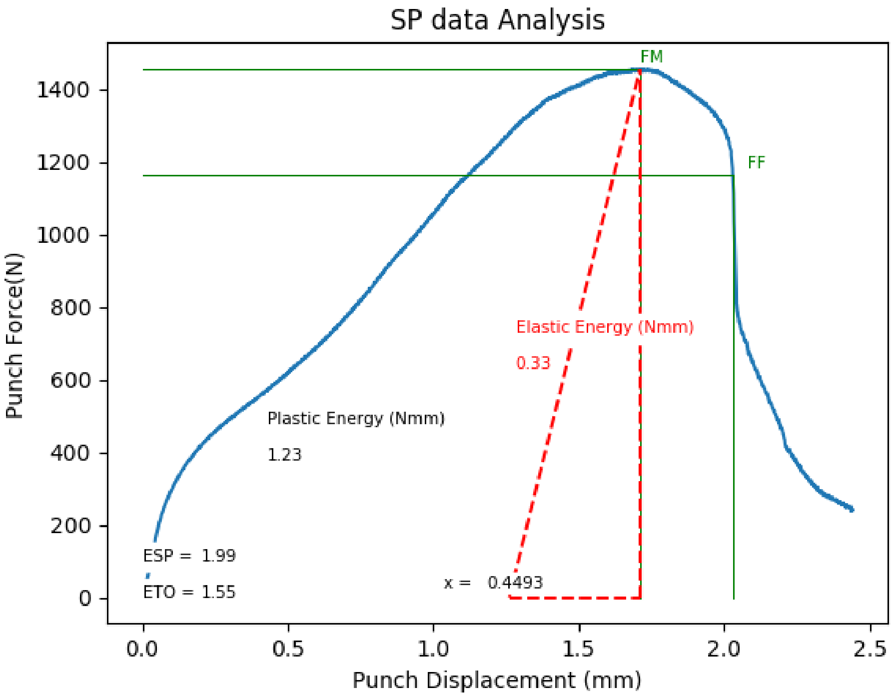

Figure 4.11: An example of the second graph produced with the Python 3 script highlighting any important values

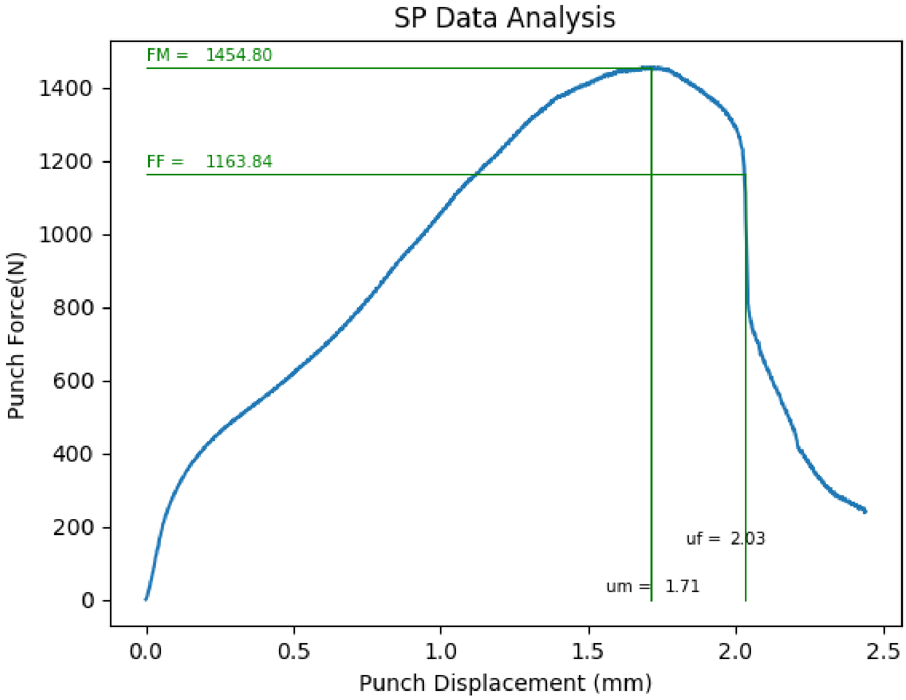

Figure 4.12: An example of the third graph produced with the Python 3 script highlighting any important values

4.3.5 Results

P91

The results from the P91 force-deflection curves can be found in Table 4.3. Due to the incomplete curves seen in samples 61, 66, and 69, the maximum punch force, and failure punch force could not be recorded. However, the first half of the curve facilitated the calculation of the elastic-plastic transition force.

Table 4.3: The results produced by the Python 3 script for the P91 small punch data

Sample	F_m (N)	u_m (mm)	F_f (N)	u_f (mm)	F_a (N)	u_a (mm)
60	1491.10	1.36	1192.88	1.68	361.00	0.05
61					380.00	0.05
62	1449.30	1.34	1159.44	1.61	364.00	0.07
63	1485.40	1.30	1188.32	1.64	419.00	0.08
64	1528.20	1.29	1222.56	1.61	421.00	0.08
65	1443.00	1.29	1154.40	1.60	393.00	0.06
66					413.00	0.07
67	1373.40	1.15	1098.72	1.30	456.00	0.07
68	1377.00	1.16	1101.60	1.34	437.00	0.06
69					411.00	0.04

F_M, F_F, and F_a were plotted in Figure 4.13. There is some variation in these values, which was to be expected, and none of these curves stood out as anomalous.

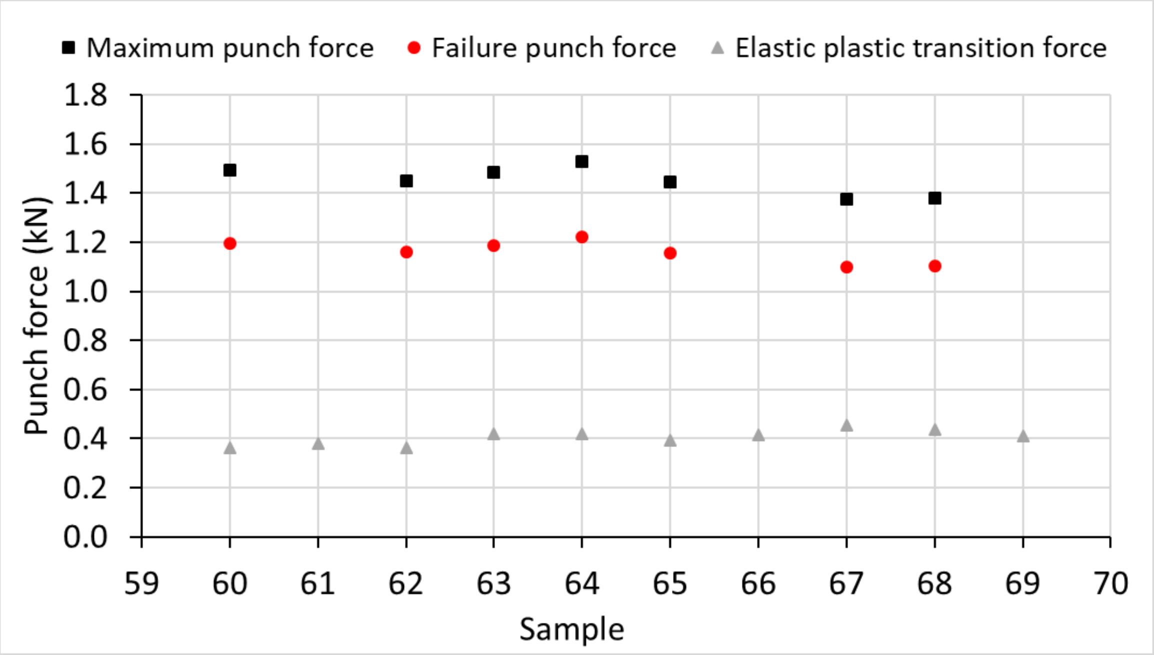

Figure 4.13: Graph showing the F_M, F_F, and F_a values for the P91 small punch tests

Eurofer97

The data for each Eurofer97 force-deflection curve can be found in Table 4.4 and Figure 4.14. Unlike the P91 data, all curves were complete thus allowing for the full analysis of each.

Table 4.4: The results produced by the Python 3 script for the Eurofer97 small punch sample deflection data

Sample	F_m (N)	u_m (mm)	F_f (N)	u_f (mm)	F_a (N)	u_a (mm)
001	1454.80	1.30	1163.84	1.59	292.00	0.04
002	1417.93	1.25	1134.34	1.55	317.00	0.04
003	1417.46	1.20	1133.97	1.57	326.00	0.03
004	1609.01	1.42	1287.21	1.56	322.00	0.04
005	1530.11	1.48	1224.09	1.60	248.00	0.04
006	1651.98	1.40	1321.58	1.54	300.00	0.04
007	1568.08	1.40	1254.46	1.50	332.00	0.04
008	1637.92	1.37	1310.34	1.53	322.00	0.03
009	1573.86	1.45	1259.09	1.58	245.00	0.04
010	1566.36	1.39	1253.09	1.55	267.00	0.04
011	1610.11	1.43	1288.09	1.56	273.00	0.03

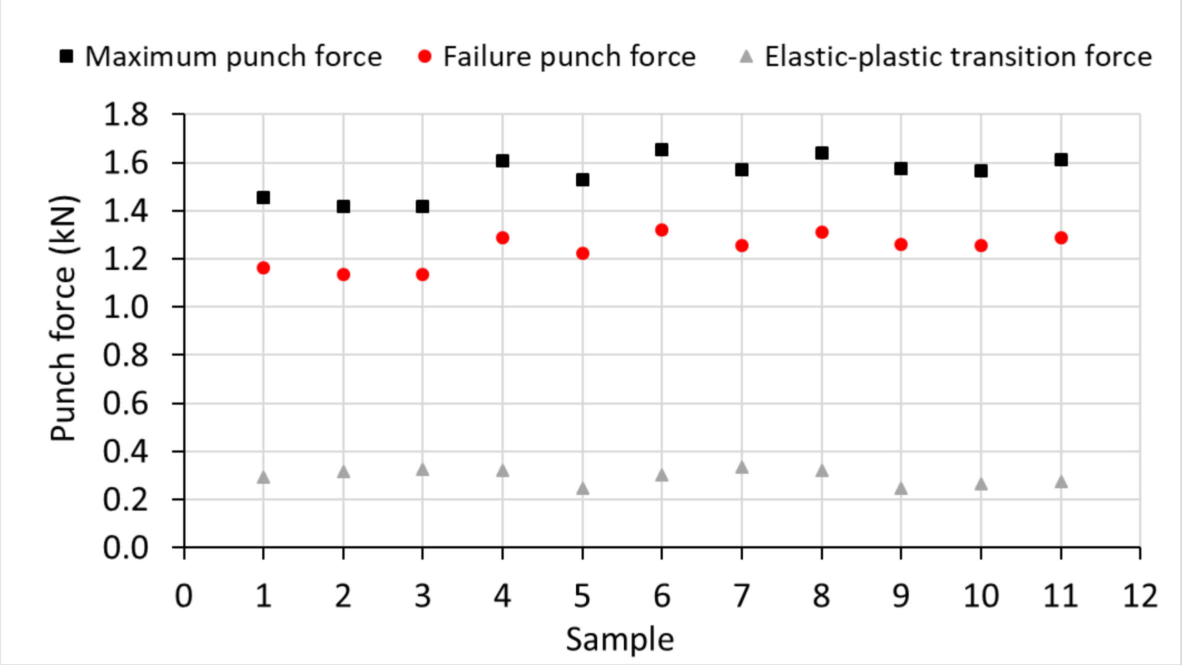

Figure 4.14: Graph showing the F_M, F_F, and F_a values for the Eurofer97 small punch sample deflection tests

The punch displacement data has been included in Table 4.5 and Figure 4.15. It must be noted at this point that the values of F_f and F_m for both displacement and deflection tests will be the same. However, F_a is calculated using either displacement or deflection values and so will vary. A closer look at these values can be found in Figure 4.16.

Table 4.5: The results produced by the Python 3 script for the Eurofer97 small punch punch displacement data

Sample	F_m (N)	v_m (mm)	F_f (N)	v_f (mm)	F_a (N)	v_a (mm)
1	1454.80	1.71	1163.84	2.03	340.00	0.11
2	1417.93	1.69	1134.34	2.03	328.00	0.11
3	1417.46	1.64	1133.97	2.05	328.00	0.10
4	1609.01	1.83	1287.21	1.97	331.00	0.10
5	1530.11	1.87	1224.09	2.00	283.00	0.13
6	1651.98	1.76	1321.58	1.90	331.00	0.11
7	1568.08	1.80	1254.46	1.89	323.00	0.10
8	1637.92	1.77	1310.34	1.93	324.00	0.10
9	1573.86	1.84	1259.09	1.98	257.00	0.09
10	1566.36	1.83	1253.09	1.98	285.00	0.13
11	1610.11	1.75	1288.09	1.88	299.00	0.09

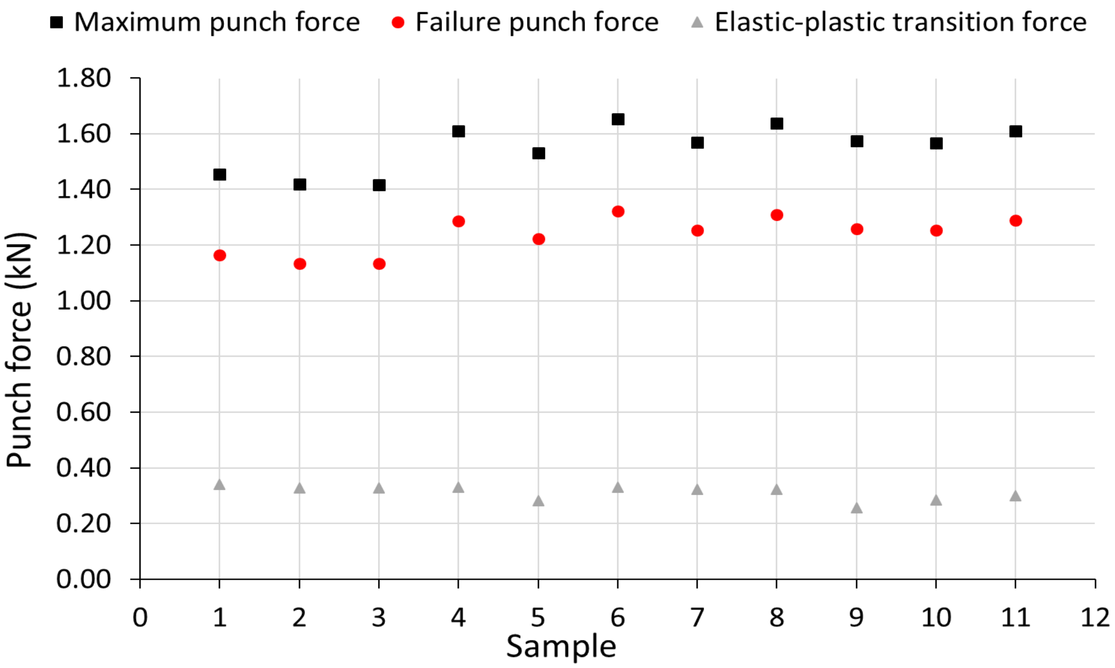

Figure 4.15: Graph showing the F_M, F_F, and F_a values for the Eurofer97 small punch displacement tests

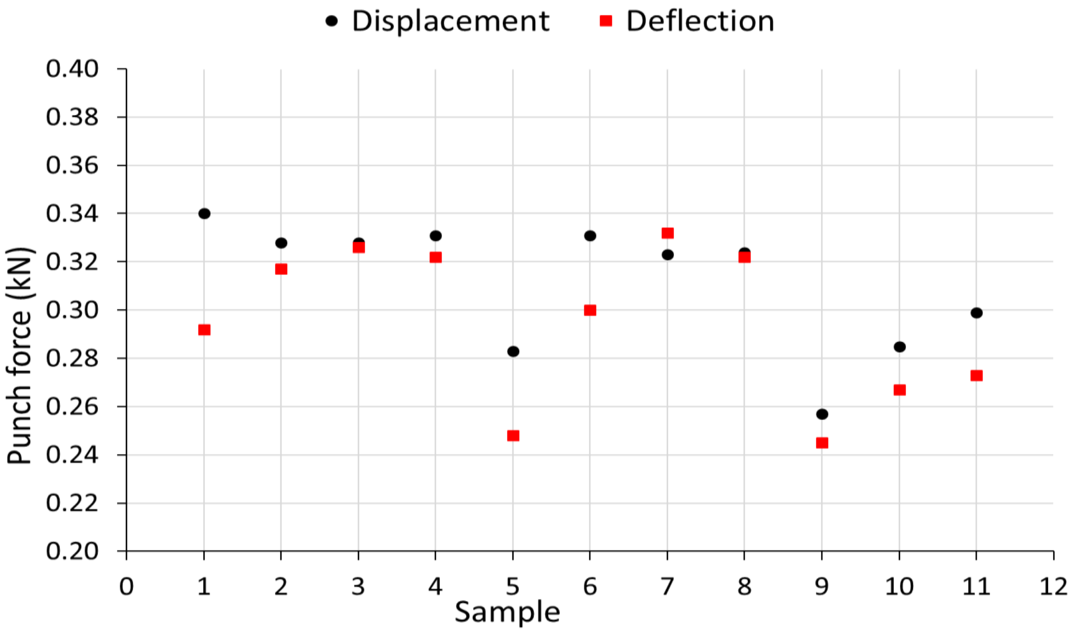

Figure 4.16: A comparison of the F_a values calculated using sample deflection and punch displacement data from Eurofer97 small punch tests

4.4 Proof stress estimations

In some ductile metals, the precise point of yield is difficult to identify. In such cases, proof stress is used. This value is found using an offset method. Typically, at 0.2% strain a point is made on the strain axis. A line is then drawn up parallel to the gradient of initial loading. Where this line crosses the stress-strain curve is the proof stress. This method provides an analogous way for finding the yield point when it would otherwise not be possible. As such, the systematic nature of proof stress makes it ideal for adaptation to a small punch test. Obtaining such values will prove useful in further Chapters where utilising as much information from the small punch curve will be crucial.

The code of best practice and ASTM standard include a method for estimating the proof stress from the force-displacement/ deflection curves. Proof stress was calculated using Equation 3.1.

4.4.1 Results

P91

The results from the proof stress calculations on P91 are included in Table 4.6 and plotted in Figure 4.17.

Table 4.6: Calculated proof stress values for the sample deflection curves for P91

Sample	F_A (N)	Proof stress (MPa)
60	361	736.44
61	380	775.2
62	364	742.56
63	419	854.76
64	421	858.84
65	393	801.72
66	413	842.52
67	456	930.24
68	437	891.48
69	411	838.44

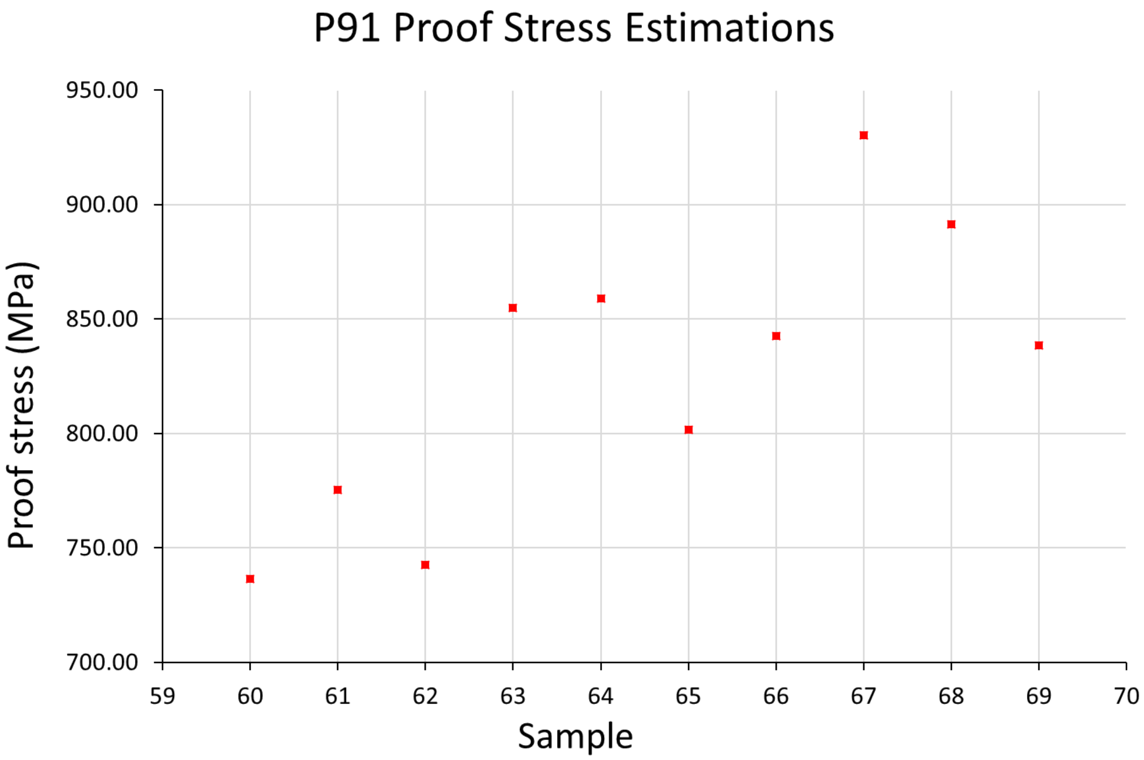

Figure 4.17: The visualisation of the proof stress estimations using the methodology outlined in the draft standard. Note the general upward trend of the proof stress values with number of tests. This may be a cause for concern

It can be noted that the estimations produced valued that exceeded that of experimental tensile test data or those reported in literature (Table 4.7).

Table 4.7: Experimental proof stress values from full scale tensile tests. Data was from the ODIN database and sourced from literature [131]

Source	**Value (MPa)**
Experimental, $\sigma_{0.2}$	507
Literature value [131]	538

Eurofer97

The results from the proof stress calculations on Eurofer97 are included in Table 4.8 and plotted in Figure 4.18.

Table 4.8: Calculated proof stress values for the sample deflection and punch displacement curves for Eurofer97

	Deflection data		Displacement data	
Sample	**F_A (N)**	**Proof stress (MPa)**	**F_A (N)**	**Proof stress (MPa)**
1	292	595.68	340	651.44
2	317	646.68	328	628.45
3	326	665.04	328	628.45
4	322	656.88	331	634.20
5	248	505.92	283	542.23
6	300	612.00	331	634.20
7	332	677.28	323	618.87
8	322	656.88	324	620.78
9	245	499.80	257	492.41
10	267	544.68	285	546.06
11	273	556.92	299	572.88

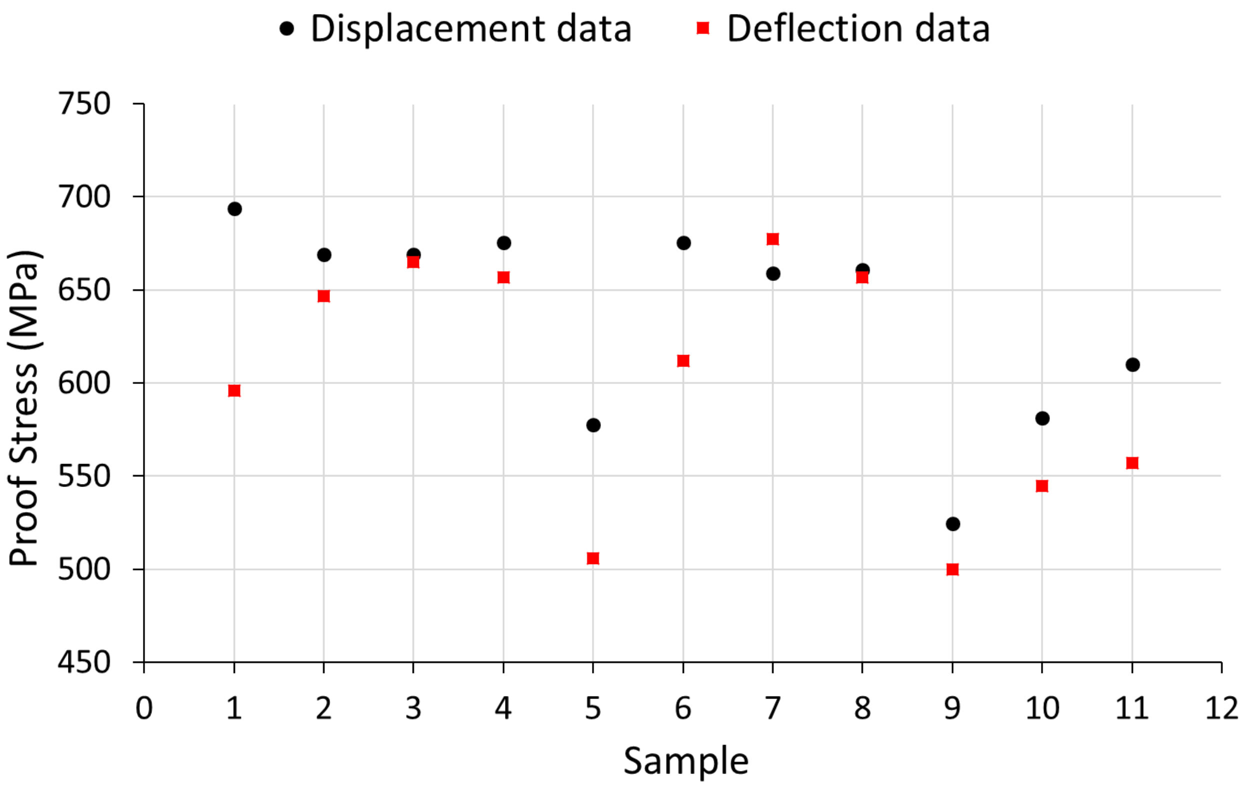

Figure 4.18: A graph displaying the comparison of Eurofer97 proof stress estimations produced by deflection and displacement data and values sources from literature.

As with the P91 results, It can be noted here that the estimations produced valued that exceeded that of experimental tensile test data or those reported in literature (Table 4.9).

Table 4.9: Experimental proof stress values from full scale tensile tests of Eurofer97. Data sourced from literature

Source	**Value (MPa)**
Literature value [131]	544
Literature value [50]	530

4.5 Ultimate tensile strength estimations

The ultimate tensile strength, UTS, is one of the most widely used values when classifying engineering alloys. It is described as the maximum engineering tensile stress that a material attains before failing. Ultimate tensile strength is measured as the maximum point of stress in an engineering stress-strain curve.

The simplicity of UTS makes it a common choice for engineers. The fact that it can be calculated using a simple tensile test means that the results can be used as a cursory viability test for many structural applications. However, it's simplicity may also be its weakness. Ultimate tensile strength does not impart any information about how the material behaves elastically or plastically up to, or after that point. Meaning that, while it is a good test for simple materials classification it cannot realistically be used for more in-depth materials analysis.

As stated above, the UTS, or R_m, is a useful value for surface level materials testing and classification. Seeing as the small punch test is designed for quick and efficient materials testing, it would be pertinent to ensure that a UTS calculation is included in the testing procedure. As with the proof stress calculations, UTS cannot be derived directly from the small punch curve, meaning that an estimation will have to suffice [128], [131], [157].

The UTS was calculated using both methods outlined in Equations 3.2 and 3.3. Equation 3.2 utilised the maximum punch force so was entitled F_m method. Equation 3.3 utilised the force at point u_i (defined as the deflection at the point of plastic instability initiation) so was entitled the F_i method.

4.5.1 Results

P91

The UTS for the P91 curves was calculated using both methods outlined above. The results for both methods can be found in Table 4.10 and Figure 4.19.

Table 4.10: The calculated UTS values for both estimations methods using the P91 sample deflection data

	F_m method (Equation 3.2)			**F_i method (Equation 3.3)**	
Test Number	**F_m (N)**	**u_m (mm)**	**σ_{UTS} (MPa)**	**F_i (N)**	**σ_{UTS} (MPa)**
60	1491	1.36	607.36	844.3	648.42
62	1448	1.31	612.36	813.1	624.46
63	1484	1.25	657.71	888.4	682.29
64	1528	1.29	656.21	897.0	688.90
65	1441	1.24	643.80	851.7	654.11
67	1373	1.15	661.43	995.8	764.77
68	1377	1.16	657.64	982.1	754.25

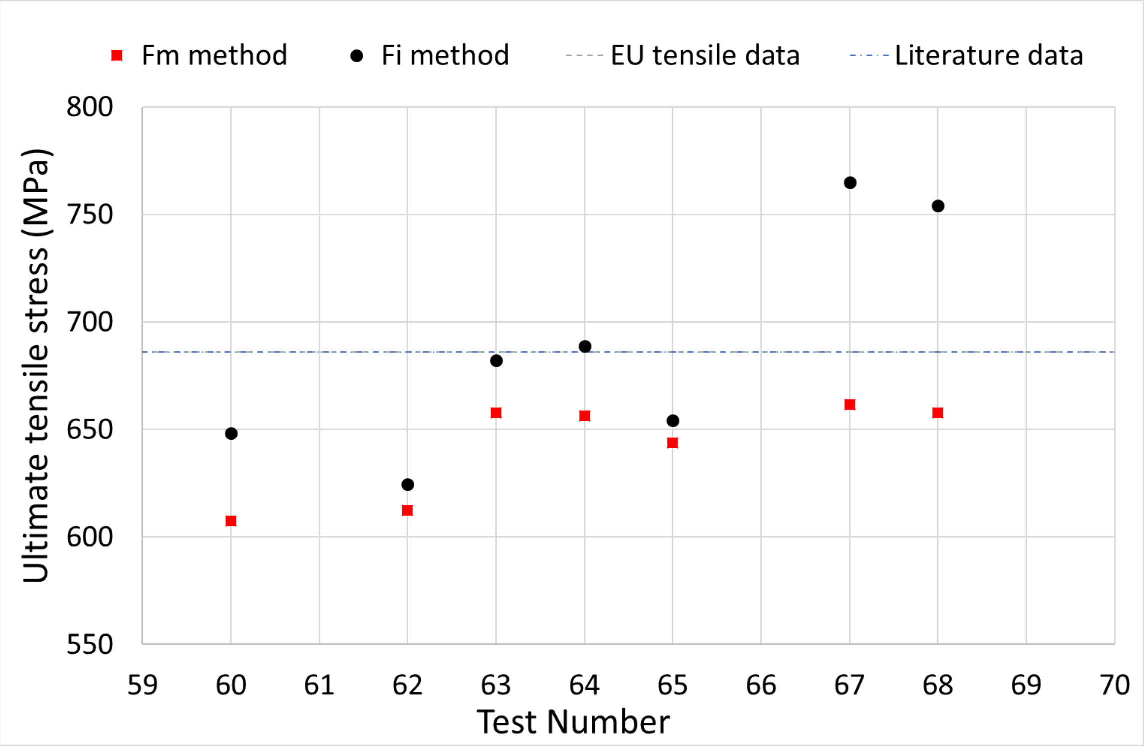

Figure 4.19: Graph showing a comparison of the two methods for estimating ultimate tensile strengths with bulk-scale values provided in Table 4.10 [131].

The method that used the maximum punch force produced slightly lower UTS estimates, whereas the plastic instability method gave results that were higher, and in some cases more than the full scale tensile data (Table 4.11).

Table 4.11: Experimental UTS values from full scale tensile tests. Data was from the ODIN tensile test and sourced from literature

Source	**Value (MPa)**
Provided with P91 tensile data	680
Literature source [131]	686

Eurofer97

The Eurofer97 small punch data provided another opportunity for a comparison of punch displacement and sample deflection results. The displacement results can be found in Table 4.12 while the deflection results are in Table 4.13. The results for both sets have also been compiled into the graph shown in Figure 4.20.

Table 4.12: The calculated UTS values for both estimations methods using the Eurofer97 punch displacement data

	F_m method (Equation 3.2)			**F_i method (Equation 3.3)**	
Test number	**F_m (N)**	**v_m (mm)**	**σ_{UTS} (MPa)**	**F_i (N)**	**σ_{UTS} (MPa)**
001	1455	1.710	471.32	883	678.14
002	1418	1.690	464.81	909	698.11
003	1417	1.640	478.82	926	711.17
004	1609	1.830	487.10	919	705.79
005	1530	1.870	453.31	818	628.22
006	1652	1.760	520.00	893	685.82
007	1568	1.800	482.62	927	711.94
008	1638	1.770	512.66	950	729.60
009	1574	1.840	473.87	877	673.54
010	1566	1.830	474.19	895	687.36
011	1610	1.750	509.71	880	675.84

Table 4.13: The calculated UTS values for both estimations methods using the Eurofer97 sample deflection data

	F_m method (Equation 3.2)			**F_i method (Equation 3.3)**	
Test number	**F_m (N)**	**u_m (mm)**	**σ_{UTS} (MPa)**	**F_i (N)**	**σ_{UTS} (MPa)**
1	1455	1.301	619.58	773	593.74
2	1418	1.252	627.45	796	611.64
3	1417	1.203	652.55	812	623.69
4	1609	1.418	628.62	813	624.00
5	1530	1.478	573.49	713	547.43
6	1652	1.405	651.39	793	608.72
7	1568	1.398	621.37	820	629.84
8	1638	1.375	659.97	840	644.97
9	1574	1.450	601.38	767	589.06
10	1566	1.393	622.80	788	604.80
11	1610	1.428	624.61	777	596.89

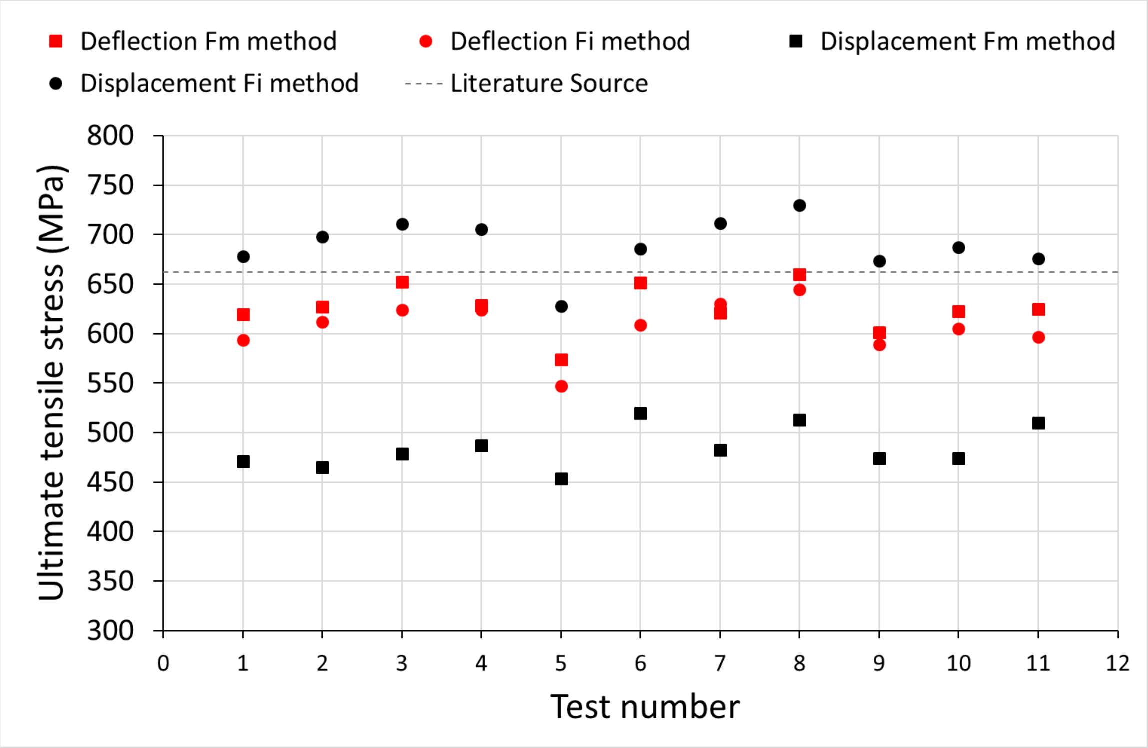

Figure 4.20: Graph showing a comparison of the two methods for estimating ultimate tensile strengths with bulk-scale values provided in Tables 4.11 and 4.12 [131].

As with the P91 results, the method that used the maximum punch force produced slightly lower UTS estimates, whereas the plastic instability method gave results that were higher, and in some cases more than the full scale tensile data (Table 4.14). A discrepancy between deflection and displacement data was also observed.

Table 4.14: Experimental UTS values from full scale tensile Eurofer97 tests. Data sourced from literature

Source	**Value (MPa)**
Literature source [131]	662
Literature source [50]	662

4.6 Discussion

4.6.2 P91 results

General

The small punch test data for the P91 samples was consistent with all tests showing similar punch force values. The only anomaly was the difference in force-deflection curve shape. This will be discussed in section 4.6.3.

Proof stress

One of the first things that became evident when looking at the proof stress estimation data was that all of the values were significantly higher than numbers produced from a full-scale tensile curve or those reported in literature (Table 4.7).

The inaccuracy of these results could have been caused by the methodology or the samples themselves. The miniature sample size could cause any bulk scale defects present to be missed on the small scale. This could lead to higher loading forces or larger amounts of elastic deformation.

The effect of the different curve shapes can also be seen here, as samples 67 and 68 have produced proof stress values larger than the rest of the group. This may be down to these two curves in particular having larger elastic loading and a more indistinct elastic-plastic transition thereby giving larger F_A values.

Another factor to consider is wearing of the punch head. It is documented that the punch head or ball will start to wear after some service [147]. If the punch is not replaced regularly, then the wear may have an adverse effect on the force-deflection curve. The punch wear was not mentioned in the experimental data, so no correlation can be made here. However, it is an effect that must be taken into consideration, when analysing the variability of small punch test data.

UTS

The two methods for estimating UTS produced different sets of results. While the standard does say that the maximum punch force method in general produces better results, it also notes that the plastic instability method is less dependent on a material’s tensile properties [131]. In a case where the proof stress calculations proved to be inaccurate, it would be logical that the method that did not rely as much on tensile properties would produce a more reliable estimation.

4.6.1 Eurofer97 results

General

When the F_a values for displacement and deflection were evaluated (Figure 4.18), it became obvious that the difference between them was not systematic. To further understand this, a comparison between the punch displacement and sample deflection was made (Table 4.15 and Figure 4.21).

Table 4.15: An overview of the differences between the values of F_a for punch force and sample deflection Eurofer97 small punch curves

Sample	001	002	003	004	005	006	001	008	009	010	011
v_a (mm)	0.11	0.11	0.10	0.10	0.13	0.11	0.10	0.10	0.09	0.13	0.09
u_a (mm)	0.04	0.04	0.03	0.04	0.04	0.04	0.04	0.03	0.04	0.04	0.03
$v_a - u_a$ (mm)	0.07	0.07	0.07	0.07	0.09	0.08	0.06	0.07	0.05	0.09	0.06

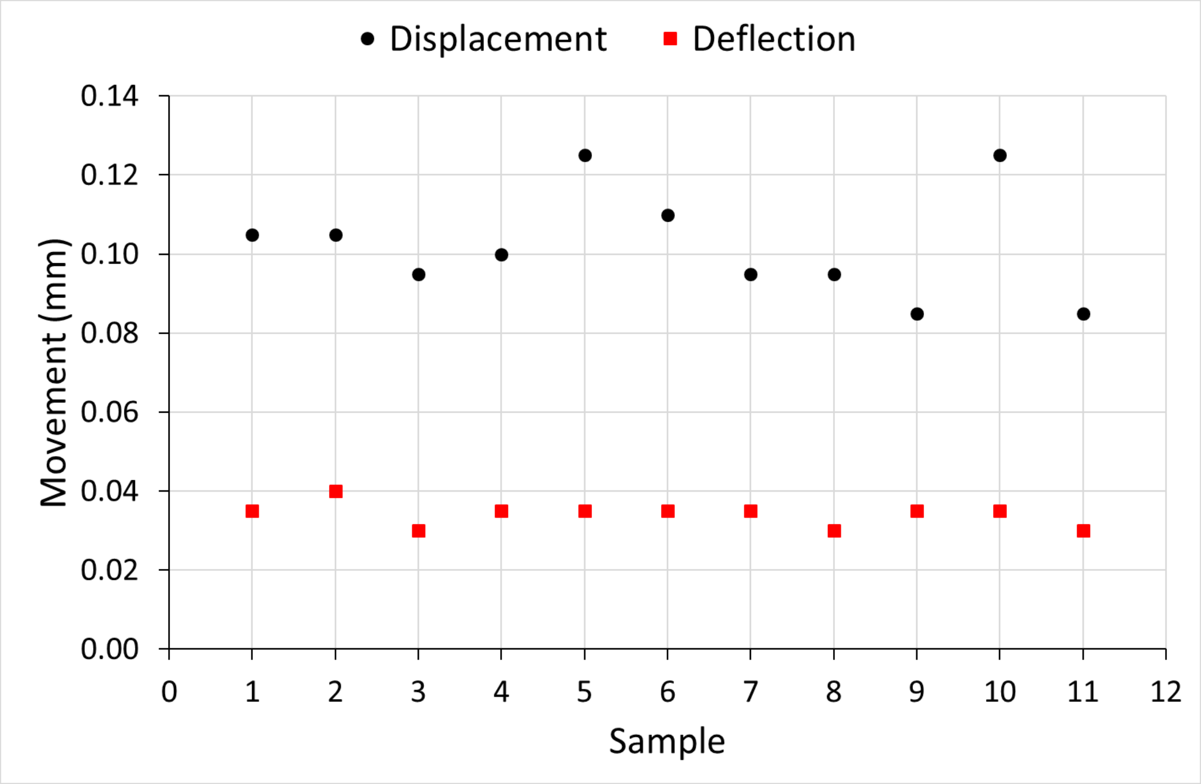

Figure 4.21: Graph showing a comparison of the punch displacement and sample deflection at Fa for each Eurofer97 test.

By inspecting the displacement and deflection data, it could be seen that the difference between the two sets was not consistent (Table 4.14 and Figure 4.20). Where there should have been a systematic difference of 0.5mm (the thickness of the samples) there was instead, a variation over the whole group of tests. It was also observed that the variation in the punch displacement data was greater than that of the sample deflection data. This was most likely due to movement in the small punch apparatus during the test. This would be recorded in the punch displacement and not the sample deflection, thus inducing variation.

Proof stress

The proof stress values for Eurofer97 are also above those provided in the literature, though not to the same extent. The majority do not and are at least 50 MPa above the highest literature value (Table 4.9). Much like the P91 tests, these results may be due to the sample microstructures and their size causing the absence of bulk level defects.

Another feature of these results is the differences between the displacement and deflection estimations. It would make sense that the difference be systematic as theoretically there would always be a 0.5mm difference between the two, but these results show that this is not the case. The percentage difference between F_A and $\sigma_{0.2}$ for the displacement data is 52.19% whereas the difference for deflection is 49.02%. Meaning that there is a 3.17% discrepancy between the two. It would stand to reason that this discrepancy would be due to the differences seen in Figure 4.20. Therefore, the excess movement recorded in punch displacement would produce a different F_A.

UTS

Much like the P91 results, the two methodologies also produced differing numbers for the Eurofer97 data. The F_m method that used the maximum punch force produced slightly lower UTS estimates, whereas the F_i method gave results that were higher. The displacement values in particular were consistently above the literature values (outlined in Table 4.14)

The Eurofer97 Figures allowed for another comparison between displacement and deflection datasets (Table 4.16). Like the proof stress estimations, the results here show a difference between displacement and deflection. Both displacement and deflection datasets produced lower values for the Fm method and higher values for the Fi method.

Table 4.16: An overview of the differences between sample deflection and punch displacement in Eurofer97 for both methods of estimating UTS

	σ_{UTS} values for the F_m method (MPa)			**σ_{UTS} values for the F_i method (MPa)**		
Sample	**deflection**	**displacement**	**difference**	**deflection**	**displacement**	**difference**
001	619.58	471.32	148.26	593.74	678.14	-84.40
002	627.45	464.81	162.64	611.64	698.11	-86.48
003	652.55	478.82	173.73	623.69	711.17	-87.48
004	628.62	487.10	141.52	624.00	705.79	-81.79
005	573.49	453.31	120.19	547.43	628.22	-80.79
006	651.39	520.00	131.40	608.72	685.82	-77.11
007	621.37	482.62	138.75	629.84	711.94	-82.10
008	659.97	512.66	147.31	644.97	729.60	-84.63
009	601.38	473.87	127.51	589.06	673.54	-84.48
010	622.80	474.19	148.61	604.80	687.36	-82.56
011	624.61	509.71	114.89	596.89	675.84	-78.95

However, the displacement data for the F_m method was lower than deflection, while the F_i results for displacement were higher than deflection (as illustrated in Figure 4.20). This implies that the punch force values have an effect on the magnitude of the estimation. For the deflection data, the F_i produced is lower than the displacement values, thus the Rm value estimated will also be lower.

However, while the displacement values do produce more accurate estimates, they are not always conservative. In the interest of quality assurance, it would be pertinent to select the method that produces similar, yet low values over one that may sometimes overestimate.

4.6.3 Comparison of both alloys

General

The variation in curve shape is consistent throughout all of the tests shown. Such differences may be down to the inherent inhomogeneity within the materials. The effect of such inhomogeneity is amplified on the small scale as such things as line defects and inclusions occupy a larger proportion of the sample when compared to a bulk tensile test. There has been previous research on this and the ductility of the sample was found to have an effect on the force-displacement curve shape [160], [202]. It would stand that certain samples were taken from areas of material that were more brittle than their siblings (Samples 4-11 for Eurofer97 and Samples 67 & 68 for P91).

Though it is not just small punch testing that is affected by variable results, small-scale testing across the board produces variable results. As discussed in the literature review, the inconsistency of small-scale testing is one of the main barriers to it being used in materials development rather than in service materials monitoring [54].

Proof stress

The large overestimation of the proof stress values is a cause for concern. While, there are some papers that do point out the inconsistencies in proof stress estimations [147]. There does not seem to be a clear reason for the results produced in this report to be so far out. Of course, there are factors like material inhomogeneity to consider, though the effects should not be so consistent across all samples.

Another cause could be a discrepancy between the processing of the small punch samples and bulk material data. However, this theory does not stand with the P91 test results as both the tensile samples and small punch samples were taken from the same block of metal.

The error function used is not as is in the standard. However, the F_A values produced are not too far off those expected from the standard error function. And even with some variation, it does not explain the large overestimation.

UTS

The results from both materials followed the same trend. Where F_i method did on, occasion produce results that were an overestimation, thus not ensuring consistent conservative results.

For the case of displacement vs deflection in UTS estimations, logic follows that the P91 displacement estimates would be higher than the current deflection ones. Thus, making them less conservative and therefore not ideal for engineering applications.

Variations in the UTS values were observed for both methods in both P91 and Eurofer97. This was most likely due to the inherent I variability in small scale test specimens producing variable ductility in the same material.

4.7 Conclusions

The variation in experimental results allowed for the identification of specimens with different levels of ductility. Leading to the successful correlation of yield stress with material ductility. i.e. the curves displaying a more brittle behaviour lead to an increase in yield stress values.

4.7.1 Aims

The aim of this Chapter of work was to produce a Python script that analysed raw small punch test data to produce values that could be further utilised to generate estimates of engineering materials properties i.e. UTS and proof stress.

From here the work developed into assessing the current recommended methods for estimating UTS and proof stress for two steel alloys, Eurofer97 and P91.

4.7.2 Main Findings

General

In general, a variation in curve shape and calculation results can be said to be due to the inherent inhomogeneity within the specimens. This was highlighted by the apparent change in ductility from specimen to specimen.

Proof Stress

An overall overestimation of proof stress values was observed in both the proof stress and ultimate tensile strength estimations. The P91 data produced a more pronounced overestimation than the Eurofer97.

Even with the overestimations a pattern within the results was observed. This was a potential correlation between increase in yield with a decrease in ductility.

Ultimate Tensile Strength

Two methods for the estimation of UTS were used, with both producing different results.

The method that utilised maximum punch force (F_m), in general produced marginally lower estimates than the method that used the point of plastic instability (F_i). With the F_i method producing the occasional overestimation.

In general, both methods followed the same trends with similar variation and estimations that were, to some extent, accurate.

4.7.3 Potential for further development

There is one clear path for the further development of this work. This is the creation of a script that can produce all of the values discussed in this Chapter. In addition to finding Fm, Fa, and Ff, the script would also calculate the proof stress and UTS estimations. Therefore, reducing the overall amount of work required to analyse a small punch test curve.

Aside from this, another area that needs further research is the issues surrounding proof stress calculations. The large overestimation seen in this Chapter is a cause for concern. Further research into the sensitivity of the Equations would be prudent.

4.7.4 Going forward

While the proof stress values are an overestimate, they will still be used in future work. This is due to a desire to keep all methods as “standard” as possible. However, if they do not aid in producing the best possible results then other methods will be considered.

For the estimation of UTS/R_m values, it can be concluded that the punch displacement data cannot be taken as equally reliable as sample deflection data and so to ensure accuracy, future calculations/simulations will be conducted using sample deflection only.

5. Construction of the finite element model

This Chapter describes the building and validation of the small punch test model. As such, it will cover all decisions made and any validation required for the formation of a reliable model.

5.1 Chapter Aims

The overall aim is to create a finite element model that is an effective simulation of a small punch test. Meaning that the methods used must produce results that sit within a certain level of confidence. This will be achieved through the following objectives:

- To build a viable model of the small punch test that accounts for all boundary conditions of the test and is computationally efficient to run on a desktop PC.
- Populate the model with robust material behaviour constitutive models to account for the material flow behaviour and that are amenable to inverse analysis.
- Produce a predicted force-deflection curve that reflects all characteristics of the experimental small punch force-deflection curve.

5.2 Software Selection

5.2.1 Software requirements

The selection of an appropriate software package was a necessary first step. To do this, simulation requirements were first outlined:

- Formation of the punch and dies as rigid non-deformable objects (not meshed).
- The translation of the punch at a constant displacement rate.
- The sample would be deformable, have elastoplastic deformation, and be capable of breaking/fracturing, with an appropriately sized mesh.
- The interactions between the components also needed to be defined, i.e., the friction between sample, dies, and punch.
- All variables must be variable to allow for sensitivity tests. They must also be recordable for analytical purposes.

5.2.2 Software selected

For this study, Abaqus CAE 2017 was selected. Abaqus has been widely used across the field of small punch testing, as illustrated in the literature survey [130], [131], [136], [161], [169], [170]. Abaqus allows for the production of a full 3D model with the capability of adding in material failure through element deletion. It comes with several built-in material constitutive flow behaviour models allowing for an adequate prediction of the test.

5.3 Making the components

Each component for the model was constructed individually. The geometries and properties of each are described below.

5.3.1 Upper die

The upper die was given an internal diameter of 3mm, as outlined in the code of best practice, ASTM standard and round robin (Figure 5.1a), and was assigned as an analytical rigid shell [93], [128], [155], [203]. The surface in which the sample would contact the upper die was defined and a reference point added along the outer circumference. The final component can be seen in Figure 5.1b.

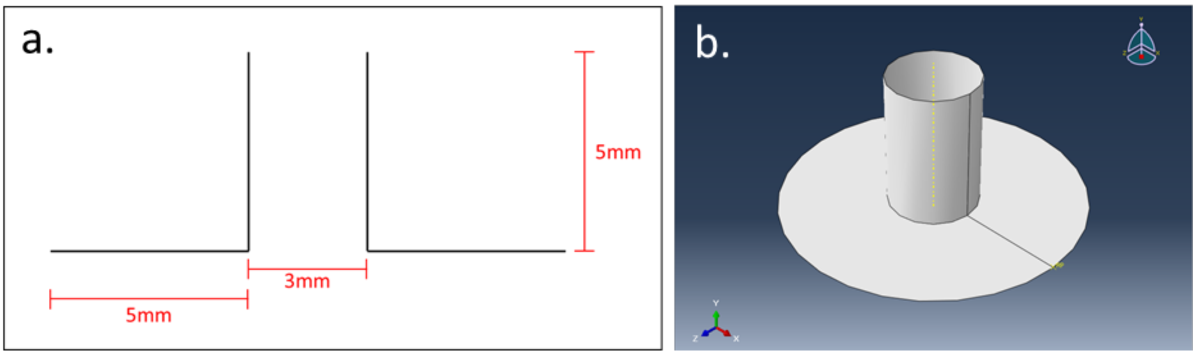

Figure 5.1: a) diagram showing the geometry of the upper die b) the die as realised in a 3d analytical rigid revolution

5.3.2 Lower die

The lower die was given an internal diameter of 4mm with 0.2mm chamfers as outlined in the code of best practice, ASTM standard and round robin (Figure 5.2a), and was assigned as an analytical rigid shell [93], [128], [155], [203]. The surface in which the sample would contact the lower die was defined and a reference point added along the outer circumference. The final component can be seen in Figure 5.2b.

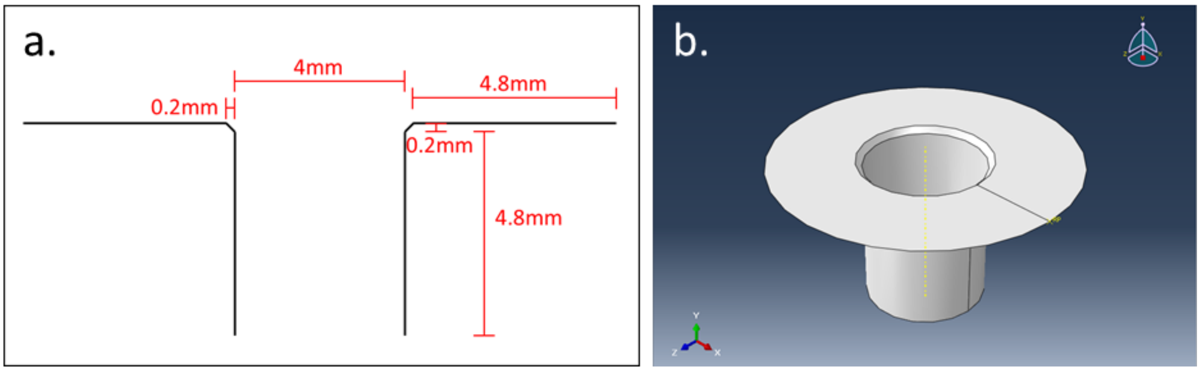

Figure 5.2: a) diagram showing the geometry of the lower die b) the die as realised in a 3d analytical rigid revolution

5.3.3 Punch

The punch was given a head radius of 1.25mm as outlined in the code of best practice (Figure 5.3a) [93], [128]. To reduce the computational cost at this stage, the punch was assigned as an analytical rigid shell. The surface in which the sample would contact the punch was defined and a reference point added along the outer circumference. The final component can be seen in Figure 5.3b.

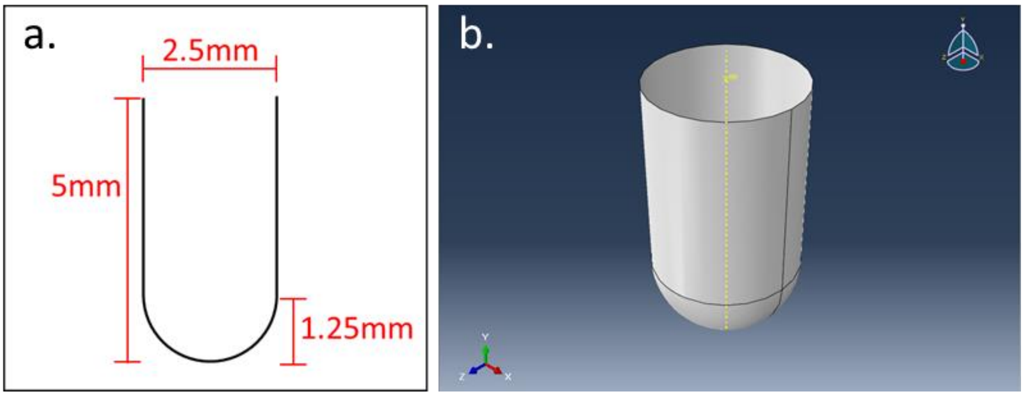

Figure 5.3: a) diagram showing the geometry of the punch b) the die as realised in a 3d analytical rigid revolution

5.3.4 Sample

Geometry

The sample was set as a deformable solid revolution, allowing the full sample to be generated and a mesh to be added. Its geometry was as recommended in the code of best practice, ASTM standard and round robin (Figure 5.4) [93], [128], [155], [203]. The top and bottom surfaces were defined to allow for interactions with the die and punch.

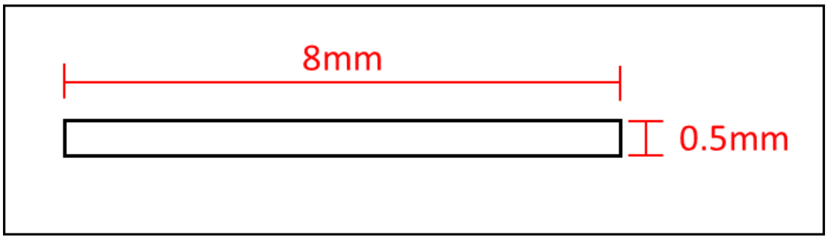

Figure 5.4: diagram showing the geometry of the small punch sample

Mesh

The selected mesh type was C3D8R, a 3-dimensional, solid continuum element with 8 nodes and reduced integration [204], [205]. This element type is generally used for modelling plastic deformation, making it ideal for simulating the small punch test [196], [206]. Reduced integration also means that the elements are computationally inexpensive, and thus good for models utilising the explicit solver (explicit solver is explained in section 5.7.1) [205].

To determine the appropriate mesh size, a mesh size sensitivity analysis was completed. This analysis would establish a balance between simulation accuracy and computational time.

The results of the sensitivity analysis are in Figures 5.5 and 5.6. The first test had a course mesh of 0.25mm. It was completed very quickly, in 52 seconds. While this mesh size did produce a suitable force-deflection curve (Figure 5.6), it was clear that it was mesh dependant, i.e., the force-deflection curve was affected by the size of the mesh applied to the specimen. Such dependency in general is not recommended [161].

After this, two further mesh sizes were tested, 0.1mm and 0.05mm. The 0.1mm mesh took 292 seconds to complete, while the 0.05mm mesh took 2308 seconds to complete. This increase in computational time was not mirrored in a relative improvement in deformation shape, plastic strain distribution, or force-deflection curve accuracy, proving that both were mesh independent (Figures 5.5 and 5.6).

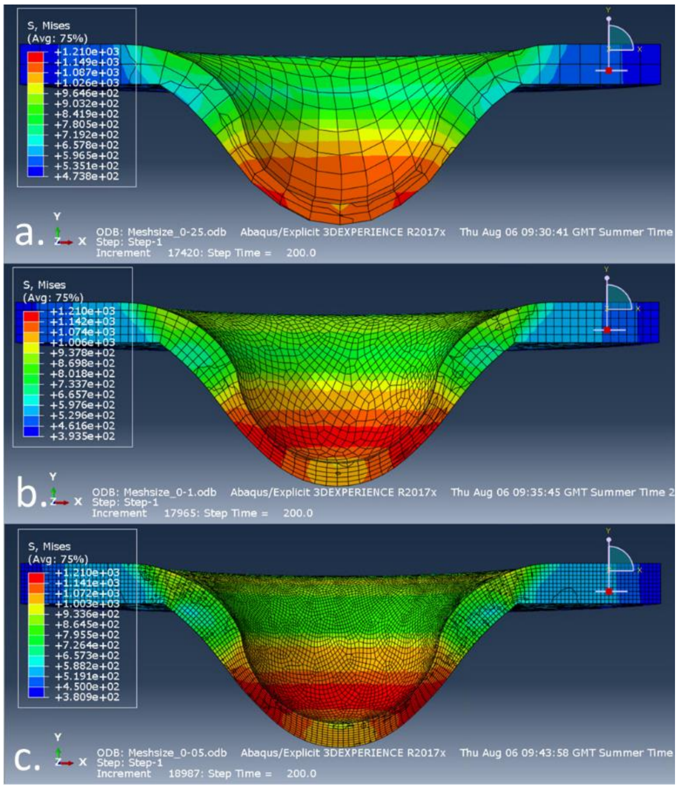

Figure 5.5: Screenshots of the deformed small punch sample at different mesh sizes a) Mesh size 0.25 – CPU time 52 seconds b) Mesh size 0.1 – CPU time 292 seconds c) Mesh size 0.05 – CPU time 2308 seconds

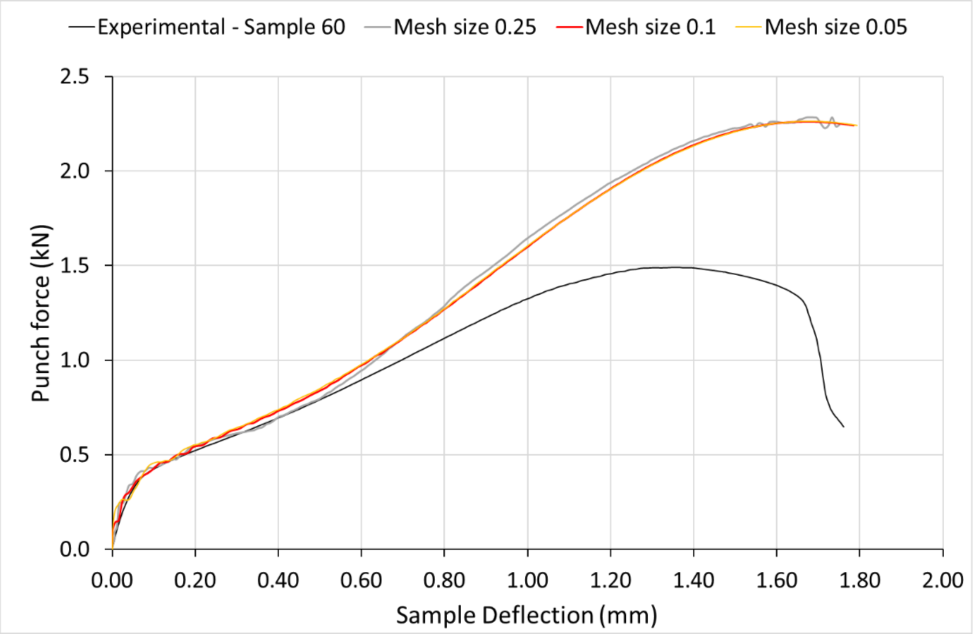

Figure 5.6: Graph of the punch force- sample deflection graphs of small punch tests at different mesh sizes.

A mesh size of 0.1mm was selected for future work. An image of the finalised mesh can be found in Figure 5.7. A partition was also added across the centre of the sample to allow for cross sectional analysis.

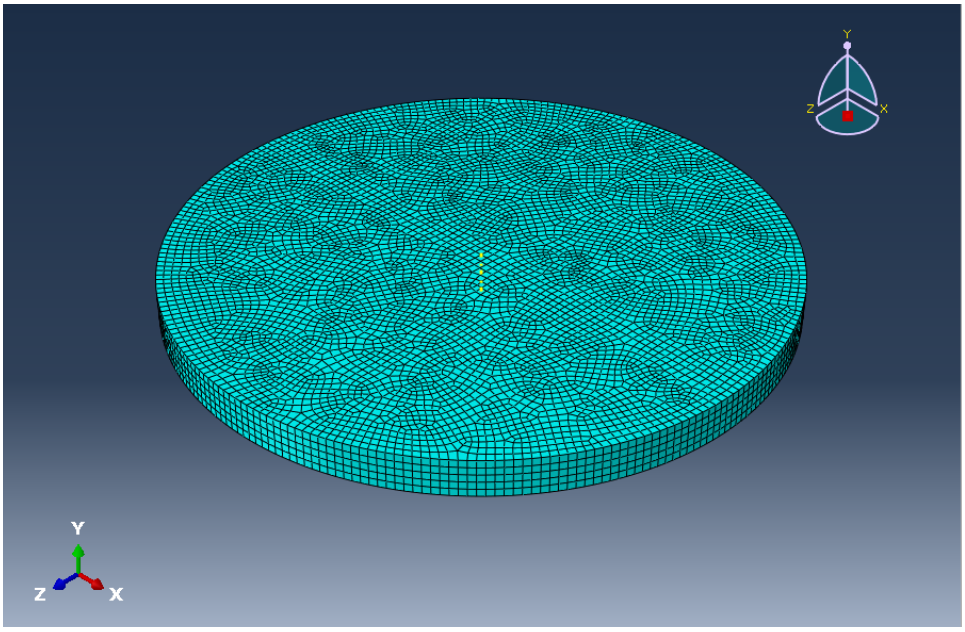

Figure 5.7: The sample with the selected mesh size of 0.1mm applied.

Element deletion was required to facilitate sample failure. Element deletion is included in the explicit packager of Abaqus and works on the basis of user defined damage criteria being fulfilled. In Abaqus this is called maximum degradation, D_{max}. The value of degradation, D, is recorded for each element and when D_{max} is reached in an element, it is deleted. By default, the value for D_{max} = 1 [207]. When applied across a mesh it allows for the simulation of fracture.

Another aspect to consider was the damage evolution. This controls how the meshed component behaves after the first element has reached the criteria for maximum degradation. Damage evolution is either energy or displacement based. As the small punch test is a displacement controlled test, the displacement criterion was selected in this case.

Much like the element size, the damage evolution also required sensitivity tests to ascertain the most appropriate value. At this time, for simplicity, linear behaviour was assumed and a basic sensitivity analysis carried out.

Simulations were carried out using a range of damage evolution values. Displacement at failure values between 0.01mm and 0.1mm were tested. The results were collated into force-displacement graphs (Figure 5.8). The shape of each curve was compared with an experimental curve. From this analysis the 0.025mm and 0.01mm curves appeared to be the best match. Where the 0.025mm test showing a better match over the top portion (necking) and 0.01mm displaying a closer match to the drop off in force over the final section of displacement.

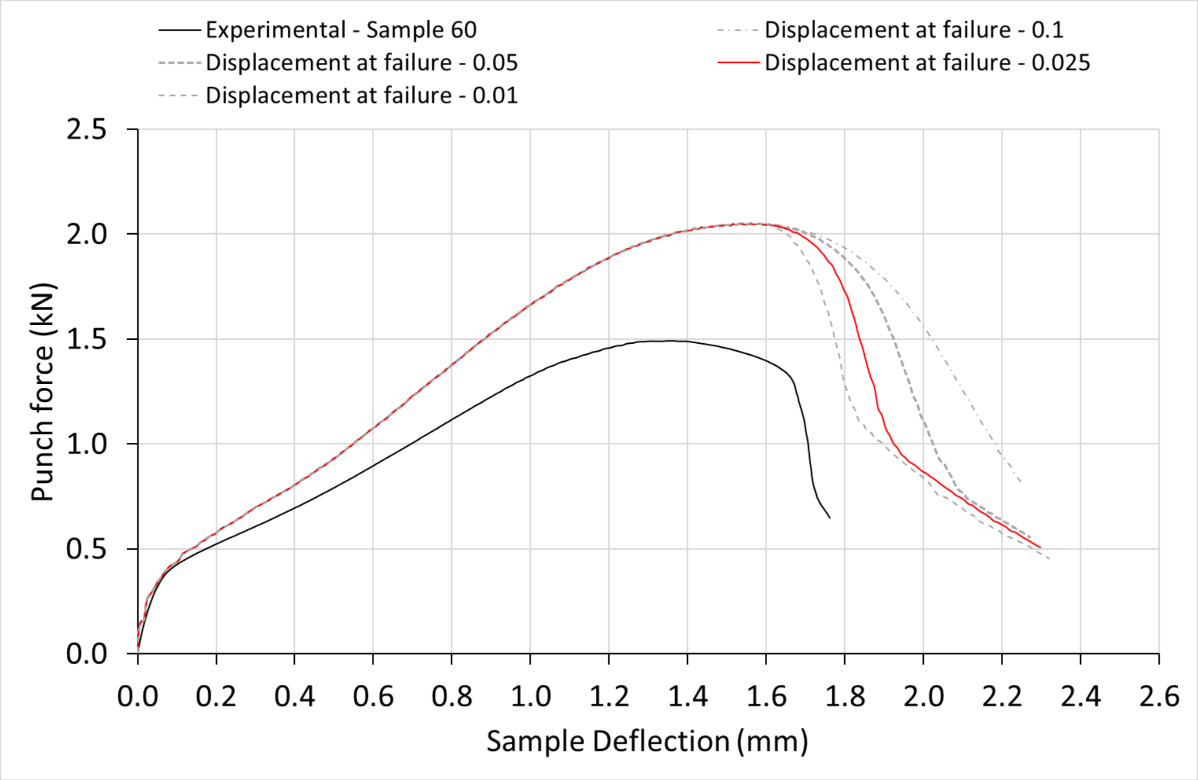

Figure 5.8: Graph showing the different curves produced by varying the damage evolution. A displacement at failure of 0.025 was chosen as it was the closest to the experimental curve in shape.

To assist in the decision, images of the fractured samples were taken and analysed (Figure 5.9). It is immediately evident here that of the two preferred tests, 0.025mm behaved substantially better than the 0.01mm test. The slightly larger value of damage evolution lead to less elements being deleted, thus producing the characteristic cap. A damage evolution of 0.025mm displacement at failure was selected.

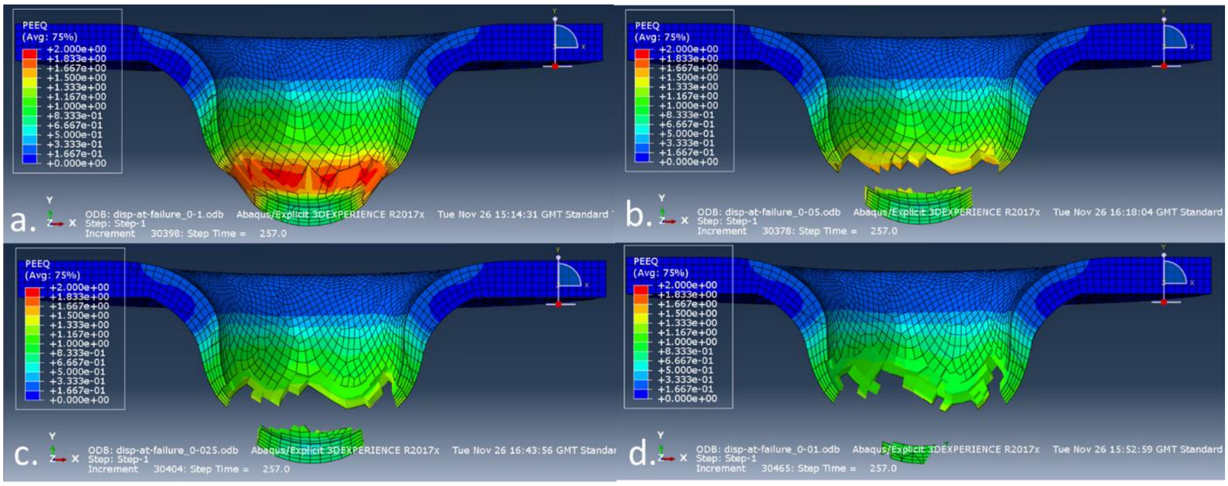

Figure 5.9: Screenshots of the deformed samples at different damage evolution values a) displacement at failure = 0.1mm b) displacement at failure = 0.05mm c) displacement at failure = 0.025mm d) displacement at failure = 0.01mm

However, morphology of the fracture using the mesh size of 0.1mm was not in line with those seen experimentally for a ductile metal (Figure 5.10). The courser mesh size led to a very jagged fracture surface rather than the expected pseudo-linear fracture surface.

Figure 5.10: XCT scan of a fractured steel small punch test sample. The morphology of the fracture surface is indicative of a ductile failure [159].

To rectify this a finer mesh was inserted into the centre portion of the sample (Figure 5.11a). This would encompass the volume of material that would undergo severe strain. The result of this refinement can be seen in Figure 5.11b. Applying this new, finer mesh did increase the CPU time significantly.

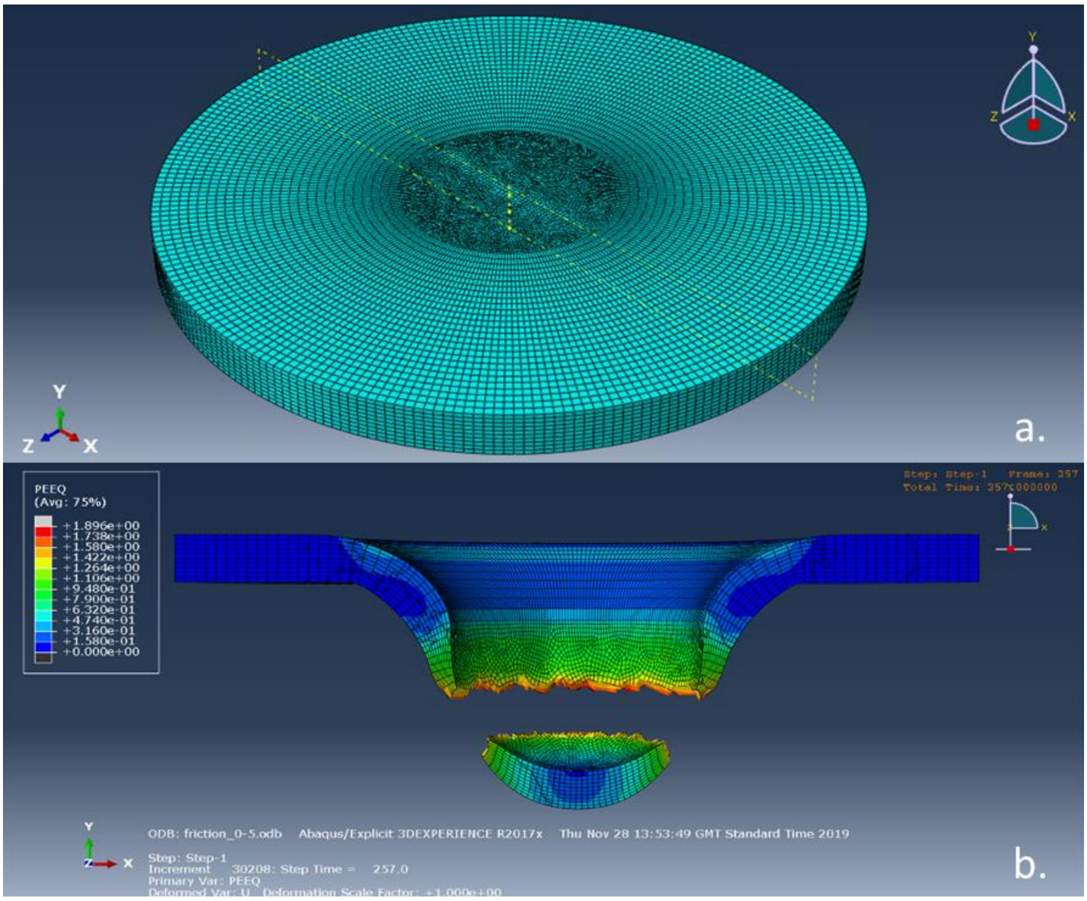

```
ODB: friction_0-5.odb    Abaqus/Explicit 3DEXPERIENCE R2017x    Thu Nov 28 13:53:49 GMT Standard Time 2019

Step: Step-1
Increment    30208: Step Time =    257.0
Primary Var: PEEQ
Deformed Var: U   Deformation Scale Factor: +1.000e+00
```

Figure 5.11: Screenshots displaying a) Sample with finer mesh at the centre b) Fractured sample with finer mesh and improved morphology.

5.4 Assembling components

Once all of the components were created, they were assembled as seen in Figure 5.12.

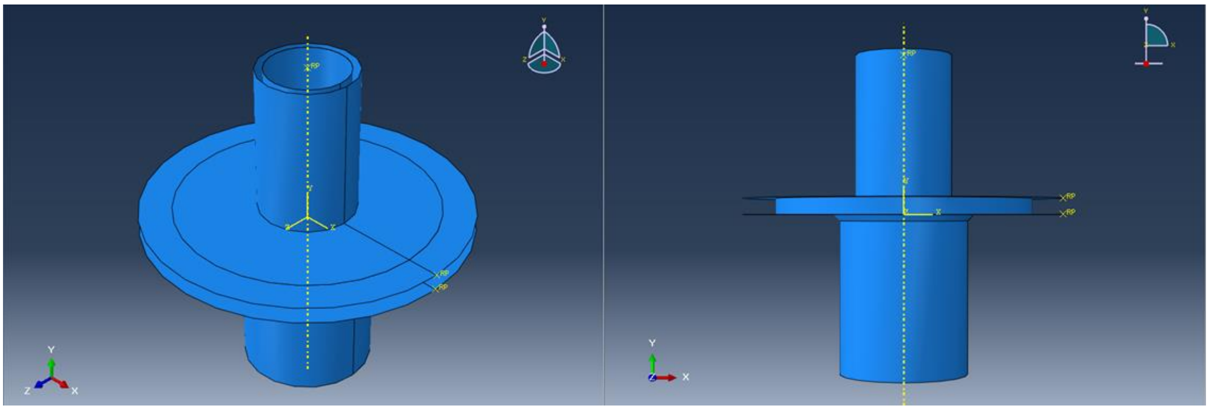

Figure 5.12: Screenshots of the assembled parts for the small punch test simulation. The Punch and both dies were analytical rigid shells with the sample beind a defomable solid with a mesh.

5.5 Material behaviour model

The Johnson-Cook models are simple and versatile, making them a popular choice for the simulation of metal forming [188], [208]–[210]. Because of this, both the Johnson-Cook plasticity and damage models were selected for use.

5.5.1 The Johnson-Cook material model

The Johnson-Cook flow stress model (Equation 3.4) is a constitutive Equation, the 5 constants of which can be determined with a small set of tensile tests [196].

An extensive literature review revealed that the Johnson-Cook material values for both P91 and Eurofer97 had not yet been published. This left two possible courses of action:

- Estimate/calculate the required constants
- Obtain values from a different steel

The Online Data & Information Network of the European Commission Joint Research Centre resource (MatDB) provided a set of tensile and small punch tests for P91 at varying temperatures [191]. This allowed for option 1. The estimation of the JCm values of P91 was then completed.

5.5.2 Estimation of the Johnson-Cook material model parameters

Using the P91 tensile data sourced from MatDB, a set of constants for the Johnson-Cook material model could be calculated.

Estimation of A

The value of A was obtained by a direct reading of yield stress from a room temperature tensile curve of the P91 and was measured as 510MPa.

This was the most direct method. However, the intention of this study was to demonstrate the applicability of small punch testing. Therefore, the possibility of obtaining a value for A from a single small punch curve was also investigated (see Chapters 4 and 6).

Calculation of B and n

As described by Banerjee et al. [196], the determination of B and n can be achieved by a power law curve fit on a single true stress-strain curve after the point of yield. A Python3 script was created using the SciPy optimize *curve_fit* functionality to achieve this (Figure 5.13).

Figure 5.2 shows the product of the curve fitting. The fit was not ideal, but for the purpose of finding a starting estimate it was deemed acceptable. with the values for B and n taken as:

- B = 666.4
- n = 0.459

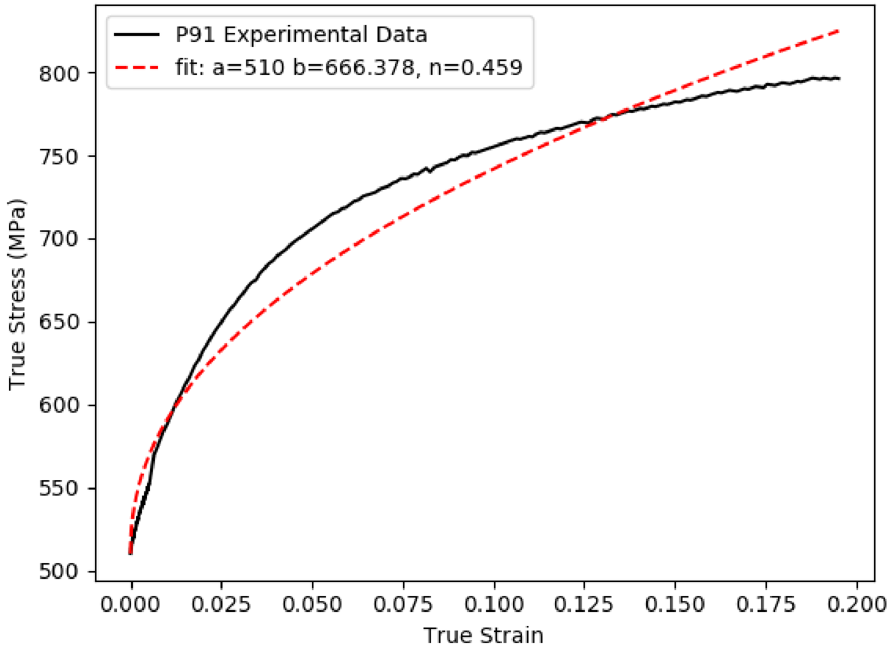

Figure 5.13: A graph showing a portion of the room temperature P91 true stress-strain curve with the fitted curve overlaid in red.

Regarding the exclusion of C

The calculation of C, required a specific set of curves over a range strain rates [196]. The tensile data that had been sourced from MatDB did not include such tests.

However, in cases where the strain rate is constant, ε_p* is often equated to 1, making $Cln\varepsilon_p^* = 0$ and therefore $\left[1 + Cln\varepsilon_p^*\right] = 1$ [206]. As the small punch tests under investigation were kept at a constant displacement rate, this was considered an acceptable compromise. If further tests were to be carried out under a changing strain rate, then C would need to be estimated and optimised.

Calculation of m

The estimation of m required a range of tests at different temperatures. Following the work of Banerjee et al. [196], the tensile curves needed to be at temperatures below the point where flow and yield stress significantly changed, i.e., above a certain temperature the material behaviour will be considerably different to that observed at lower temperatures. The tensile test data that was obtained from MatDB included tests completed over a range of temperatures [191]. To ascertain which tests were suitable for the calculation of m, the yield and tensile strength of each test was plotted (Figure 5.14).

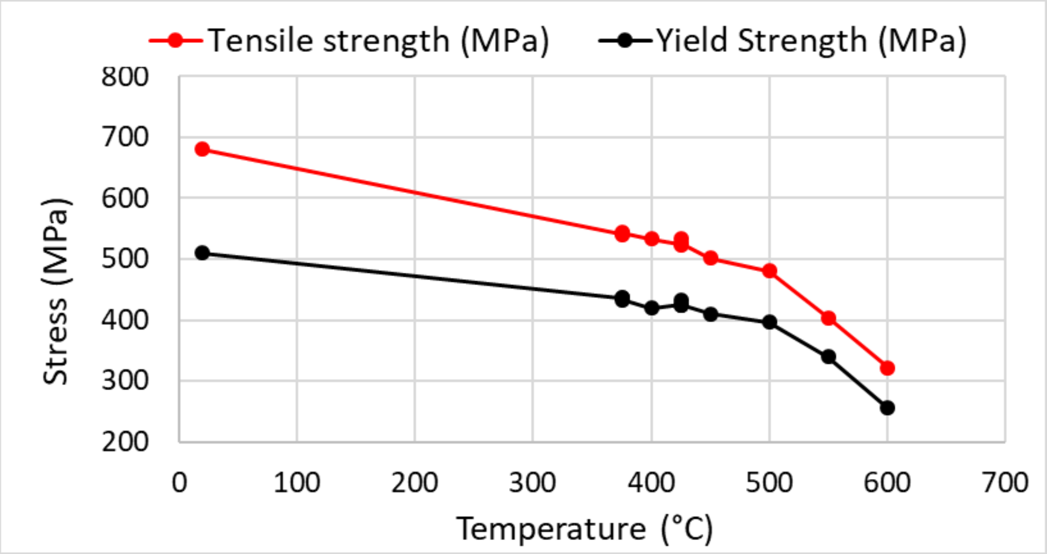

Figure 5.14: Change in P91 Tensile and Yield strength with respect to temperature

Figure 5.15 illustrates a significant depreciation in stress response after 500°C. Therefore, the tests at 400°C, 450°C, and 500°C were selected for this analysis as they display a steady change in properties with increasing temperature.

To determine m, the method outlined by Banerjee et al. was followed [196].

Since A, B and n, were known and C was discounted, σ became:

$$\sigma = \left[A + B\varepsilon_p^n\right]\left[1 - T_H^m\right]$$

Equation 5.3

Rearranging and multiplying both sides by the natural log gave:

$$m \ln T_H = \ln\left[1 - \frac{\sigma}{A + B\varepsilon_p^n}\right]$$

Equation 5.4

If $\ln T_H$ was plotted against $\ln\left[1 - \frac{\sigma_y}{A+B\varepsilon_p^n}\right]$, and a linear trend line fitted, then the gradient of the resulting slope could be taken as the value for m.

From these three curves, points were taken at three values of plastic strain, 0.05, 0.1, and 0.15.

The first step was to calculate the homologous temperature for each curve:

- $T_{room} = 20℃$
- $T_{melt} = 1420℃$

$$T_1 = 400℃$$

$$T_{1H} = (400 - 20)/(1420 - 20) = 0.2714$$

$$T_2 = 450℃$$

$$T_{2H} = (450 - 20)/(1420 - 20) = 0.3071$$

$$T_3 = 500℃$$

$$T_{3H} = (500 - 20)/(1420 - 20) = 0.3429$$

The engineering stress and strain values were converted to true stress and strain and then plotted with the elastic portion of the curve omitted. The stress values were plotted at each predefined strain point, and the $\ln\left[1 - \frac{\sigma_y}{A+B\varepsilon_p^n}\right]$ calculated:

$\boldsymbol{T_1} = \mathbf{400}℃$

$\varepsilon_{pl} = 0.05 \quad \sigma = 558$

$$\ln\left[1 - \frac{558}{510 + 666(0.05)^{0.459}}\right] = \ln\left[1 - \frac{558}{678.4}\right] = -1.729$$

$\varepsilon_{pl} = 0.10 \quad \sigma = 583$

$$\ln\left[1 - \frac{583}{510 + 666(0.1)^{0.459}}\right] = \ln\left[1 - \frac{583}{741.5}\right] = -1.543$$

$\varepsilon_{pl} = 0.15 \quad \sigma = 589$

$$\ln\left[1 - \frac{589}{510 + 666(0.15)^{0.459}}\right] = \ln\left[1 - \frac{589}{788.8}\right] = -1.373$$

$\boldsymbol{T_2} = \mathbf{450}℃$

$\varepsilon_{pl} = 0.05 \quad \sigma = 527$

$$\ln\left[1 - \frac{527}{510 + 666(0.05)^{0.459}}\right] = \ln\left[1 - \frac{527}{678.4}\right] = -1.450$$

$\varepsilon_{pl} = 0.10 \quad \sigma = 545$

$$\ln\left[1 - \frac{545}{510 + 666(0.1)^{0.459}}\right] = \ln\left[1 - \frac{545}{741.5}\right] = -1.328$$

$\varepsilon_{pl} = 0.15 \quad \sigma = 549$

$$\ln\left[1 - \frac{549}{510 + 666(0.15)^{0.459}}\right] = \ln\left[1 - \frac{549}{788.8}\right] = -1.191$$

$\boldsymbol{T_3 = 500}$℃

$\varepsilon_{pl} = 0.05 \quad \sigma = 499$

$$\ln\left[1 - \frac{499}{510 + 666(0.05)^{0.459}}\right] = \ln\left[1 - \frac{499}{678.4}\right] = -1.330$$

$\varepsilon_{pl} = 0.10 \quad \sigma = 508$

$$\ln\left[1 - \frac{508}{510 + 666(0.1)^{0.459}}\right] = \ln\left[1 - \frac{508}{741.5}\right] = -1.155$$

$\varepsilon_{pl} = 0.15 \quad \sigma = 507.5$

$$\ln\left[1 - \frac{507.5}{510 + 666(0.15)^{0.459}}\right] = \ln\left[1 - \frac{507.5}{788.8}\right] = -1.031$$

The results from the above calculations were collated into a graph, from which, the gradient of the Equation of the trend line was m (Figure 5.15).

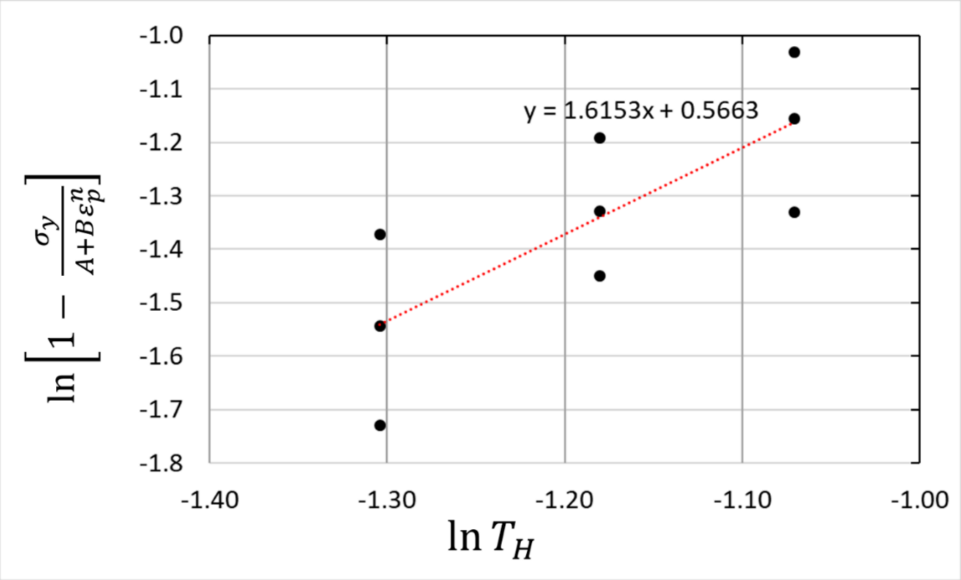

Figure 5.15: A graph showing the points calculated to give the value of m for the Johnson-Cook plasticity model.

Consequently, the estimated Johnson-Cook values for P91 steel are:

- $A = 510\ MPa$
- $B = 666.4\ MPa$
- $n = 0.459$
- $m = 1.6153$

A comparison of the Johnson-Cook estimates with a room temperature P91 tensile curve can be seen in Figure 5.16. This Figure acts as the starting point for the optimisation of the Johnson-Cook material model for P91.

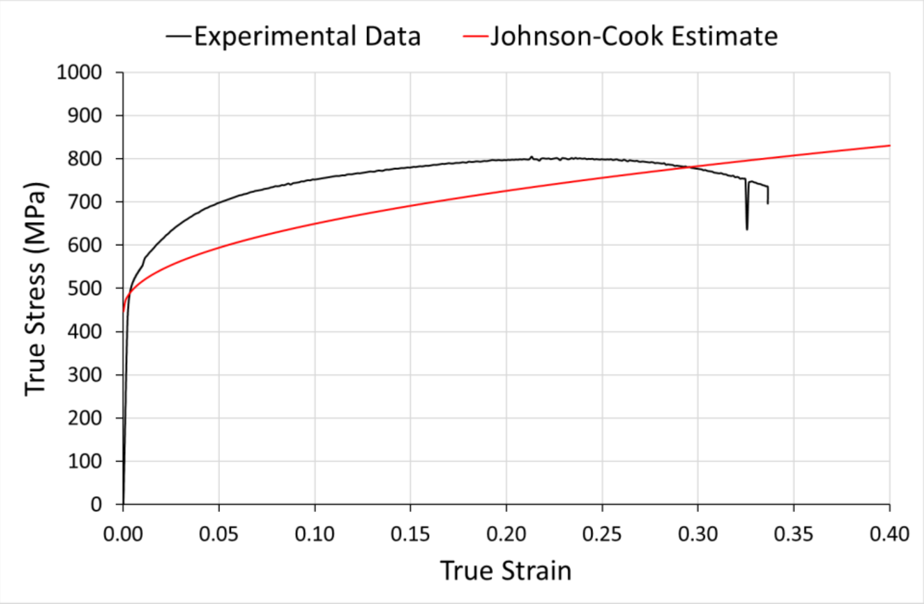

Figure 5.16: The true stress-strain curve for P91 plotted with the stress-strain response predicted using the Johnson-Cook materials model estimation.

5.5.3 The Johnson-Cook failure model

As discussed above, it was decided that the failure model would also be Johnson-Cook (Equation 3.5).

A literature search showed that calculating an estimate for the Johnson-Cook failure constants required specialised tests [211], [212]. This meant that calculating them with the tensile curves available was not possible. As a compromise, constants for other steels were sourced and the most appropriate fit was selected. The most relevant room temperature Johnson-Cook failure values are included in table 5.1. These values were used for the initial tests for the P91 steel.

Table 5.1: An overview of the Johnson-Cook failure constants sourced for testing in the small punch finite element model, The numerical values were true as of 31/03/2020.

Material	Constants
AISI 1045 [213] (labelled AISI 1045 1)	$D_1 = 0.06$ $D_2 = 3.31$ $D_3 = -1.96$ $D_4 = 0.0018$ $D_5 = 0.58$
AISI 1045 – round and notched [214] (labelled AISI 1045 2)	$D_1 = 0.04$ $D_2 = 16.93$ $D_3 = - 14.8$ $D_4 = 0.0214$ $D_5 = 0$
4340 Steel [208]	$D_1 = 0.05$ $D_2 = 3.44$ $D_3 = -2.12$ $D_4 = 0.002$ $D_5 = 0.61$
Armour steel [196]	$D_1 = 0.05$ $D_2 = 0.8$ $D_3 = - 0.44$ $D_4 = - 0.046$ $D_5 = 0$

A set of simulations were completed using each of the Johnson-Cook failure constants in table 5.1. The results of which can be found in Figures 5.17 and 5.18.

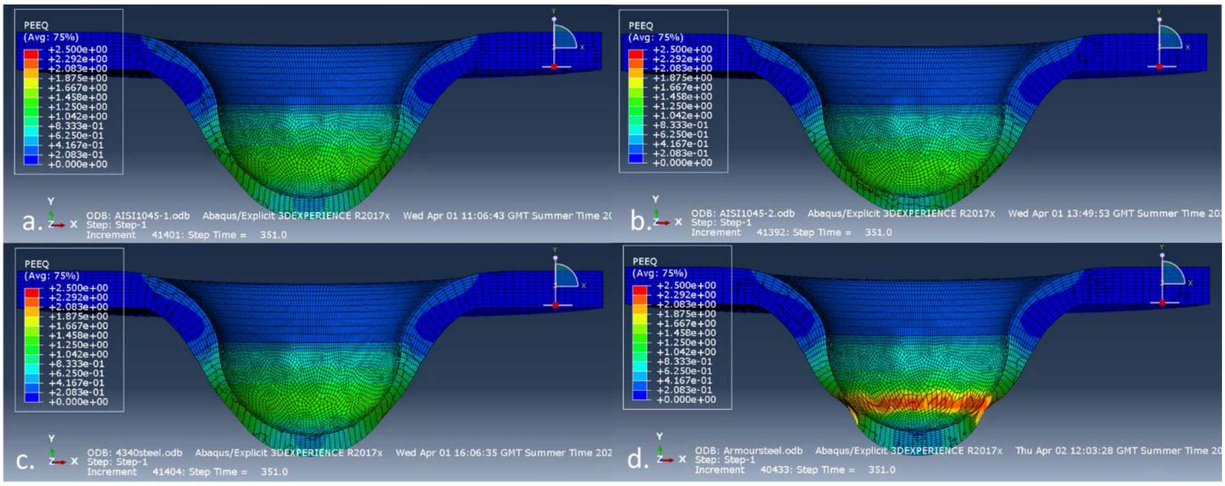

Figure 5.17: Screenshots of the cross section of a simulated deformed small punch test. Each image corresponding to a different alloy: a) AISI 1045 1 b) AISI 1045 2 c) 4340 Steel d) Armour steel. Note that the armour steel was the only one to display any form of necking at this displacement.

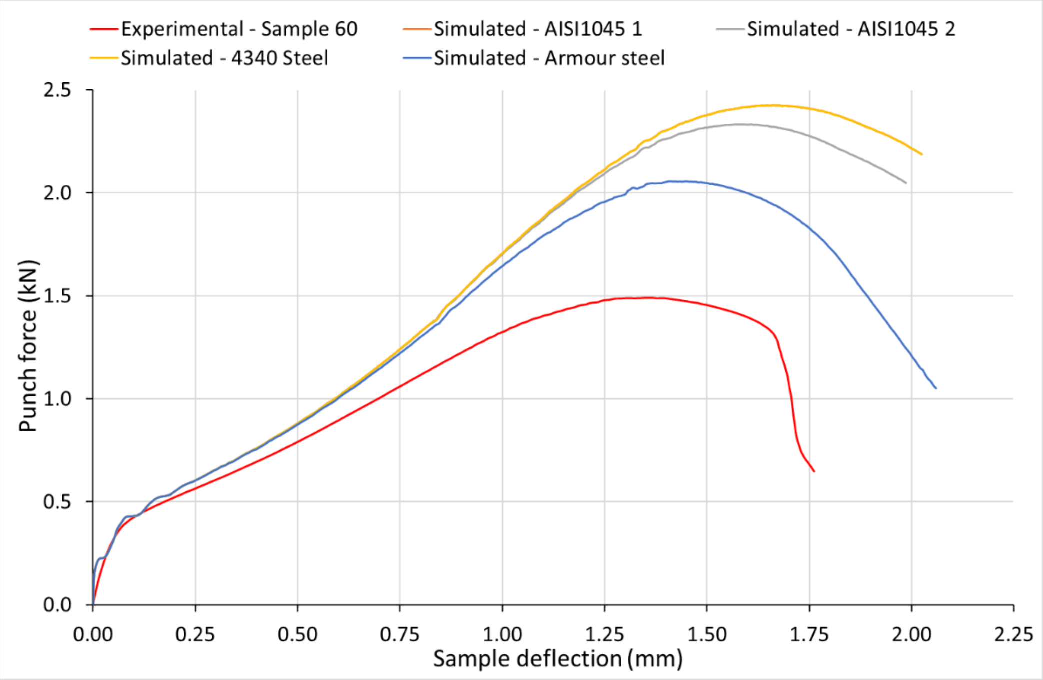

Figure 5.18: A graph displaying the force deflection curves for the selected Johnson-Cook damage models. Note that the values for AISI1045 1 and the 4340 steel are very much alike and have produced identical curves. Meaning that the 4340 cannot be seen.

From Figure 5.17 it is evident that only the armour steel values produced a result that was anywhere near sample failure. Observing the Figures shows that the other alloys did not display the levels of strain or deformation morphology indicative of necking and failure. This is most likely because they were much more ductile. The force-deflection graph in Figure 5.18 agrees with this observation. The armour steel displays a low maximum force, and exhibits a sharp decrease in applied force which is similar to that of the P91 experimental curve.

D_5 is proportional to the homologous temperature, T_H. At room temperature, T_H becomes 0 (Equation 5.5), thus invalidating any value that D_5 had [196], [208], [210], [215]. All tests analysed in this study were taken at room temperature, consequently $D_5 = 0$ for the remainder this project.

5.6 Interactions

The interactions between the sample and the small punch apparatus had the potential to dictate how it would deform, so defining them correctly was imperative.

5.6.1 Sample – Dies

The friction coefficient between both dies and the specimen was set as $\mu = 0.3$, i.e., the typical metallic interaction friction coefficient [120], [125].

5.6.2 Punch – Samples

A friction coefficient of 0.3 is often used in small punch simulations for the interaction between punch and specimen [125], [216]. But the interactions between the punch and sample is complex, as is theorised that the effect of friction changes over the course of a single test [217]. Because of this, a friction coefficient sensitivity analysis was completed. It analysed results from tests with friction coefficients ranging from $\mu = 0.1$ to $\mu = 0.57$ (sticking friction) [172].

The results of this analysis are included in Figures 5.19 and 5.20.

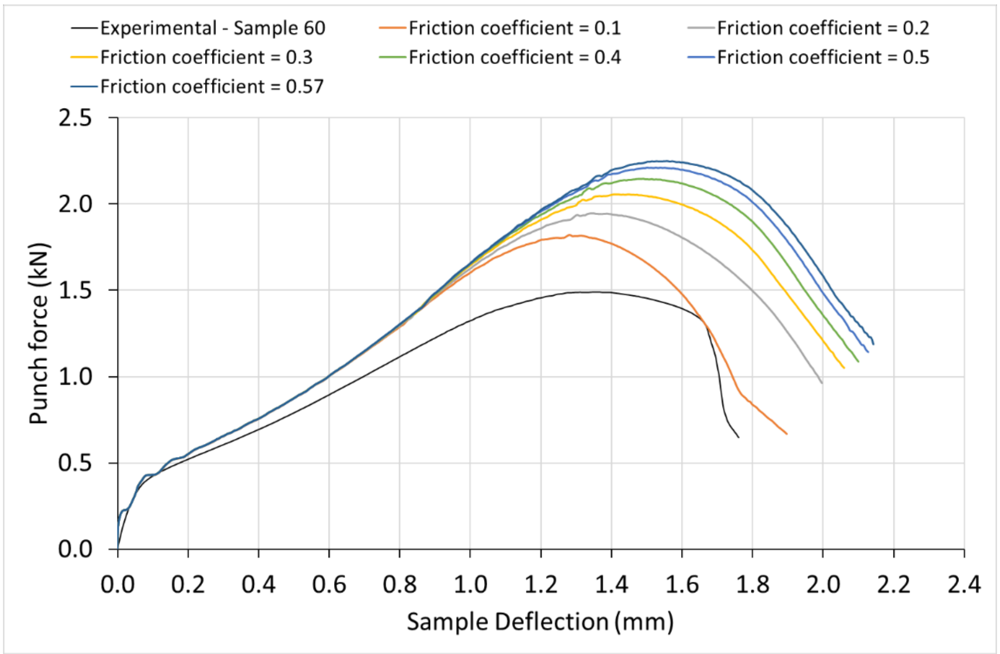

Figure 5.19: Force-deflection graphs of the simulated small punch test for a range of friction coefficients. Starting with μ = 0.1 and incrementally increasing to μ = 0.57. The frictionless test was omitted here as the failure occurred at the top of the deformation dome and so the node being recorded was deleted.

The results shown in Figure 5.20 agrees with the theory put forward by Cortellino et al. [217]. All friction coefficients display identical force-deflection behaviour until a specific point (around 0.9mm deflection in this case). This is thought to be the point in which the specimen deformation transitions from purely bending to bending and sliding. After this transition point, the sliding motion experienced is controlled by friction, thus the friction coefficient becomes relevant.

As is seen in Figure 5.20, an increase in friction coefficient lead to an increase in punch force. This change was due to the formation of stagnant or dead zones at the point of maximum deflection (illustrated in Figure 5.21).

Such a zone alters the total volume experiencing the largest amount of strain, thus changing the point in which a sample will fail. The lower friction coefficients have little-to-no such dead zone, therefore the area experiencing a large amount of strain is greater (Figure 5.19), leading to fracture at a lower maximum force.

The effect of the change in friction coefficient can also be observed in the deformed specimens (Figure 5.21).

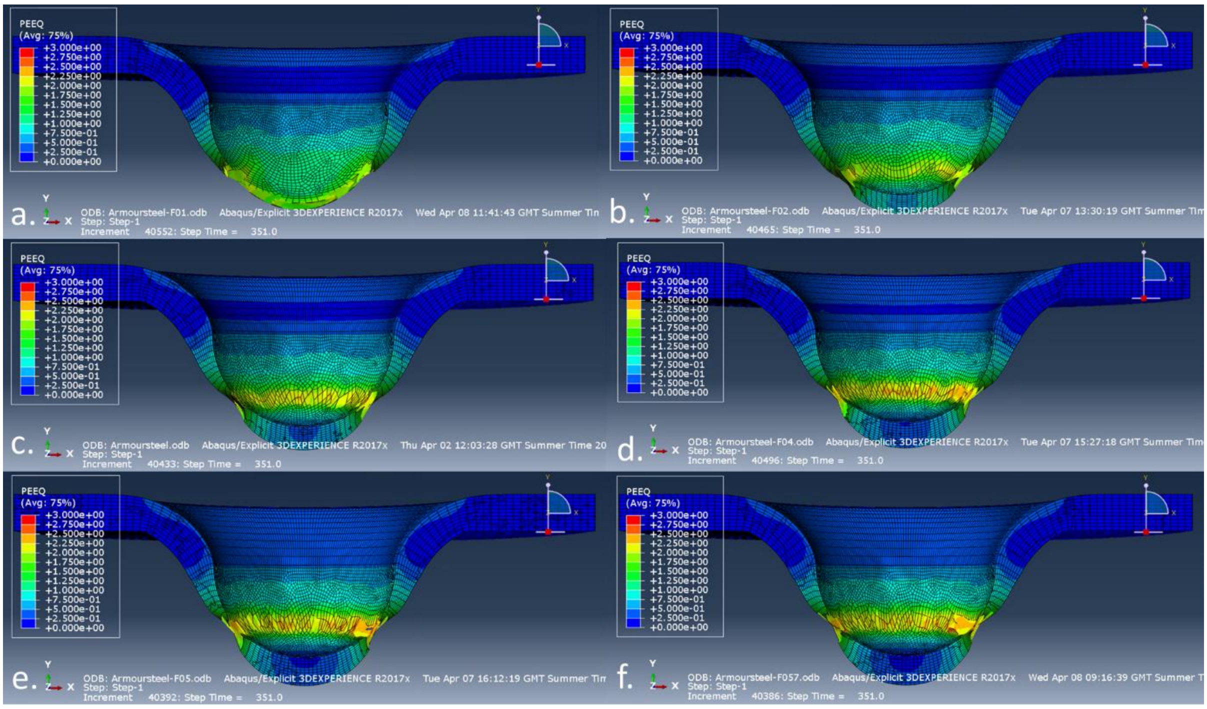

Figure 5.20: Screenshots of the deformed samples at various friction coefficients a) μ = 0.1 b) μ = 0.2 c) μ = 0.3 d) μ = 0.4 e) μ = 0.5 f) μ = 0.57. Note the formation of a dead zone at the top of the deformation dome. This changed the location of the stress concentration and thus the location of the failure. The higher friction coefficients seemed to produce a more realistic deformation shape.

To aid in the selection of a friction coefficient, the morphology of the simulated samples was compared with an experimental example (Figure 5.21). The lower friction coefficients did not create the required area of little/no strain at the top, and therefore the cap was not formed. While the lower friction coefficients could be easily discounted, the higher coefficients could not. This was due to a lack of data on the specimen thinning at the cap of the sample, both numerically and visually.

Figure 5.21: XCT scan of a fractured steel small punch test sample. Friction is essential for the formation of a cap at the top of the sample [128].

Because of the late onset of the effect of friction, it was concluded that it would not have an effect on the optimisation of the plastic behaviour. So a friction coefficient of $\mu=0.3$ was selected for the plastic analysis.

However, because friction has such a significant effect on the failure behaviour of the small punch test, it was decided that this required further investigation alongside the inverse analysis of the Johnson-Cook damage parameters (see Chapter 7)

5.7 Step

5.7.1 Implicit or explicit solver

To decide on whether the implicit (standard), or the explicit solver was appropriate for this simulation, the basic concept of each must be understood.

Implicit analysis is primarily used for static problems which are linear in nature, i.e., follow a simple f=kx pattern which can be solved in a single increment. As such, this solver is ideal for simple analysis where any changes are slow. However, Abaqus standard can come into problems where k or x are non-linear, thus requiring a solution in multiple increments. In this case the solution can become computationally expensive or unsolvable.

If this is the case, then the explicit solver may be more appropriate. The explicit solver is generally used for dynamic problems where mass and stiffness are defined. This is usually applied in simulations with large displacement rates or wave speeds. Explicit analysis can also be used in static analysis where large relative displacements, strains, and damage evolution is present, i.e., metal forming [218].

Explicit analysis also is advantageous as it is known to save on disk space, particularly in more complex static/ quasi-static applications. Because of the large relative displacements, strains, present in small punch testing and the requirement for damage evolution, the explicit solver was selected for this model.

5.7.2 Time scale

A time step of 350 seconds for a 2mm punch displacement was chosen.

5.7.3 Mass Scaling

Explicit analysis in general is computationally expensive, one way to reduce the expense is to apply mass scaling. Mass scaling is a functionality within Abaqus that can improve the computational time requirements of a quasi-static simulation. Mass scaling works by identifying elements that are computationally demanding to solve. It then alters their mass, thereby making them easier to resolve. If done correctly the CPU time required to complete a simulation can be greatly reduced without a significant sacrifice in accuracy.

To determine whether mass scaling was appropriate, the stable time increment of the model was considered. This phenomenon is defined as the time required for a stress wave to cross the smallest element dimension in the model. If there is a short time increment with a high wave speed, then it is likely that the total dynamic response will occur in a time frame that is within a few orders of magnitude of the stress wave. If this is the case, the simulation would not be quasi-static, and mass scaling may not be appropriate.

To determine whether mass scaling is appropriate, the kinetic energy of the system was compared to the internal energy. If $E_K \ll E_{Int}$ then the model could be considered quasi-static. It can be checked simply by comparing the time period studied and the displacement rate. In this case it is:

$$t = 350\ seconds$$

$$u = 0.005\ \ mm/s$$

By looking at these values it could be taken that the stress wave would be considerably faster than the 0.005 mm/s displacement rate of the model. Suggesting that the model was quasi-static and therefore mass scaling was appropriate.

5.8 Boundary conditions

The boundary conditions of the simulation define the degrees of freedom, and any displacement a particular component has over the time step. For the small punch simulation, two sets boundary conditions were required.

5.8.1 Hold dies in place

The first boundary condition held both the upper and lower dies in place. This was achieved by applying an encastre condition to the reference points on each. The encastre condition ensured that no displacement or rotation could occur.

5.8.2 Punch movement

The second boundary condition defined the punch displacement. For this, the punch was confined to movement only along the y axis with no rotation. A tubular amplitude was applied to ensure a constant displacement rate over the whole time step (table 5.2).

Table 5.2: The displacement rate defined for the punch.

Time	**Amplitude**
0	0
350	1

5.9 Field Output requests

In order to record, and properly extract the data from the simulation, output requests were required. These allow for the recording of displacement and forces, as well as stresses and strains experienced in the meshed components. Some key output requests were selected:

- STATUS – records the status of an element in a mesh with respect to the damage criterion input by the user. It is essential for element deletion.
- UT or spatial displacement – records the displacement of nodes and reference points throughout the simulation.
- RT or Reaction force – records the forces experienced on all nodes, reference points, and elements in reaction to the displacement applied.
- PEEQ or equivalent plastic strain – records the equivalent plastic strain experienced in a meshed component. This data can be extracted numerically on a node or element basis or can be presented visually through a contour map.
- MISES or Von Mises equivalent stress - records the mises equivalent stress experienced in a meshed component. This data can be extracted numerically on a node or element basis or can be presented visually through a contour map.

5.10 Job

The job was created by defining the number of CPUs required and the "precision" of the simulation. For the small punch simulation, the number of CPUs was 4 and double precision was selected.

5.11 Results

There are two main sources of results from the simulations. The first being the numerical xy data, the second being screenshots of the deformed samples. Once the simulation was complete, the whole assembly could be viewed. This allowed for the production of animations and screenshots of the meshed components changing with time.

5.11.1 XY data

The xy data was the most important source of information as it facilitated all numerical analysis. Xy data was extracted from reference points, elements, and nodes. Force-deflection curves could be drawn by extracting the punch force and displacement, and specimen deflection. This lead to estimations of UTS and proof stress. This form of data was able to be readily compared with its experimental counterpart. Thus providing a representation of the simulation accuracy. The extraction and use of this data was the basis of the inverse analysis, covered in Chapters 6 and 7.

5.11.2 Visual

Screenshots and animations were particularly useful for illustrating certain details of the small punch simulations. Effects like the necking and fracture of the samples could readily be seen along with contour maps of mises stress and plastic strain, allowing for the identification of areas of concentrated stress and strain. When applied in conjunction with the numerical results, a more complete picture of the small punch test could be realised.

5.12 Other Considerations: Machinery Compliance

The model created in this Chapter only considered the deformation of the specimen. However, in reality the dies do not stay perfectly still and the punch may not be perfectly aligned. The force needed to deform and break a sample will also cause a certain amount of elastic distortion within the whole system. This can be considered as machinery compliance. The overall effect of this compliance is not fully understood [93], [128], [133]. However, it is known that the effects of this can be somewhat negated if sample-deflection is used in place of punch-displacement (outlined in the literature review).

Although machinery compliance was not simulated, it must be considered when assessing the accuracy of results. A more developed/complex model will be required in the future to aid in determining its overall effect on small punch testing.

5.13 Summary and next steps

In this Chapter, a finite element model of the small punch test was created. Each component was then sensitivity tested and validated to ensure it was suitable for the task at hand.

Estimates for the Johnson-Cook plasticity model were calculated for P91 steel, along with a suitable substitute for the Johnson-Cook damage model parameters.

This model will now be used as the basis for the inverse analysis required to produce more accurate Johnson-Cook estimations. This analysis will help facilitate the next step in developing a viable method of predicting bulk scale behaviour from small scale test results.

6. Inverse analysis of the Johnson-Cook materials model

6.1 Introduction

After the construction of the finite element model was completed, the development of the inverse analysis phase could begin. This would entail the creation of a script that would simultaneously control the simulation and perform optimisation on the specified set of Johnson-Cook constants.

6.1.1 Chapter 5 overview

The focus of the previous Chapter (Chapter 5) was to produce a working finite element model of the small punch test, with a view to adapt it for the optimisation of material behaviour constants. This included the production of initial estimates for the metals used in this study (P91 and Eurofer97); and the application of sensitivity tests to ensure that the model was created with an appropriate balance between accuracy and efficiency.

Such as the project was designed, it was possible to take the results and model from Chapter 5 and further develop it to fit the needs for this current Chapter. The base model was taken as the initial estimate with all inverse analysis working off it.

The simulations for this study were reliant on the two Johnson-Cook models: material, and failure. These two models would need to be investigated separately, with the Johnson-Cook material model analysed in this Chapter.

6.1.2 Chapter aim and objectives

The Chapter has one main aim:

To produce a set of conservative Johnson-Cook material model constant values for both P91 and Eurofer97

This aim could be divided into three distinct objectives:

1. To produce a script that simultaneously runs the small punch simulation and performs the optimisation of the Johnson-Cook plasticity values through successive iterative simulations.
2. To predict the plastic behaviour of a small punch test by optimisation of Johnson-Cook plasticity constants.
3. To assess/validate the optimised results by means of empirical correlations.

Owing to the project driver being to create an engineering solution, ensuring the applicability of the method was vital. This included making processes time and cost efficient.

6.1.3 Basic concepts

The small punch force-deflection curve

The deformation behaviour of a ductile metal sample in a small punch test can be split into six sections, covering elastic deformation, plastic deformation, and necking to failure, as seen in Figure 6.1. The elastic portion of the force-deflection curve is defined as the beginning portion of the curve, ranging from a displacement of 0 to the elastic plastic transition force (as defined in the code of best practice, ASTM standard and round robin). The second and third regions encompass plastic deformation and membrane stretching and can be defined as ranging from the elastic-plastic transition to the point of necking/damage evolution. Regions 4 and 5 are defined as necking, crack initiation, and softening, with section 6 indicating the final fracture of the specimen [147].

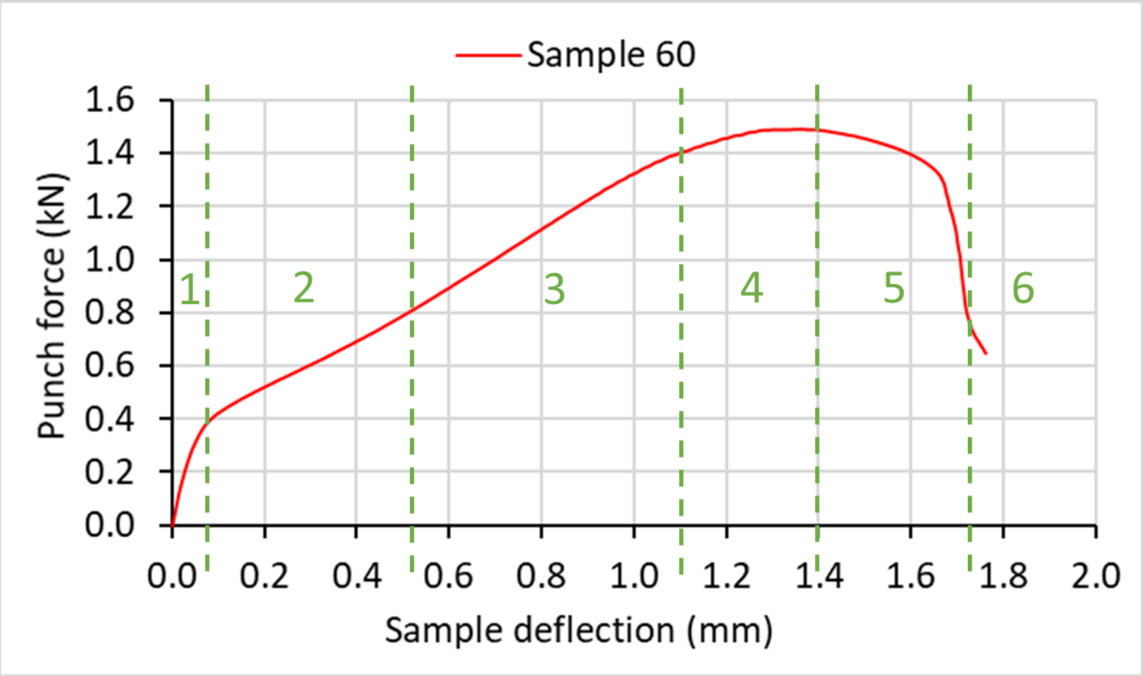

Figure 6.1: A P91 punch force – sample deflection curve The six main features have been highlighted. 1. Elastic loading 2. plastic deformation 3. membrane stretching 4. necking 5. fracture softening 6. failure.

FEA

The simulation of engineering processes involves complex mathematical models which are computationally expensive to resolve. To overcome this, the system (i.e. the small punch test), can be discretised into small elements to which the mathematical Equations can be applied. With the Equations applied to each element the system as a whole can be solved. Employing this method can greatly reduce the computational time, without sacrificing much accuracy [164]. Further information can be found in the literature review.

Inverse analysis

Inverse analysis is the optimisation of a function through iterating the input variables until a best fit is found. In engineering an inverse problem typically consists of a set of experimental data with unknown governing Equation parameters. With the assistance of simulation, it is possible to use inverse analysis to obtain the values of the governing Equation. Usually the error between simulated and experimental data is calculated and used as a goal function for the inverse process, i.e., the algorithm will change variables to reduce this error as much as possible, ideally to zero [174].

6.1.4 Chapter overview

The finite element model of the small punch test, and the initial estimates for the Johnson-Cook material model had all been created and validated (see Chapter 5). From here it was possible to move onto inverse analysis.

The first objective for this Chapter was the development of a script for the optimisation for the Johnson-Cook materials model. The script that would be run within Abaqus itself, which would perform the inverse analysis by means of an optimisation algorithm. The Abaqus scripting and customisation capabilities are written in Python, thus this was selected as the language for the optimisation. Figure 3.9 outlines the flow chart for the optimisation routine used.

Once the script was finalised, the next step was to decide on a set of viable initial values. This involved running multiple optimisation simulations using the various inputs and then analysing the results using both visual and mathematical validation techniques. This portion of the test was completed using the data from P91 small punch tests. Using this information an optimal method was devised and then applied to the Eurofer97 SP data. The Eurofer97 was treated as the unknown and, thus, was a test of the method's validity on new or even irradiated alloys.

6.2 Summary of previous results

6.2.1 Tensile data

To aid in the validation of the optimised results, tensile data was required. The data was provided by the Online Data & Information Network of the European Commission Joint Research Centre [219]. In this case only a singular room temperature curve was available (Figure 6.2). From this curve a yield stress of 510MPa and a UTS of 680MPa was obtained.

It is worth noting at this point, that at room temperature P91 steel does not exhibit large strain rate dependence, particularly at the low strain rates seen in small punch testing [220]. So a singular stress strain curve is acceptable at this stage

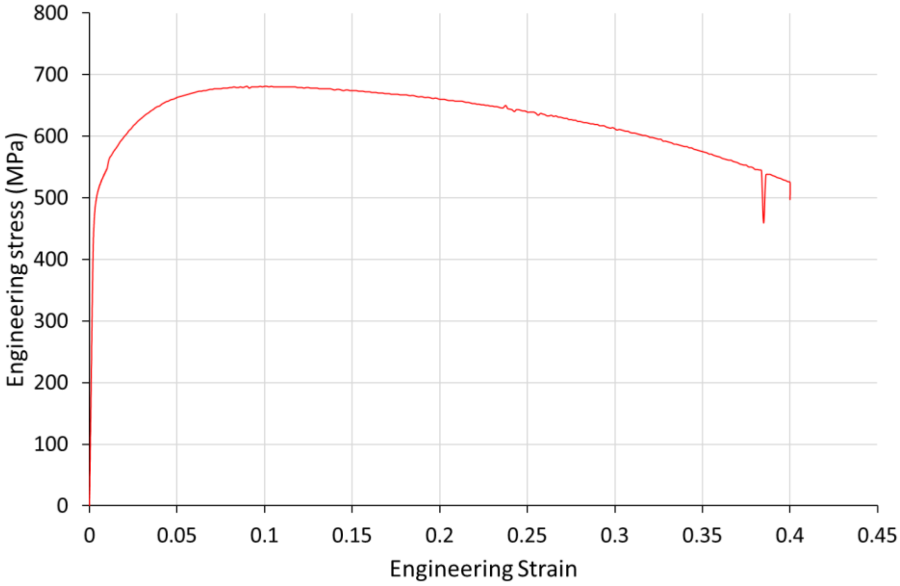

Figure 6.2: Room temperature P91 engineering stress-strain graph [219]

6.2.2 Results from Chapter 5

Four of the constants in the Johnson-Cook plasticity model (Equation 3.4), A, B, n, and m were selected for inverse analysis. C was discounted as strain rate sensitivity was not considered vital because of the low deformation rates involved in a small punch test.

To obtain the estimates, both a tensile test and small punch curves were used (see Chapter 5). The tensile test allowed for the estimation of all constants, while the small punch curves could only be used for an estimation of A (σ_y, or 0.85*UTS).

Thus, the results from tensile Johnson-Cook plasticity estimations were:

- A = 510 MPa, σ_y, or 0.85*UTS
- B = 666 MPa
- n = 0.459
- m = 1.615
- T_m = 1420 ˚C
- T_T = 25 ˚C

The value for A could be interpreted as either the yield or proof stress. Based on the work completed in Chapter 4 it was evident that using the small punch curve itself for these values was possible. However, due to the variability of these values and the importance of A in this model it was decided that several different methods should be used. Thus, A was tested as 510 MPa, proof/yield stress (σ_y), or 0.85*UTS.

6.3 Inverse analysis

6.3.1 Why inverse analysis

The use of inverse analysis is common within the field of finite element modelling, and for the development of testing techniques in particular [79], [187], [221]. Therefore, it was a natural step to apply such techniques to this project. It was thought that the use of inverse analysis and FEM in conjunction with the small punch test would improve the overall accuracy and viability of the testing method in general.

6.3.2 Application in Abaqus and Python

The use of Abaqus with Python is widespread, with the main use case for the python being a bridge between Abaqus and MATLAB. However, Python's own mathematical capabilities meant that it was possible to use it along with Abaqus without the need for a third party software, i.e., MATLAB.

6.3.3 Python optimisation – SciPy. optimize. minimize

Python runs as a single base kernel with optional add-ons that can be introduced as needed. One such add-on is SciPy. SciPy is an open source 'Python-based ecosystem' designed for science, mathematics and engineering and when used with NumPy, it proves to be a powerful tool for such applications [197].

Within the SciPy environment there is a module, *SciPy. optimize*, which contains a series of commonly used optimisation algorithms. Of the ones available within the module, *scipy.optimize.minimize*, contained various minimisation functions which would be ideal for the application in question [197].

As described in the literature review, the Nelder and Mead (or Simplex) algorithm is a direct search method for multidimensional unconstrained optimisation [177], [180]. The Nelder-Mead method has been proved to be robust and computationally compact. However, as with most direct search methods, there is a possibility of the algorithm finding a false minimum. So, such methods must rely on good starting estimates [177]. The simplex method is commonly used in engineering and has proved itself a valuable tool for simulation and function optimisation. The lack of boundary requirements in the Nelder-Mead algorithm may also prove beneficial when working with unknown/irradiated materials where properties may be vastly different to their original counterparts.

The Nelder-Mead method is also appropriate here as small punch testing has inherent error/variation in experimental data, so a direct search method is apt [176]

6.3.4 The Error Function

The application of the Nelder-Mead method required the use of an error or objective function. For this project it was appropriate to use a function that measured the absolute difference between an experimental force-deflection curve and its simulated counterpart. The error function, r, was given as:

$$r = \sum (simulated\ data - experimental\ data)^2$$

Equation 6.5

6.3.5 Abaqus scripting functionality

As stated above, Python can be used with Abaqus to perform the inverse analysis. Allowing for the program to be run and the inverse analysis to be completed within the same script.

6.4 Construction of the inverse analysis code

Once the base model was created, the optimisation script could be written. By using the scripting functionality, it was possible to write a script that will both run a simulation and perform the inverse analysis. To do this the steps that needed completing were outlined:

1. Input the current estimate of the Johnson-Cook constants
2. Run the simulation and wait for completion
3. Collect the force-deflection data for the current estimates
4. Put this data into the error function and produce a new set of estimates
5. Change the input to the new set of estimates
6. Rerun the simulation

These 6 steps are repeated until the error function reaches a minimum.

To create the basic script, the Abaqus macro manager was used. The macro manager would record every action carried out by the user and save it to a macro. If done correctly this macro can then be used as a script. Once the macro was extracted, it was altered to allow for the optimisation loop. Relevant sections of the script can be found in Appendix 2.

The main body was focused on running the simulation. For the plastic tests a punch displacement of up to 1mm over a total step time of 200 seconds was chosen. Because of the computationally expensive nature of explicit analysis, mass scaling was also applied at this point (exact values included in Chapter 3, Section 3.4.6).

Once the simulation had completed, the next step is to extract the force displacement/deflection data. Force and displacement data were extracted from a reference point placed in the punch (Figure 6.3a). Sample deflection was recorded from a node on the bottom surface of the sample, directly under the punch head (Figure 6.3b).

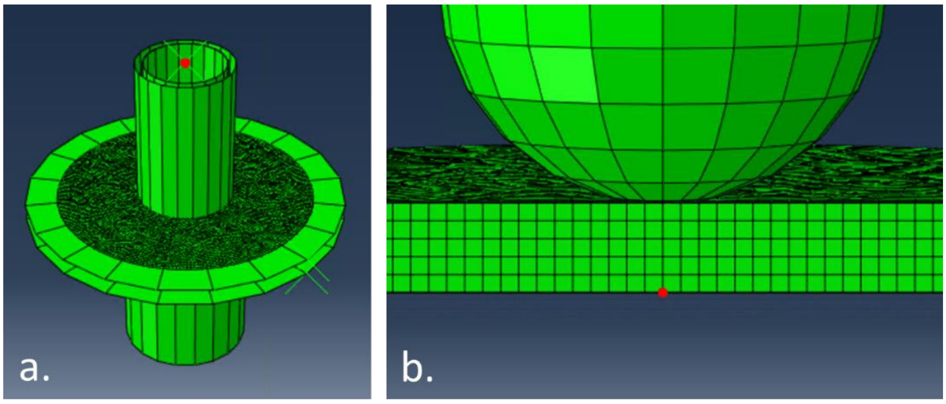

Figure 6.3: Screenshots of the Abaqus results file with the nodes selected for xy data recording. a) the point on the punch records the reaction force and spatial displacement, whereas in b) the point on the sample records spatial displacement only.

6.5 Tests with P91 data

6.5.1 Displacement

As with the choice of starting Johnson-Cook values, different sample deflection values were also selected for testing. The first measuring a deflection from 0mm to 1mm and the second test was from a deflection of 0mm to 0.552mm (i.e. the point of onset of plastic instability as defined in Table 2.3 [128], [157]).

The 0-1mm deflection tests were decided from a visual evaluation of the force-deflection curves. 1mm was the point at which most curves started to turn over, thus indicating necking and material damage. This was obviously not the most rigorous of selection methods, but it seemed an appropriate starting point.

After consulting the code of best practice, ASTM standard and round robin a sample deflection of 0-0.552mm was also selected for analysis. This was due to the general consensus that a sample deflection of 0.552mm could be taken as the point of onset of plastic instability for most ductile steels [128], [133].

As discussed in Chapter 5 (section 5.6.2) there comes a point along the force deflection curve where the friction between the punch and sample becomes important. This is thought to be the point in which deformation moves from solely bending to bending + sliding, thus any friction will start to have a tangible effect. Because of this effect, a third sample deflection was selected for analysis. This would be the point in which the force deflection curves for different friction coefficients start to deviate from one another. Figure 6.4 displays this effect using the starting Johnson-Cook materials and failure constants, with a P91 experimental curve for comparison. A series of simulations were completed using a range of friction coefficients from $\mu = 0.1$ to $\mu = 0.57$. The point in which the graphs deviate from each other was then identified as a deflection of 0.865mm. This was used as the sample deflection in the final set of optimisation tests.

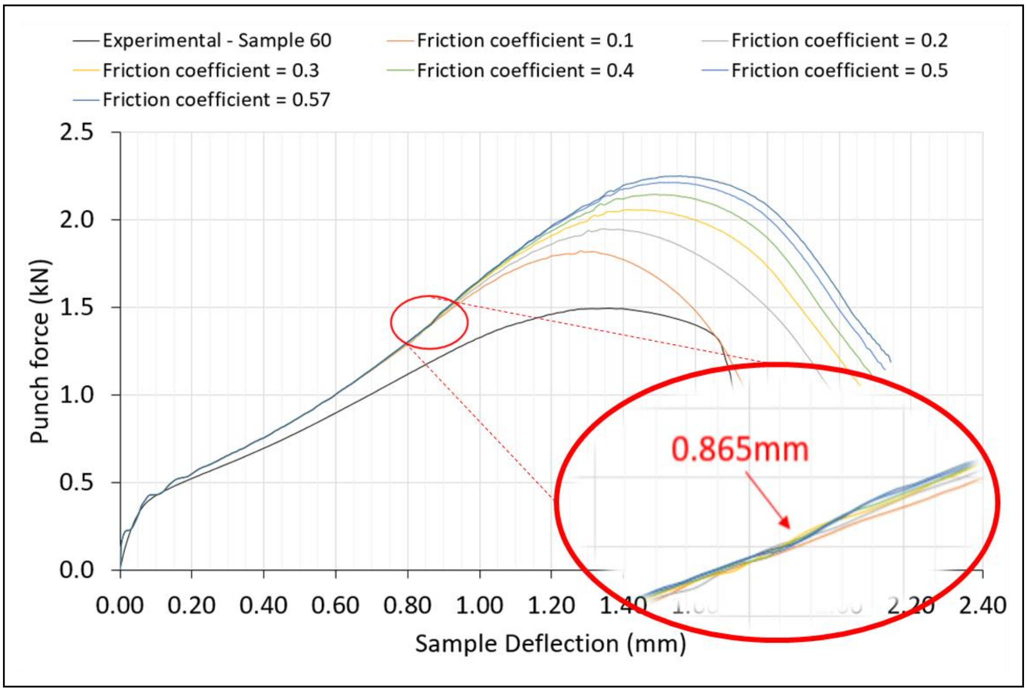

Figure 6.4: Force-deflection graph for a range of friction coefficients with a P91 experimental curve for comparison. This identifying the point in which friction starts to have an effect. Indicating the transition from bending to bending + sliding.

All deflections were subject to a range of tests and the results compared to determine the most effective method.

6.5.2 Time

The time of 200 seconds for a 1mm punch displacement was chosen on the basis of several experimental tests taking around 350 seconds for a displacement of 1.75mm. So, it was reasonable to assign such a displacement rate for the simulated tests.

For the 0.6mm displacement tests 120 seconds was chosen.

Both displacements were applied with a tubular amplitude.

6.5.3 Mesh

For the plastic optimisation, the mesh was kept the same as during the initial development tests.

6.5.4 Mass scaling

Due to the computationally expensive nature of a 3D explicit model, mass scaling was vital. This allowed for the hundreds of iterations required for the optimisation to be completed in hours rather than days/weeks. If necessary, additional simulations could be run using optimised constants and a less severe level of mass scaling to produce a cleaner curve i.e. one with less vibration during the initial/elastic loading. As can be seen in Figure 6.5, this phenomenon was limited to the very start of the force-deflection curve.

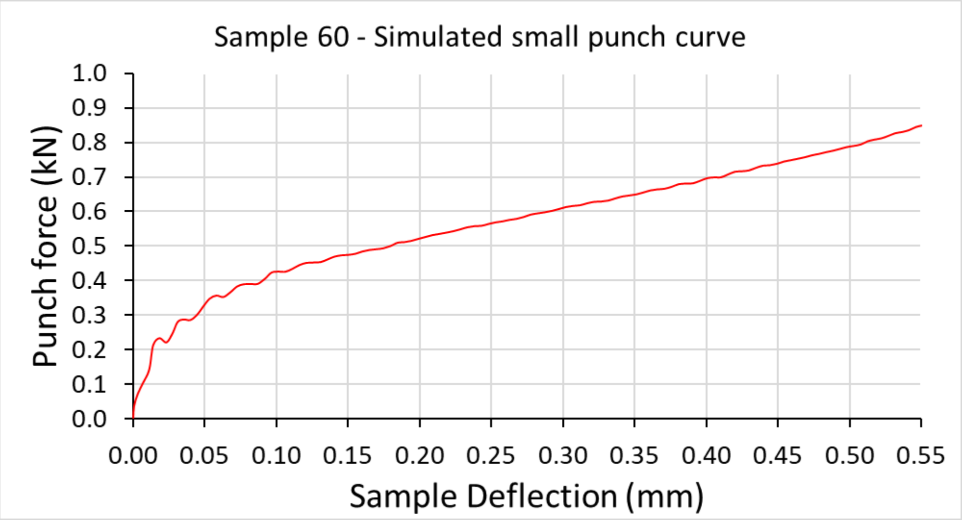

Figure 6.5: A graph showing the beginning portion of the simulated force-deflection curve for P91 sample 60. Note the vibration at the very start of the curve. This is a result of the mass scaling applied to the model.

6.5.5 Deflection vs displacement

Throughout the initial research and examination of the draft standard it became clear that both punch displacement and sample deflection were being used in equal measure. This allowed for the choice of either, depending on available data. For this project, sample deflection was selected for use. By selecting sample deflection any effects from machinery compliance in experimental data would be greatly reduced. This was especially important as neither the die or punch could deform in the simulations, thus selecting an experimental curve with reduced compliance would be beneficial.

6.5.6 Outputs

The as previously stated the outputs selected for analysis were punch force, punch displacement, and sample deflection. They were saved in an Abaqus report file. The current Johnson-Cook estimations were also saved as a text file. All output files were saved with their respective test number for future reference.

6.5.7 Starting Johnson-Cook values

Two methods were devised for this section. The first was to use the P91 Yield stress given by the tensile curve and keep that as a singular value for A i.e. it would not be changed. The values for B, n, and m were kept as the values estimated in Chapter 5 and would be varied using the optimisation script.

The second method was based on using as many values from the small punch test as possible. With the available data it was possible to ascertain an estimate of the proof stress for each curve (see Chapter 4). This value was then used as A. The values for B, n, and m were selected as the values estimated in Chapter 5. All constants (A, B, n, and m) would be varied using the optimisation script.

While this project only achieved the estimation of A from a small punch curve. It was considered to be a starting point of further work which could see the other Johnson-Cook plasticity constants estimated in a similar manner.

6.6 Overview of P91 Tests

From the small punch data for P91 provided, a total of 10 room temperature curves were available for use in the plasticity optimisation. A general overview of the optimisation tests undertaken can be seen below.

The initial Johnson-Cook estimates are given in Table 6.1.

Table 6.1: The initial Johnson-Cook plasticity estimations. The full derivation can be found in Chapter 5.

	A	**B**	**n**	**m**
Initial estimate	510MPa, or $\sigma_{0.2}$,or 0.85*UTS	666.4	0.459	1.615

The alternative estimates for A are included in Table 6.2.

*Table 6.2: The proof stress, UTS and 0.85*UTS data for the P91 samples. The proof stress and 0.85*UTS values will be used as values for A in the Johnson-Cook model starting estimations*

Sample	Proof Stress Estimation (MPa)	UTS Estimation (MPa)	0.85*UTS (MPa)
60	736.44	648.42	551.16
62	742.56	624.46	530.79
63	854.76	682.29	579.94
64	858.84	688.90	585.57
65	801.72	654.11	556.00
67	930.24	764.77	650.05
68	891.48	754.25	641.11

The complete set of simulations run is included in Table 6.3. This series of tests was formed on an iterative process starting with an initial method (method a) and was improved upon with each new set.

Table 6.3: The complete set of simulations run with each sample. These were labelled methods a-f

Method	Start (mm)	End (mm)	Initial estimate for A (MPa)	Comments
a	0.0	1.0	510	Kept A constant and varied B, n, and m
b	0.0	1.0	σ_y	Varied all constants
c	0.0	0.552	510	Kept A constant and varied B, n, and m
d	0.0	0.552	σ_y	Varied all constants
e	u_a	0.552	σ_y	Varied all constants
f	u_a	0.552	0.85* UTS	Varied all constants
g	u_a	0.865	0.85*UTS	Varied all constants

6.7 P91 results

6.7.1 Change in constants over an optimisation

To aid in providing a full understanding of the optimisation, the results from each stage of the optimisation were recorded. Thus, allowing the monitoring of each parameter as it changed with each simulation. An example of this is shown in Figures 6.6 and 6.7.

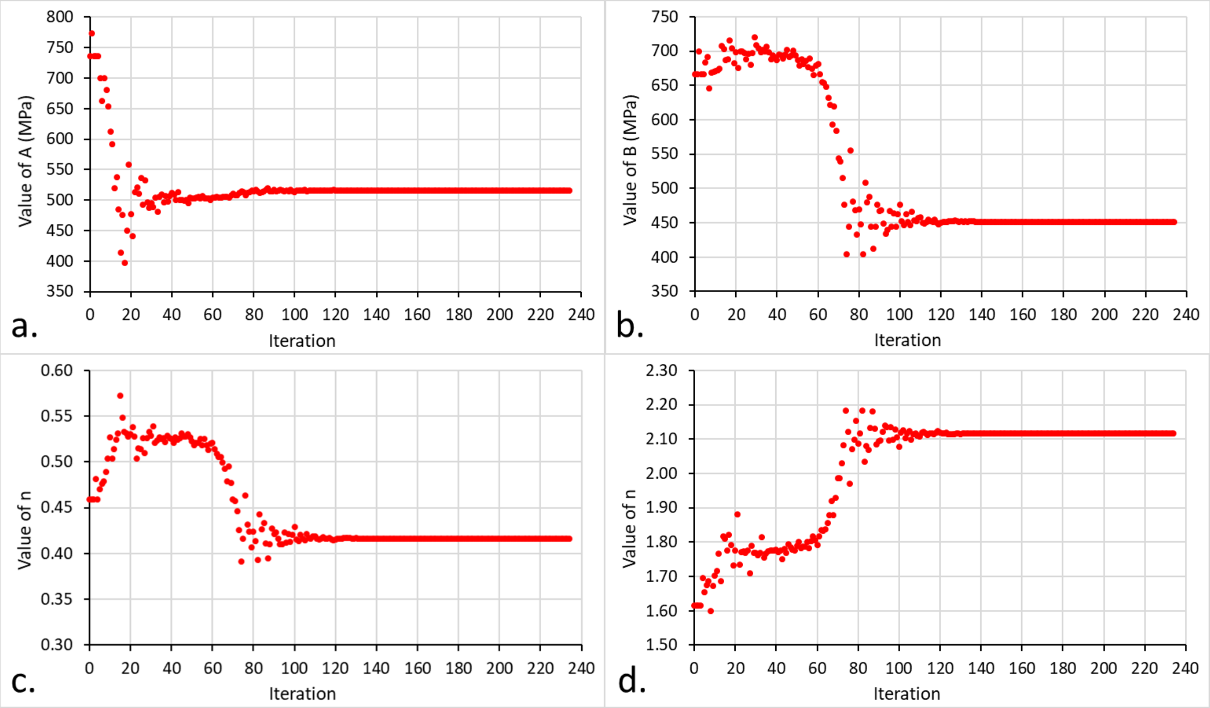

Figure 6.6: Optimisation progression data of sample 60. Where: a. Change in A over a single optimisation; b. change in B over a single optimisation: c. change in n over a single optimisation; d. change in m over a single optimisation

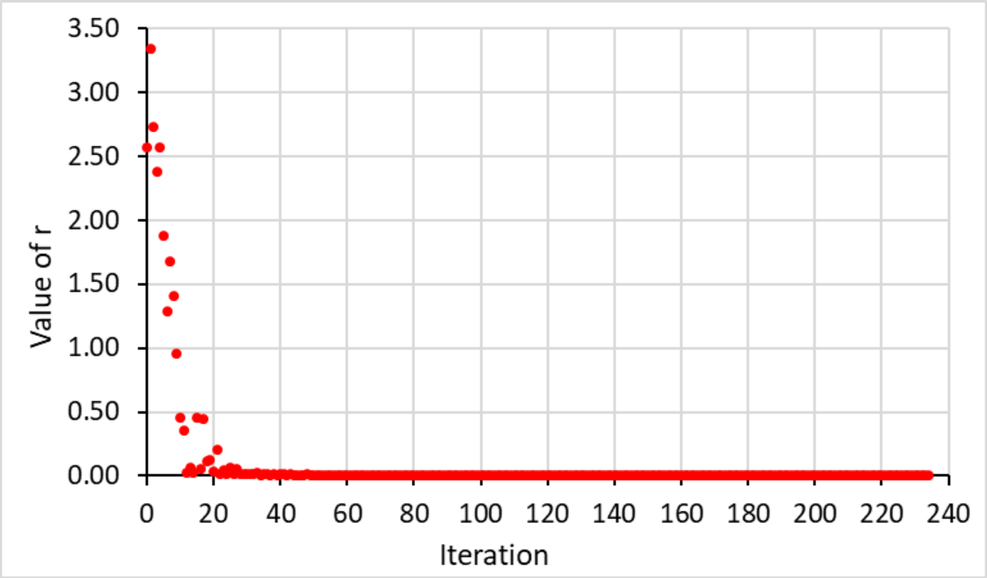

Figure 6.7: Sample 60, change in r over a single optimisation

6.7.2 Tabulated data

The results from each series of inverse analysis can be seen in Tables 6.4-6.10. These results take the form of the optimised Johnson-Cook parameters along with the final r value for each. Note: some particular optimisations failed to complete due to the algorithm attempting to input negative Johnson-Cook constants. In these cases, they have been greyed out to signify the failure to complete.

Table 6.4: Table of the optimised Johnson-Cook Values for P91. Deflection was set to a maximum of 1mm and the value for A was set to 510MPa. The value of A was excluded from the optimisation routine and thus stayed at 510MPa

	A (MPa)	B (MPa)	n	m	r
60	510.00	304.97	0.27	1.80	0.0108
61	510.00	303.86	0.22	1.33	0.0098
62	510.00	456.14	0.55	1.77	0.0227
63	510.00	309.98	0.21	2.41	0.0313
64	510.00	335.78	0.21	3.58	0.0282
65	510.00	265.70	0.20	1.64	0.0153
66	510.00	267.05	0.16	1.86	0.0254
67					
68					
69					
Standard deviation	-	59.90	0.12	0.69	0.0079

Table 6.5: Table of the optimised Johnson-Cook Values for P91. Deflection was set to a maximum of 0.552mm and the value for A was set to 510MPa. The value of A was excluded from the optimisation routine and thus stayed at 510MPa

	A (MPa)	B (MPa)	n	m	r
60	510.00	593.68	0.49	1.66	0.0067
61	510.00	336.01	0.25	2.95	0.0045
62	510.00	530.99	0.54	1.70	0.0181
63	510.00	675.55	0.46	1.67	0.0385
64	510.00	688.53	0.45	1.62	0.0317
65	510.00	380.90	0.32	2.86	0.0157
66	510.00	460.29	0.33	2.20	0.0269
67	510.00	780.39	0.34	1.75	0.0359
68	510.00	418.74	0.15	3.57	0.0147
69	510.00	763.02	0.43	1.66	0.0072
Standard deviation	-	152.87	0.11	0.67	0.0119

Table 6.6: Table of the optimised Johnson-Cook Values for P91. Deflection was set to a maximum of 1mm and the value for A was set as the σ_y calculated from the standard. Unlike the previous tests, the value of A was included in the optimisation routine

	A (MPa)	B (MPa)	n	m	r
60	603.43	477.91	0.96	1.75	0.0136
61	597.20	320.14	0.57	0.89	0.0104
62	550.74	422.17	0.69	0.65	0.0196
63	612.85	325.93	0.61	1.28	0.0352
64	630.84	419.24	0.78	1.54	0.0336
65	622.35	362.51	0.96	0.37	0.0176
66					
67					
68					
69					
Standard deviation	25.86	56.77	0.16	0.49	0.0095

Table 6.7: Table of the optimised Johnson-Cook Values for P91. Deflection was set to a maximum of 0.552mm and the value for A was set as the σ_y calculated from the standard. Unlike the previous tests, the value of A was included in the optimisation routine

	A (MPa)	B (MPa)	n	m	r
60	516.19	451.11	0.42	2.12	0.0061
61	577.72	471.41	0.59	1.37	0.0040
62	473.88	703.69	0.54	1.80	0.0161
63	536.12	703.53	0.54	1.79	0.0387
64	544.82	698.93	0.54	1.80	0.0322
65	515.59	694.34	0.54	1.78	0.0191
66	537.16	696.66	0.54	1.80	0.0280
67	641.21	682.56	0.53	1.78	0.0279
68	622.53	356.78	0.28	2.07	0.0153
69	706.28	186.03	0.36	2.90	0.0033
Standard Deviation	66.58	176.90	0.09	0.38	0.0118

Table 6.8: Table of the optimised Johnson-Cook Values for P91. Deflection was set to a maximum of 0.552mm. The deflection ranges for the optimisation started at u_a and ended at 0.552mm. The value for A was set as the σ_y calculated from the standard. The value of A was included in the optimisation routine.

	A (MPa)	B (MPa)	n	m	r
60	554.54	623.69	0.67	1.73	0.0006
61	583.49	454.98	0.60	1.18	0.0019
62	478.11	695.87	0.54	1.79	0.0017
63	539.89	695.88	0.54	1.80	0.0034
64	548.49	698.76	0.54	1.79	0.0037
65	515.35	696.93	0.53	1.80	0.0071
66	574.94	514.94	0.55	1.26	0.0006
67	641.21	685.42	0.53	1.78	0.0145
68	625.72	681.85	0.51	1.68	0.0139
69	730.33	318.24	0.76	1.87	0.0025
Standard Deviation	68.03	126.22	0.08	0.23	0.0049

Table 6.9: Table of the optimised Johnson-Cook Values for P91. Deflection was set to a maximum of 0.552mm. The deflection ranges for the optimisation started at u_a and ended at 0.552mm. The value for A was set as the 0.85 UTS calculated from the standard. The value of A was included in the optimisation routine.*

	A (MPa)	B (MPa)	n	m	r
60	545.90	535.93	0.58	1.58	0.0007
62	498.16	617.10	0.56	1.71	0.0009
63	565.18	576.10	0.55	1.43	0.0036
64	566.85	578.74	0.53	1.56	0.0029
65	570.43	452.90	0.58	1.68	0.0007
67	690.81	474.68	0.57	1.39	0.0105
68	698.17	392.96	0.58	1.32	0.0068
Standard Deviation	69.46	74.60	0.02	0.14	0.0034

Table 6.10: Table of the optimised Johnson-Cook Values for P91. Deflection was set to a maximum of 0.865mm. The deflection ranges for the optimisation started at u_a and ended at 0.685mm. The value for A was set as the 0.85 UTS calculated from the standard. The value of A was included in the optimisation routine.*

	A (MPa)	B (MPa)	n	m	r
60	583.64	356.16	0.64	1.56	0.0041
62	525.06	365.03	0.48	1.35	0.0046
63	617.47	305.81	0.59	1.83	0.0083
64	627.35	380.68	0.69	1.54	0.0101
65	608.47	247.60	0.62	1.80	0.0037
67					
68					
Standard Deviation	36.66	48.68	0.07	0.18	0.0026

6.8 P91 discussion

The results from the P91 test can now be discussed.

6.8.1 Overview

The tests that included the 0.85*UTS as the estimates for A did could not include samples 61, 66, or 69. This was because the curves did not reach F_m, so calculating the UTS values was not possible. However, as there was no explanation given to the premature failure, it was decided that keeping them for the other tests was practical. This was done to see if it was possible to gain usable optimisation results from incomplete curves. A thing that may prove useful when dealing with irradiated materials (which tend to be more brittle and will therefore fail earlier than their unirradiated counterparts).

Another feature in the above results is the presence of some optimisations that failed, and so are greyed out in the tables. This was due to the algorithm attempting to input a negative Johnson-Cook constant value. This is not possible and so caused an error in Abaqus and thus the termination of that particular optimisation. This highlights one of the main weaknesses of the Nelder-Mead algorithm, and that is the inability to apply boundaries. While in some cases this can be beneficial, here it can cause premature termination. A solution to this will be discussed further on.

To show the progress made by the iterative method development the results from sample 60 were collated in Table 6.11. Here it can be seen that the overall r value decreases over the progressive tests, indicating that the results were more accurate with subsequent tests.

Once the value of A was included in the optimisation process, its value increased by around 40MPa. The main cause of this was the change from starting at 0mm deflection, to U_a (around 0.5mm deflection). The values for B were variable, with the change from 1mm deflection to 0.552mm deflection causing a significant increase in values. The values for n also were variable, but with noticeable increases with the addition of varying A, and deflection ranges. The m values varied with no real pattern discernible with the changes applied to the method.

Table 6.11 example comparison of the different methods – sample 60

Optimisation variables	A (MPa)	B (MPa)	n	m	r
1mm	510.00	304.97	0.27	1.80	0.0108
1mm (A= σ_y)	603.43	477.91	0.96	1.75	0.0136
0.552mm	510.00	593.68	0.49	1.66	0.0067
0.552mm (A = σ_y)	516.19	451.11	0.42	2.12	0.0061
u_a - 0.552 mm (A = σ_y)	554.54	623.69	0.67	1.73	0.0006
u_a - 0.552 mm (A = 0.85*UTS)	545.90	535.93	0.58	1.58	0.0007
u_a - 0.865 mm (A = 0.85*UTS)	583.64	356.16	0.64	1.56	0.0041

Another way of analysing the changes in methodology is to examine the force-deflection graphs produced with each optimisation. The graphs for sample 60 can be seen in Figure 6.9. A visual inspection of the graphs shows that the variation seen in the numbers does not have a large effect on the shape of the curve (Figure 6.8). Though it is possible to see the accuracy increase with subsequent iterations, as reflected in the r values above (Table 6.11).

While methods c-f numerically produced fits with lower r values, inspection of the force-deflection graphs in Figure 6.9 shows a marked deviation from the experimental curve from a deflection of

0.552mm onward, whereas methods a and b fit right up to the 1mm mark. This would indicate that the 1mm deflection tests produced a better fit over a greater portion of the curve. However, the sensitivity tests completed in Chapter 5 (Section 5.6) showed that the contact friction between punch and specimen starts to become relevant before 1mm of deflection. Because of this, a third and final deflection was tested, 0.865mm. This was taken from the sensitivity tests as the point in which deformation switches from predominately bending to bending and sliding, thus indicating the end of the purely plastic region. This method produced an r value that was in the middle of the two displacement values, at the lower end in fact (Table 6.10). And the increase in deflection led to a better fit over the range of the plastic section (Figure 6.8).

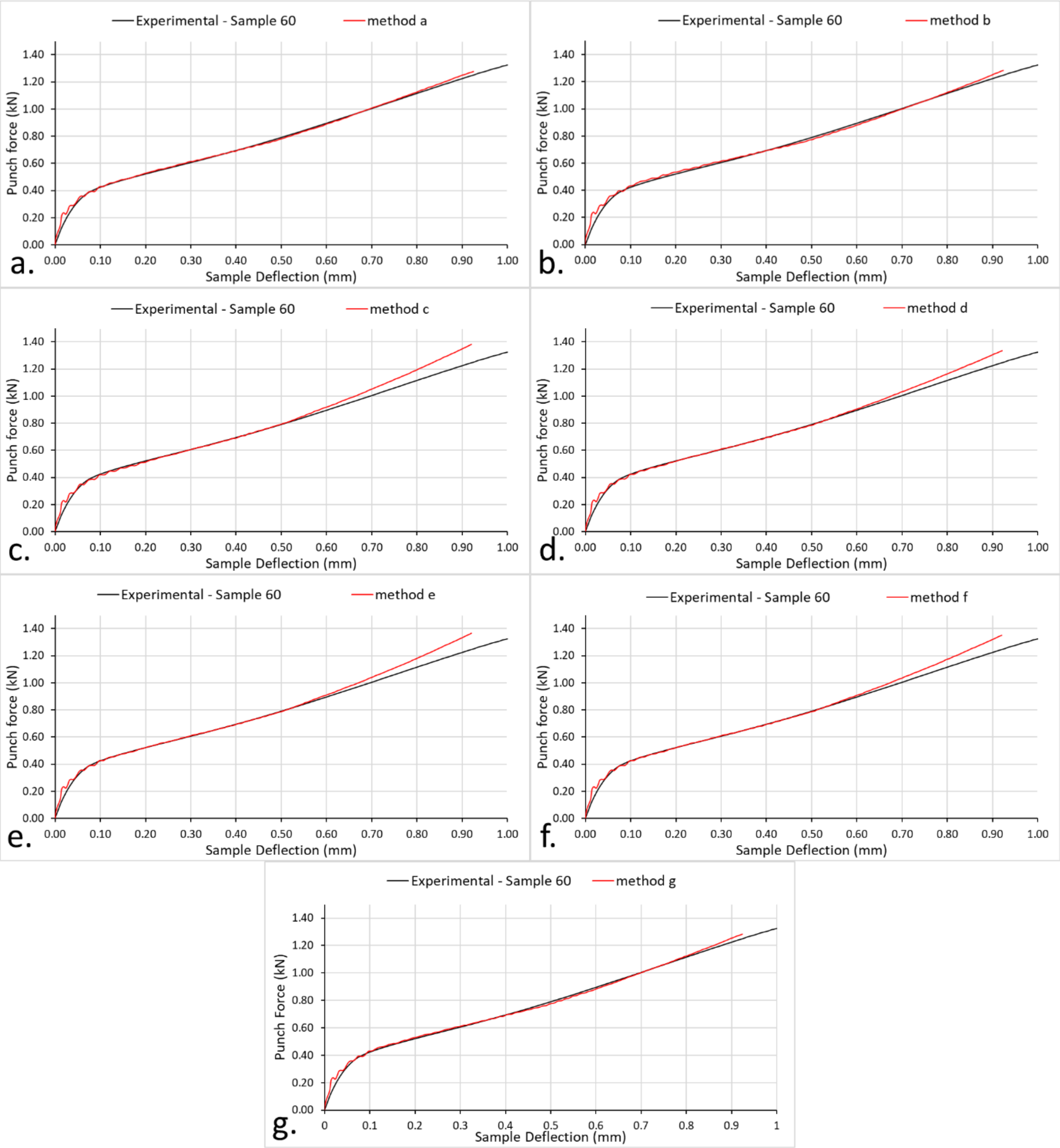

Figure 6.8: Force-deflection graphs for sample 60 showing the optimised curve for each method (a-g)

6.8.2 Empirical method for validation of optimised results

While it is apparent that the accuracy of each iteration of the inverse methodology has been increased, this does not provide a quantitative measure of whether these values produce conservative results on the bulk scale. And, therefore, cannot provide the necessary quality assurance.

According to the Handbook of Software Quality Assurance, quality assurance is a set of procedures to be carried out in a systematic manner that independently assess the quality of any simulated results produced [222], [223]. So, for the work completed in this thesis to be considered of an acceptable level, a set of quality assurance measures must be completed. This was accomplished using the Considére criterion.

As described in the literature survey (section 2.3.1), the Considére criterion can be used to predict the onset of necking. Each set of optimised Johnson-Cook plasticity results could be assessed this way. By plotting the Johnson-Cook Equation with respect to strain, a pseudo stress-strain curve is drawn. The differential of this is then plotted on the same axes, with the crossover point of both curves being an approximation for UTS. If this point is less than that of the experimental equivalent then it can be taken that the results are conservative, thus providing a level of assurance. Such a method can be used as validation here as it is completely separate from previous methods for estimating UTS, thus ensuring no bias.

For the P91 results an experimental value for the UTS of 680MPa measured from a tensile curve was selected.

The results from sample 60 can be seen in Table 6.12, and Figures 6.9 and 6.10.

When plotting the results of the UTS estimations, upper and lower bounds were created using two standard deviations each way. So, it can be taken, with 95% confidence, that any other results will fall between the two bounds.

Table 6.12: The Considére criterion results for sample 60 including each optimisation method

Method	Optimisation variables	UTS – true (MPa)	True strain	Engineering strain	UTS – engineering (MPa)
a	0 - 1mm (A = 510MPa)	590.42	0.058	0.06	557.15
b	0 - 1mm (A = σ_y)	533.75	0.001	0.00	533.22
c	0 - 0.552mm (A = 510MPa)	661.77	0.156	0.17	566.18
d	0 - 0.552mm (A = σ_y)	649.35	0.106	0.11	584.04
e	u_a - 0.552 mm (A = σ_y)	665.17	0.172	0.19	560.06
f	u_a - 0.552 mm (A = 0.85*UTS)	623.63	0.137	0.15	543.79
g	u_a - 0.865 mm (A = 0.85*UTS)	554.20	0.056	0.06	524.02

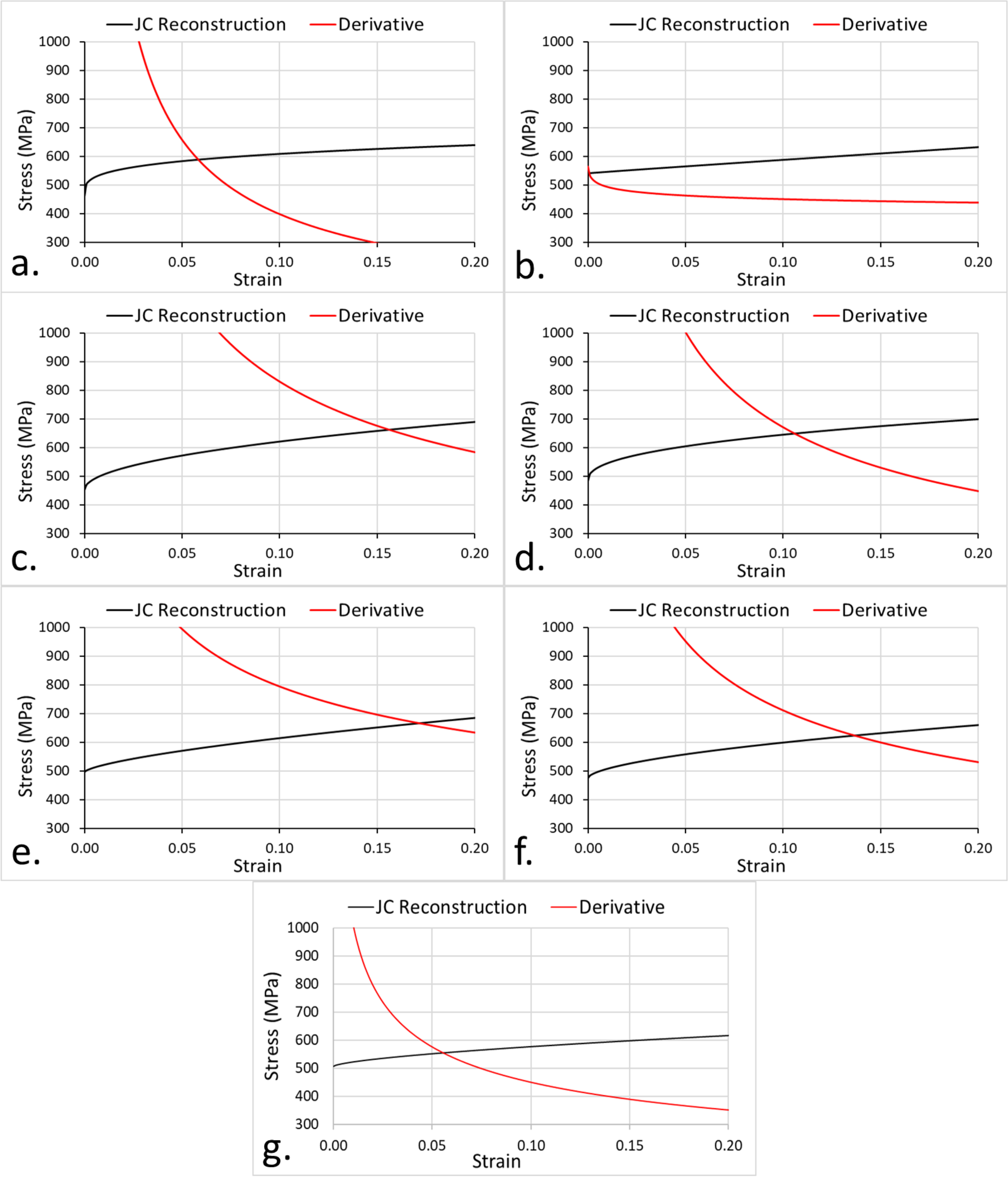

Figure 6.9: Stress-strain and graphs for Sample 60 showing each method a-f. Each graph shows the derivative of the stress curve. The point in which the two curves cross are the true stress and strain values.

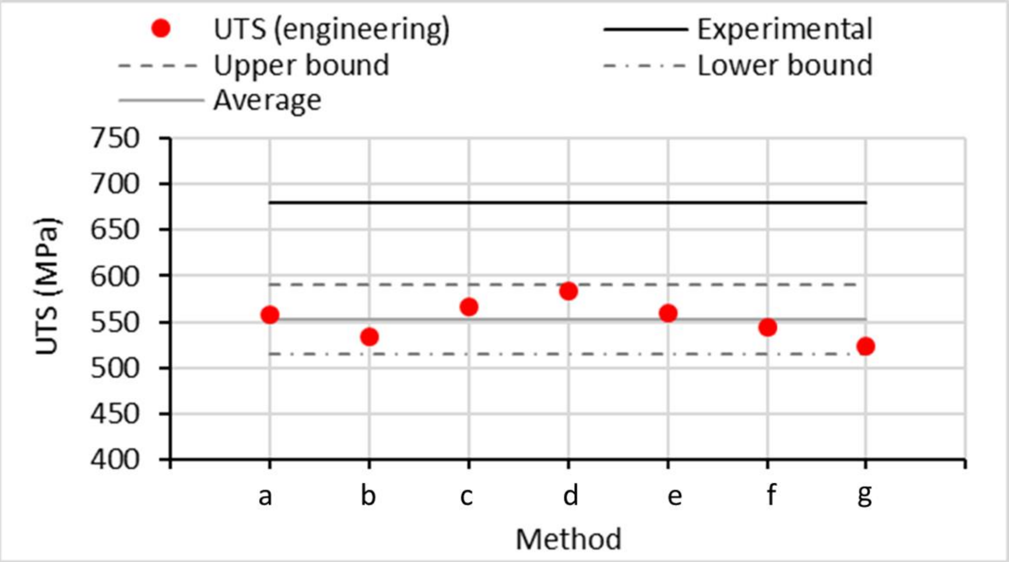

Figure 6.10: Sample 60 UTS estimations from optimised Johnson-Cook parameters. Methods a-f.

All of the given methods produced different values for the UTS estimation. As an example, results for sample 60 for each method were plotted in Figure 6.10. In this instance the results were relatively consistent across each iteration. This is not the case for every sample, where larger spreads and some over estimations are present. So, for a proper examination each method will be shown, rather than sample-by-sample. These can be seen in Figures 6.11-6.17.

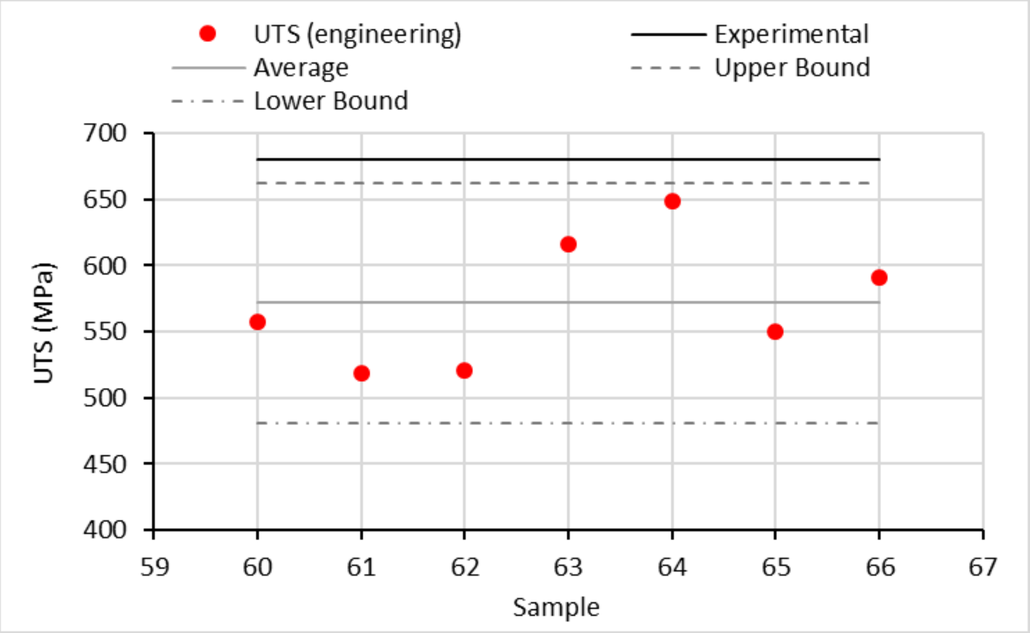

*Figure 6.11: Method a, UTS estimations from optimised Johnson-Cook parameters. The upper and lower bounds are calculated using 2*standard deviation. The standard deviation for method a is 45.19*

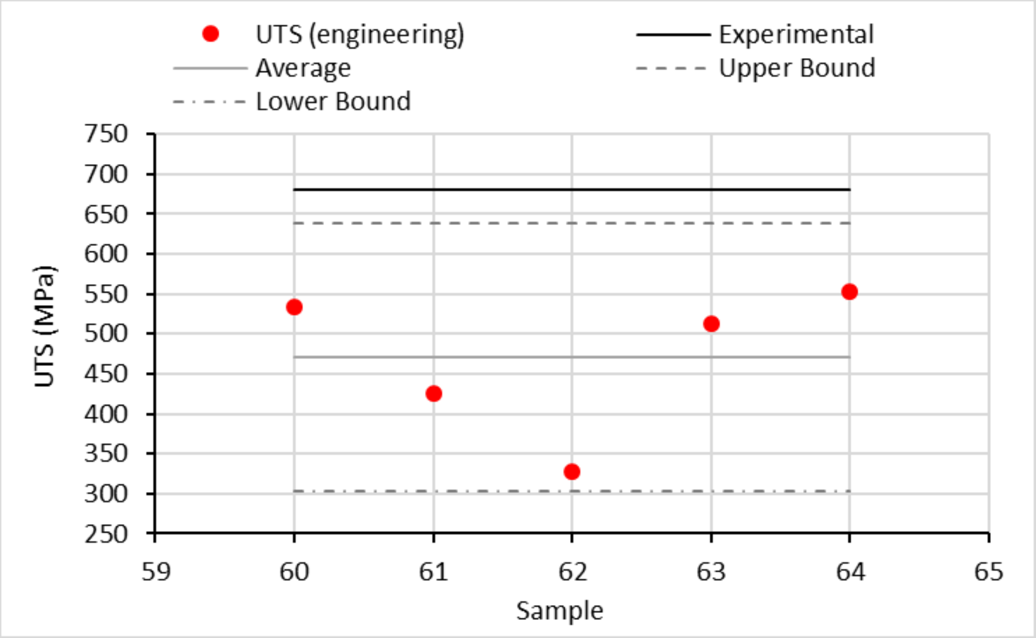

*Figure 6.12: Method b UTS estimations from optimised Johnson-Cook parameters. The upper and lower bounds are calculated using 2*standard deviation. The standard deviation for method b is 83.73*

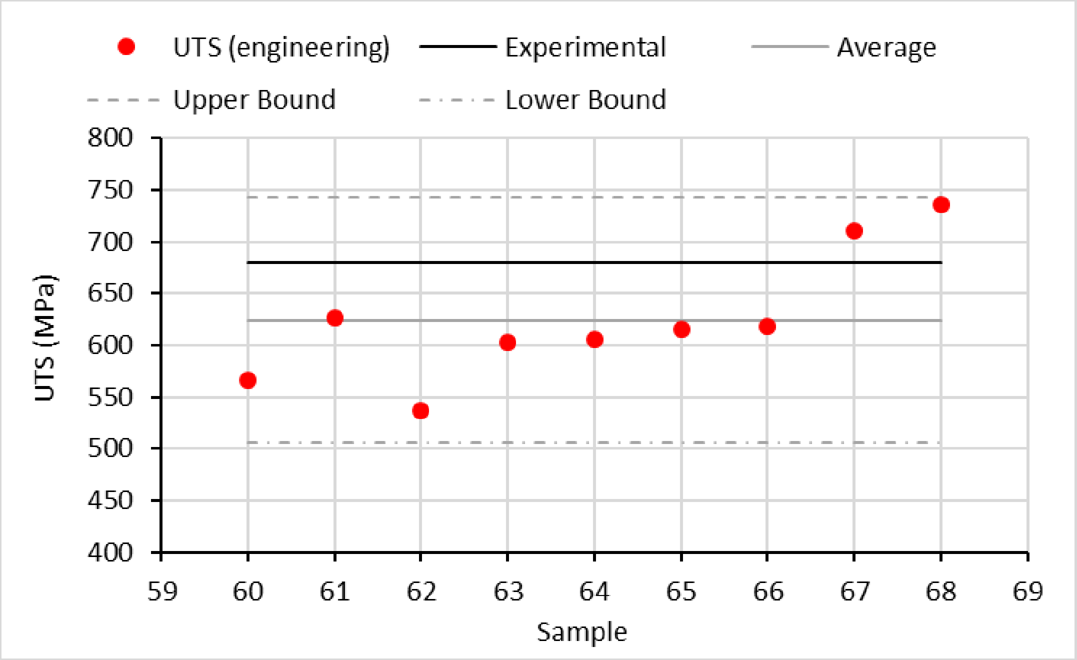

*Figure 6.13: Method c UTS estimations from optimised Johnson-Cook parameters. The upper and lower bounds are calculated using 2*standard deviation. The standard deviation for method c is 59.35*

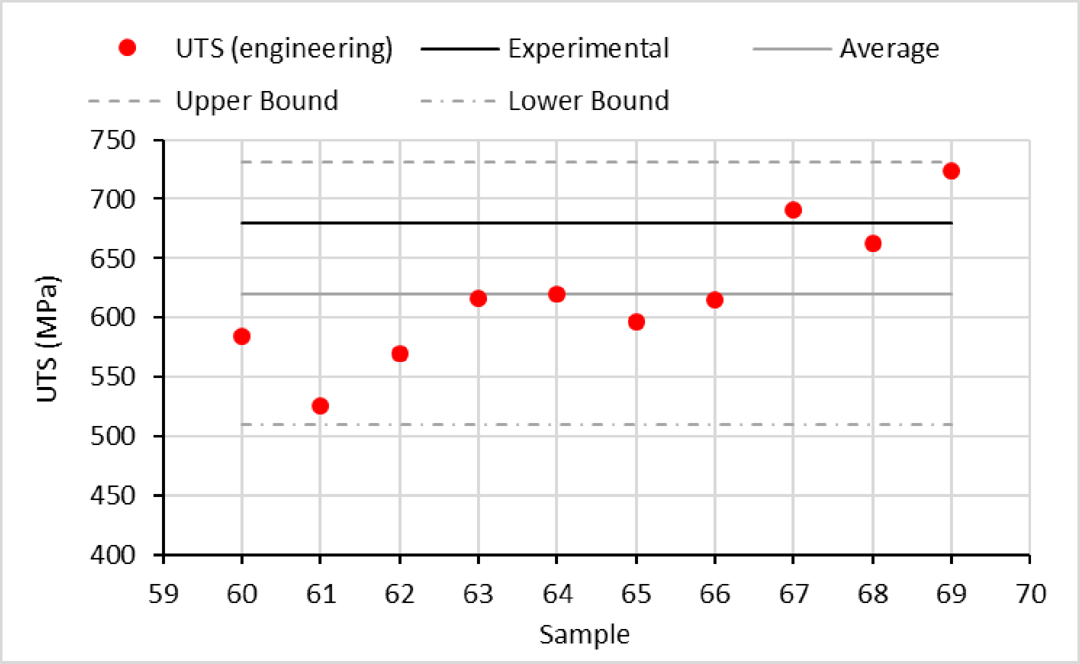

*Figure 6.14: Method d UTS estimations from optimised Johnson-Cook parameters. The upper and lower bounds are calculated using 2*standard deviation. The standard deviation for method d is 55.51*

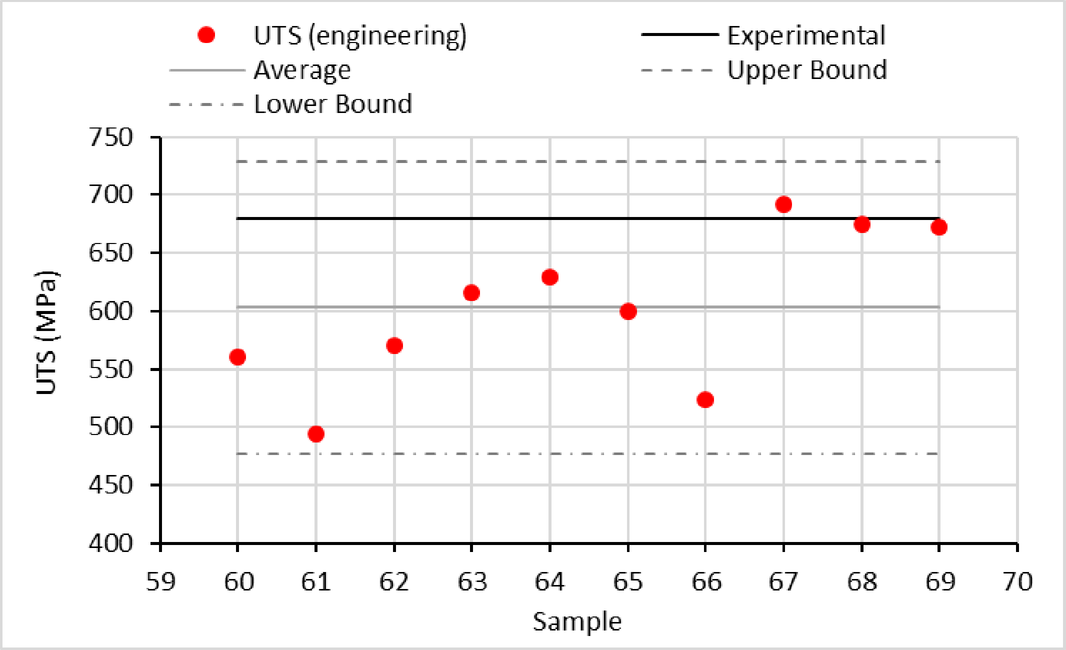

*Figure 6.15: Method e UTS estimations from optimised Johnson-Cook parameters. The upper and lower bounds are calculated using 2*standard deviation. The standard deviation for method e is 63.01*

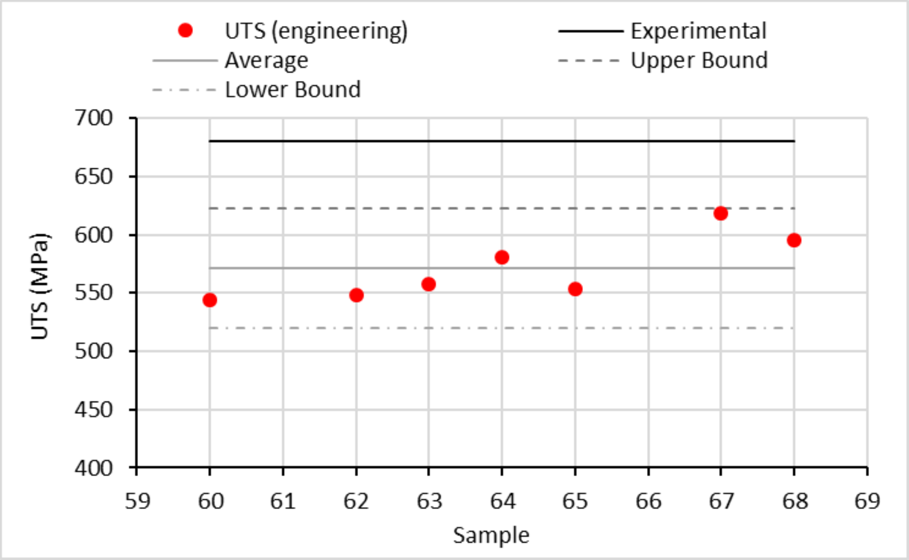

*Figure 6.16: Method f UTS estimations from optimised Johnson-Cook parameters. The upper and lower bounds are calculated using 2*standard deviation. The standard deviation for method f is 25.71*

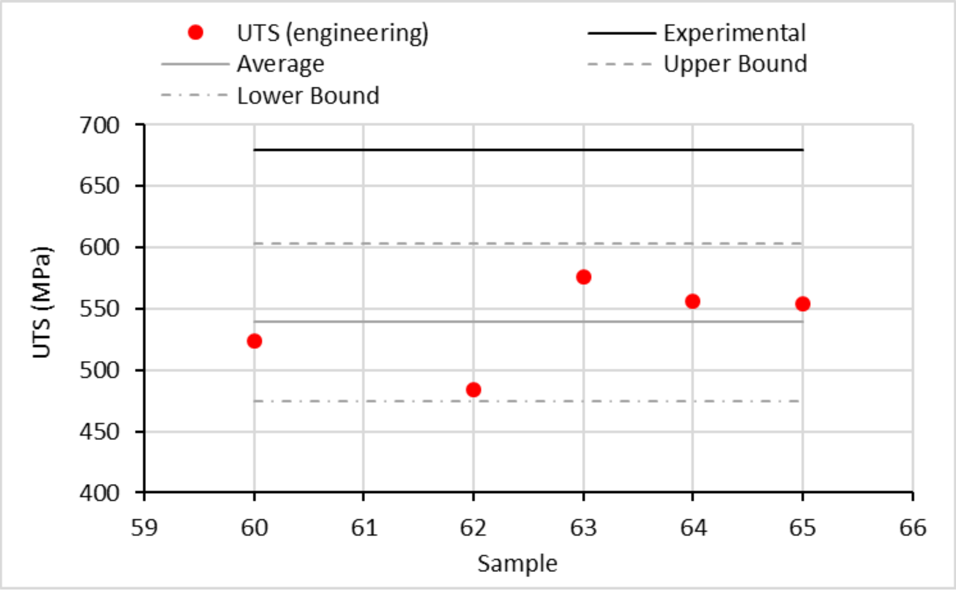

*Figure 6.17: Method g UTS estimations from optimised Johnson-Cook parameters. The upper and lower bounds are calculated using 2*standard deviation. The standard deviation for method g is 32.18*

When analysing each iteration of the optimisation method, some trends/features were observed:

As a development from methods a and b, methods c and d analysed a sample deflection of 0-0.552mm. This was in keeping with 0.552mm being widely considered the point of onset of plastic instability in the small punch test in a steel alloy [93], [128], [131], [133]. Unfortunately, these methods produced were inferior than the initial 0-1mm attempts. With a similarly large range, they were just as inconsistent, but the biggest problem was that both produced more than 1 result that was an overestimation of the UTS. Such non-conservative results meant that these two methods could not be used with any confidence. However, while there were over estimations present, the overall accuracy of the results seemed to increase, with the range being closer to that of the experimental value of

680MPa. Taking this into consideration, it was decided that the 0-0.552mm methods would be iterated on in an effort to produce consistently conservative results.

Techniques a-d illustrated the effect that a change in the total displacement analysed could have on the UTS estimation. Looking to the code of best practice, ASTM standard and round robin, the point of elastic-plastic transition in the small punch curve had also been defined [93], [128], [133]. This point (u_a) could then be identified for each sample and used as the starting point for the range analysed in the optimisations. This led to method e, which analysed the curve between u_a-0.552mm (A= σ_y and variable).

Method e produced results that were visibly less consistent than that of the previous two attempts. With a singular over estimation and a large range of results.

However, with the lessons learned in Chapter 4, it was possible that the proof stress estimations were the cause of some of the inaccuracies. Chapter 4 displayed that the proof stress estimation techniques suggested in the code of best practice, ASTM standard and round robin were highly inaccurate and produced values greater than the UTS estimated using methods suggested in the same guide. Therefore, a commonly used ratio between yield strength and UTS was used [224], [225]:

$$\sigma_y = 0.85 \times \sigma_{UTS}$$

Equation 6.6

The UTS estimations using the code of best practice, ASTM standard and round robin were used here. So, a new yield/proof stress was produced for each sample (Table 6.2).

Method f was a cumulation of the lessons learned from the previous iterations. The results reflect this with a greatly reduced range (around half the value of the original tests). All of the results were conservative with the double standard deviation range also being conservative.

As described in section 8.6.1, method f produced numerically good values, but the fit was constrained only to a point with a significant deviation from 0.552mm onward. This led to the development of method g. With a larger section of curve selected, the optimised values should be a better representation of plastic behaviour. Like method f, method g used estimates for A based on the maximum punch force and so some curves could not be included (samples 61, 66, and 69). Due to the lack of applied bounds in the Nelder-Mead algorithm, the optimisation of some samples could not be completed. This led to a smaller pool of optimised results. That being said, the results produced here were still consistently conservative with a standard deviation of 32.18, which is still a significant improvement on method a.

Overall the results showed a greater accuracy, and with further refinement it may be possible to improve the methodology further.

Over the course of this section the method for optimisation has been iterated upon. The overall improvement is minimal (a decrease in spread and somewhat more accurate individual results). However, even small improvements are vital in the development of the small punch testing method as a whole.

An argument could be made that the first technique used was acceptable, with minimal setup and pre-optimisation calculations needed. However, not much consideration was given to the code of best practice, ASTM standard and round robin here. Applying the information provided with the guide allowed for the implementation of more bespoke optimisation and so may make the process more applicable to different alloys.

Another benefit of a more tailored optimisation is the reduction on the chances of the algorithm trying to use impossible values (thus causing the optimisation to fail) or the results being a false minimum. Such high failure rates can be seen in methods a and b.

More accurate starting values and specific deflection ranges should aid in the production of reliable, conservative results.

The cumulation of the optimisation analysis can be seen in Figure 6.18. This graph shows all of the extracted UTS values for all samples. The UTS estimations calculated in Chapter 4 (Section 4.5) were plotted along with the UTS value produced with the initial estimates and the experimental value for reference.

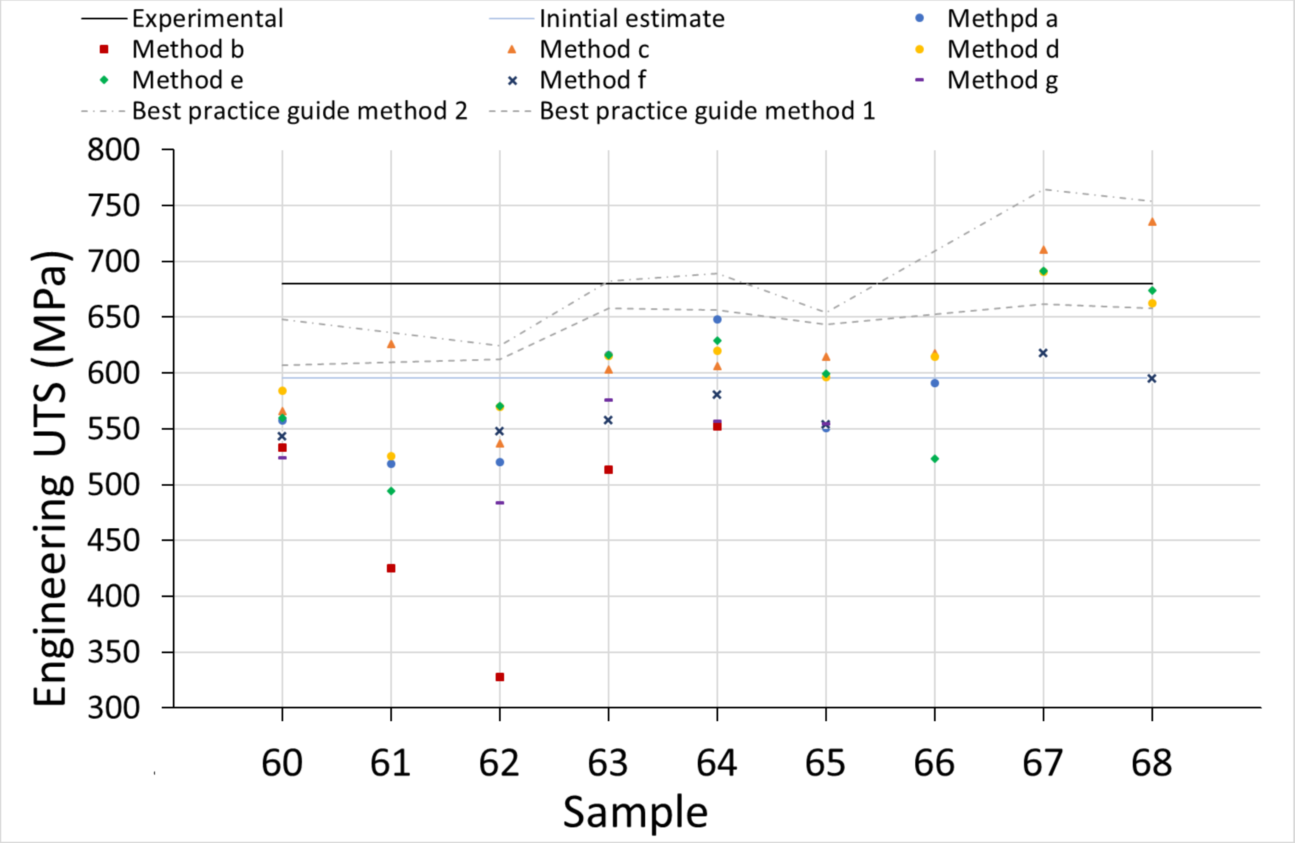

Figure 6.18: Overview of the UTS estimations from all optimisation methods. Also displayed are the UTS estimations using the best pracitce guide methods, and an experimental value calculated from a P91 tensile curve.

By using this method for validation, it is now easy to see the effect the different optimisation methods had on the bulk material data. This allows for the selection of the more optimal methods to be carried forward for use with the Eurofer97 tests.

6.9 Optimised method for Johnson-Cook constant optimisation

The three methods chosen to carry forward to the Eurofer97 tests are:

- method e, u_a – 0.552mm (A= σ_y)
- method f, u_a – 0.552 mm (A = 0.85*UTS)
- method f, u_a – 0.865 mm (A = 0.85*UTS)

These were selected on the grounds that they both utilise as much of the standard practices as possible. It is worth noting that the σ_y method has shown the potential to produce non-conservative results. However, the use of the proof stress estimation method means that it can be applied to curves that do not reach the point of maximum force/necking, thus allowing for the evaluation of a wider range of curves. The 0.85*UTS does require a full SP curve, however it produced only conservative results with nearly/the lowest standard deviation of the set. Thus making this the best technique used in this project.

6.10 Overview of Eurofer97 Tests

From the small punch data for Eurofer97 provided, a total of 11 room temperature curves were available for use in the plasticity optimisation.

The initial Johnson-Cook estimates are the same at those for P91 given in Table 6.1.

However, using the lessons learned from the P91 tests, the value for A was varied and based off two estimates taken from the small punch curves for each sample. These values are provided in Table 6.13.

*Table 6.13: The proof stress, UTS and 0.85*UTS data for the Eurofer97 samples. The proof stress and 0.85*UTS values will be used as values for A in the Johnson-Cook model starting estimations*

Sample	Proof Stress Estimation (MPa)	UTS Estimation (MPa)	0.85*UTS (MPa)
001	595.68	593.74	504.68
002	646.68	611.64	519.89
003	665.04	623.69	530.14
004	656.88	624.00	530.40
005	505.92	547.43	465.32
006	612.00	608.72	517.41
007	677.28	629.84	535.36
008	656.88	644.97	548.22
009	499.80	589.06	500.70
010	544.68	604.80	514.08
011	556.92	596.89	507.36

The complete set of simulations run can be seen in Table 6.14.

Table 6.14: The methods chosen for the optimisation of Eurofer97 data

Method	Start (mm)	End (mm)	Initial estimate for A (MPa)	Comments
e	u_a	0.552	σ_y	Varied all constants
f	u_a	0.552	0.85* UTS	Varied all constants
g	u_a	0.865	0.85*UTS	Varied all constants

6.11 Eurofer97 results

The results from each series of inverse analysis can be seen in Tables 6.15, 6.16, and 6.17. These results take the form of the optimised Johnson-Cook parameters along with the final r value for each.

Table 6.15: Table of the optimised Johnson-Cook Values for Eurofer97. Deflection was set to a maximum of 0.552mm. The deflection ranges for the optimisation started at u_a and ended at 0.552mm. The value for A was set as the σ_y calculated from the code of best practice, ASTM standard and round robin. The value of A was included in the optimisation routine.

Sample	A	B	n	m	r
1	472.27	489.01	0.49	2.26	0.0016
2	487.90	474.62	0.48	2.44	0.0010
3	467.96	363.83	0.30	2.03	0.0019
4	504.76	569.99	0.56	1.84	0.0005
5	362.42	829.71	0.55	1.36	0.0015
6	460.83	599.98	0.49	2.05	0.0017
7	463.41	397.00	0.30	2.02	0.0023
8	491.24	690.84	0.52	1.72	0.0048
9	287.71	823.75	0.35	1.58	0.0026
10	375.08	870.78	0.47	1.61	0.0019
11	434.49	693.58	0.52	1.70	0.0014
Standard deviation	64.16	169.31	0.09	0.30	0.0011

Table 6.16: Table of the optimised Johnson-Cook Values for Eurofer97. Deflection was set to a maximum of 0.552mm. The deflection ranges for the optimisation started at u_a and ended at 0.552mm. The value for A was set as the 0.85 UTS calculated from the code of best practice, ASTM standard and round robin. The value of A was included in the optimisation routine.*

Sample	A	B	n	m	r
1	477.45	532.68	0.54	1.71	0.0016
2	499.02	528.87	0.56	1.83	0.0010
3	521.50	528.56	0.61	1.73	0.0014
4	508.78	598.02	0.59	1.75	0.0005
5	333.40	712.72	0.44	1.75	0.0012
6	462.41	605.08	0.50	1.80	0.0017
7	525.43	541.47	0.60	1.85	0.0016
8	526.91	578.61	0.57	1.79	0.0029
9	279.34	826.06	0.34	1.75	0.0026
10	360.25	840.71	0.44	1.49	0.0017
11	428.12	681.32	0.50	1.67	0.0013
Standard deviation	82.39	110.47	0.08	0.09	0.0006

Table 6.17: Table of the optimised Johnson-Cook Values for Eurofer97. Deflection was set to a maximum of 0.865mm. The deflection ranges for the optimisation started at ua and ended at 0.865mm. The value for A was set as the 0.85 UTS calculated from the code of best practice, ASTM standard and round robin. The value of A was included in the optimisation routine.*

Sample	A	B	n	m	r
1	488.56	582.79	0.62	1.74	0.0017
2	512.11	510.11	0.60	1.75	0.0019
3	521.82	485.77	0.57	2.03	0.0022
4	522.89	450.83	0.55	1.35	0.0016
5	377.12	680.34	0.52	1.64	0.0025
6	478.65	482.80	0.48	2.11	0.0023
7	534.29	445.24	0.56	2.16	0.0019
8	529.12	410.90	0.46	2.19	0.0028
9	330.21	621.38	0.32	1.46	0.0058
10	429.42	678.95	0.52	1.70	0.0071
11	474.30	540.43	0.56	1.43	0.0033
Standard deviation	64.01	89.41	0.08	0.29	0.0017

6.12 Eurofer97 discussion

6.12.1 Overview

Much like the results from the P91 tests, the Eurofer97 tests were also analysed using the Considére criterion. The results from which can be seen in Tables 16 and 17. For comparison, experimental UTS values were used. These were provided in the IAEA "*Technical Specifications EUROFER Material Database*"; and from "*Reduced Activation Ferritic/Martensitic Steel Eurofer'97 as Possible Structural Material for Fusion Devices. Metallurgical Characterization on As-Received Condition and After Simulated Service Conditions*". The values were: 666MPa and 662MPa [50], [190]

After assessing the optimised Johnson-Cook constants using the Considére criterion the results were collated and presented in graphs (Figures 6.18, 6.19, and 6.20). As with the P91 results, method e produced results that were less consistent than method f. However, the values produced by method e were generally closer to the experimental values, whereas method f estimates lower values but with a smaller spread. Method g produced values similar to that of methods e and f.

For each method, the results for samples 5 and 9 were markedly different to the others in the set. This would go on to have an effect on the UTS estimations explained below.

The first thought was that the experimental data for samples 5 and 9 were different from the rest of the set (Tables 6.18, 6.19), exhibiting more brittle hehaviour, for example. On closer examination, it became clear that the two samples behaved differently to the others in the set (Figures 4.16, 4.18, 4.20, and Table 4.16).

The most noticable difference was the significantly lower values of A and higher values for B, indicating a lower yield stress and higher strain hardening. Such a variation in the data again indicates the inconsistency of small scale testing.

Table 6.18: Optimised Johnson-Cook values for Sample 5. Note the low values for A and the high values for B

Method	A	B	n	m	r
e	362.42	829.71	0.55	1.36	0.0015
f	333.40	712.72	0.44	1.75	0.0012
g	377.12	680.34	0.52	1.64	0.0025

Table 6.19: Optimised Johnson-Cook values for Sample 9. Note the low values for A and the high values for B

Method	A	B	n	m	r
e	287.71	823.75	0.35	1.58	0.0026
f	279.34	826.06	0.34	1.75	0.0026
g	330.21	621.38	0.32	1.46	0.0058

6.12.2 Empirical method for validation of optimised results

Overall, all three methods were consistently conservative with the upper bound falling well below the experimental UTS value (Figures 6.19, 6.20, and 6.21).

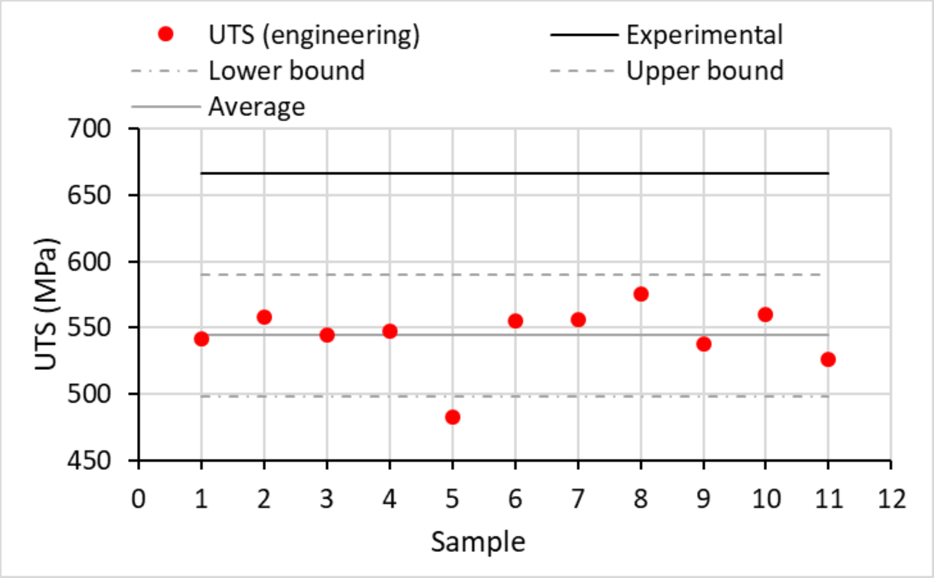

*Figure 6.19: method e UTS estimations from optimised Johnson-Cook parameters. The upper and lower bounds are calculated using 2*standard deviation. The standard deviation for method e is 22.95*

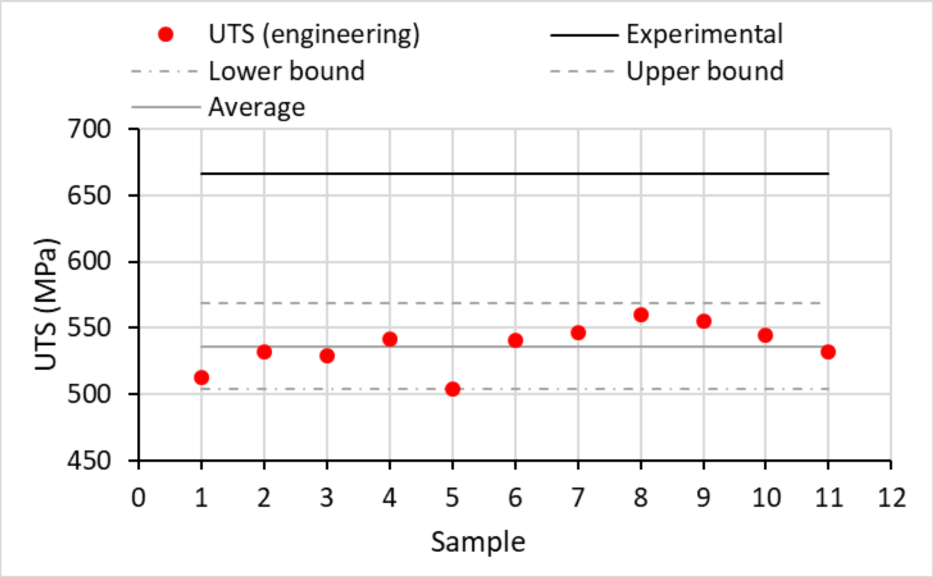

*Figure 6.20: method f UTS estimations from optimised Johnson-Cook parameters. The upper and lower bounds are calculated using 2*standard deviation. The standard deviation for method f is 16.12*

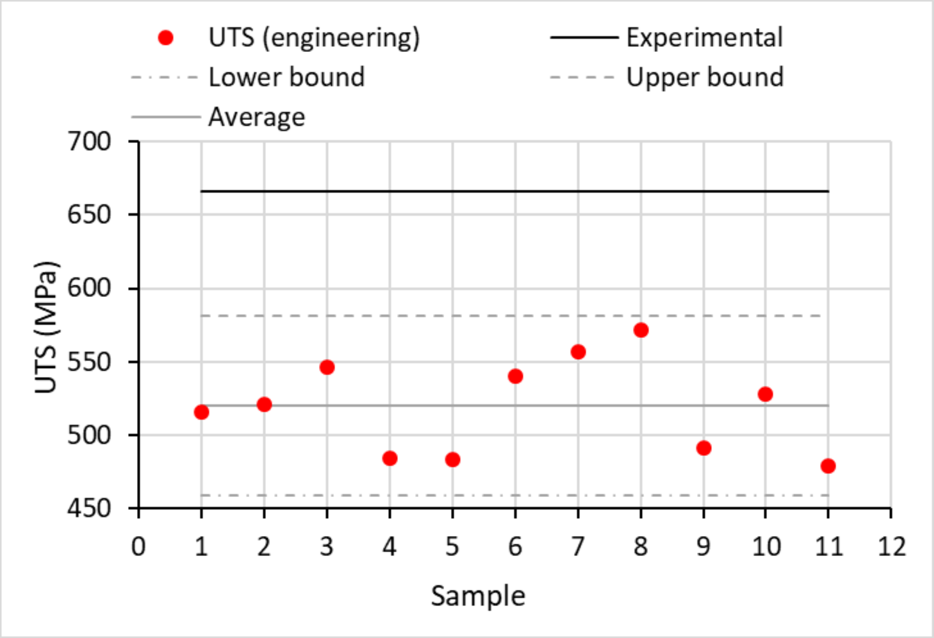

*Figure 6.21: method g UTS estimations from optimised Johnson-Cook parameters. The upper and lower bounds are calculated using 2*standard deviation. The standard deviation for method g is 30.54*

In both sets of results, sample 5 and sample 9 produced values that were significantly different than the others. And in the case of method e, the value fell beneath the lower bound. When the experimental curve was inspected it was not dissimilar to the others in the set. However, when the Johnson-Cook values were analysed it became clear that they were very different from the others. The value of A was around 100 MPa lower than expected and B was about 100 MPa higher than expected.

Figure 6.22 shows an overview of all UTS values produced in this thesis for Eurofer97. This includes the values produced using the code of best practice, ASTM standard and round robin. By displaying the results this way, some observations can be made.

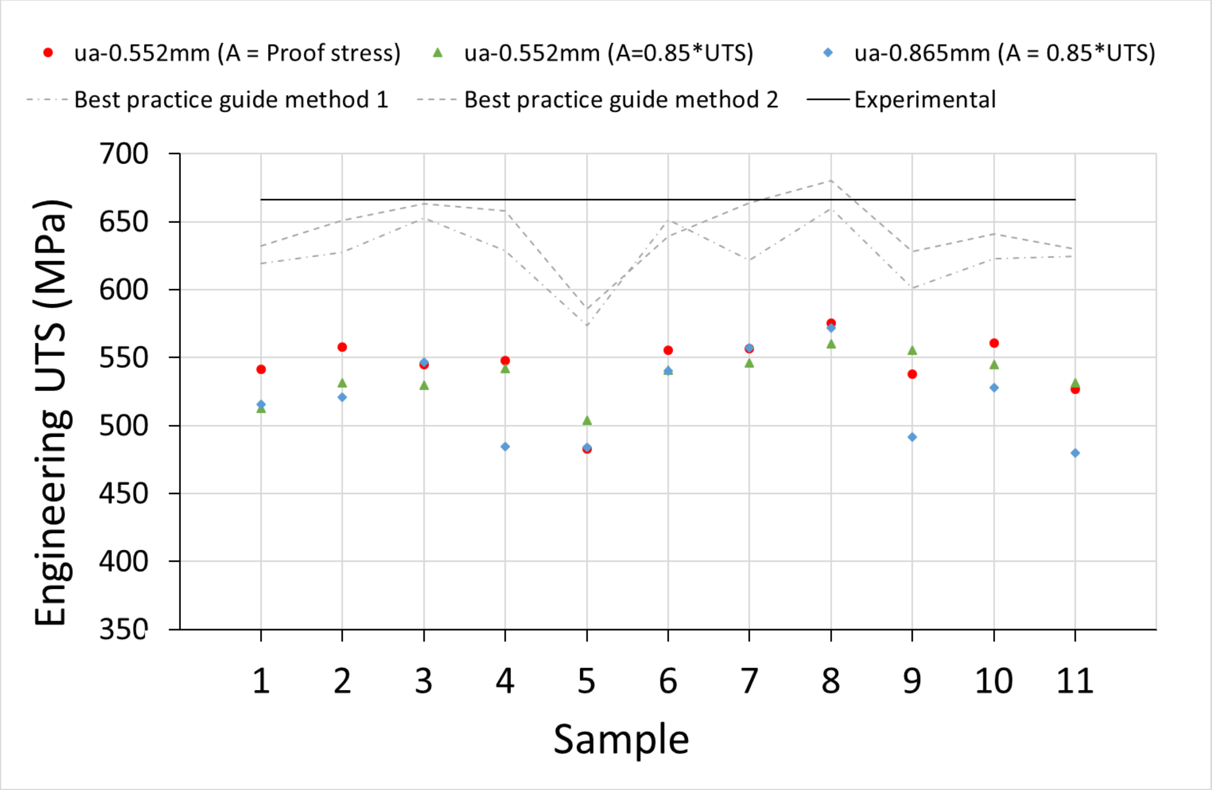

Figure 6.22: Overview of the UTS estimations from all optimisation methods. Also displayed are the UTS estimations using the best practice guide methods, and an experimental value provided in the literature search [50], [190].

In general, the optimisation method produced values that were conservative to a confidence of 95%.

6.13 General Discussion

6.13.1 Optimisation script

The Python 2 script used in this Chapter was evolving throughout, with each iteration on the optimisation methods taken as another developmental step. This can be seen in the body of results produced from the P91 experimental data. Each incremental change in method, included an increase in understanding of both the small punch test and the finite element model.

While most of the FEM fundamentals were fine-tuned in Chapter 5, further improvements were seen here. This took the form of the use of the scripting package available within Abaqus and then gaining the understanding on how to build the model from the script.

Once the basic script was working, it was then adapted to include a loop which facilitated the optimisation process. Thus, allowing the values of the Johnson-Cook plasticity parameter to be altered automatically. The improvements on the optimisation methods were then made.

Sections 6.7 and 6.8 display the process of iterating on and improving the optimisation. From there the two most successful methods were selected for application to the Eurofer97 experimental data (sections 6.10 to 6.12).

Here the overall effectiveness of the optimisation scripts and the algorithm used will be discussed.

6.13.2 Discussion of the Python script

As stated above the script used in this Chapter was in a constant state of development, and even after all of the necessary work was completed there are still some improvements that could be made.

To start with, some of the positives will be outlined.

By using the inbuilt scripting package within Abaqus and the optimisation packages in Python2, was that there was no need to employ a third piece of software. Thus, making the whole process simpler, and more economical. The typical way of performing inverse analysis in Abaqus is to use MATLAB as the optimisation script, and Python as the communicator between the two. By the using Python as the optimisation script, the need for MATLAB is negated.

However, while the script did work as intended, there is still room for improvement. Notably in user readability and efficiency. For example, changing the way that the Johnson-Cook constants were saved. As it stands, the results from each iteration are saved in their own files, a ".rpt" file for the force-displacement data and a ".txt" file for the Johnson-Cook constants. Each optimisation can take up to 250 iterations, meaning that up to 500 separate files are saved. Thus, making the tracking of the Johnson-Cook parameters over the course of the optimisation labour intensive. So, to improve on this, an alteration could be made that would save each new set of JC parameters as a new line on a single text file, instead of the ~250 produced currently.

6.13.3 Discussion of the optimisation algorithm

After initial research (see Chapter 2: Literature review) the algorithm deemed most appropriate was the Nelder-Mead, or simplex, method. It was selected on the basis of wide spread application, lack of required derivatives, and its applicability in irregular data sets.

Overall this algorithm did appear to produce viable values, and upon iteration of its application an overall improvement in the quality of the Johnson-Cook parameter predictions was seen. This would be quantified in a decrease in overall spread of the data and improvement of accuracy. As evident in the differences between method b and f. This was due to, in part, by the lack of largely inaccurate predictions. As evidenced by the change in the sample 62 predictions between the two methods (Figures 6.12 and 1.16).

The Nelder-Mead algorithm did have some drawbacks, however. While the lack of applied bounds to the algorithm did allow for the prediction of a wider range of unknowns, it did also cause several of the optimisations to fail. This was almost completely due to the algorithm attempting to input a negative constant, which is not possible in the Johnson-Cook model. The application of bounds would have prevented this type of failure and therefore increased the success rate. So, a new algorithm may need to be applied here.

The direct search method in general is simple to apply, does not require derivatives of the curves, and is computationally inexpensive. However, as it is not a global search technique is there is the distinct possibility of the algorithm getting stuck in a false minimum and therefore not correctly predicting the

Johnson-Cook parameters. A global search method like a genetic algorithm, for example, would solve this problem. However, such methods are computationally expensive and require significantly more set up. And as this project is looking to produce a usable tool for engineers, such methods may not be applicable due to computational limitations.

Instead an emphasis on producing high quality/accurate initial estimates for the Johnson-Cook model should be a priority, so, if the algorithm does find itself in a false minimum, it should be close enough to the true values (or within a set of limits) to be considered acceptable.

6.13.4 P91 and Eu97 results overall discussion

The overall results between the P91 and Eurofer97 will now be discussed.

In general, the experimental data provided was variable. The force-deflection curves had varying shapes leading to a wide range in final results.

For the P91 data, the standard deviations for each optimisation method display the effect of the iterative process used to improve the overall results. With each iteration more attention was paid to the code of best practice, ASTM standard and round robin and the values that could be calculated using it. This led to a decrease in accuracy, which was rectified by the final method used (method e).

Method e produced the most consistent results with exclusively conservative values. The increase in consistency may be due, in part, to the starting estimates. This was the only method that used the maximum punch force as the source of the value for A. In general, the maximum punch force for each test was a similar value and so could produce more consistent estimations (see Table 4.3).

For Eurofer97 the two final methods (e and f) were selected. The results of which displayed a similar improvement in standard deviation as P91. This confirmed the last method as the most applicable of those developed.

Although the results above have been described as consistent, it must be noted that the overall variation in results is large. This must be put down to the intrinsic variability of small punch test data, and indeed small scale test data as a whole. As explained in the literature review, the decrease in specimen length scale leads to a rise in the influence of defects and grain size. Thus, increasing the likelihood of a growth in data spread.

To reduce any extra variation in the system the quality of starting estimates for optimisation must be kept to a sufficient level. This was the intention in which the iterations in the methodology were made, with each step increasing the level of reliance on the individual force-deflection curve.

While this did produce a definite increase in the overall quality of the final estimation, there is still room for improvement. Two main additions to the method will be vital for further improvement. The first being the development of a method for estimating the other Johnson-Cook plasticity values using small punch curves in place of a set of tensile curves. Secondly using an optimisation algorithm that allows the use of bounds for each variable. This will reduce the likelihood of false minima and impossible values being produced.

6.14 Conclusions and recommendations

The inverse analysis methodology developed in this Chapter provided Johnson-Cook plasticity constants that were conservative. This was successfully validated through the use of the Considére criterion.

6.14.1 Reiteration of Aims and Objectives

The focus of this thesis was to provide a level of quality assurance for small punch testing. To achieve this, finite element modelling and inverse analysis were employed. Three distinct objectives were drawn:

1. To produce a script that runs a small punch simulation in Abaqus and optimise the Johnson-Cook plasticity values through successive iterations of the model.
2. To predict the plastic behaviour of a small punch test by optimisation of Johnson-Cook plasticity constants.
3. To ensure that the Johnson-Cook values produced were conservative and therefore considered potentially viable for engineering applications.

6.14.2 Was this successful?

The work completed in this Chapter was partially successful.

The methodology developed produced Johnson-Cook and UTS estimations that were conservative. This was achieved with a limited amount of experimental small punch data, and a single tensile test. The completion of the work on two separate alloys proved that the method is repeatable and reliable. Thus providing a proof of concept.

All of the work completed was done to be able to work within the code of best practice, ASTM standard and round robin guidelines, utilising as much of the small punch data as possible. This lead to results that were comparable to the estimates produced using the code of best practice, ASTM standard and round robin methods. Providing a great basis for further development and prediction of material behaviour through finite element modelling and inverse analysis.

However, over the analysis and validation of results it became clear that there were several flaws in this method that must be rectified. These were:

1. Lack of boundary conditions in the inverse analysis algorithm
2. High levels of assumption and estimation in the initial portion of the method
3. Lack of method for calculating B, C, n, and m of the Johnson-Cook model mean the continued reliance on tensile data

6.14.3 Recommendations

From these conclusions some recommendations for future work can be made:

1. Use a different optimisation algorithm that allows for the application of boundaries
2. Develop a method for estimating further Johnson-Cook constants, using small punch data alone. This may include completing a series of tests over a range of temperatures and displacement rates.

3. Analyse a wider range of materials. Both of the alloys analysed here were ductile steels. In reality a range of materials will need to be tested, including brittle samples. This will be especially important when analysing irradiated materials.
4. A last and more general recommendation would be the addition of the punch and dies as deformable solids. This would greatly increase the computational expense required but would provide the opportunity to assess the influence of machinery compliance.

7. Johnson-Cook failure estimation

7.1 Introduction

Over the course of this study a finite element model of the small punch test has been developed, iterated and improved upon. The plastic behaviour of a ductile steel has been predicted using the Johnson-Cook model and inverse analysis. Now the final step can begin, the prediction of the damage and failure behaviour of the same ductile steels.

Much work has been presented on the plastic behaviour and UTS of small punch test samples [112], [137], [149], [170], [173]. However, relating the damage and failure of the small punch test piece to tensile behaviour is still in its early stages [130], [138]. Further understanding, and a development of a clear, concise and reliable method is needed.

In this final experimental Chapter, the development of a method for predicting damage behaviour will be presented.

7.1.1 Aims and objectives

The aim of this Chapter is to produce a basis for the further optimisation of a routine that will effectively predict the failure of a material using small punch data, and analyse and understand the importance of friction on the behaviour on the small punch test piece during necking and failure.

This will be achieved with the following objectives:

- Adapt the optimisation script from Chapter 6 for analysis of the Johnson-Cook failure constants
- Analyse the effect of friction on the optimisation of the Johnson-Cook failure constants for P91

7.2 Inverse analysis

As summarised in Chapter 6, inverse analysis is the optimisation of a function through iterating the input variables until a best fit is found. With the assistance of simulation, it is possible to use inverse analysis to obtain the values of the governing Equation [174].

Again, the script that would run within Abaqus and perform the inverse analysis by means of an optimisation algorithm. The scripting language used was to be Python 2. Figure 3.9 outlines the flow chart for the optimisation routine used.

7.2.1 Python optimisation – SciPy. optimize. Minimize

The *scipy.optimize.minimize* module within Python was also utilised for this Chapter [197]. As with Chapter 6, the Nelder and Mead (or Simplex) algorithm was selected for optimisation [177], [180].

7.2.2 Error function

The application of the Nelder-Mead method required the use of an error or objective function. For this project it was good to use a function that measured the absolute difference between an experimental force-deflection curve and its simulated counterpart. The error function, r, was given as:

$$r = \sum (simulated\ data - experimental\ data)^2$$

Equation 7.1

7.3 Adaptation of the optimisation script

As stated in the Chapter objectives, the script for this phase would be an adaptation of the one created for the optimisation of the Johnson-Cook materials constants. As such some amendments were made and are described below (relevant sections of code are included in Appendix 2).

7.3.1 Displacement

In Chapter 6, the importance of selecting the optimal displacement range for the inverse analysis was shown. So for this Chapter the displacement range was taken from the onset of friction effects, 0.865mm, to the point of failure, uf, as defined in the code of best practice, ASTM standard and round robin [128], [133], [155]. The ranges selected for each sample can be found in Table 7.1.

Table 7.1: The deflection range analysed for each sample

Material	Sample	Starting point	End point (u_f)
P91	60	0.865mm	1.68mm

7.3.2 Time

A time step of 350 seconds for a total displacement of 1.75mm was selected, matching the displacement rate chosen in Chapter 6.

7.3.3 Mesh

The mesh for the optimisation of the failure constants was the adapted version, discussed in Chapter 5 (Figure 7.1). The refinement of the mesh at the centre of the disk allowed for a more realistic fracture morphology. However, such a refinement did increase the simulation time and therefore will have an effect on the computational time needed to complete an optimisation cycle.

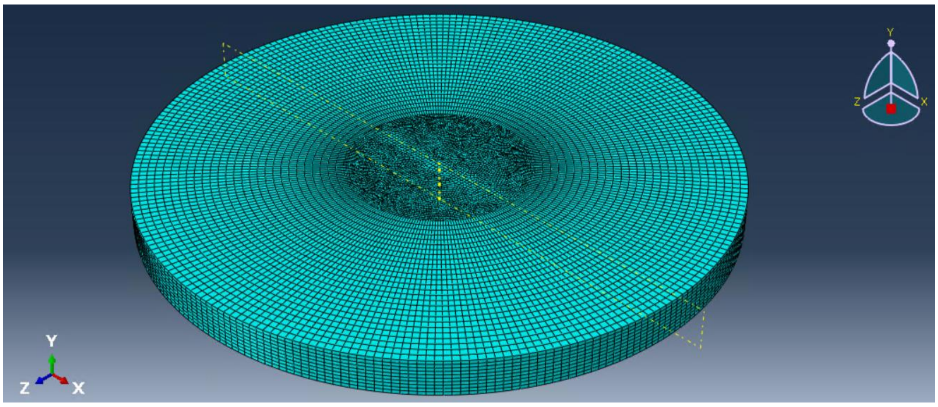

Figure 7.1: Image of the refined mesh used for the simulation of small punch sample fracture.

7.4 Friction

Analysis into the effect of friction on the small punch test completed in Chapter 5 showed that it has a marked effect on the latter half of the force-deflection curve. This is due to the combination of specimen bending, and sliding between the punch and specimen. As such, friction is an important consideration when looking to optimise the Johnson-Cook failure constants.

Finding the most appropriate friction coefficient for this portion of the small punch test will be a main focus of this Chapter. If the friction coefficient is too low the formation of a stagnant/dead zone will not occur and thus the distinctive cap will not form. If the friction coefficient is too high, the dead zone formed will be too big and potentially cause high stress concentrations around the circumference of the deformed area, leading to premature failure.

7.5 P91 Tests

Due to the time restrictions imposed as part of a PhD, only a small body of simulations were selected for this portion of the study. The focus would therefore be a more comprehensive analysis on the effect of friction and hopefully provide a basis for further work in this area.

7.5.1 Curves selected for analysis

P91

The curve chosen for P91 was sample 60, the relevant force-deflection curve can be seen in Figure 7.2.

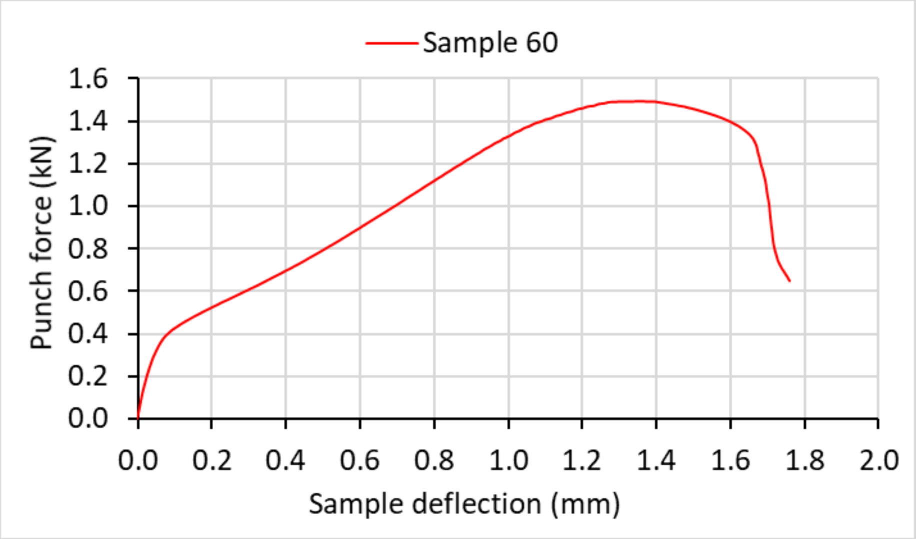

Figure 7.2: Punch force – Sample deflection graph of P91 steel, sample 60, provided by the European Commission Joint Research Centre

7.5.2 Results from Chapter 6

The optimised plasticity results were integrated into this Chapter, with the relevant Johnson-Cook materials constants applied to each sample. Of the results produced in Chapter 6, those produced by method f, were selected for use here. These can be seen below in Table 7.2.

Table 7.2: Johnson-Cook materials model constants for P91 sample 60, and Eurofer97 sample 001

Sample	**A (MPa)**	**B (MPa)**	**n**	**m**
60 (P91)	583.64	356.16	0.64	1.56

7.5.3 Initial Johnson-Cook failure constants

P91 was assigned initial Johnson-Cook failure estimates, which are given in Table 7.3.

Table 7.3: The initial Johnson-Cook plasticity estimations. The selection reasoning can be found in Chapter 5.

	D_1	**D_2**	**D_3**	**D_4**	**D_5**
Initial estimate	0.05	0.8	- 0.44	- 0.046	0.0

As discussed in Chapter 5 all experimental data for this study was taken at room temperature, thus ensuring that D_5 = 0 throughout. Because of this, it was not included in the inverse analysis of the Johnson-Cook failure constants.

7.5.4 Overview of optimisation tests completed

This Chapter was mainly focused on analysing the effect of friction, and the optimisations tests completed reflected this.

From analysis in Chapter 5 (Section 5.6), it appeared that the friction coefficient for the small punch tests could be anywhere between μ = 0.3 and μ = 0.57. To aid in the determination of the friction coefficient, a series of optimisation tests were devised. These would hopefully provide a basis for furthering understanding of friction in small punch tests.

A table outlining the tests completed for this section can be seen below:

Table 7.4: An overview of the optimisation tests completed for P91 and Eurofer97.

Material	**Sample**	**Displacement range (mm)**	**Friction coefficients**
P91	60	0.865 – 1.68	0.3 0.4 0.5 0.57

7.6 Results

7.6.1 Change in constants over an optimisation

To aid in providing a full understanding of the optimisation. The results from each stage of the optimisation were recorded. Thus allowing the monitoring of each parameter as it changed with each simulation. An example of this is shown in Figures 7.3 and 7.4.

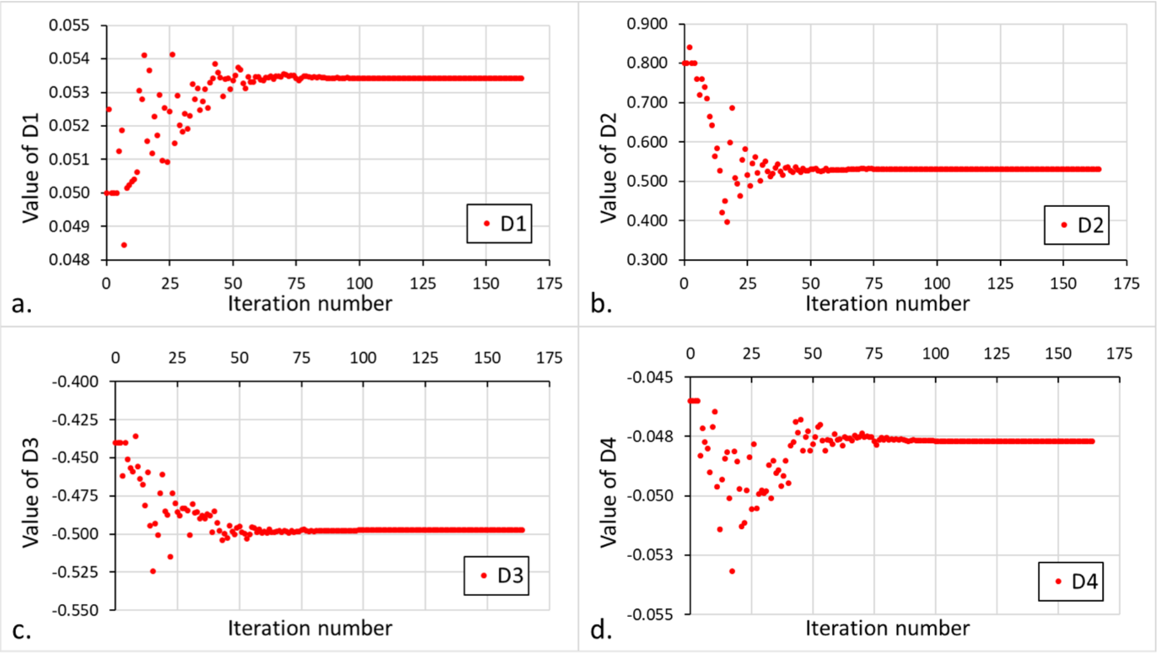

Figure 7.3: Optimisation progression data of sample 60 (μ=0.3),. Where: a. Change in D_1 over a single optimisation; b. change in D_2 over a single optimisation: c. change in D_3 over a single optimisation; d. change in D_4 over a single optimisation

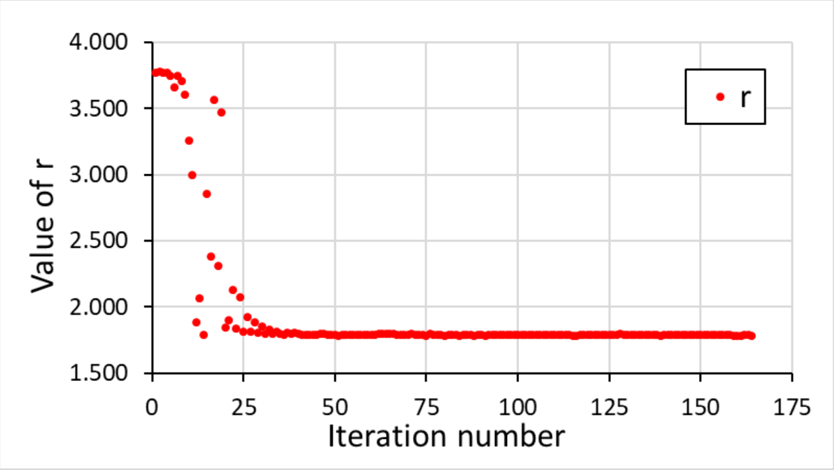

Figure 7.4: Sample 60 (μ=0.3), change in r over a single optimisation

7.6.2 Tabulated data

The results from each series of inverse analysis are included in Table 7.5 and plotted in Figure 7.5. These results take the form of the optimised Johnson-Cook parameters along with the final r value for each.

Table 7.5: A collation of the optimised Johnson-Cook damage model constants using different friction coefficients

Test	**D_1**	**D_2**	**D_3**	**D_4**	**r**
Sample 60 (μ = 0.3)	0.053	0.531	-0.497	-0.048	1.78
Sample 60 (μ = 0.4)	0.057	0.471	-0.458	-0.051	1.97
Sample 60 (μ = 0.5)	0.061	0.431	-0.469	-0.048	1.94
Sample 60 (μ = 0.57)	0.063	0.409	-0.559	-0.047	1.88

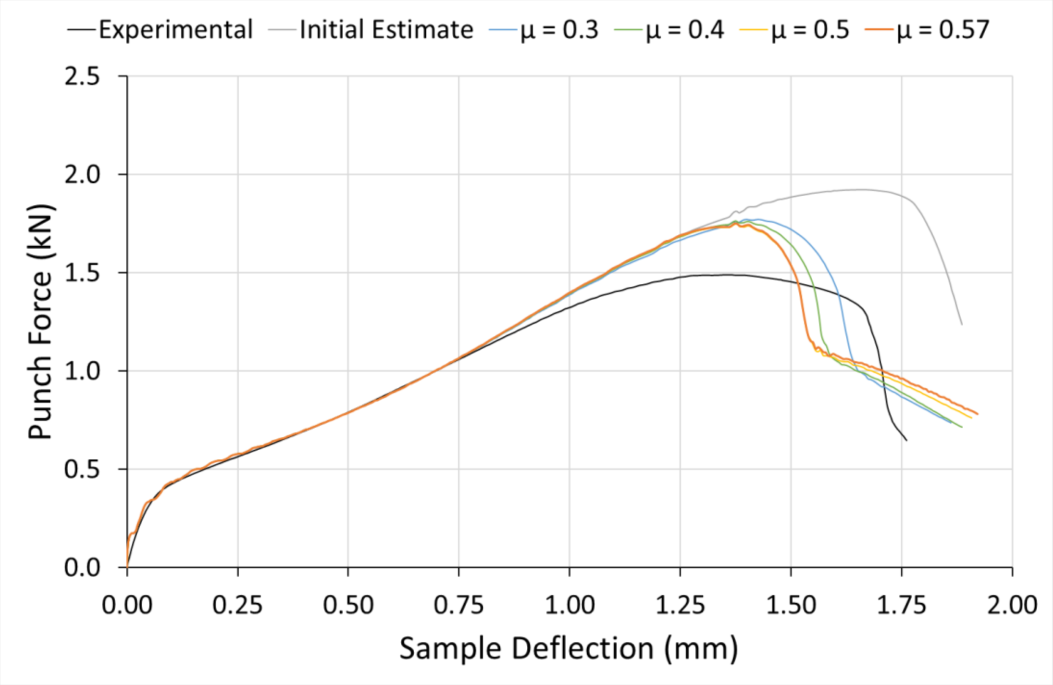

Figure 7.5: The force-deflection curves for each friction coefficient, along with the initial estimate and the relevant experimental curve.

7.6.3 Visual Results

Images were taken of the failed samples for each of the optimisation tests (Figure 7.6), and compared with an example using the initial estimate constants (Figure 7.7). This would help identify any differences in the morphology of the failed specimens with changing friction coefficients.

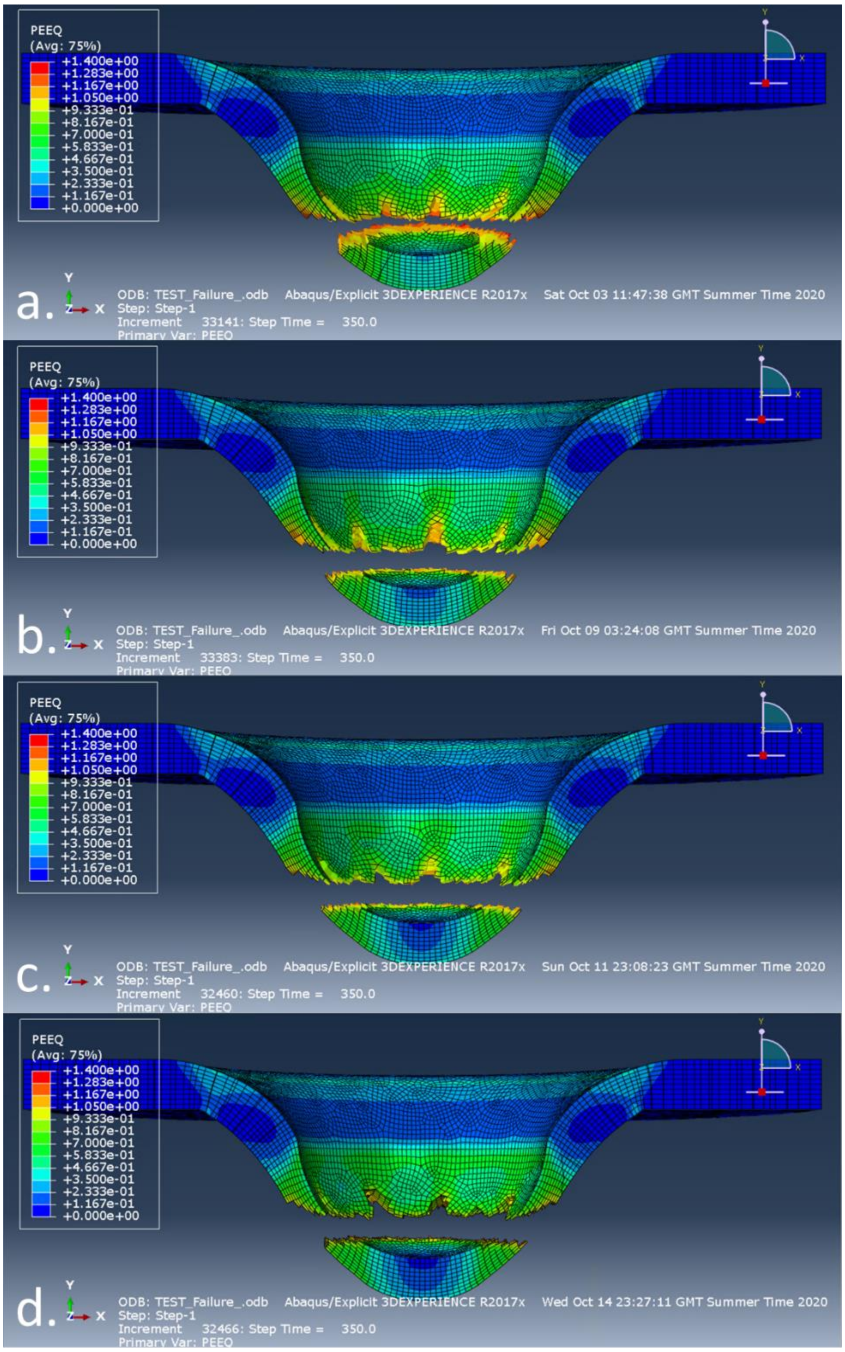

Figure 7.6: Visual results for the optimised Johnson-Cook failure simulations at different friction coefficients: a. μ = 0.3, b. μ = 0.4, c. μ = 0.5, d. μ = 0.57.

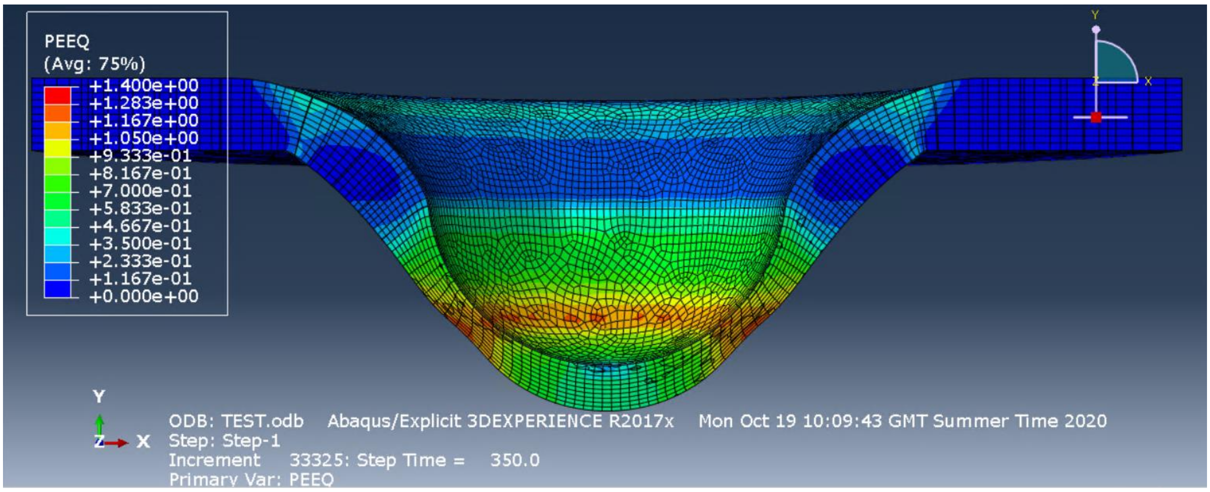

Figure 7.7: Image of the deformed sample using the Johnson-Cook failure initial estimate constants and a friction coefficient of μ=0.3.

7.7 Discussion

7.7.1 Optimised results

Numerical results

The optimisation completed in this Chapter has produced a marked improvement on the original estimate. The inverse analysis pushed the maximum force down and reduced the displacement at failure to within a conservative range. However, as the initial estimate was taken from a different steel, this was not to be unexpected.

The overall objective of this Chapter was to look at the effect of the friction between punch head and specimen. This was achieved by running 4 different optimisations of the same experimental curve, with the same starting values, varying only the friction coefficient. From this, some observations could be made.

The first being that an increase in friction coefficient led to a significant decrease in deflection to failure and a smaller decrease in force at failure. This may be due to change in volume of material undergoing high levels of strain. The dead zone formed at these friction coefficients would decrease this area and therefore cause a higher stress/strain concentration, thus leading to earlier necking and failure.

The difference between a friction coefficient of 0.5 and 0.57 was minimal, indicating that the effect that said friction had on the specimen deformation reached a limit around this point.

The second observation to be made was the optimised curves did not fit well with their experimental counterpart. The experimental curve shows, what appears to be, necking between a deflection of 1.25mm and 1.6mm followed by an almost abrupt failure at 1.68mm. This was not mirrored in the optimised curves, which continued to follow an almost linear increase in force followed by a smaller necking region between 1.25mm and 1.4mm deflection, and a smooth transition into fracture. Such behaviour is more indicative of a brittle specimen (outlined in Chapter 4, Section 4.6).

The failure to produce an acceptable fit over the damage portion of the force-deflection curve highlights the need for further development.

Visual results

The first, and most obvious feature to note is the failure of the specimens. The initial estimate did not succeed in fracture or failure, whereas the optimised results did. This is a significant improvement, that displays the potential that this method holds. While numerically the optimised tests were not close to the experimental analogue, the visual results show the progress that the optimisation has made.

When comparing the optimised results at different friction coefficients, some minor differences were observed. The fracture surface moved up the sample with increasing friction due to the increase in dead zone size. The larger the volume of specimen that isn't being deformed, the higher up the specimen the deformation will occur. This leads to a larger overall area being deformed and thus a change in punch force and sample deflection at failure.

While these results alone cannot prove the applicability of an optimised result, they do prove an important tool in understanding the effects of changing friction. Therefore, it is recommended that visual analysis is used in future simulations, in particular when assessing the influence of friction, punch misalignment, and machinery compliance.

7.7.2 Optimisation algorithm

As discussed in Chapter 6, the optimisation algorithm selected for this project has some distinct disadvantages. In addition to those discussed in section 6.13, there was another problem discovered here. This was inefficiency. As displayed in Figures 7.3 and 7.4, the variation of all constants and r over the course of the optimisation decreases significantly after 30-75 iterations. While the overall optimisation would take on average 167 iterations.

Table 7.6 shows iterations 75 and 164 for $\mu = 0.3$. When rounded to 3 decimal places, the results are identical. Which leads to the question, what is the point of iterations 76 to 164?

The optimisation for the Johnson-Cook plasticity samples were similarly inefficient, but the individual simulations took much less time to complete, with the whole optimisation taking 8-10 hours. The optimisation of the Johnson-Cook damage constants took much longer, with each simulation being much more computationally expensive. In this case the optimisation could take up to 4 days.

Table 7.6: A comparison of iteration 75 with iteration 164 of the Johnson-Cook Damage constants for Sample 60 $\mu = 0.3$.

Iteration number	**D_1**	**D_2**	**D_3**	**D_4**	**r**
75	0.053	0.531	-0.497	-0.048	1.78
164	0.053	0.531	-0.497	-0.048	1.78

Such inefficiency has the potential to hinder the progress of the research. Therefore, further development of the script is required along with the selection of a different search algorithm will be required.

The work presented in this Chapter is the cumulation of the Chapters preceding it. Analysis of curves used in Chapter 4 allow for a more precise starting point and deflection boundaries for optimisation. The friction analysis from Chapter 5 was built upon here. The understanding gained in this Chapter allowed for an examination of the optimised results with respect to friction. Results from Chapter 6 were used as the plastic behaviour for this set of results. The optimised plasticity constants facilitated the best possible starting point for the damage optimisation.

7.8 Conclusions and Recommendations

7.8.1 Conclusions

The optimisation of the Johnson-Cook damage model produced an improvement on the initial estimates. While the optimisation was not a satisfactory fit, the method does show potential for improvement.

The variance between optimised force-deflection for different friction coefficients highlighted the importance of understanding the friction between the sample and punch head.

The work shown in this Chapter will provide a basis for further development into producing a model that can effectively predict bulk scale material behaviour from small punch test data.

7.8.2 Recommendations

To further develop on the finite element simulation and optimisation script, significant further work is required. This would include:

- An improvement in the ductile damage and necking behaviour of the model. This may require adjusting mesh settings
- Changing the optimisation algorithm to one that is more efficient, and includes bounds to improve on the computational time.
- Additional research into the behaviour of less ductile metals, with a view to simulating and optimising Johnson-Cook constants. This will be of particular importance as irradiated materials become available for testing.
- The final recommendation is to look toward the implementation of a tensile test simulation for the purposes of validation. This would allow for a somewhat direct comparison of and optimised Johnson-Cook results with bulk scale behaviour. The production of this simulation would become another step toward providing a robust level of quality assurance in small punch testing.

Chapter 8 – Conclusions and Recommendations

8.1 Conclusions

The further development of nuclear fusion power relies on the continuation of the improvements to small scale mechanical testing. In this thesis a novel approach for the estimation of full scale material behavioural properties using small punch test data was demonstrated.

At the start of this thesis, three distinct aims were outlined:

1. To develop a robust and consistent methodology for extracting bulk mechanical material property data from the data acquired from the small punch test.
2. To develop criterion that establishes the level of confidence in the quality of the bulk mechanical material property data using the method developed.
3. Give recommendations on the worthiness of small punch testing for further research investment on the roadmap for qualification of fusion related materials.

This was achieved by completing the following objectives:

a) Develop a comprehensive understanding of the best practise guide for small punch testing and its role in ensuring consistency and reliability.

b) Using the code of best practice, ASTM standard and round robin as a basis, create a finite element model of the small punch test using the Abaqus 2017 software package.

c) Utilise robust material behaviour models included in the software, namely the Johnson-Cook materials and damage models.

d) Complete sensitivity testing and validation of the model.

e) Adapt the model for an investigation into the use of inverse analysis for the prediction of the Johnson-Cook material and damage model parameters.

f) Create a python script that uses the simplex method to find optimal values for each of the Johnson-Cook material and damage model parameters.

g) Where possible validate any optimised results via established correlations.

From this, the following conclusions can be drawn:

- The two methods for calculating UTS values from force-deflection curves proposed in the code of best practice, ASTM standard and round robin provided reasonable estimates for both P91 and Eurofer97 specimens. However, the method that relied on pinpointing the onset of plastic instability exhibited a tendency to produce values that were an over estimation.
- Analysis of the proof stress estimation methods provided in the code of best practice, ASTM standard and round robin displayed a large over estimation for the majority of specimens. In some cases, values exceeded UTS estimations of the corresponding specimens.
- The comparison of punch displacement and sample deflection data of Eurofer97 small punch test data further demonstrated the importance of apparatus compliance. With punch

displacement results producing results that were inconsistent when compared to those of the sample deflection.

- The observation of a consistent variation in force-deflection curve shape was successfully correlated to a variation in specimen ductility, highlighting one of the inherent inconsistencies in small scale testing methods.
- This initial section of the project provided a basis of understanding of the small punch test, and the analysis of its results. However, as with a lot research, this work was time sensitive. As such, the results shown here may no longer be consistent with the most recent research and publications.
- The contribution of this research is the validation of already established empirical methods used in the analysis of small punch test data. Areas of inconsistency were highlighted and the importance of machinery compliance restated.
- The development of an inverse analysis method using finite element modelling for the prediction of Johnson-Cook material model parameters from small punch test data was presented. The Considére criterion was used to provide UTS estimations from the optimised results for each specimen. This provided a form of validation for the inverse analysis method, providing evidence that the results produced were conservative.
- This work was completed using a limited amount of experimental small punch data, and a single full scale tensile test. Even with the narrow range of data, a robust proof of concept for the inverse analysis methodology was produced.
- However, the analysis and validation of results was not without limitations:
    - Lack of boundary conditions in the inverse analysis algorithm led to several specimens failing to reach an optimised result
    - High levels of assumption and estimation in the initial stages, meant that a robust validation practice must be developed before applying the method to unknown/irradiated specimens
    - Lack of method for calculating B, C, n, and m of the Johnson-Cook model ensures the continued reliance on tensile data. Therefore, further research and development is required to allow for the elimination of tensile data completely.
- The contribution of this research is the development of a computation method for the analysis of small punch test results, that can provide full scale material behavioural data. The results of this could lead to further development of the inverse analysis method for predicting material behaviour from small punch test data, with eventual application in irradiated specimens.
- The inverse analysis method was further advanced to look at the optimisation of the Johnson-Cook damage model. Time restrictions meant that only the initial stages of development could be completed. As such focus was aimed at analysing the effect of friction in the damage and failure portion of the force-deflection curve.
- The importance of the role of friction between the punch head and specimen was also demonstrated. This was achieved by completing a series of optimisations using a range of

friction coefficients (μ=0.3 – 0.57). This demonstrated that an increase in friction coefficient lead to a decrease in displacement at failure.

- The optimisation produced an improvement on the initial estimates. Displacement at failure displaying the most significant improvement, with all results falling well below the experimental values. The force at failure, while also displaying an improvement, did not produce conservative results, thus highlighting an area for further development.
- This final section of the project presented the starting point for the development of the optimisation of damage and failure behaviour in the small punch test. As such, the results were limited, revealing the areas in need of significant improvement.
- However, the effective improvement in the sample deflection values showed the potential this methodology holds for predicting the damage and failure behaviour of small punch test specimens.
- Overall the methodology presented in this thesis offers another means of confidently estimating bulk-scale material properties, using small punch test data.

8.2 Recommendations

From these conclusions, future work can be advised:

- The script developed for the analysis of experimental test results could be improved by addition of proof stress and ultimate tensile strength calculations. This would produce a program that would analyse the force deflection curve and calculate relevant estimates in one step, with the potential to add in further calculations as understanding of the small punch test increases.
- Further research surrounding the overestimations present in the best practice proof stress calculations is also recommended.
- The Nelder-Mead algorithm was used for optimisation throughout the project. While computationally efficient, is somewhat simplistic and a more sophisticated algorithm may be required. The selection of a different algorithm would mean that boundary conditions could be applied for each constant, ensuring a higher success rate and increased overall efficiency
- Additional research into the behaviour of less ductile metals, with a view to simulating and optimising Johnson-Cook constants. This will be of particular importance as the irradiated materials become available for testing.
- The addition of the punch and dies as deformable solids is suggested. This would greatly increase the computational expense required but would provide the opportunity to assess the influence of machinery compliance.
- The development of a secondary simulation that is a 90˚ rotation of a specimen instead of the full 360˚ to improve on computational cost and time. A 90˚ rotation should also allow for the simulation of misaligned sample and inhomogeneous materials.
- An overall improvement in the ductile damage and necking behaviour of the model is required. This may require the adjustment of mesh settings, or further optimisation of other behaviour parameters. In general, a more thorough understanding of the deformation and failure behaviour is essential. This would involve extensive experimental analysis of necking and fracture of the small punch test specimens.

- The addition of micro-CT scan 3D renders of deformed and failed samples may aid in the estimation of the friction coefficient between punch head and specimen by means of visual analysis.

- The model could be further improved by the inclusion of additional materials propertied to the model. For example, the addition of properties to the punch and dies would allow for the assessment of the influence of their distortion throughout the test. Thus providing a better picture of the overall compliance within the testing rig. This however would greatly increase the computational cost of the simulation and so this must be done in concurrence with previously stated efficiency changes, i.e., the creation of a 90˚ rotation model.

- The final recommendation is to look toward the implementation of a tensile test simulation for the purposes of validation. This would allow for a somewhat direct comparison of and optimised Johnson-Cook results with bulk scale behaviour. The production of this simulation would become another step toward providing a robust level of quality assurance in small punch testing.

References

[1] J. Ongena and G. Van Oost, “Energy for future centuries: Prospects for fusion power as a future energy source,” *Fusion Sci. Technol.*, vol. 61, no. 2 T, pp. 3–16, 2012.

[2] M. Victoria, N. Baluc, and P. Spätig, “Structural materials for fusion reactors,” *Nucl. Fusion*, vol. 41, no. 8, pp. 1047–1053, 2002.

[3] S. J. Zinkle, “Advanced materials for fusion technology,” *Fusion Eng. Des.*, vol. 74, no. 1–4, pp. 31–40, Nov. 2005.

[4] R. H. Jones, H. L. Heinisch, and K. A. McCarthy, “Low activation materials,” *J. Nucl. Mater.*, vol. 271–272, pp. 518–525, May 1999.

[5] M. R. Gilbert and J. C. Sublet, “Neutron-induced transmutation effects in W and W-alloys in a fusion environment,” *Nucl. Fusion*, vol. 51, no. 4, 2011.

[6] T. S. Ashton, *The Industrial Revolution 1760-1830*. Oxford University Press, 1997.

[7] J. G. Canadell *et al.*, “Contributions to accelerating atmospheric CO2 growth from economic activity, carbon intensity, and efficiency of natural sinks.,” *Proc. Natl. Acad. Sci. U. S. A.*, vol. 104, no. 47, pp. 18866–70, Nov. 2007.

[8] NASA, “Global Climate Change - Global Temperature,” 2017. [Online]. Available: https://climate.nasa.gov/vital-signs/global-temperature/. [Accessed: 22-Jun-2017].

[9] R. T. Pierrehumbert, M. Sato, R. Ruedy, K. Lo, D. W. Lea, and M. Medina-Elizade, “Climate change and the tropical Pacific: the sleeping dragon wakes.,” *Proc. Natl. Acad. Sci. U. S. A.*, vol. 97, no. 4, pp. 1355–8, Feb. 2000.

[10] M. McGrath, “‘Reasons to be hopeful’ on 1.5C global temperature target,” *BBC News*, 03-Oct-2018.

[11] E. E. Angino, “High-Level and Long-Lived Radioactive Waste Disposal,” *Science (80-.).*, vol. 198, 1977.

[12] M. J. Goodfellow, H. R. Williams, and A. Azapagic, “Nuclear renaissance, public perception and design criteria: An exploratory review,” *Energy Policy*, vol. 39, no. 10, pp. 6199–6210, 2011.

[13] G. Steinhauser, A. Brandl, and T. E. Johnson, “Comparison of the Chernobyl and Fukushima nuclear accidents: A review of the environmental impacts,” *Sci. Total Environ.*, vol. 470–471, pp. 800–817, 2014.

[14] R. Toschi, “Nuclear fusion, an energy source,” *Fusion Eng. Des.*, vol. 36, no. 1, pp. 1–8, Apr. 1997.

[15] M. S. El Naschie, “From E = mc2 to E = mc2/22—A Short Account of the Most Famous Equation in Physics and Its Hidden Quantum Entanglement Origin,” *J. Quantum Inf. Sci.*, vol. 04, no. December, pp. 284–291, 2014.

[16] B. Viswanathan, “Chapter 6 - Nuclear Fusion,” B. B. T.-E. S. Viswanathan, Ed. Amsterdam: Elsevier, 2017, pp. 127–137.

[17] W. J. Nuttall, “Fusion as an energy source: Challenges and Opportunities,” 2008.

[18] H. Yukawa, “On the Interaction of Elementary Particles. I,” *Prog. Theor. Phys. Suppl.*, vol. 1, pp. 46–71, 1934.

[19] H. Yukawa and S. Sakata, “On the interaction of elementary particles II,” *Prog. Theor. Phys. Suppl.*, no. 1, pp. 1689–1699, 1937.

[20] H. Yukawa, S. Sakata, and M. Taketani, “On the Interaction of Elementary Particles III,” *Prog. Theor. Phys. Suppl.*, vol. 319–340, 1937.

[21] M. A. Hussein, “Chapter 1 - Mechanisms,” E. M. A. B. T.-R. M. Hussein, Ed. Oxford: Elsevier Science Ltd, 2007, pp. 1–65.

[22] “If the strong nuclear force is stronger than electrostatic repulsion, why don’t nuclei collapse into a point?,” 2016. [Online]. Available: https://physics.stackexchange.com/q/270246.

[23] M. H. Pryce, “The energy levels of Pb205,” *Nucl. Phys.*, vol. 2, pp. 226–238, 1956.

[24] L. Meitner and O. R. Frisch, “Disintegration of Uranium by Neutrons: a New Type of Nuclear Reaction,” *Nature*, vol. 143, no. 3615, pp. 239–240, 1939.

[25] IAEA, “Climate change and nuclear power 2016,” 2016.

[26] G. Audi, A. H. Wapstra, and C. Thibault, “The Ame2003 atomic mass evaluation - (II). Tables, graphs and references,” *Nucl. Phys. A*, vol. 729, no. 1, pp. 337–676, 2003.

[27] J. Ongena, R. Koch, R. Wolf, and H. Zohm, “Erratum: Magnetic-confinement fusion,” *Nat. Phys.*, vol. 12, no. 7, pp. 717–717, 2016.

[28] R. W. . Conn, “Nuclear Fusion,” *Encyclopedia Britannica*. Encyclopædia Britannica, inc., 2019.

[29] J. H. You *et al.*, “Conceptual design studies for the European DEMO divertor: Rationale and first results,” *Fusion Eng. Des.*, vol. 109–111, no. PartB, pp. 1598–1603, 2016.

[30] “Fusion Energy: How fusion works.” [Online]. Available: http://www.ccfe.ac.uk/How_fusion_works.aspx. [Accessed: 11-Feb-2019].

[31] T. Donné, “European Research Roadmap to the Realisation of Fusion Energy,” 2018.

[32] M. R. Gilbert, S. L. Dudarev, S. Zheng, L. W. Packer, and J.-C. Sublet, “An integrated model for materials in a fusion power plant: transmutation, gas production, and helium embrittlement under neutron irradiation,” *Nucl. Fusion*, vol. 52, no. 8, p. 083019, 2012.

[33] J. A. Brinkman, “On the nature of radiation damage in metals,” *J. Appl. Phys.*, vol. 25, no. 8, pp. 961–970, 1954.

[34] G. H. Kinchin and R. S. Pease, “The Displacement of Atoms in Solids by Radiation,” *Reports Prog. Phys.*, vol. 18, no. 1, p. 1, 1955.

[35] S. J. Zinkle and G. S. Was, “Materials challenges in nuclear energy,” *Acta Mater.*, vol. 61, no. 3, pp. 735–758, 2013.

[36] O. D. Kazachkovskii, “Radiation swelling of materials,” *At. Energy*, vol. 81, no. 2, pp. 605–610, 1996.

[37] M. R. Gilbert, S. L. Dudarev, S. Zheng, and L. W. Packer, “Transmutation , gas production , and helium embrittlement in materials under neutron irradiation,” 2012.

[38] A. Kryukov, L. Debarberis, U. von Estorff, F. Gillemot, and F. Oszvald, “Irradiation embrittlement of reactor pressure vessel steel at very high neutron fluence,” *J. Nucl. Mater.*, vol. 422, no. 1–3, pp. 173–177, Mar. 2012.

[39] D. Olander, “Chapter 19 - Fundamental Aspects of Nuclear Reactor Fuel Elements,” Us Dept of Energy, 1976.

[40] E. A. Little, “Void-swelling in irons and ferritic steels: I. Mechanisms of swelling suppression,” *J. Nucl. Mater.*, vol. 87, no. 1, pp. 11–24, Nov. 1979.

[41] D. McLean, “The physics of high temperature creep in metals,” *Reports Prog. Phys.*, vol. 29, no. 1, p. 301, 1966.

[42] M. E. Kassner and M. T. Prez-Prado, “Five-power-law creep in single phase metals and alloys,” *Prog. Mater. Sci.*, vol. 45, no. 1, pp. 1–102, 2000.

[43] D. L. Porter and F. A. Garner, “Irradiation creep and embrittlement behavior of AISI 316 stainless steel at very high neutron fluences,” *J. Nucl. Mater.*, vol. 159, no. C, pp. 114–121, 1988.

[44] A. Boltax, J. P. Foster, R. A. Weiner, and A. Biancheria, “Void swelling and irradiation creep relationships,” *J. Nucl. Mater.*, vol. 65, no. C, pp. 174–183, 1977.

[45] D. Stork *et al.*, “Developing structural, high-heat flux and plasma facing materials for a near-term DEMO fusion power plant: The EU assessment,” *J. Nucl. Mater.*, vol. 455, no. 1–3, pp. 277–291, 2014.

[46] P. Garin and M. Sugimoto, “Main baseline of IFMIF/EVEDA project,” *Fusion Eng. Des.*, vol. 84, no. 2–6, pp. 259–264, Jun. 2009.

[47] M. Martone, “IFMIF - International Fusion Materials Facility Conceptual Design Activity,” 2000.

[48] P. Rocco and M. Zucchetti, “Criteria for defining low activation materials in fusion reactor applications,” *Fusion Eng. Des.*, vol. 15, no. 3, pp. 235–244, 1992.

[49] A. Möslang *et al.*, “Towards reduced activation structural materials data for fusion DEMO reactors,” *Nucl. Fusion*, vol. 45, no. 7, pp. 649–655, 2005.

[50] P. Fernandez, A. M. Lancha, J. Lapena, D. Gomez-Briceno, M. Serrano, and M. Hernandez-Mayoral, “Reduced Activation Ferritic/Martensitic Steel Eurofer’97 as Possible Structural Material for Fusion Devices. Metallurgical Characterization on As-Received Condition and After Simulated Service Conditions.,” *Inf. Técnicos Ciemat*, p. 73, 2004.

[51] L. El-Guebaly, V. Massaut, K. Tobita, and L. Cadwallader, “Evaluation of Recent Scenarios for Managing Fusion Activated Materials: Recycling and Clearance, Avoiding Disposal,” Madison, 2008.

[52] M. J. Gorley, “Critical Assessment 12: Prospects for reduced activation steel for fusion plant,” *Mater. Sci. Technol.*, vol. 31, no. 8, pp. 975–980, 2015.

[53] N. Taylor, S. Ciattaglia, P. Cortes, M. Iseli, S. Rosanvallon, and L. Topilski, “ITER safety and licensing update,” *Fusion Eng. Des.*, vol. 87, no. 5–6, pp. 476–481, Aug. 2012.

[54] P. Hosemann, “Small-scale mechanical testing on nuclear materials: bridging the experimental length-scale gap,” *Scr. Mater.*, vol. 143, pp. 161–168, Jan. 2018.

[55] A. M. Abazari, S. M. Safavi, G. Rezazadeh, and L. G. Villanueva, “Size Effects on Mechanical Properties of Micro / Nano Structures,” *Sensors*, vol. 15, no. 11, pp. 1–19, 2015.

[56] S. Nunomura, A. Hishinuma, and R. Nunomura, “Evaluation of Tensile Properties Using a TEM Disk-Size Specimen,” in *Small Specimen Test Techniques Applied to Nuclear Reactor Vessel Thermal Annealing and Plant Life Extension*, 2019.

[57] J. R. Greer and J. T. M. De Hosson, “Plasticity in small-sized metallic systems: Intrinsic versus

extrinsic size effect," *Prog. Mater. Sci.*, vol. 56, no. 6, pp. 654–724, 2011.

[58] E. W. Hart, "Theory of the tensile test," *Acta Metall.*, vol. 15, no. 2, pp. 351–355, 1967.

[59] J. R. Davis, *Tensile Testing, 2nd Edition*. ASM International, 2004.

[60] D. J. Han and W. Chen, *Plasticity for structural engineers*. Springer US, 1988.

[61] I. S. Yasnikov, A. Vinogradov, and Y. Estrin, "Revisiting the Considère criterion from the viewpoint of dislocation theory fundamentals," *Scr. Mater.*, vol. 76, pp. 37–40, 2014.

[62] M. Considére, "L'emploi du fer et de L'acier dans les constructions," *Ann. des ponts chaussées*, vol. 34, no. 1, pp. 574–583, 1885.

[63] H. W. Swift, "Plastic instability under plane stress," *J. Mech. Phys. Solids*, vol. 1, pp. 1–18, 1952.

[64] R. Hill, "On discontinuous reference plastic states, with reference to localised necking in thin sheets," *J. Mech. Phys. Solids*, vol. 1, pp. 19–30, 1952.

[65] M. S. Loveday, T. Gray, and J. Aegerter, "Tensile Testing of Metallic Materials : A Review," 2004.

[66] ASTM Committee on Mechanical Testing, "ASTM E8/E8M - Standard Test Methods for Tension Testing of Metallic Materials," *ASTM Int.*, vol. ASTM Stds., no. Designation: E8/E8M-13a, pp. 1–28, 2013.

[67] BSI, "BSI Standards Publication Metallic materials — Tensile testing Part 1 : Method of test at room temperature," *Bsi*, 2016.

[68] U. F. Kocks, "The relation between polycrystal deformation and single-crystal deformation," *Metall. Mater. Trans.*, vol. 1, no. 5, pp. 1121–1143, 1970.

[69] D. Diez and J. DeRose, "How to Adapt Grain Size Analysis of Metallic Alloys to Your Needs," *Leica Microsystems*, 2019. [Online]. Available: https://www.leica-microsystems.com/science-lab/how-to-adapt-grain-size-analysis-of-metallic-alloys-to-your-needs/. [Accessed: 05-Aug-2020].

[70] ASTM Committee on Mechanical Testing, "ASTM E09-19 - Standard Test Methods of Compression Testing of Metallic Materials at Room Temperature," vol. 09, no. Reapproved 2018, pp. 1–11, 2012.

[71] H. S. Valberg, *Applied Metal Forming: Including FEM Analysis*. 2010.

[72] M. Al-Chalabi and C. L. Huang, "Stress distribution within circular cylinders in compression," *Int. J. Rock Mech. Min. Sci. Geomech.*, vol. 11, no. 2, pp. 45–56, 1974.

[73] J. F. Labuz and J. M. Bridell, "Reducing frictional constraint in compression testing through lubrication," *Int. J. Rock Mech. Min. Sci. Geomech.*, vol. 30, no. 4, pp. 451–455, 1993.

[74] L. N. G. Filon, "On the elastic equilibrium of circulat cylinders under certain practical systems of load," 1901.

[75] B. T. Brady, "An exact solution to the radially end-constrained circular cylinder under triaxial loading," *Int. J. Rock Mech. Min. Sci.*, vol. 8, no. 2, pp. 165–178, 1971.

[76] J. Rasti, A. Najafizadeh, and M. Meratian, "Correcting the stress-strain curve in hot compression test using finite element analysis and Taguchi method," *Int. J. ISSI*, vol. 8, no. 1, pp. 26–33, 2011.

[77] ASTM Committee on Mechanical Testing, “ASTM E290 - 14: Standard Test Methods for Bend Testing of Material for Ductility,” ASTM-E290, 1998.

[78] ASTM, “D790 - Flexural Properties of Unreinforced and Reinforced Plastics and Electrical Insulating Materials,” 2017.

[79] K. M. Zhao and J. K. Lee, “Finite element analysis of the three-point bending of sheet metals,” *J. Mater. Process. Technol.*, vol. 122, no. 1, pp. 6–11, 2002.

[80] S. L. Zang, M. G. Lee, L. Sun, and J. H. Kim, “Measurement of the Bauschinger behavior of sheet metals by three-point bending springback test with pre-strained strips,” *Int. J. Plast.*, vol. 59, pp. 84–107, 2014.

[81] ASTM Committee on Mechanical Testing, “ASTM E92 - Standard Test Methods for Vickers Hardness and Knoop Hardness of Metallic Materials,” 2019.

[82] P. Zhang, S. X. Li, and Z. F. Zhang, “General relationship between strength and hardness,” *Mater. Sci. Eng. A*, vol. 529, no. 1, pp. 62–73, 2011.

[83] ASTM Committee on Mechanical Testing, “ASTM E23 − 18 Standard Test Methods for Notched Bar Impact Testing of Metallic Materials,” *Am. Soc. Test. Mater.*, pp. 1–26, 2018.

[84] K. W. Strabala, “The Effects of Combined Compression and Aging on the Properties of Glassy Polycarbonate,” 2009.

[85] M. F. Ashby, *Materials*. 2014.

[86] Y. N. Rabotnov, “Creep Rupture,” *Int. Union Theor. Appl. Mech.*, 1969.

[87] ASTM Committee on Mechanical Testing, “ASTM E139 - 11: Standard Test Method for Conducting Creep, Creep-Rupture, and Stress-Rupture Tests of Metallic Materials,” 2018.

[88] ASTM Committee on Mechanical Testing, “ASTM E466 -15: Practice for conducting force controlled constant amplitude axial fatigue tests of metallic materials,” 2015.

[89] A. P. B. T.-I. to A. M. Mouritz, Ed., “5 - Mechanical and durability testing of aerospace materials,” Woodhead Publishing, 2012, pp. 91–127.

[90] ASTM Committee on Mechanical Testing, “ASTM E468-11 - Standard Practice for Presentation of Constant Amplitude Fatigue Test Results for Metallic Materials,” 2011.

[91] S. Thomas, “Power-plant life extension,” *Energy*, vol. 13, no. 10, pp. 767–786, 1988.

[92] P. Trampus, “Role and importance of NDE in nuclear power plant life extension,” *Procedia Struct. Integr.*, vol. 16, pp. 161–168, 2019.

[93] “CWA 15627 - Small Punch Test Method for Metallic Materials,” 2007.

[94] K. Kumar *et al.*, “Use of miniature tensile specimen for measurement of mechanical properties,” *Procedia Eng.*, vol. 86, pp. 899–909, 2014.

[95] D. Marriot, S. Read, and A. Sreeranganathan, “The Use of Miniature Test Specimens in Fitness-for-Service Evaluation,” *Inspection Engineering*, 2016.

[96] A. Sesonske, *Nuclear Power Plant Design Analysis*, vol. 19, no. 2. United States Atomic Energy Commission, 1973.

[97] D. Mun and J. Yang, “An integrated translation of design data of a nuclear power plant from a specification-driven plant design system to neutral model data,” *Ann. Nucl. Energy*, vol. 37, no. 3, pp. 389–397, 2010.

[98] M. Ciampoli and B. R. Ellingwood, "Probabilistic methods for assessing current and future performance of concrete structures in nuclear power plants," *Mater. Struct. Constr.*, vol. 34, no. 245, pp. 3–14, 2002.

[99] A. Moeslang, V. Heinzel, H. Matsui, and M. Sugimoto, "The IFMIF test facilities design," *Fusion Eng. Des.*, vol. 81, no. 8–14, pp. 863–871, Feb. 2006.

[100] K. Ehrlich and A. Möslang, "IFMIF – An international fusion materials irradiation facility," *Nucl. Instruments Methods Phys. Res. Sect. B Beam Interact. with Mater. Atoms*, vol. 139, no. 1–4, pp. 72–81, Apr. 1998.

[101] Perkin Elmer, "A Guide to the Safe Handling of Radioactive Materials in Research," Waltham, 2007.

[102] IAEA, "Hot Cell Post-irradiation Examination and Poolside Inspection of Nuclear Fuel," in *IAEA-HOTLAB*, 2011.

[103] B. C. Oberlander, M. Espeland, and N. O. Solum, "Experiences from Refurbishment of Metallography Hot Cells & Application of a New Preparation Concept for Materialography Samples," in *Proceedings of XXXIX Plenary Meeting of the European Working Group. Hot Laboratories and Remote Handling*, 2001.

[104] Westinghouse Electric Company LLC, "Westinghouse Hot Cell Facility and Laboratories," 2017.

[105] M. Ohmi, J. Saito, and T. Ishii, "Development of a Remote Controlled Small Punch Testing Machine for Nuclear Fusion Research," in *JAERI-Conf 99-009*, 1999, pp. 151–162.

[106] "Argonne National Laboratory - Irradiated materials facility," *ANL*, 2020. [Online]. Available: https://www.anl.gov/nse/irradiated-materials-laboratory. [Accessed: 27-May-2020].

[107] S. Murugan, V. Karthik, K. A. Gopal, R. V. Kumar, J. Joseph, and T. Jayakumar, "Irradiation Experiment to Determine Effect of Long Term Low Dose Irradiation on FBTR Grid Plate Material," Kalpakkam, 2013.

[108] J. Bredl, M. Dany, H.-C. Schneider, and O. Kraft, "Instrumented indentation at elevated temperatures for determination of material properties of fusion relevant materials," *Nucl. Mater. Energy*, vol. 9, pp. 502–507, Dec. 2016.

[109] G. E. Lucas, "Review of small specimen test techniques for irradiation testing," *Metall. Trans. A*, vol. 21, no. 5, pp. 1105–1119, 1990.

[110] D. S. Gianola and C. Eberl, "Micro- and nanoscale tensile testing of materials," *Nanomechanical Characterization*, pp. 24–35, 2009.

[111] K. J. Hemker and W. N. Sharpe, "Microscale Characterization of Mechanical Properties," *Annu. Rev. Mater. Res.*, vol. 37, no. 1, pp. 93–126, 2007.

[112] W. Vandermeulen, J.-L. Puzzolante, and M. Scibetta, "Understanding of Tensile Test Results on Small Size Specimens of Certified Reference Material BCR-661," *J. Test. Eval.*, vol. 45, no. 2, p. 20150377, 2017.

[113] P. Hosemann, C. Shin, and D. Kiener, "Small scale mechanical testing of irradiated materials," *J. Mater. Res.*, vol. 30, no. 9, pp. 1231–1245, 2015.

[114] M. D. Uchic, D. M. Dimiduk, J. N. Florando, and W. D. Nix, "Sample dimensions influence strength and crystal plasticity," *Science*, vol. 305, no. 5686, pp. 986–989, 2004.

[115] K. Akira and K. Hirotatsu, “SiC / SiC composite materials for nuclear applications,” *Nucl. Saf. Simul.*, vol. 4, no. 2, pp. 72–79, 2013.

[116] D. Di Maio and S. G. Roberts, “Measuring fracture toughness of coatings using focused-ion-beam-machined microbeams,” *J. Mater. Res.*, vol. 20, no. 2, pp. 299–302, 2005.

[117] Q. Wang, N. Guo, F. Long, and M. R. Daymond, “Effects of heavy ion irradiation on Zr-2.5Nb pressure tube alloy. I. Orientation dependent mechanical response,” *J. Appl. Phys.*, vol. 125, no. 8, 2019.

[118] W. D. Nix and H. Gao, “Indentation size effects in crystalline materials: A law for strain gradient plasticity,” *J. Mech. Phys. Solids*, vol. 46, no. 3, 1998.

[119] S. P. Baker, “Nanoindentation Techniques,” *Encycl. Mater. Sci. Technol.*, pp. 5908–5915, Jan. 2001.

[120] J. H. Lee, T. Kim, and H. Lee, “A study on robust indentation techniques to evaluate elastic-plastic properties of metals,” *Int. J. Solids Struct.*, vol. 47, no. 5, pp. 647–664, 2010.

[121] J. Kazakeviciute, J. P. Rouse, D. S. A. De Focatiis, and C. J. Hyde, “The development of a novel technique for small ring specimen tensile testing,” *Theor. Appl. Fract. Mech.*, vol. 99, no. October 2018, pp. 131–139, 2019.

[122] C. J. Hyde, T. H. Hyde, W. Sun, S. Nardone, and E. De Bruycker, “Small ring testing of a creep resistant material,” *Mater. Sci. Eng. A*, vol. 586, pp. 358–366, 2013.

[123] T. H. Hyde, B. S. M. Ali, and W. Sun, “Analysis and design of a small, two-bar creep test specimen,” *J. Eng. Mater. Technol. Trans. ASME*, vol. 135, no. 4, 2013.

[124] T. H. Hyde, W. Sun, and J. A. Williams, “Requirements for and use of miniature test specimens to provide mechanical and creep properties of materials: A review,” *Int. Mater. Rev.*, vol. 52, no. 4, pp. 213–255, 2007.

[125] J. P. Rouse, F. Cortellino, W. Sun, T. H. Hyde, and J. Shingledecker, “Small punch creep testing: review on modelling and data interpretation,” *Mater. Sci. Technol.*, vol. 29, no. 11, pp. 1328–1345, 2013.

[126] K. Milička and F. Dobeš, “Small punch testing of P91 steel,” *Int. J. Press. Vessel. Pip.*, 2006.

[127] J. Petzová, M. Březina, M. Kapusňák, and K. L, “Application of small punch testing methods for thermal ageing monitoring at primary circuit components in nuclear power plant,” in *ASME 2015 Pressure Vessels and Piping Conference*, 2015.

[128] M. Bruchhausen *et al.*, “European standard on small punch testing of metallic materials,” in *Ubiquity Proceedings*, 2018, vol. 1, no. S1, p. 11.

[129] M. Song, K. Guan, W. Qin, and J. A. Szpunar, “Comparison of mechanical properties in conventional and small punch tests of fractured anisotropic A350 alloy forging flange,” *Nucl. Eng. Des.*, vol. 247, pp. 58–65, Jun. 2012.

[130] K. Li, J. Peng, and C. Zhou, “Construction of whole stress-strain curve by small punch test and inverse finite element,” *Results Phys.*, vol. 11, pp. 440–448, Dec. 2018.

[131] E. Altstadt, M. Houska, I. Simonovski, M. Bruchhausen, S. Holmström, and R. Lacalle, “On the estimation of ultimate tensile stress from small punch testing,” *Int. J. Mech. Sci.*, vol. 136, no. November 2017, p. E. Altstadt, M. Houska, I. Simonovski, M. B, 2018.

[132] E. M. Rabenberg, “Small specimen test techniques for evaluating radiation-induced changes

in mechanical properties," Boise State University, 2012.

[133] D. T. Blagoeva and R. C. Hurst, "Application of the CEN (European Committee for Standardization) small punch creep testing code of practice to a representative repair welded P91 pipe," *Mater. Sci. Eng. A*, vol. 510–511, no. C, pp. 219–223, 2009.

[134] *Computer-Aided Materials Selection During Structural Design*. Washington, DC: National Academies Press, 1995.

[135] *Testing for Prediction of Material Performance in Structures and Components*. American Soc. for Testing and Materials, 1972.

[136] T. Nakata, S. ichi Komazaki, Y. Kohno, and H. Tanigawa, "Development of a small punch testing method to evaluate the creep property of high Cr ferritic steel: Part II - Stress analysis of small punch test specimen by finite element method," *Mater. Sci. Eng. A*, vol. 666, pp. 80–87, 2016.

[137] M. F. Moreno, G. Bertolino, and A. Yawny, "The significance of specimen displacement definition on the mechanical properties derived from Small Punch Test," *Mater. Des.*, vol. 95, pp. 623–631, 2016.

[138] I. Peñuelas, I. I. Cuesta, C. Betegón, C. Rodriguez, and F. J. Belzunce, "Inverse determination of the elastoplastic and damage parameters on small punch tests," *Fatigue Fract. Eng. Mater. Struct.*, vol. 32, no. 11, pp. 872–885, 2009.

[139] R. Kopriva, I. Eliasova, and M. Kytka, "Implementation of small punch testing and automated ball indentation in the process of irradiated NPP materials degradation evaluation," in *International Conference on Nuclear Engineering, Proceedings, ICONE*, 2016, vol. 5, pp. 1–5.

[140] M. P. Manahan, A. S. Argon, and O. K. Harling, "The development of a miniaturized disk bend test for the determination of postirradiation mechanical properties," *J. Nucl. Mater.*, vol. 104, pp. 1545–1550, Jan. 1981.

[141] M. P. Manahan, "A New Post-irradiation Mechanical Behavior Test- The Miniaturized Disk Bend Test - Manahan," *Nucl. Technol.*, vol. 63, 1983.

[142] "Scopus - Analyze search results," *Scopus*, 2020. [Online]. Available: https://www.scopus.com/term/analyzer.uri?sid=f1d0456a2c49e5d2cb4502f916892bba&origin=resultslist&src=s&s=TITLE-ABS-KEY%28Small+punch+testing%29&sort=cp-f&sdt=b&sot=b&sl=34&count=1081&analyzeResults=Analyze+results&txGid=2126753956e545d1a2d45838f8f9c485.

[143] T. Misawa, H. Sugawara, R. Miura, and Y. Hamaguchi, "Small specimen fracture toughness tests of HT-9 steel irradiated with protons," *J. Nucl. Mater.*, vol. 133–134, pp. 313–316, Aug. 1985.

[144] J. Kameda and O. Buck, "Evaluation of the ductile-to-brittle transition temperature shift due to temper embrittlement and neutron irradiation by means of a small-punch test," *Mater. Sci. Eng.*, vol. 83, no. 1, pp. 29–38, Oct. 1986.

[145] T. Misawa, T. Adachi, M. Saito, and Y. Hamaguchi, "Small punch tests for evaluating ductile-brittle transition behavior of irradiated ferritic steels," *J. Nucl. Mater.*, vol. 150, no. 2, pp. 194–202, Oct. 1987.

[146] X. Mao and H. Takahashi, "Development of a further-miniaturized specimen of 3 mm diameter for tem disk (ø 3 mm) small punch tests," *J. Nucl. Mater.*, vol. 150, no. 1, pp. 42–52, Sep. 1987.

[147] M. Bruchhausen *et al.*, “Recent developments in small punch testing: Tensile properties and DBTT,” *Theor. Appl. Fract. Mech.*, vol. 86, pp. 2–10, Dec. 2016.

[148] E. N. Campitelli, P. Spätig, R. Bonadé, W. Hoffelner, and M. Victoria, “Assessment of the constitutive properties from small ball punch test: Experiment and modeling,” *J. Nucl. Mater.*, 2004.

[149] K. Kumar *et al.*, “Evaluation of ultimate tensile strength using Miniature Disk Bend Test,” *J. Nucl. Mater.*, vol. 461, pp. 100–111, Jun. 2015.

[150] R. J. Lancaster, S. P. Jeffs, H. W. Illsley, C. Argyrakis, R. C. Hurst, and G. J. Baxter, “Development of a novel methodology to study fatigue properties using the small punch test,” *Mater. Sci. Eng. A*, vol. 748, no. January, pp. 21–29, 2019.

[151] D. T. S. Lewis, R. J. Lancaster, S. P. Jeffs, H. W. Illsley, S. J. Davies, and G. J. Baxter, “Characterising the fatigue performance of additive materials using the small punch test,” *Mater. Sci. Eng. A*, vol. 754, no. March, pp. 719–727, 2019.

[152] H. Wang, T. Xu, and J. Zou, “Comparative study between small punch test and hydraulic bulge test,” in *Ubiquity Proceedings*, 2018, vol. 1, no. S1, p. 46.

[153] CEN (Comité Européen de Normalisation), “Workshop Agreement Small Punch Test Method for Metallic Materials,” *Small Punch Test Method Met. Mater.*, pp. 1-38 Part A and 1–32 Part B, 2006.

[154] CEN (Comité Européen de Normalisation), “BS EN 10371:2021 Metallic materials - Small punch test method,” 2021.

[155] ASTM Committee on Mechanical Testing, “ASTM E3205 - 20: Standard test method for small punch testing of metallic materials.”

[156] T. Nakata, S. ichi Komazaki, Y. Kohno, and H. Tanigawa, “Development of a small punch testing method to evaluate the creep property of high Cr ferritic steel: Part I-Effect of atmosphere on creep deformation behavior,” *Mater. Sci. Eng. A*, vol. 666, pp. 54–60, 2016.

[157] T. E. García, C. Rodríguez, F. J. Belzunce, and C. Suárez, “Estimation of the mechanical properties of metallic materials by means of the small punch test,” *J. Alloys Compd.*, vol. 582, pp. 708–717, Jan. 2014.

[158] M. Bruchhausen, S. Holmström, J. M. Lapetite, and S. Ripplinger, “On the determination of the ductile to brittle transition temperature from small punch tests on Grade 91 ferritic-martensitic steel,” *Int. J. Press. Vessel. Pip.*, vol. 155, pp. 27–34, 2017.

[159] S. Holmström, I. Simonovski, D. Baraldi, M. Bruchhausen, E. Altstadt, and R. Delville, “Developments in the estimation of tensile strength by small punch testing,” *Theor. Appl. Fract. Mech.*, vol. 101, pp. 25–34, Jun. 2019.

[160] S. Rasche and M. Kuna, “Improved small punch testing and parameter identification of ductile to brittle materials,” *Int. J. Press. Vessel. Pip.*, 2015.

[161] I. Simonovski, S. Holmström, and M. Bruchhausen, “Small punch tensile testing of curved specimens: Finite element analysis and experiment,” *Int. J. Mech. Sci.*, vol. 120, pp. 204–213, Jan. 2017.

[162] T. Nakata, S. Komazaki, Y. Kohno, and H. Tanigawa, “Effects of Geometry and Dimension of Specimen and Rig on Small Punch Creep Property,” *Exp. Mech.*, vol. 57, no. 3, pp. 487–494, 2017.

[163] H. Dawson, M. Richardson, M. Gorley, and E. Surrey, "The effect of testing environment on small punch creep," *Ubiquity Proc.*, vol. 1, no. S1, p. 15, 2018.

[164] G. Liu and S. Quek, "Chapter 3 - Fundamentals for Finite Element Method," in *The Finite Element Method: A Practical Course: Second Edition*, G. R. Liu and S. S. B. T.-T. F. E. M. (Second E. Quek, Eds. Oxford: Butterworth-Heinemann, 2014, pp. 43–79.

[165] G. R. Liu and S. S. Quek, "Chapter 11 - Modelling Techniques," in *The Finite Element Method: A Practical Course: Second Edition*, Butterworth-Heinemann, 2014, pp. 301–346.

[166] M. Yazdani, V. Jahdngiri, and M. S. Marefat, "Seismic performance assessment of plain concrete arch bridges under near-field earthquakes using incremental dynamic analysis," *Eng. Fail. Anal.*, vol. 106, no. May, p. 104170, 2019.

[167] M. Firat, "Computer aided analysis and design of sheet metal forming processes: Part I - The finite element modeling concepts," *Mater. Des.*, vol. 28, no. 4, pp. 1298–1303, 2007.

[168] P. Deshmukh and S. K. Pradhan, "Transient thermo-physical finite element analysis of brass wire during electro-discharge machining of INCONEL material," *Mater. Today Proc.*, vol. 27, no. 3, pp. 1990–1995, 2019.

[169] S. S. Yang, X. Ling, Y. Qian, and R. B. Ma, "Yield Strength Analysis by Small Punch Test Using Inverse Finite Element Method," *Procedia Eng.*, vol. 130, pp. 1039–1045, Jan. 2015.

[170] S. Yang, Y. Cao, X. Ling, and Y. Qian, "Assessment of mechanical properties of Incoloy800H by means of small punch test and inverse analysis," *J. Alloys Compd.*, vol. 695, pp. 2499–2505, Feb. 2017.

[171] R. J. Lancaster, H. W. Illsley, G. R. Davies, S. P. Jeffs, and G. J. Baxter, "Modelling the small punch tensile behaviour of an aerospace alloy," *Mater. Sci. Technol.*, vol. 0836, no. June, pp. 1–9, 2016.

[172] P. Egan, M. P. Whelan, F. Lakestani, and M. J. Connelly, "Small punch test: An approach to solve the inverse problem by deformation shape and finite element optimization," *Comput. Mater. Sci.*, vol. 40, pp. 33–39, 2007.

[173] C. Soyarslan, B. Gülçimen, S. Bargmann, and P. Hähner, "Modeling of fracture in small punch tests for small- and large-scale yielding conditions at various temperatures," *Int. J. Mech. Sci.*, vol. 106, pp. 266–285, 2016.

[174] G. E. Stavroulakis, G. Bolzon, Z. Waszczyszyn, and L. Ziemianski, *Inverse Analysis*. Elsevier, 2016.

[175] T. Sobh, *Innovations and Advances in Computer Sciences and Engineering*. Springer Netherlands, 2010.

[176] W. H. Swann, "Direct search methods," 1972.

[177] J. A. Nelder and R. Mead, "A Simplex Method for Function Minimization," *Comput. J.*, vol. 7, no. 4, pp. 308–313, 1965.

[178] L. Nazareth and P. Tseng, "Gilding the Lily: A Variant of the Nelder-Mead Algorithm Based on Golden-Section Search," *Comput. Optim. Appl.*, vol. 22, no. 1, pp. 133–144, 2002.

[179] A. Wouk, *New Computing Environments: Microcomputers in Large-scale Computing - Volume 27 of Proceedings in Applied Mathematics*. Society for Industrial and Applied Mathematics, 1987.

[180] V. K. Mehta and B. Dasgupta, "A constrained optimization algorithm based on the simplex search method," *Eng. Optim.*, vol. 44, no. 5, pp. 537–550, 2012.

[181] D. Whitley, "A genetic algorithm tutorial," *Stat. Comput.*, vol. 4, no. 2, pp. 65–85, 1994.

[182] G. R. Harik, F. G. Lobo, and D. E. Goldberg, "The compact genetic algorithm," *IEEE Trans. Evol. Comput.*, vol. 3, no. 4, pp. 287–297, 1999.

[183] J. Isselin, A. Iost, J. Golek, D. Najjar, and M. Bigerelle, "Assessment of the constitutive law by inverse methodology: Small punch test and hardness," *J. Nucl. Mater.*, vol. 352, no. 1–3, pp. 97–106, 2006.

[184] R. Natarajan, "Analysis of a Radial Drilling Machine Structure using Finite Element Method," *Comput. Struct.*, vol. 6, pp. 55–60, 1975.

[185] A. Shrot and M. Bäker, "A Study of Non-uniqueness During the Inverse Identification of Material Parameters," *Procedia CIRP*, vol. 1, pp. 72–77, Jan. 2012.

[186] S. V. Laakso and E. Niemi, "Using FEM simulations of cutting for evaluating the performance of different johnson cook parameter sets acquired with inverse methods," *Robot. Comput. Integr. Manuf.*, vol. 47, no. October 2016, pp. 95–101, 2017.

[187] S. V. A. Laakso and E. Niemi, "Determination of material model parameters from orthogonal cutting experiments," *Proc. Inst. Mech. Eng. Part B J. Eng. Manuf.*, vol. 230, no. 5, pp. 848–857, 2016.

[188] J. E. Plumeri, Ł. Madej, and W. Z. Misiolek, "Constitutive modeling and inverse analysis of the flow stress evolution during high temperature compression of a new ZE20 magnesium alloy for extrusion applications," *Mater. Sci. Eng. A*, Oct. 2018.

[189] L. Tan, L. L. Snead, and Y. Katoh, "Development of new generation reduced activation ferritic-martensitic steels for advanced fusion reactors," *J. Nucl. Mater.*, vol. 478, pp. 42–49, 2016.

[190] IAEA, "Technical Specifications EUROFER Material Database," 2008.

[191] "Online Data Information Network for Energy," *European Commission Joint Research Centre*, 2020. [Online]. Available: https://odin.jrc.ec.europa.eu/odin/controller?query=Login&target=/alcor/Main.jsp. [Accessed: 16-Jun-2020].

[192] M. Akhtar and A. Khajuria, "Effects of prior austenite grain size on impression creep and microstructure in simulated heat affected zones of boron modified P91 steels," *Mater. Chem. Phys.*, vol. 249, no. January, 2020.

[193] H. K. Al-Abedy, I. A. Jones, and W. Sun, "Small punch creep property evaluation by finite element of Kocks-Mecking-Estrin model for P91 at elevated temperature," *Theor. Appl. Fract. Mech.*, vol. 98, no. October, pp. 244–254, 2018.

[194] M. Eddahbi, M. A. Monge, T. Leguey, P. Fernández, and R. Pareja, "Texture and mechanical properties of EUROFER 97 steel processed by ECAP," *Mater. Sci. Eng. A*, vol. 528, no. 18, pp. 5927–5934, 2011.

[195] H. Z. M. Rieth, M. Schirra, A. Falkenstein, P. Graf, S. Heger, H. Kempe, R. Lindau, "Eurofer 97 Tensile, Charpy, Creep and Structural Tests," 2003.

[196] A. Banerjee, S. Dhar, S. Acharyya, D. Datta, and N. Nayak, "Determination of Johnson cook material and failure model constants and numerical modelling of Charpy impact test of armour steel," *Mater. Sci. Eng. A*, vol. 640, pp. 200–209, Jul. 2015.

[197] "SciPy," 2020. [Online]. Available: https://www.scipy.org/. [Accessed: 24-Feb-2020].

[198] "NumPy," 2020. [Online]. Available: https://numpy.org/. [Accessed: 24-Feb-2020].

[199] "matplotlib," 2020. [Online]. Available: https://matplotlib.org/. [Accessed: 24-Feb-2020].

[200] "TkInter," 2019. [Online]. Available: https://wiki.python.org/moin/TkInter. [Accessed: 20-Feb-2020].

[201] "pandas," 2020. [Online]. Available: https://pandas.pydata.org/. [Accessed: 24-Feb-2020].

[202] C. Rodríguez, M. Fernández, J. G. Cabezas, T. E. García, and F. J. Belzunce, "The use of the small punch test to solve practical engineering problems," *Theor. Appl. Fract. Mech.*, vol. 86, pp. 109–116, 2016.

[203] N. R, "HyperPhysics," 2001. [Online]. Available: http://hyperphysics.phy-astr.gsu.edu/hbase/hframe.html. [Accessed: 21-Jun-2017].

[204] "Solid (Continuum) elements," *MIT*. [Online]. Available: https://abaqus-docs.mit.edu/2017/English/SIMACAEELMRefMap/simaelm-c-solidcont.htm. [Accessed: 28-Aug-2020].

[205] "Element Definition," *MIT*. [Online]. Available: https://abaqus-docs.mit.edu/2017/English/SIMACAEMODRefMap/simamod-c-element.htm. [Accessed: 28-Aug-2020].

[206] X. Wang and J. Shi, "Validation of Johnson-Cook plasticity and damage model using impact experiment," *Int. J. Impact Eng.*, vol. 60, pp. 67–75, 2013.

[207] "Damage evolution and element removal for ductile metals," *MIT*. [Online]. Available: https://abaqus-docs.mit.edu/2017/English/SIMACAEMATRefMap/simamat-c-damageevolductile.htm.

[208] G. R. Johnson and W. H. Cook, "Fracture characteristics of three metals subjected to various strains, strain rates, temperatures and pressures," *Eng. Fract. Mech.*, vol. 21, no. 1, pp. 31–48, Jan. 1985.

[209] H. Hentati, I. Ben Naceur, W. Bouzid, and A. Maalej, "Numerical analysis of damage thermo-mechanical models," *Adv. Appl. Math. Mech.*, vol. 7, no. 5, pp. 625–643, 2015.

[210] K. Wang, "Calibration of the Johnson-Cook failure parameters as the chip separation criterion in the modelling of orthogonal metal cutting process," McMaster University, 2016.

[211] W. Dabboussi and J. A. Nemes, "Modeling of ductile fracture using the dynamic punch test," *Int. J. Mech. Sci.*, vol. 47, no. 8, pp. 1282–1299, Aug. 2005.

[212] Y. Prawoto, M. Fanone, S. Shahedi, M. S. Ismail, and W. B. Wan Nik, "Computational approach using Johnson-Cook model on dual phase steel," *Comput. Mater. Sci.*, vol. 54, no. 1, pp. 48–55, 2012.

[213] M. N. A. Nasr, "Effects of Sequential Cuts on Residual Stresses when Orthogonal Cutting Steel AISI 1045," *Procedia CIRP*, vol. 31, pp. 118–123, Jan. 2015.

[214] M. Murugesan and D. W. Jung, "Johnson cook material and failure model parameters estimation of AISI-1045 medium carbon steel for metal forming applications," *Materials (Basel).*, vol. 12, no. 4, 2019.

[215] G. H. Majzoobi and F. R. Dehgolan, "Determination of the constants of damage models," *Procedia Eng.*, vol. 10, pp. 764–773, Jan. 2011.

[216] S. Yang, J. Zhou, X. Ling, and Z. Yang, “Effect of geometric factors and processing parameters on plastic damage of SUS304 stainless steel by small punch test,” *Mater. Des.*, vol. 41, pp. 447–452, 2012.

[217] F. Cortellino, W. Sun, and T. Hyde, “On the effects of friction modelling on small punch creep test responses: A numerical investigation,” *J. Strain Anal. Eng. Des.*, vol. 51, no. 7, pp. 493–506, 2016.

[218] A. Kumar, “Implicit vs. explicit schemes in Abaqus,” *TATA Technologies*, 2017. [Online]. Available: http://blog.myigetit.com/2017/09/18/implicit-vs-explicit-schemes-in-abaqus/.

[219] “European Commission Joint Research Centre’s Online Data Information Network for Energy,” 2019. [Online]. Available: https://odin.jrc.ec.europa.eu/odin/controller?query=Login&target=/alcor/Main.jsp. [Accessed: 12-Mar-2019].

[220] A. Ruiz-Moreno, P. Hähner, F. Fumagalli, V. Haiblikova, M. Conte, and N. Randall, “Stress−strain curves and derived mechanical parameters of P91 steel from spherical nanoindentation at a range of temperatures,” *Mater. Des.*, vol. 194, pp. 1–12, 2020.

[221] L. Kruszka, M. Grązka, G. Riganti, J. Janiszewski, E. Cadoni, and D. Forni, “Identification Methods of Parameters for Johnson-Cook Constitutive Equation – Comparison,” *Appl. Mech. Mater.*, vol. 566, pp. 97–103, 2014.

[222] J. L. Bryant and N. P. Wilburn, “Handbook of Software Quality Assurance Techniques Applicable to the Nuclear Industry,” 1897.

[223] G. G. Schulmeyer and J. I. McManus, *Handbook of Software Quality Assurance*. 1992.

[224] R. Asfahani and S. Manganello, “Effect of Molybdenum on Transverse Quarterthickness Strength Molybdenum (wt .%),” 6056833, 2000.

[225] A. C. Bannister and S. J. Trail, “Structural Integrity Assessment Procedures for European Industry Sintap Sub-Task 2 . 1 Report : the Significance of the Yield Stress / Tensile Stress Ratio,” 1996.

Appendices

Appendix 1 – Chapter 6: Optimisation of Johnson-Cook material model - deflection tests

A1.1 Results from inverse analysis – P91

A1.1.1 Tables

Table A2.1: Results from the inverse analysis of P91 experimental data using method a: 0 - 1mm (A = 510MPa)

Specimen	A	B	n	m	r
60	510.00	304.97	0.27	1.80	0.0108
61	510.00	303.86	0.22	1.33	0.0098
62	510.00	456.14	0.55	1.77	0.0227
63	510.00	309.98	0.21	2.41	0.0313
64	510.00	335.78	0.21	3.58	0.0282
65	510.00	265.70	0.20	1.64	0.0153
66	510.00	267.05	0.16	1.86	0.0254
67					
68					
69					
Standard deviation	-	59.90	0.12	0.69	0.0079

Table A2.2: Results from the inverse analysis of P91 experimental data using method b: 0 - 1mm (A = $\sigma_{0.2}$)

Specimen	A	B	n	m	r
60	603.43	477.91	0.96	1.75	0.0136
61	597.20	320.14	0.57	0.89	0.0104
62	550.74	422.17	0.69	0.65	0.0196
63	612.85	325.93	0.61	1.28	0.0352
64	630.84	419.24	0.78	1.54	0.0336
65	622.35	362.51	0.96	0.37	0.0176
66					
67					
68					
69					
Standard deviation	25.86	56.77	0.16	0.49	0.0095

Table A2.3: Results from the inverse analysis of P91 experimental data using method c: 0 - 0.552mm (A = 510MPa)

Specimen	A	B	n	m	r
60	510.00	593.68	0.49	1.66	0.0067
61	510.00	336.01	0.25	2.95	0.0045
62	510.00	530.99	0.54	1.70	0.0181
63	510.00	675.55	0.46	1.67	0.0385
64	510.00	688.53	0.45	1.62	0.0317
65	510.00	380.90	0.32	2.86	0.0157
66	510.00	460.29	0.33	2.20	0.0269
67	510.00	780.39	0.34	1.75	0.0359
68	510.00	418.74	0.15	3.57	0.0147

69	510.00	763.02	0.43	1.66	0.0072
Standard deviation	-	152.87	0.11	0.67	0.0119

Table A2.4: Results from the inverse analysis of P91 experimental data using method d: 0 - 0.552mm ($A = \sigma_{0.2}$)

Specimen	**A**	**B**	**n**	**m**	**r**
60	516.19	451.11	0.42	2.12	0.0061
61	577.72	471.41	0.59	1.37	0.0040
62	473.88	703.69	0.54	1.80	0.0161
63	536.12	703.53	0.54	1.79	0.0387
64	544.82	698.93	0.54	1.80	0.0322
65	515.59	694.34	0.54	1.78	0.0191
66	537.16	696.66	0.54	1.80	0.0280
67	641.21	682.56	0.53	1.78	0.0279
68	622.53	356.78	0.28	2.07	0.0153
69	706.28	186.03	0.36	2.90	0.0033
Standard Deviation	66.58	176.90	0.09	0.38	0.0118

Table A2.5: Results from the inverse analysis of P91 experimental data using method e: u_a - 0.552mm ($A = \sigma_{0.2}$)

Specimen	**A**	**B**	**n**	**m**	**r**
60	554.54	623.69	0.67	1.73	0.0006
61	583.49	454.98	0.60	1.18	0.0019
62	478.11	695.87	0.54	1.79	0.0017
63	539.89	695.88	0.54	1.80	0.0034
64	548.49	698.76	0.54	1.79	0.0037
65	515.35	696.93	0.53	1.80	0.0071
66	574.94	514.94	0.55	1.26	0.0006
67	641.21	685.42	0.53	1.78	0.0145
68	625.72	681.85	0.51	1.68	0.0139
69	730.33	318.24	0.76	1.87	0.0025
Standard Deviation	68.03	126.22	0.08	0.23	0.0049

*Table A2.6: Results from the inverse analysis of P91 experimental data using method f: u_a - 0.552mm (A = 0.85*UTS)*

Specimen	**A**	**B**	**n**	**m**	**r**
60	545.90	535.93	0.58	1.58	0.0007
62	498.16	617.10	0.56	1.71	0.0009
63	565.18	576.10	0.55	1.43	0.0036
64	566.85	578.74	0.53	1.56	0.0029
65	570.43	452.90	0.58	1.68	0.0007
67	690.81	474.68	0.57	1.39	0.0105
68	698.17	392.96	0.58	1.32	0.0068
Standard Deviation	69.46	74.60	0.02	0.14	0.0034

*Table A2.7: Results from the inverse analysis of P91 experimental data using method g: u_a - 0.865mm (A = 0.85*UTS)*

Specimen	A	B	n	m	r
60	583.64	356.16	0.64	1.56	0.0041
62	525.06	365.03	0.48	1.35	0.0046
63	617.47	305.81	0.59	1.83	0.0083
64	627.35	380.68	0.69	1.54	0.0101
65	608.47	247.60	0.62	1.80	0.0037
Standard Deviation	36.66	48.68	0.07	0.18	0.0026

A1.2 UTS Estimations – P91

A1.2.1 Tables

Table A2.8: UTS estimations using the optimised Johnson-Cook values and the Considére criterion for method a: 0 - 1mm (A = 510MPa)

Specimen	True UTS (MPa)	True strain at UTS	Engineering strain at UTS	Engineering UTS (MPa)
Experimental	-	-	0.08	680.00
Initial estimate	704.38	0.168	0.18	595.45
60	590.42	0.058	0.06	557.15
61	546.42	0.052	0.05	518.73
62	586.61	0.120	0.13	520.28
63	648.07	0.051	0.05	615.85
64	685.57	0.056	0.06	648.23
65	574.51	0.043	0.04	550.33
66	613.18	0.037	0.04	590.91
67				
68				
69				
Standard Deviation	43.61	0.03	0.03	45.19

Table A2.9: UTS estimations using the optimised Johnson-Cook values and the Considére criterion for method b: 0 - 1mm (A = $\sigma_{0.2}$)

Specimen	True UTS (MPa)	True strain at UTS	Engineering strain at UTS	Engineering UTS (MPa)
Experimental	-	-	0.08	680.00
Initial estimate	704.38	0.168	0.18	595.45
60	533.75	0.001	0.00	533.22
61	446.93	0.051	0.05	424.71
62	356.52	0.085	0.09	327.47
63	536.97	0.045	0.05	513.34
64	575.08	0.040	0.04	552.53
65	-	-		
66				
67				
68				

69				
Standard Deviation	78.78	0.03	0.03	83.73

Table A2.10: UTS estimations using the optimised Johnson-Cook values and the Considére criterion for method c: 0 - 0.552mm (A = 510MPa)

Specimen	**True UTS (MPa)**	**True strain at UTS**	**Engineering strain at UTS**	**Engineering UTS (MPa)**
Experimental	800.00	0.225	0.08	680.00
Initial estimate	704.38	0.168	0.18	595.45
60	661.77	0.156	0.17	566.18
61	665.28	0.061	0.06	625.91
62	620.85	0.145	0.16	537.05
63	714.80	0.170	0.19	603.05
64	719.10	0.171	0.19	606.07
65	665.08	0.079	0.08	614.56
66	680.75	0.097	0.10	617.82
67	826.30	0.151	0.16	710.49
68	773.96	0.051	0.05	735.48
69				
Standard Deviation	60.04	0.05	0.05	59.35

Table A2.11: UTS estimations using the optimised Johnson-Cook values and the Considére criterion for using method d: 0 - 0.552mm (A = $\sigma_{0.2}$)

Specimen	**True UTS (MPa)**	**True strain at UTS**	**Engineering strain at UTS**	**Engineering UTS (MPa)**
Experimental	-	-	0.08	680.00
Initial estimate	710.22	0.168	0.18	600.39
60	649.35	0.106	0.11	584.04
61	583.14	0.104	0.11	525.54
62	703.13	0.210	0.23	569.95
63	741.56	0.186	0.20	615.70
64	744.51	0.183	0.20	620.00
65	721.56	0.191	0.21	596.10
66	738.57	0.184	0.20	614.44
67	800.33	0.147	0.16	690.92
68	778.66	0.162	0.18	662.20
69	739.36	0.022	0.02	723.27
Standard Deviation	59.74	0.05	0.06	55.51

Table A2.12: UTS estimations using the optimised Johnson-Cook values and the Considére criterion for method e: ua - 0.552mm (A = $\sigma_{0.2}$)

Specimen	True UTS (MPa)	True strain at UTS	Engineering strain at UTS	Engineering UTS (MPa)
Experimental	-	-	0.08	680.00
Initial estimate	704.38	0.168	0.18	595.45
60	665.17	0.172	0.19	560.06
61	543.9	0.096	0.10	494.11
62	700.49	0.206	0.23	570.08
63	739.61	0.183	0.20	615.92
64	754.53	0.182	0.20	628.98
65	725.66	0.191	0.21	599.49
66	589.9	0.12	0.13	523.19
67	801.52	0.148	0.16	691.26
68	790.21	0.159	0.17	674.05
69	673.35	0.0009	0.00	672.74
Standard Deviation	78.76	0.06	0.06	63.01

*Table A2.13: UTS estimations using the optimised Johnson-Cook values and the Considére criterion for using method f: ua - 0.552mm (A = 0.85*UTS)*

Specimen	True UTS (MPa)	True strain at UTS	Engineering strain at UTS	Engineering UTS (MPa)
Experimental	-	-	0.08	680.00
Initial estimate	704.38	0.17	0.18	595.45
60	623.63	0.14	0.15	543.79
62	655.71	0.18	0.20	547.70
63	642.68	0.14	0.15	557.60
64	668.90	0.14	0.15	580.93
65	612.15	0.10	0.11	553.90
67	669.37	0.08	0.08	617.91
68	649.03	0.09	0.09	594.95
Standard Deviation	20.11	0.03	0.04	25.71

*Table A2.14: UTS estimations using the optimised Johnson-Cook values and the Considére criterion for using method g: ua - 0.865mm (A = 0.85*UTS)*

Specimen	True UTS (MPa)	True strain at UTS	Engineering strain at UTS	Engineering UTS (MPa)
Experimental	-	-	0.08	680.00
Initial estimate	704.38	0.17	0.18	595.45
60	554.20	0.06	0.06	524.02
62	526.35	0.08	0.09	483.94
63	600.79	0.04	0.04	576.08
64	583.89	0.05	0.05	556.53
65	567.97	0.02	0.02	554.50
Standard Deviation	25.47	0.02	0.02	32.18

A1.2.2 Graphs

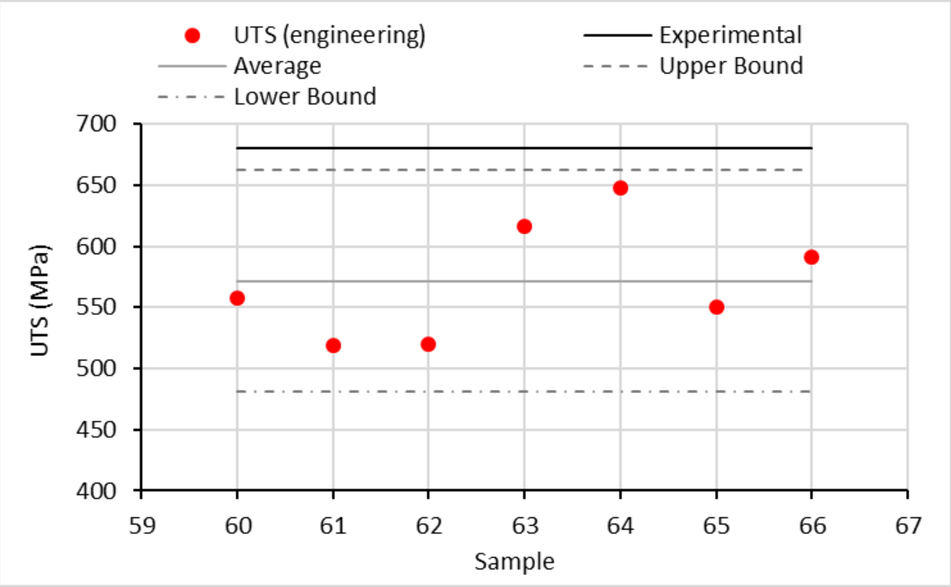

Figure A2.1: Graph showing the UTS estimations using the optimised Johnson-Cook values and the Considére criterion for a: 0 - 1mm (A = 510MPa). Bounded by the double standard deviation of the data

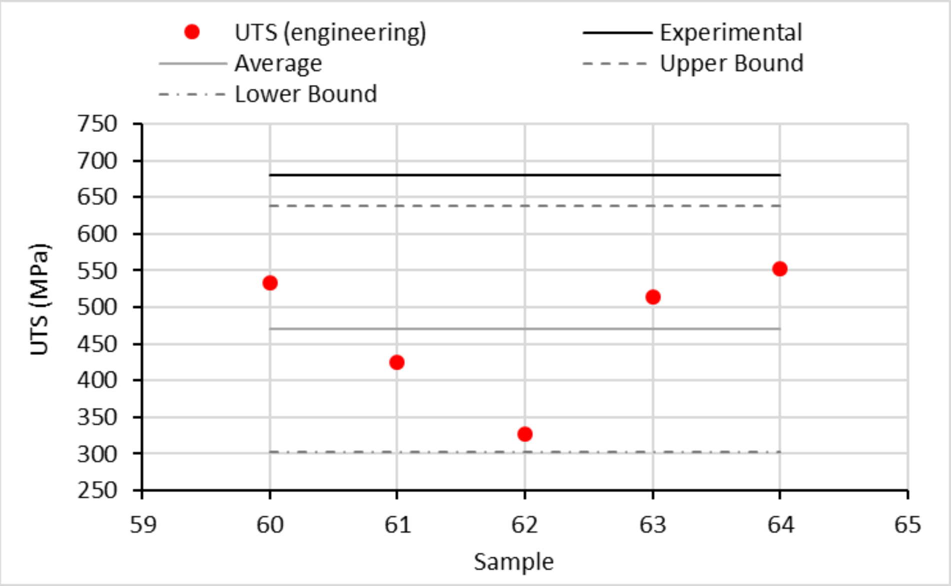

Figure A2.2 Graph showing the UTS estimations using the optimised Johnson-Cook values and the Considére criterion for method b: 0 - 1mm (A = $\sigma_{0.2}$). Bounded by the double standard deviation of the data

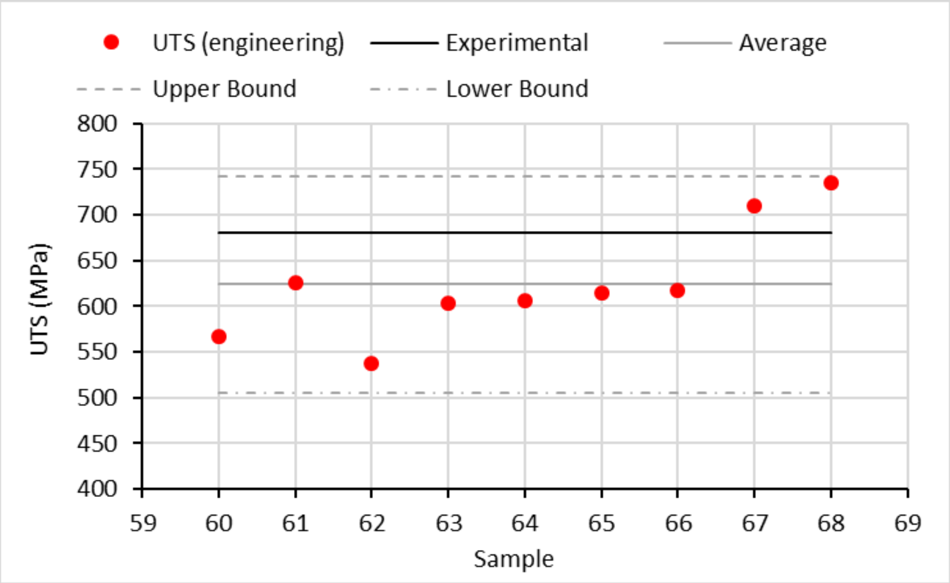

Figure A2.3 Graph showing the UTS estimations using the optimised Johnson-Cook values and the Considére criterion for method c: 0 - 0.552mm (A = 510MPa). Bounded by the double standard deviation of the data

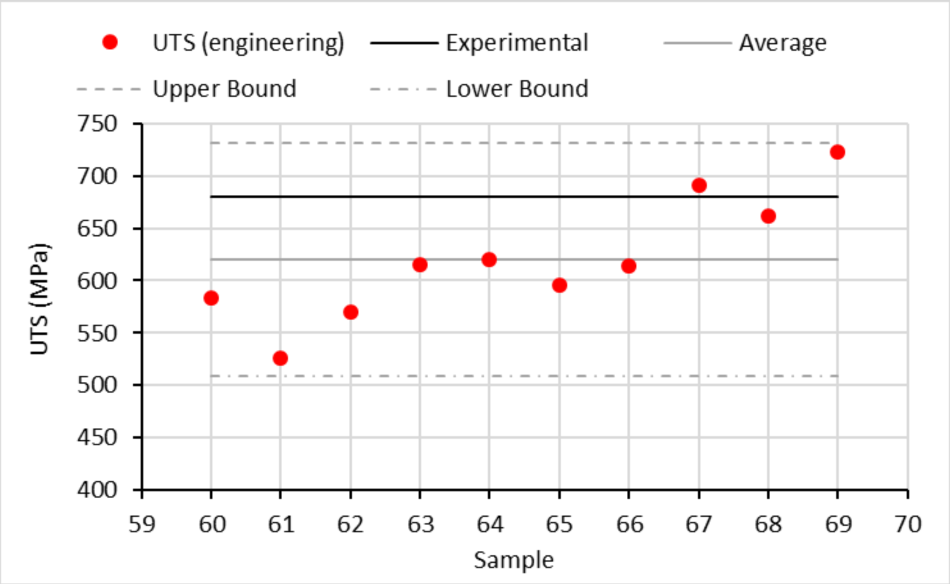

Figure A2.4 Graph showing the UTS estimations using the optimised Johnson-Cook values and the Considére criterion for method d: 0 - 0.552mm (A = $\sigma_{0.2}$). Bounded by the double standard deviation of the data

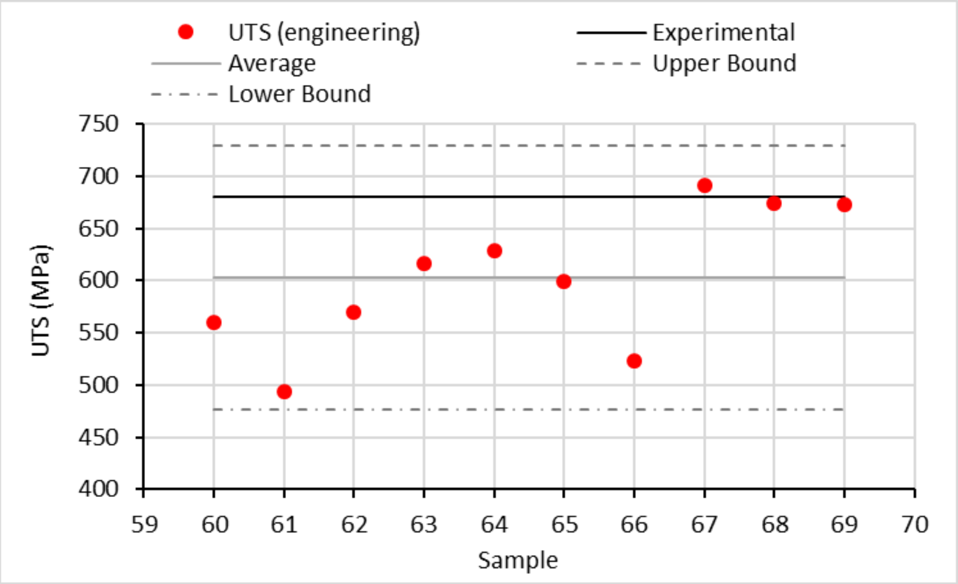

Figure A2.5 Graph showing the UTS estimations using the optimised Johnson-Cook values and the Considére criterion for method e: u_a *- 0.552mm (A =* $\sigma_{0.2}$*). Bounded by the double standard deviation of the data*

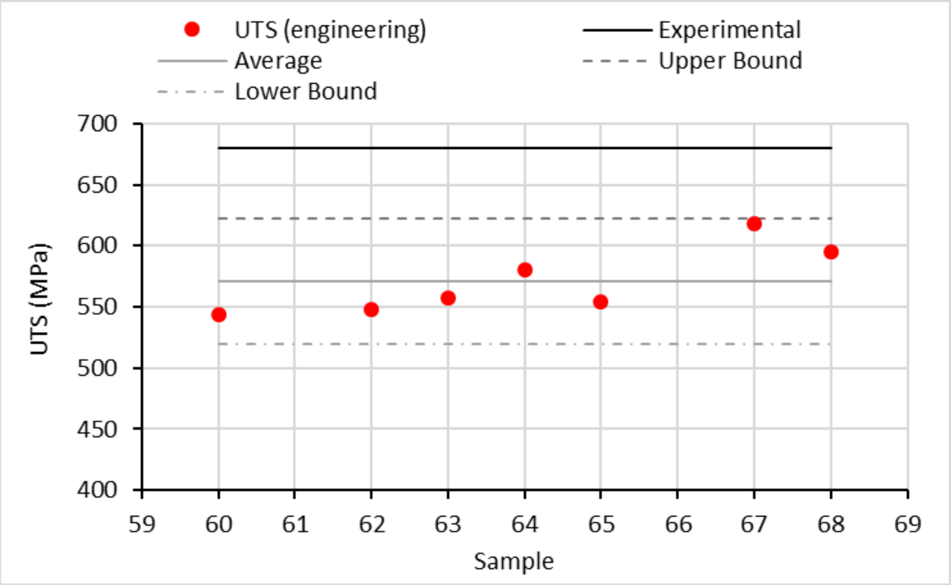

Figure A2.6 Graph showing the UTS estimations using the optimised Johnson-Cook values and the Considére criterion for method f: u_a *- 0.552mm (A = 0.85*UTS). Bounded by the double standard deviation of the data*

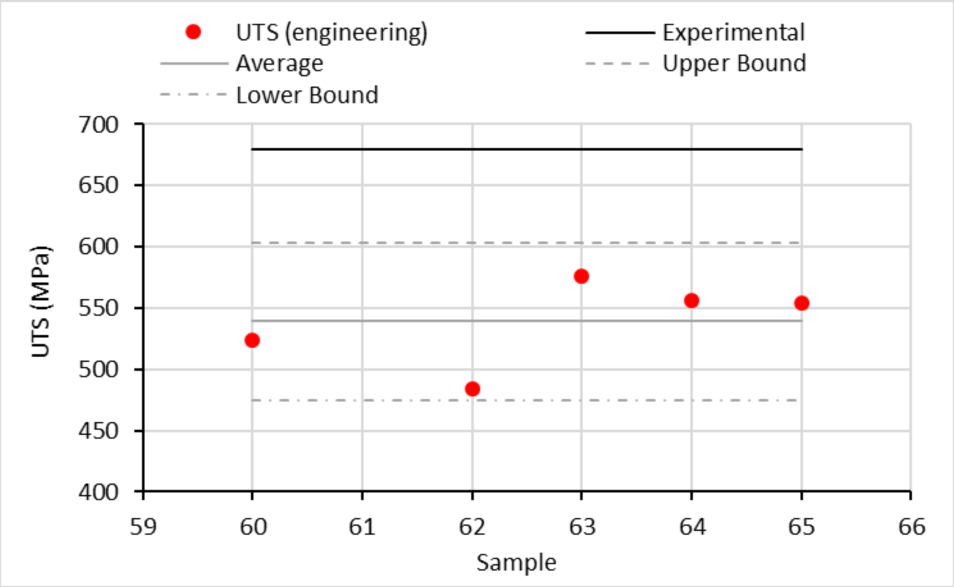

*Figure A2.7 Graph showing the UTS estimations using the optimised Johnson-Cook values and the Considére criterion for method g: u_a - 0.865mm (A = 0.85*UTS). Bounded by the double standard deviation of the data*

A1.3 Results from inverse analysis – Eurofer97

A1.3.1 Tables

Table A2.15: Results from the inverse analysis of Eurofer97 small punch data using method e: u_a *- 0.552mm (*$A = \sigma_{0.2}$*).*

Specimen	**A**	**B**	**n**	**m**	**r**
001	472.27	489.01	0.49	2.26	0.0016
002	487.90	474.62	0.48	2.44	0.0010
003	467.96	363.83	0.30	2.03	0.0019
004	504.76	569.99	0.56	1.84	0.0005
005	362.42	829.71	0.55	1.36	0.0015
006	460.83	599.98	0.49	2.05	0.0017
007	463.41	397.00	0.30	2.02	0.0023
008	491.24	690.84	0.52	1.72	0.0048
009	287.71	823.75	0.35	1.58	0.0026
010	375.08	870.78	0.47	1.61	0.0019
011	434.49	693.58	0.52	1.70	0.0014
Standard deviation	64.16	169.31	0.09	0.30	0.0011

Table A2.16: Results from the inverse analysis of Eurofer97 small punch data using method f: u_a *- 0.552mm (A = 0.85*UTS).*

Sample	**A**	**B**	**n**	**m**	**r**
001	477.45	532.68	0.54	1.71	0.0016
002	499.02	528.87	0.56	1.83	0.0010
003	521.50	528.56	0.61	1.73	0.0014
004	508.78	598.02	0.59	1.75	0.0005
005	333.40	712.72	0.44	1.75	0.0012
006	462.41	605.08	0.50	1.80	0.0017
007	525.43	541.47	0.60	1.85	0.0016
008	526.91	578.61	0.57	1.79	0.0029
009	279.34	826.06	0.34	1.75	0.0026
010	360.25	840.71	0.44	1.49	0.0017
011	428.12	681.32	0.50	1.67	0.0013
Standard deviation	82.39	110.47	0.08	0.09	0.0006

*Table A2.17: Results from the inverse analysis of Eurofer97 small punch data using method g: u_a - 0.865mm (A = 0.85*UTS).*

Sample	A	B	n	m	r
001	488.56	582.79	0.62	1.74	0.0017
002	512.11	510.11	0.60	1.75	0.0019
003	521.82	485.77	0.57	2.03	0.0022
004	522.89	450.83	0.55	1.35	0.0016
005	377.12	680.34	0.52	1.64	0.0025
006	478.65	482.80	0.48	2.11	0.0023
007	534.29	445.24	0.56	2.16	0.0019
008	529.12	410.90	0.46	2.19	0.0028
009	330.21	621.38	0.32	1.46	0.0058
010	429.42	678.95	0.52	1.70	0.0071
011	474.30	540.43	0.56	1.43	0.0033
Standard deviation	64.01	89.41	0.08	0.29	0.0017

A1.4 UTS Estimations – Eurofer97

A1.4.1 Tables

Table A2.18: UTS estimations using the optimised Johnson-Cook values and the Considére criterion for Eurofer97 using method e: ua - 0.552 mm (A = $\sigma_{0.2}$).

Specimen	True UTS (MPa)	True strain at UTS	Engineering strain at UTS	Engineering UTS (MPa)
Experimental	-	-	-	666.00
1	621.39	0.138	0.15	541.29
2	633.89	0.128	0.14	557.73
3	590.49	0.080	0.083	545.09
4	644.19	0.162	0.176	547.85
5	650.78	0.298	0.347	483.07
6	662.55	0.176	0.192	555.63
7	606.89	0.087	0.091	556.32
8	699.82	0.196	0.217	575.26
9	670.27	0.220	0.25	537.90
10	729.07	0.263	0.30	560.47
11	655.08	0.218	0.244	526.77
Standard deviation	37.93	0.066	0.079	22.95

*Table A2.19: UTS estimations using the optimised Johnson-Cook values and the Considére criterion for Eurofer97 using method f: ua - 0.552 mm (A = 0.85*UTS).*

Specimen	True UTS (MPa)	True strain at UTS	Engineering strain at UTS	Engineering UTS (MPa)
Experimental	-	-	-	666.00
1	599.59	0.157	0.170	512.47
2	617.68	0.150	0.162	531.64
3	612.15	0.145	0.156	529.52
4	645.57	0.175	0.191	541.93
5	635.09	0.231	0.260	504.10
6	646.45	0.178	0.195	541.04
7	633.25	0.148	0.160	546.13
8	656.00	0.158	0.171	560.13
9	690.19	0.217	0.24	555.55
10	694.89	0.243	0.28	544.98
11	655.71	0.210	0.234	531.51
Standard deviation	28.42	0.034	0.042	16.12

*Table A2.20: UTS estimations using the optimised Johnson-Cook values and the Considére criterion for Eurofer97 using method f: ua - 0.865 mm (A = 0.85*UTS).*

Specimen	True UTS (MPa)	True strain at UTS	Engineering strain at UTS	Engineering UTS (MPa)
Experimental	-	-	-	666.00
1	618.09	0.181	0.20	515.76
2	600.07	0.141	0.15	521.15
3	621.32	0.128	0.137	546.67
4	543.18	0.114	0.121	484.66
5	615.82	0.241	0.273	483.94
6	617.35	0.133	0.142	540.47
7	620.65	0.108	0.114	557.11
8	629.40	0.096	0.101	571.79
9	578.04	0.162	0.18	491.59
10	654.37	0.215	0.24	527.78
11	565.03	0.164	0.178	479.56
Standard deviation	30.38	0.04	0.05	30.54

A1.4.2 Graphs

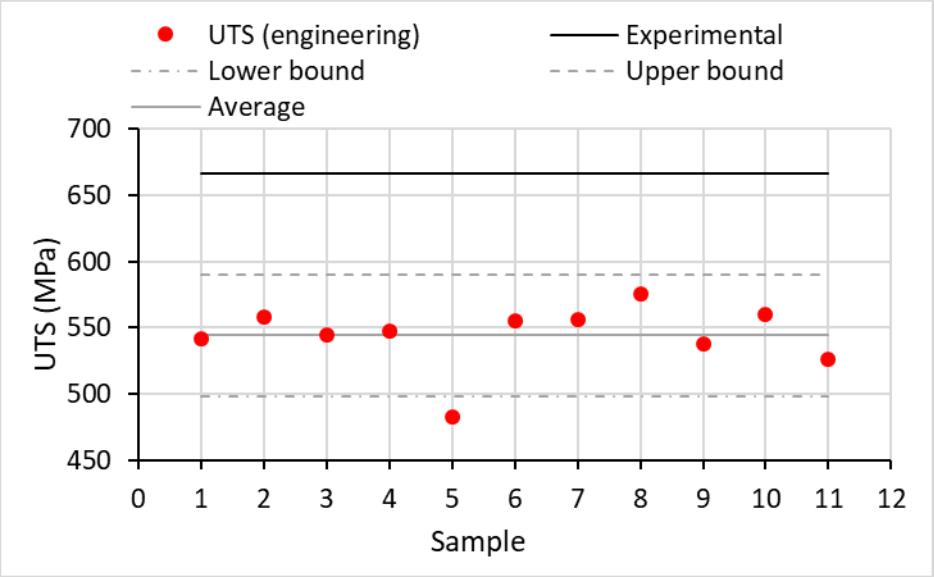

Figure A2.8: Graph showing the UTS estimations using the optimised Johnson-Cook values and the Considére criterion for Eurofer97 using method e: ua - 0.552 mm (A = $\sigma_{0.2}$). Bounded by the double standard deviation of the data.

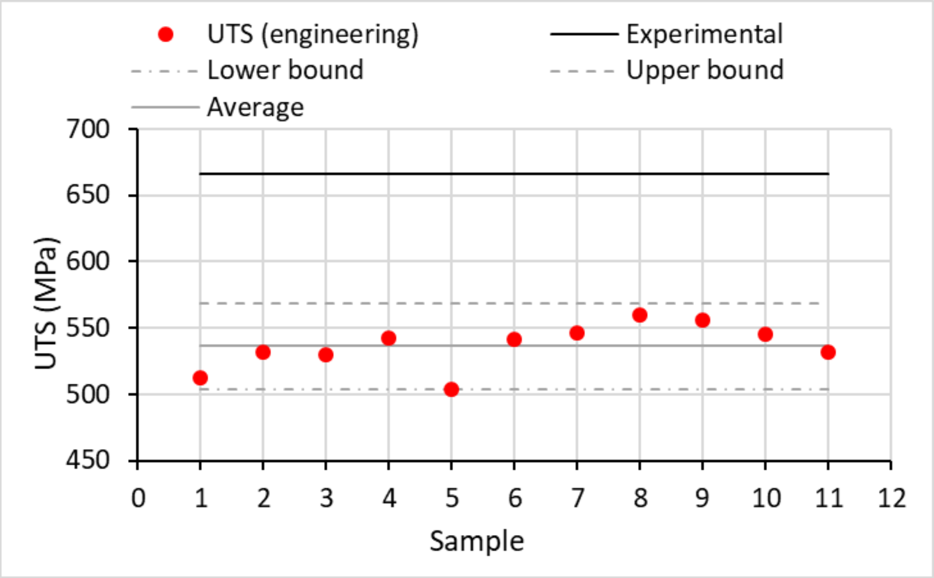

*Figure A2.9: Graph showing the UTS estimations using the optimised Johnson-Cook values and the Considére criterion for Eurofer97 using method f: ua - 0.552 mm (A = 0.85*UTS). Bounded by the double standard deviation of the data.*

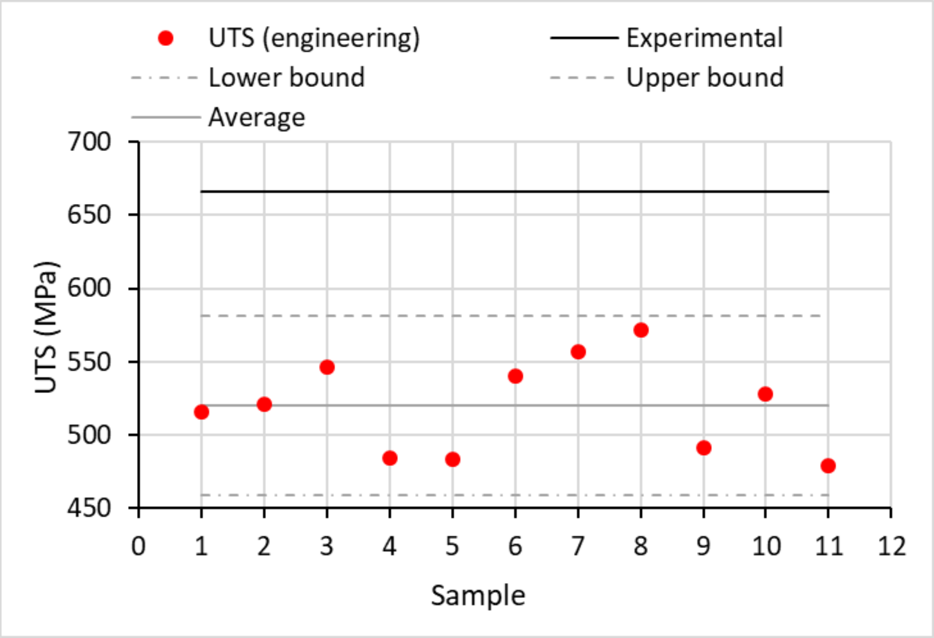

*Figure A2.10: Graph showing the UTS estimations using the optimised Johnson-Cook values and the Considére criterion for Eurofer97 using method g: ua - 0.865 mm (A = 0.85*UTS). Bounded by the double standard deviation of the data.*

Appendix 2 – Python optimisation script

A2.1 Relevant sections of the Python script for Johnson-Cook plasticity optimisation

Creation of material and assignment of properties. Note the Johnson-Cook plasticity constants have been formatted so they can be assigned and changed with the optimisation:

```
# Create material - Eurofer97 and section
mdb.models['Model-1'].Material(name='Eurofer97')
mdb.models['Model-1'].materials['Eurofer97'].Density(table=((7.76e-09,),))
mdb.models['Model-1'].materials['Eurofer97'].Elastic(table=((210000.0, 0.3),))
mdb.models['Model-1'].materials['Eurofer97'].Plastic(hardening=JOHNSON_COOK,
                                                     table=((JC[0], JC[1], JC[2],
JC[3], 1420.0, 25.0),))
```

The following section shows the extraction of data from the simulated results and it being saved to a text file:

```
global iternum
    iternum = 'TEST_0-552_' + np.str(iteration)
    forcename = 'Force N - ' + iternum
    sdispname = 'Sample Deflection mm - ' + iternum
    pdispname = 'Punch Displacement mm - ' + iternum

    itertext = 'C:/temp/' + iternum + '.rpt'
    session.xyDataObjects.changeKey(fromName='RT:Magnitude PI: PUNCH-1 N: 1',
        toName=forcename)
    session.xyDataObjects.changeKey(fromName='UT:Magnitude PI: SAMPLE-1 N: 44',
        toName=sdispname)
    session.xyDataObjects.changeKey(fromName='UT:Magnitude PI: PUNCH-1 N: 1',
        toName=pdispname)

    x0 = session.xyDataObjects[forcename]
    x1 = session.xyDataObjects[sdispname]  # deflection
    x2 = session.xyDataObjects[pdispname]  # displacement

    session.writeXYReport(fileName=itertext, xyData=(x0, x1, x2))

    # ABAQUS JOB COMPLETED AND RESULTS COLLECTED
```

The saved simulation data is then read by the script and formatted to allow for comparison with the experimental data:

```
    # simulated data
    simfile = np.loadtxt(itertext, skiprows=4)
    simdata = np.array(simfile)
    simy1 = simdata[:, 1]  # force
    simy = simy1 / 1000
    simx = simdata[:, 2]  # displacement
    simdisp = np.linspace(0.06, 0.865, 50)
    simint = np.interp(simdisp, simx, simy)
    sim_data_array = np.array(simint)
    iteration = iteration + 1
    return sim_data_array
```

The objective function is then defined, in which the error function is created, and the current Johnson-Cook plasticity constant estimates are saved to a text file along with the error function values for that specific set of estimates:

```
# experimental data
def obj(x, *ex_data_array):
    print('x = ', x)
    JCcalcs = modelfunc(x)
    print('simulated data array:', JCcalcs)
    r = np.sum((JCcalcs - ex_data_array) ** 2)
    print('r = ', r)
    global filenum
    JC_A = np.float(x[0])
    JC_B = np.float(x[1])
    JC_n = np.float(x[2])
    JC_m = np.float(x[3])
    r_and_JC = (JC_A, JC_B, JC_n, JC_m, r)
    print(r_and_JC)
    np.savetxt('C:/temp/r_and_JC_TEST_ua-865_' + np.str(filenum) + '.txt',
r_and_JC, delimiter=' ')
    filenum = filenum + 1
    return r
```

definition of the “main” function. This opens the experimental data text file and extracts of the force-deflection curve. The initial constant estimates are input here. Finally the optimisation function is defined and run:

```
def main():
    exfile = np.loadtxt('C:/temp/MATDB_68.txt', skiprows=1)
    exdata = np.array(exfile)
    exx = exdata[:, 1]  # displacement
    exy1 = exdata[:, 0]  # force
    exy = exy1/1000
    exdisp = np.linspace(0.06, 0.865, 50)
    exint = np.interp(exdisp, exx, exy)
    ex_data_array = np.array(exint)

    x0 = np.array([641.11, 666.4, 0.459, 1.615])

    res = optimize.minimize(obj, x0, method='Nelder-Mead', args=ex_data_array)
    print('res = ', res['x'])
    modelfunc(res['x'])
```

The full script is available on request.

A2.2 Relevant sections of the Python script for Johnson-Cook damage optimisation

The script for the Johnson-Cook plasticity was adapted for the optimisation of Johnson-Cook damage. However, the majority of it remained unchanged aside from in a few key areas:

The creation, definition and input of the Johnson-Cook constants:

```
# SET UP AND RUN ABAQUS JOB
# Create material - Eurofer97 and section
mdb.models['Model-1'].Material(name='P91')
mdb.models['Model-1'].materials['P91'].Density(table=((7.76e-09,),))
mdb.models['Model-1'].materials['P91'].Elastic(table=((210000.0, 0.3),))
mdb.models['Model-1'].materials['P91'].Plastic(hardening=JOHNSON_COOK,   # 0.865
(0.85*Rm)
                                                     table=((583.64, 356.16, 0.64,
1.56, 1420.0, 25.0),))
mdb.models['Model-1'].materials['P91'].JohnsonCookDamageInitiation(
    table=((JC[0], JC[1], JC[2], JC[3], 0.0, 1420.0, 25.0, 1.0),))
mdb.models['Model-1'].materials['P91'].johnsonCookDamageInitiation.DamageEvolution(
    type=DISPLACEMENT, table=((0.025,),))
```

The definition of the displacement range analysed:

```
# simulated data
    simfile = np.loadtxt(itertext, skiprows=4)
    simdata = np.array(simfile)
    simy1 = simdata[:, 1]  # force
    simy = simy1 / 1000
    simx = simdata[:, 2]  # displacement
    simdisp = np.linspace(0.865, 1.68, 50)
    simint = np.interp(simdisp, simx, simy)
    sim_data_array = np.array(simint)
    iteration = iteration + 1
    return sim_data_array
```

And finally, the definition of the initial estimates:

```
def main():
    exfile = np.loadtxt('C:/temp/MATDB_60.txt', skiprows=1)
    exdata = np.array(exfile)
    exx = exdata[:, 1]  # displacement
    exy1 = exdata[:, 0]  # force
    exy = exy1/1000
    exdisp = np.linspace(0.865, 1.68, 50)
    exint = np.interp(exdisp, exx, exy)
    ex_data_array = np.array(exint)

    x0 = np.array([0.05, 0.8, -0.44, -0.046])
    res = optimize.minimize(obj, x0, method='Nelder-Mead', args=ex_data_array)
    print('res = ', res['x'])
    modelfunc(res['x'])
```